

In-situ Scanning Transmission X-ray Microscopic Study of Dry Methane Reforming Catalysts

Dissertation

Zur Erlangung des Grades eines Doktors der Naturwissenschaften
der Fakultät für Chemie und Biochemie
der Ruhr-Universität Bochum

vorgelegt von

Abbas Beheshti Askari

Mülheim an der Ruhr

This study was performed at the Max-Planck Institute for Chemical Energy Conversion (CEC) in Mülheim an der Ruhr in the period of November 2016 to January 2020. This project was supervised by Prof. Dr. Serena DeBeer.

Referentin: Prof. Dr. Serena DeBeer

Korreferent: Prof. Dr. Martin Muhler

Prüfer: Prof. Wolfgang Kleist

Table of Contents

| | |
|--|-----|
| Acknowledgements | VI |
| Abbreviations | VII |
| Chapter Contributions | IX |
| Chapter 1 Introduction | 1 |
| Chapter 2 In-situ X-ray Microscopy reveals particle dynamics in a NiCo dry methane reforming catalyst under operating conditions | 36 |
| <i>Supporting Information</i> | 53 |
| Chapter 3 In situ X-ray emission and high-resolution X-ray absorption study applied to Ni-based Bimetallic Dry Methane Reforming Catalyst | 66 |
| <i>Supporting Information</i> | 82 |
| Chapter 4 The promoting effect of Co vs. Fe on the activation and catalytic activity of supported Ni-based bimetallic dry methane reforming catalysts | 95 |
| <i>Supporting Information</i> | 112 |
| Conclusions | 124 |
| Outlook | 126 |
| List of publications | 127 |

Acknowledgements

I would like to thank my supervisor at the Max Planck Institute for Chemical Energy Conversion (CEC), Prof. Serena DeBeer for giving me the opportunity to join her research group and work on this interesting PhD project. I'm grateful for her comments, suggestions, discussions and support during this project. I would like to acknowledge my second supervisor at Ruhr Universität Bochum (RUB), Prof. Martin Muhler for his scientific support and useful discussions. Finally, I would like to thank Prof. Kleist for his kind support.

In addition, I would like to thank all team members at MPI CEC, RUB and collaborators for their kind help and especially to:

- Mustafa al Samarai for his professional support during the STXM and hard X-ray beamtimes at SOLEIL, SLS and Spring-8. Furthermore, his help during data collection/discussion, STXM holder design and revising the manuscripts are greatly acknowledged.
- Bruno Morana for his help during the STXM beamtimes, advice and providing the STXM nanoreactors.
- Lukas Tillmann for measuring the activity of the DMR catalysts investigated in this project and TPR measurements at RUB.
- Norbert Pfänder for the STEM-EDX measurements. Christian W. Lehmann from the Max-Planck-Institut für Kohlenforschung for supporting the STEM measurements.
- Bidyut Sarma at the Max-Planck-Institut für Kohlenforschung for performing the TPR measurements.
- Noushin Arshadi for doing the nitrogen physisorption experiments at RUB.

I would like to thank my family and specially my mother and Yusef for assisting me during the hard times. Last but not least, I would like to thank Fatemeh for her continues support during my PhD project.

Abbreviations

CEC = Chemical Energy Conversion
RUB = Ruhr Universität Bochum
NG = Natural Gas
CH₄ = methane
CO₂ = carbon dioxide
DMR = Dry Methane Reforming
H₂ = hydrogen
CO = carbon monoxide
FT = Fisher Tropsch
XAS = X-ray Absorption Spectroscopy
DFT = Density Functional Theory
XES = X-ray Emission Spectroscopy
XRD = X-ray diffraction
STXM = Scanning Transmission X-ray Spectroscopy
VE = Valence Electrons
E_F = Fermi Energy
XANES = X-ray Absorption Near Edge Structure
EXAFS = Extended X-ray Absorption Fine Structure
TFY = Total Fluorescence Yield
TEY = Total Electron Yield
E_{ex} = excitation energy
FZP = Fresnel Zone Plates
OSA = Order Sorting Aperture
OD = Optical Density
RGB = Red, Green, and Blue
SiN_x = silicon nitride
VtC = valence to core
REXS = Resonant Elastic X-ray Scattering
RIXS = Resonant Inelastic X-ray Scattering
DM = diamond monochromator
DCM = double crystal monochromator
HRM = high resolution monochromator
FM = focussing mirror
TEM = Transmission Electron Microscopy
STEM = Scanning Transmission Electron Microscope

EDX = Energy Dispersive X-ray

XPS = X-ray Photoelectron Spectroscopy (XPS)

Micro Electro Mechanical System

TPR = Temperature Programmed Reduction (TPR)

OD = Optical Density (OD)

HERFD XAS= High Energy Resolution Fluorescence Detected X-ray absorption spectroscopy

Chapter Contributions

The experiments performed in this study were supported by our collaborators and their contributions are detailed below.

Chapter 2:

Serena DeBeer supervised this study. Mustafa al Samarai assisted the synthesis of the DMR catalysts. Bruno Morana designed and produced the nanoreactor, the holder and, the gas-system. Mustafa al Samarai helped with the design of the holder, and Aleksandra Wandzilak helped with the design of the gas-system. Lukas Tillmann performed the activity measurements. Norbert Pfänder performed the STEM-EDX measurements. Mustafa al Samarai helped collecting and processing the STXM data at SOLEIL and SLS. Rachid Belkhou, Benjamin Watts, Mustafa al Samarai and Bruno Morana helped during beamtimes. Serena DeBeer and Martin Muhler helped in planning the experiments, discussing the data, and interpreting the data.

Chapter 3:

Frank M. F. de Groot and Ad M. J. van der Eerden from Utrecht University (Netherlands) provided the hard X-ray reactor used in this study. Lukas Tillmann performed the activity measurements. Nozomu Hiraoka and Hirofumi Ishii supported our beamtime application and helped with the experiments. Mustafa al Samarai assisted during the beamtimes by collecting and processing the data. Norbert Pfänder performed the STEM-EDX measurements on the DMR catalysts. Mustafa al Samarai, Martin Muhler and Serena DeBeer helped in planning the experiments, discussing the data, and interpreting the data.

Chapter 4:

Mustafa al Samarai assisted with the synthesis of the DMR catalysts. Bruno Morana, Benjamin Watts and Mustafa al Samarai helped during the STXM beamtimes. Bruno Morana designed and produced the nanoreactor, the holder and, the gas-system. Norbert Pfänder performed the STEM-EDX measurements. Christian W. Lehmann from the Max-Planck-Institut für Kohlenforschung supported the STEM measurements. Noushin Arshadi helped with performing the physisorption measurements. Serena DeBeer and Martin Muhler helped in the planning experiments, discussing the data, and interpreting the data.

1. Motivation

Fossil fuels are considered to be the main source of energy for the modern society [1-3]. The most prominent resources used to harvest the ever-increasing energy demand of the modern society are I: Natural Gas (NG), II: Petroleum, and III: Coal [4-6]. In general, during the combustion process of fossil fuels, hydrocarbons are oxidized while water and carbon dioxide (CO_2) are emitted. Moreover, due to the higher hydrogen to carbon ratio for NG significantly less CO_2 is emitted when compared to the combustion of petroleum and coal [7]. Surprisingly, up to a few decades ago, the tremendous effects of greenhouse gasses e.g. CO_2 , methane (CH_4) and nitrous oxide (N_2O) on the atmosphere was not recognized. As a consequence, the concentration of these harmful gasses in the atmosphere increased dramatically. Figure 1 shows the significant increase in the concentration of CO_2 following the industrial revolution from approximately 280ppm to 400ppm [8]. The ever-growing concerns regarding the worldwide climate change has resulted in the desire to reduce and eventually eliminate the emission of greenhouse gasses into the atmosphere.

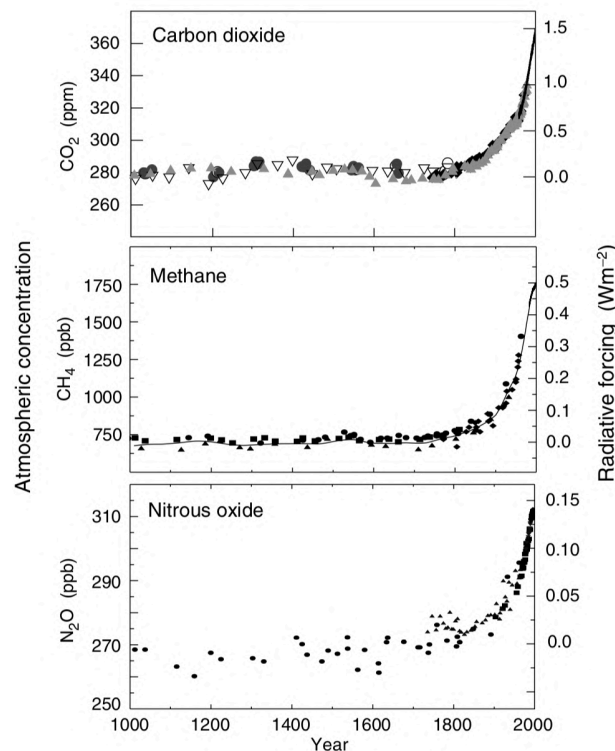


Figure 1: The evolution in the CO_2 , CH_4 and N_2O concentration are shown for the past 1000 years. For this first time in history, following the industrial revolution, the CO_2 concentration exceeded the 300ppm threshold. Printed with permission from IPCC. Climate Change 2001: The Scientific Basis. Contribution of Working Group I to the Third Assessment Report of the Intergovernmental Panel on Climate Change, Figure 2(a). Cambridge University Press [8].

Therefore, the development of renewable energy sources with high energy densities has been the focus of various research groups that seek to reduce the primary source of greenhouse emissions [9-11]. More specifically, aiming to decrease the devastating impact of the main contributors to the greenhouse effect namely, CO₂ and CH₄, it is of paramount importance to develop catalytic reactions that are able to convert these gasses into environmentally friendly fuels or feedstock for other reactions. One reaction that has received a substantial attention is the Dry Methane Reforming (DMR) process [12-14]. This reaction is exceptionally attractive since it converts a mixture of CO₂ and CH₄ into hydrogen (H₂) and carbon dioxide (CO), and is regarded as a promising candidate in the field of environmentally friendly fuels (eq. 1). The DMR process is highly endothermic (ΔH^0 (25°C) = +247 kJmol⁻¹) and proceeds at relatively high temperatures (T>650°C). The resulting gas-mixture from the DMR reaction can be used as feedstock for various other reactions e.g. Fisher Tropsch (FT) process, ammonia synthesis, and hydrogenation reactions. For example, since the H₂/CO ratio of the DMR reaction is close to unity, it is regarded as an ideal feedstock for the FT reaction [14-15]. The FT reaction involves the conversion of H₂ and CO, also known as syngas, to synthetic liquid fuels [16-17]. However, the DMR reaction is very sensitive to the reaction environment and the used gas composition. For instance, when the DMR reaction temperature is too low, side reactions such as the reverse water-gas-shift reaction, steam reforming of methane, methane decomposition and CO disproportion can occur which reduce the catalytic activity and lifetime of the catalyst (2-5) [15,18-19].

| | | |
|---|--|----------------------------------|
| (1) CH ₄ + CO ₂ ↔ 2H ₂ + 2CO | ΔH^0 (25°C) = +247 kJmol ⁻¹ | Dry methane reforming |
| (2) H ₂ + CO ₂ ↔ H ₂ O + CO | ΔH^0 (25°C) = +46 kJmol ⁻¹ | Reverse water-gas-shift reaction |
| (3) H ₂ O + CH ₄ ↔ 3H ₂ + CO | ΔH^0 (25°C) = +206 kJmol ⁻¹ | Steam reforming of methane |
| (4) CH ₄ ↔ 2H ₂ + C | ΔH^0 (25°C) = +75 kJmol ⁻¹ | Methane decomposition |
| (5) 2CO ↔ C + CO ₂ | ΔH^0 (25°C) = -171 kJmol ⁻¹ | CO disproportion |

Methane reforming reactions are typically operated at elevated temperatures (650-1000 °C) to ensure high syngas yields, while hampering the coke formation [20-21]. Moreover, in the low temperature regime (T<650°C) the DMR catalyst is rapidly deactivated due to coke deposition on the catalytic active phase.

Within this context noble-metal based DMR catalysts have the highest activity towards the DMR reaction and maintain a long lifetime. However, due to their scarcity, a large-scale industrial application is not feasible [22]. As a consequence, many studies have endeavored to develop transition metal-based DMR catalyst with high activity, selectivity, and stability [19, 23-24]. Ni-based catalyst are known to possess the highest activity towards the DMR reaction if compared to other 3d transition metals-based systems [25-26]. In addition, Ni-based catalysts are promising candidates due to their abundance and high selectivity [27]. Nevertheless, their most notorious/prominent drawback is deactivation due to the coking process, which limits the scale up to industrial applications. To circumvent this disadvantage many studies attempted to I: synthesize and develop bimetallic catalysts [28-30], II: use various support materials [31-32], and III: decrease particle size of the active phase [33]. Among these strategies the development of highly active bimetallic DMR catalyst have been very successful with NiCo as the most studied system [26]. Various studies focused on increasing the catalytic activity and preventing the coke deposition on the active phase, whereas the exact catalytic role and structure of each metal was usually not investigated. While the high

methane reforming activity is directly related to the presence of Ni, the exact role of Co remains debatable [30,34-35].

A challenge associated with the synthesis of Ni-based DMR catalysts is the ability to obtain catalysts with high DMR activity, selectivity and resistivity. Firstly, the introduction of a second metal e.g. cobalt and iron, is known to have a promoting role on the catalytic activity of the Ni-based catalyst. Secondly, the activity of DMR catalyst can be increased by decreasing the particle size, which ultimately results in a higher surface area and thus a larger number of available catalytic active sites. Finally, the lifetime of the catalyst can be maintained by supporting the catalytic active phase on various oxide materials. The most frequent used support materials for methane reforming catalysts are Al_2O_3 , SiO_2 , MgO , and TiO_2 .

The mechanism of the DMR process has been extensively studied by many research groups in the last few decades [36-38]. The mechanism that is generally accepted for monometallic Ni/Co and bimetallic NiCo catalysts has been proposed by Takanabe et al. [38]. In this study a combination of in-operando X-ray Absorption Spectroscopy (XAS) and DFT calculations were used to reveal the DMR mechanism on catalyst surfaces. It was suggested that strongly bound O species which originate from the activation of CO_2 on a pure Co surface cause site occupation. This results in the gradual oxidation of the metallic Co particle and eventually leads to deactivation. On the other hand, as a result of the weak oxophilicity of pure Ni catalysts, accumulation of O on the catalysts surface is not preferred. Further, due to the low O coverage the formed carbonaceous species are not removed from the catalyst surface which ultimately leads to carbon deposition on the Ni active sites. Finally, it was illustrated that the bimetallic NiCo catalyst has a balanced kinetics for both CO_2 and CH_4 activation which prevents oxidation of the metals and deactivation due to carbon deposition.

In the last decade in-situ X-ray spectroscopy experiments such as XAS, X-ray Emission Spectroscopy (XES) and X-ray diffraction (XRD), have made a significant progress by the development of the required setups that facilitate probing different types of catalysts under operating conditions [39-43]. These developments allowed the simultaneous elucidation of changes in the electronic state of the catalyst particles under operating conditions. However, precious knowledge regarding the changes in the morphology of the DMR catalyst during the reaction is largely missing due to the limitations of the current state of the experimental setups. By studying the changes in the morphology, combined with elemental distributions in the catalyst active phase under catalyst activation and operating conditions information regarding the role of the present elements on the catalysis can be revealed. Within this context Scanning Transmission X-ray Spectroscopy (STXM) offers the opportunity to probe the changes in the electronic structure and visualizes the variations in the morphology of the catalytic active phase [44-46]. The combination of this spectromicroscopic technique with the required gas-phase setup offers the opportunity to elucidate the role of various elements on the DMR catalysis.

By using element specific X-ray based techniques it is possible to follow the changes occurring during the DMR process. By this approach we aim to understand how the electronic structure and morphology of the catalyst are altered under activation and subsequent DMR conditions. By correlating the data for the monometallic and bimetallic

DMR catalysts we will be able to assign the role of the promotor and follow the changes in the oxidation state of the 3d metals while also searching for intermediate species under reaction conditions. Finally, these findings will allow the development of DMR catalyst with improved activity, selectivity and coke resistance.

1.1 X-ray Spectroscopy

X-ray spectroscopy is a powerful tool to obtain insight into the chemical, electronic and geometric structure of various materials including heterogeneous catalysts. In general, the most notable advantage of X-ray based spectroscopic techniques is their element selectivity which allows studying materials under the required conditions. Furthermore, these measurements provide valuable information about the sample characteristics e.g. electronic structure, oxidation state, coordination, morphology, geometry, and the nature of species under the selected reaction conditions.

X-rays with an energy of a few up to tens of KeV are mainly absorbed through the photoelectric effect. In the first part of this process, a core electron is excited if the energy of the incident X-rays is equal or larger than the core electron binding energy (Figure 2). In the event of X-ray absorption, a core electron is promoted to an unoccupied orbital or the continuum (energy higher than the fermi level) whereby a core-hole is generated in the excited atom. The formed core-hole is very instable and can decay via both radiant and non-radiant relaxation pathways [47-48]. The combination of XAS and XES can be used to study this reaction mechanism in detail [49]. As will be explained in the next sections, XAS and XES yield valuable information about the unoccupied- and occupied orbitals, respectively [50]. Furthermore, when considering heterogeneous catalysts, their catalytic properties are mainly determined by the electronic state of the Valence Electrons (VE) [51-54]. In general, heterogeneous catalysts contain one or multiple transition metals where the partially filled valence band can be studied in detail by XAS and XES.

In this thesis both X-ray absorption and X-ray emission spectroscopies are used to elucidate the properties of the transition metals in the catalyst active phase. These techniques will be described in detail in sections 1.2 (XAS) and 1.7 (XES).

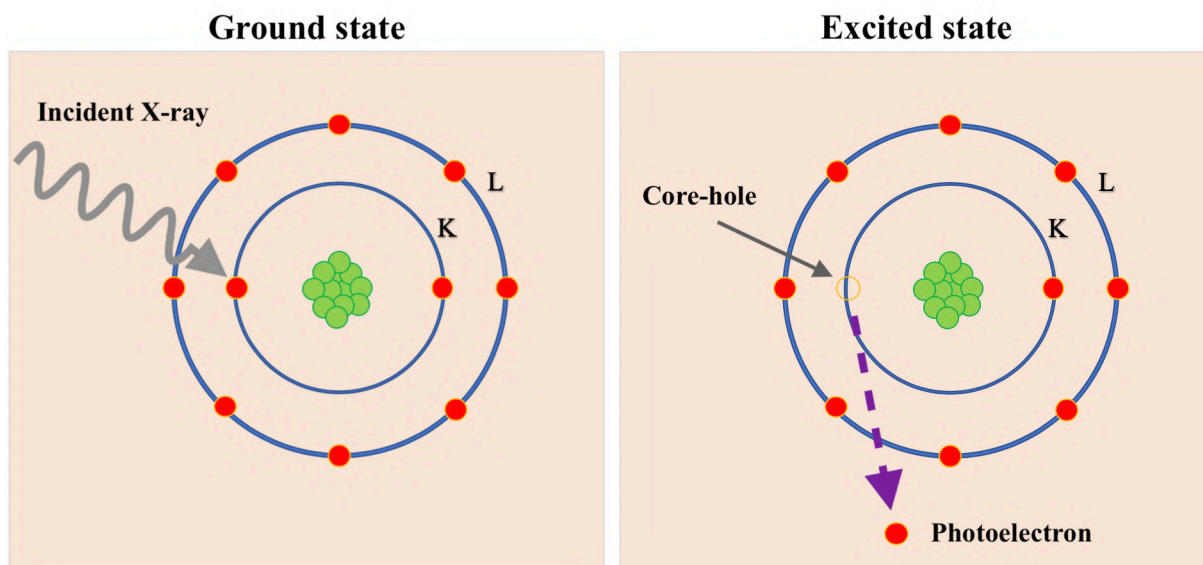


Figure 2: Schematic illustration shows the event of X-ray absorption when the energy of the incident photon is equal or higher than the excitation energy and thus promotes a core electron to higher energies.

1.2 X-ray Absorption Spectroscopy

In the event of X-ray absorption, following the absorption of an X-ray photon an electron is excited to the bound empty density of states (XAS), or to a continuum when the photon energy is higher than the bound energy states (XPS). In general, XAS allows determining the electronic structure and local geometry of the sample of interest [55-58]. Nowadays, this technique is regularly being used in the field of bio-(chemistry), chemistry, semiconductors, earth science and physics to acquire information about the various properties of the sample of interest. This method is extremely sensitive to subtle fluctuations in the oxidation and degree of hybridization of metal and ligand orbitals, implying that its very suitable for in-situ and operando experiments [59-62]. Furthermore, changes in the local symmetry, ligand sphere, and coordination chemistry are directly reflected in the XAS spectra [50]. The recent developments in the in-situ XAS setups has opened the possibility to study the changes in transition metal oxidation state under operating conditions. In this method the absorption cross section is measured as a function of the incident energy and provides information regarding the dipole-allowed transitions which arise from the core-levels to the unoccupied orbitals and into the continuum [63-65].

However, the main challenge associated with a XAS experiment is related to the absorption coefficient (μ) which is directly related to the probability of X-ray absorption by matter. This probability is described by the Lambert-Beer law, eq. 6 [66-67], whereby: I_0 is the incident intensity, I correspond to the transmitted intensity through the sample, μ is the absorption coefficient and d represents the sample thickness.

$$(6) \quad I(E) = I_0(E)e^{-\mu(E)d}$$

For most X-ray energies the absorption coefficient is directly related to the energy. This value can be described by eq. 7 and depends on the sample density (ρ), atomic mass (A), atomic number (Z), and X-ray Energy (E).

$$(7) \quad \mu = \frac{\rho Z^4}{AE^3}$$

Eq. 7 shows that the absorption coefficient is highly dependent on the atomic number and mass, thus suggesting that small deviations can result in values that differ order of magnitudes. In addition, the absorption coefficient decreases when the X-ray energy increases. This strong correlation allows for distinction between elements in a sample.

As aforementioned, during the XAS process a core electron is excited into the unoccupied molecular/atomic orbitals with energies higher than the Fermi Energy (E_F), (Figure 3a). When the incident X-ray energy is tuned to be equal to the core-electron binding energy, a sharp rise in absorption is observed which results in an absorption peak in the XAS spectrum.

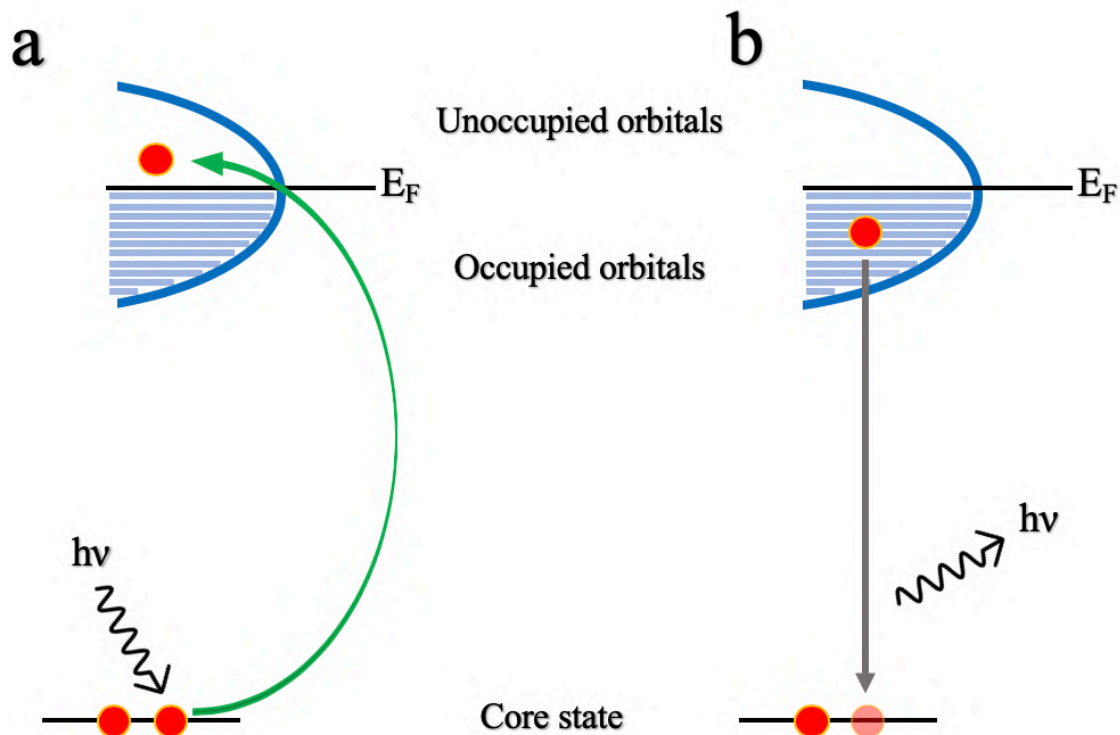


Figure 3: a) During the XAS measurement an electron from a core-state is excited to the unoccupied orbitals which have an energy larger than the fermi energy. The resulting core-hole can be filled with any emission of an electron from the occupied orbitals. b) XES emission involves filling of the core hole by an electron from the higher orbitals which is associated with the emission of a photon.

A typical XAS spectrum can be divided into two spectral regions, as illustrated in Figure 4. The first region is the so-called X-ray Absorption Near Edge Structure (XANES) region [68-69]. The XANES region originates from the excitation of a core electron to the valence and conduction bands [70]. In addition, if hard X-ray absorption experiments on transition metals with partially filled 3-d orbitals are considered, then the XANES region is further split up in the pre-edge and rising-edge regions. These regions provide information about the electronic structure and symmetry of the system [71]. The pre-edge

features arises from the weak dipole-forbidden and quadrupole allowed transitions of the 1s electrons into the valence 3d orbitals. The near-edge or rising-edge region covers the rising-edge, white-line and $\sim+50$ eV above the white-line peak position. The second region involves core excitations to the continuum and is called the Extended X-ray Absorption Fine Structure (EXAFS) region [70]. This region comprises the area with an energy >50 eV above the main-edge and its origin is described by the process where a core electron is excited by X-ray photons with energies higher than the core potential barrier. The EXAFS region contains valuable information regarding the coordination numbers and ligand to metal bond distances [71]. Further, the resulting photoelectron can be represented by an outgoing wave in this process. The next stage involves scattering of the outgoing wave with neighbor (ligand)-atoms which results in either destructive or constructive interference with the ingoing waves. The resulting interference pattern provides information about the local geometry of the atom and is the origin of the observed fine structure in the EXAFS region.

The EXAFS region can be described by the EXAFS fine structure function χ (eq. 8) as,

$$(8) \quad \chi(E) = \frac{\mu(E) - \mu_1(E)}{\Delta\mu_0(E)}$$

Where $\mu(E)$ is the measured absorption coefficient, $\mu_1(E)$ is the absorption coefficient of the isolated atom and $\Delta\mu_0(E)$ represents the rise in absorption $\mu(E)$ at the threshold energy E_0 .

Since EXAFS is described in terms of waves (ingoing and outgoing) which are generated following the absorption process, it is advantageous to convert the X-ray energy into the wavenumber of the photo-electron (k) by,

$$(9) \quad k = \sqrt{\frac{2m(E-E_0)}{\hbar^2}}$$

where m is the electron mass and E_0 is the absorption energy edge. The various frequencies appearing in χ correspond to different neighbour coordination shells which are described by the EXAFS equation,

$$(10) \quad \chi(k) = \sum \frac{N_j f_j(k) e^{-2k^2 \sigma_j^2}}{k R_j^2} \sin[2kR_j + \delta_j(k)]$$

where $f(k)$ and $\delta(k)$ are the scattering properties of the neighboring atoms, N represents the number of neighbor atoms, R is the distance to the neighbor atom and σ^2 is the disorder in the neighbor distance.

The state-of-the-art high resolution XAS beamlines in combination with high-brilliance third generation synchrotron facilities allow us to study the fine structures in both the XANES and EXAFS by offering the possibility to select incident energy from wide energy range.

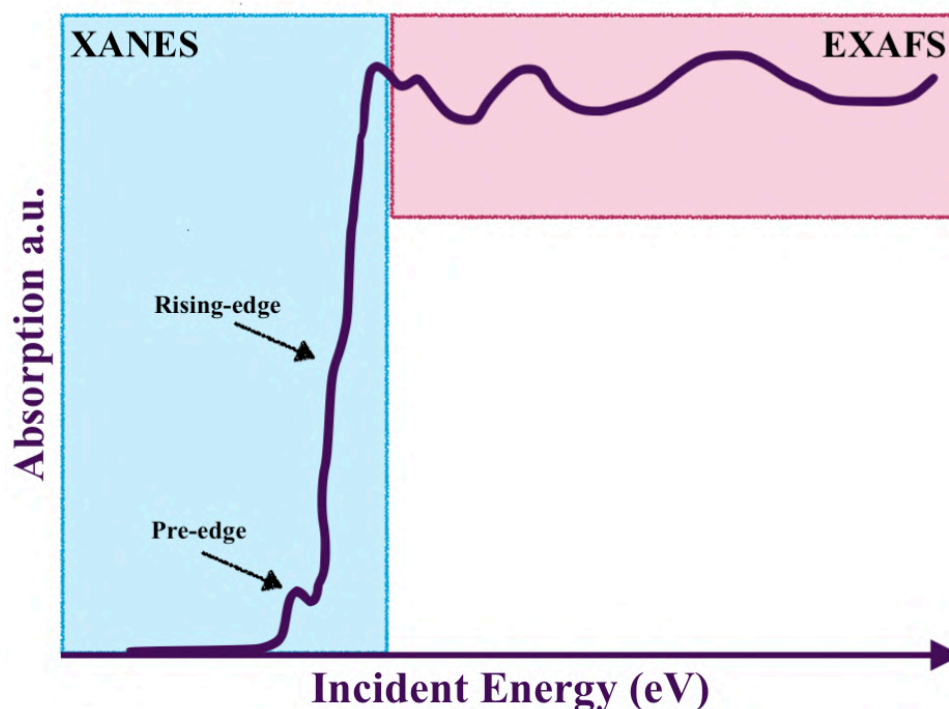


Figure 4: The obtained XAS spectrum can be divided into two parts. The XANES region provides information about the species and oxidation state of the element while the EXAFS region gives valuable information about the local geometry of the sample e.g. distance to neighbor atom and which type atoms are in the proximity.

1.3 XAS detection modes

The XAS spectrum is directly correlated to the probability of a core electron excitation to empty orbitals by varying the excitation energy. In general, an absorption spectrum is collected either in the: I: Transmission mode, II: Total Fluorescence Yield (TFY) mode, or III: Total Electron Yield (TEY) mode [72].

In the transmission mode, the X-ray beam is focused on the sample of interest and the transmission signal is detected. Hereby, the intensity of the beam before (I_0) and after (I) the sample are measured to obtain the transmitted intensity as shown in Figure 5. Upon the X-ray transmission process the beam is attenuated to a certain extent according to the Lambert-Beer law, eq. 6. According to this equation, a specimen with a relatively large thickness suffers from a higher attenuation and subsequent lower transmission intensity. For instance, X-rays with an energy smaller than 1 KeV have an attenuation length of $<1 \mu\text{m}$, suggesting that for soft X-ray (50-2000 eV) based experiments the sample has to be extremely thin. As a consequence, the transmission of soft X-rays through a relatively thick particle ($>1\mu\text{m}$) is saturated and the peaks are significantly suppressed and broadened [73]. On the contrary, for hard X-rays (3500-20000 eV) these effects are generally ignored due to their relatively longer attenuation length and thus results in a higher transmission signal.

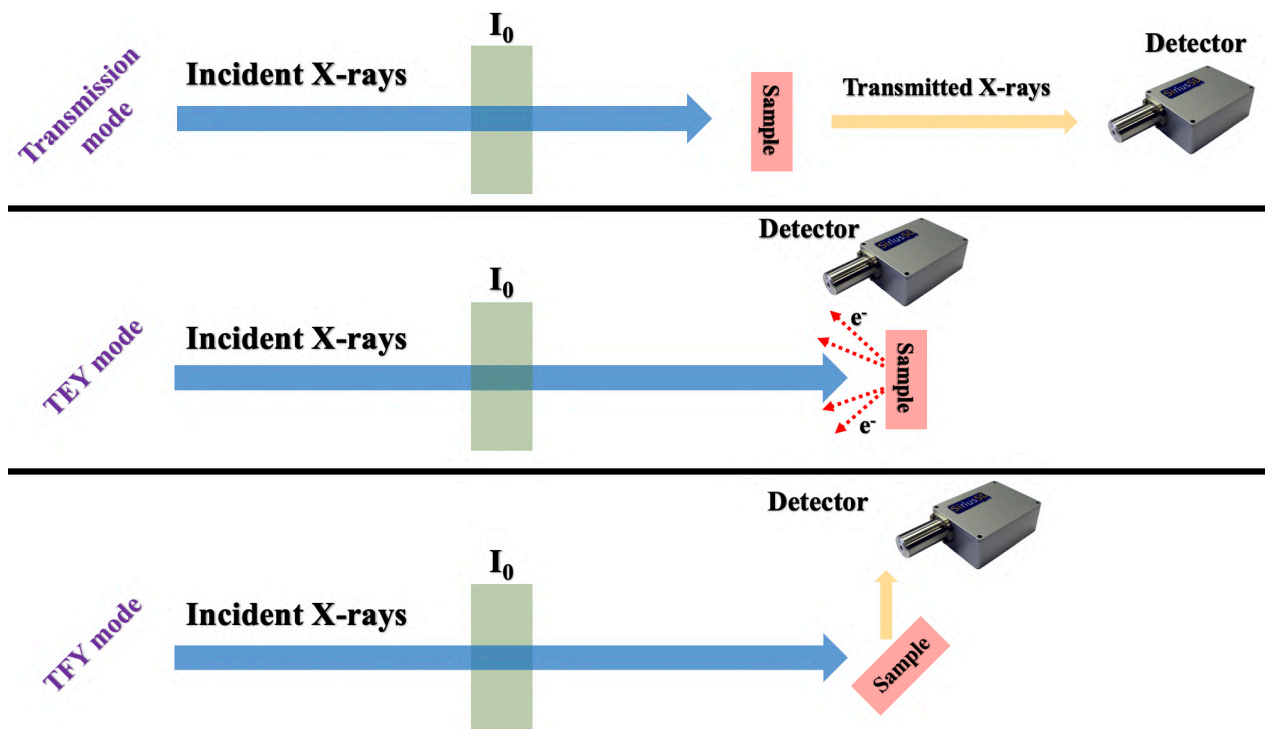


Figure 5: Illustration showing the three different measuring modes used during XAS measurements. For the transmission mode, first the intensity before the sample (I_0) is determined. In this mode the transmission through the sample is measured by the detector whereby the obtained transmission signal is converted to absorption by the Lambert-Beer law. For the total electron yield mode (TEY) the I_0 before the sample is determined, and the emitted/scattered electrons the sample are detected by the detector. Finally, for the total fluorescence yield (TFY) mode the fluorescence of the sample after interacting with X-rays is detected.

Next, in the TFY mode XAS spectra are measured by detecting the scattered photons from the sample [74-75]. In this process, following the absorption of X-rays by the core electron, core-holes are created. Subsequently, electrons from higher orbitals emit and fill the formed hole. More specifically, following the emission process a fluorescence photon is emitted/scattered. In this mode photons with broad energy spectrum are detected which originate from all possible radiative channels. Nevertheless, despite the undesired re-absorption effects a significant advantage of the TFY relative to the transmission mode is its smaller sensitivity towards saturation effects which leads to distorted XAS spectra.

Finally, in the case of the TEY mode the total number of electrons (photo, Auger and secondary electrons) ejected from the sample as a result of X-ray absorption are measured [76-77]. The number of ejected electrons is proportional to the excitation energy and it is relatively straightforward to detect the ejected electrons. However, specimens with large bandgap or insulators can inhibit the TEY measurement. Also, samples with a large bandgap hinder the flow of charge and hence reduce the signal intensity. Consequently, samples with this property experience the so-called charging phenomenon and are not suitable for TEY measurements. Finally, the ejection of electrons from the sample obliges the use of conductive samples to prevent any unwanted effects due to the sample charging.

1.4 Core-hole state

The formation of a core-hole during a XAS experiments occurs as a result of the excitation of an electron from a core level to empty density of states e.g. valance orbitals or to the continuum [78-79]. The first stage in this process involves the promotion of a core electron into the empty density of states below the ionization threshold or Fermi level by absorption of an X-ray photon. The core-hole is very unstable and has a finite lifetime which is in the order of a couple of femtoseconds and decays via a relaxation process. This process is described by the Heisenberg uncertainty principle, eq. 11 [80].

$$(11) \quad \Delta x \cdot \Delta p = h/4\pi$$

Next, the formed core-hole can be filled via two different decay pathways, I: X-ray fluorescence (radiative decay), II: Auger electron emission (non-radiative decay) [81-82]. In the fluorescence pathway an electron from the valence shell relaxes and fills the core-hole and a photon is emitted. However, in the case of Auger decay an electron from the higher shell fills the core-hole and the excess energy associated within this process causes the excitation of another electron to higher orbitals. As illustrated in Figure 6, Auger and fluorescence yields modes are dependent on the atomic number [83]. In the case of Auger decay pathway, the decay probability decreases with increasing atomic number. This implies that light elements are more prone to the creation of Auger electrons. On the contrary, the fluorescence decay pathway is dominant for the heavier elements.

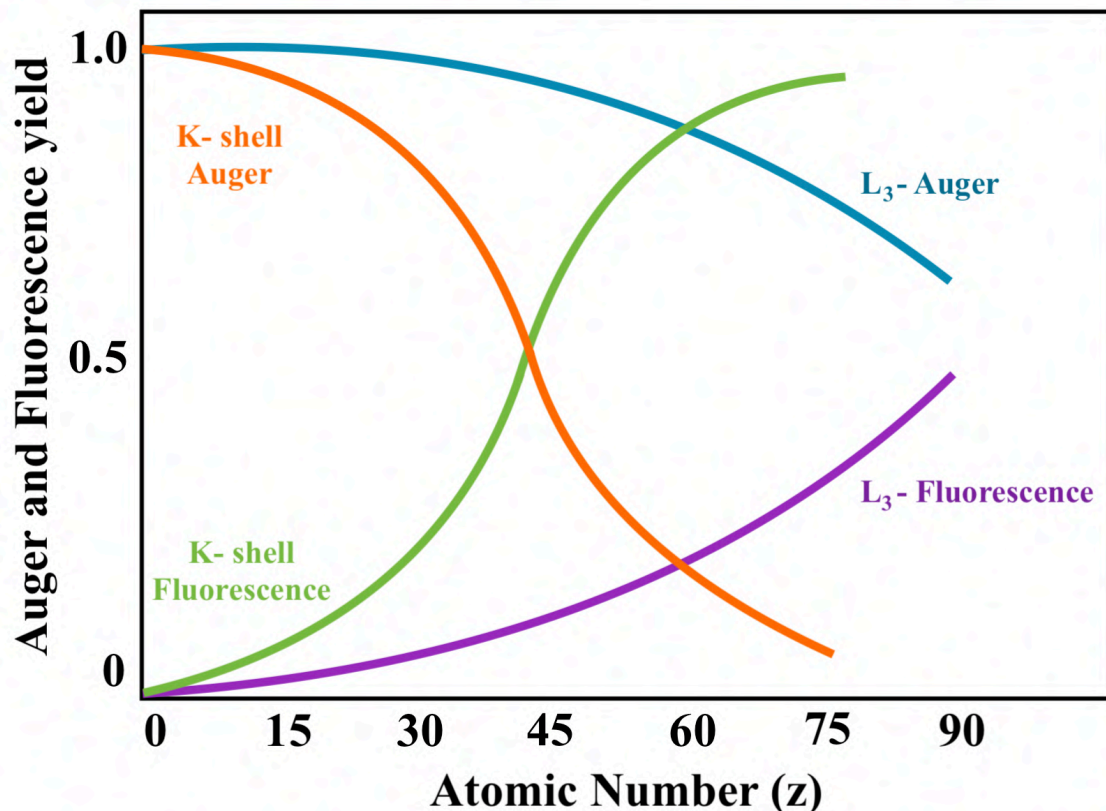


Figure 6: The probabilities of Auger and fluorescence decay as a function of the atomic number [83]. In this scheme it is shown that with increasing atomic number the Auger emission probability decreases while fluorescence probability increase.

1.5 Synchrotron radiation facility

The ability to perform XAS and XES measurements demands the use of synchrotron radiation facility's that are capable of providing: I: high flux, II: very monochromatic beam and III: high brightness [84-86]. In addition, the flux originating from a synchrotron radiation facility is orders of magnitude higher than in house instruments. Further, XAS and XES are both resonant based techniques which demand the use of synchrotron radiation. Resonant implies that the excitation energy (E_{ex}) has exactly the same value as the difference between the ground state and the higher level. The probability for a resonant radiation is orders of magnitude lower if compared to non-radiative decay process. In addition, since the spectra are measured in a small energy region, the use of third generation synchrotron radiation facility's that provide a high flux and brilliance is required.

The development, improvement and upgrade of synchrotrons has facilitated performing challenging experiments that were previously not possible. Figure 7 shows a schematic presentation of a synchrotron radiation facility and depicts the components that are involved. A synchrotron consists of the following parts [87]:

- I: Electron gun**
- II: Linear accelerator**
- III: Booster Synchrotron**
- IV: Storage ring**
- V: Bending magnets**
- VI: Insertion devices**
- VII: optics and experimental hutch**
- VIII: Beamline**

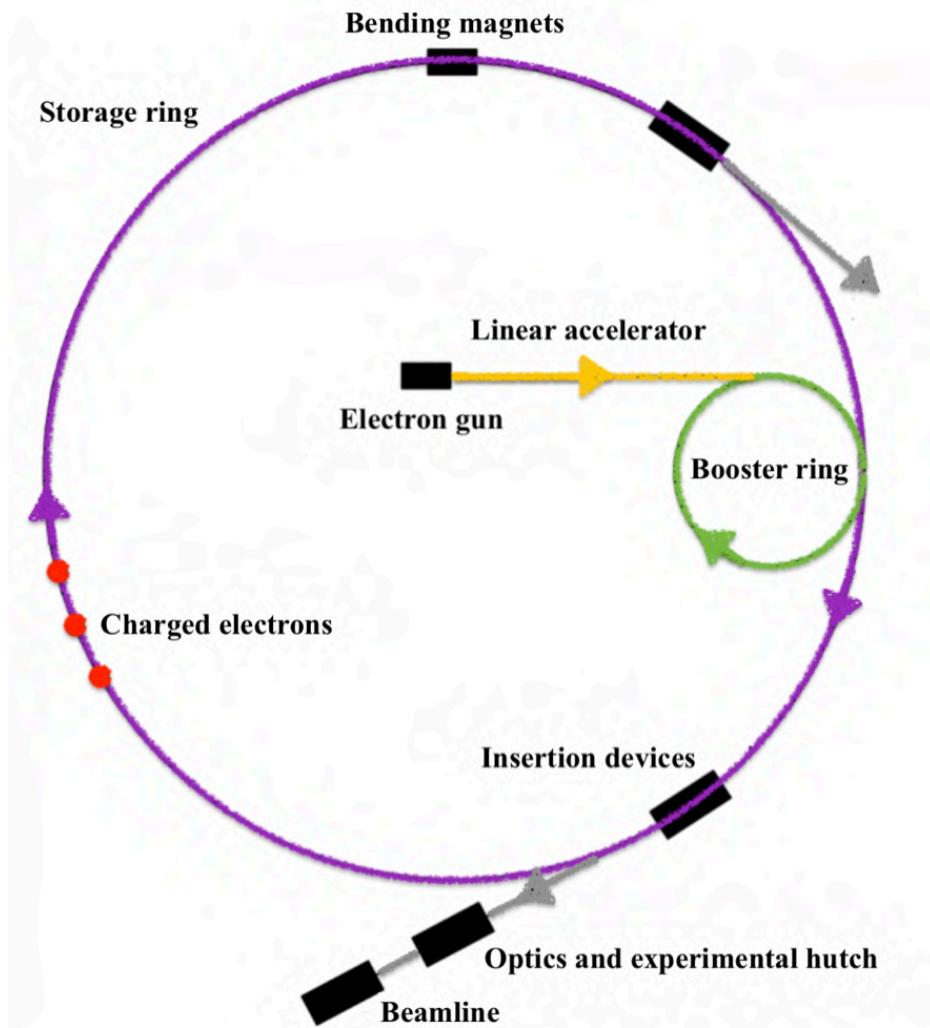


Figure 7: a) All components of a synchrotron radiation facility are illustrated.

The first stage of producing X-rays from a synchrotron involves the emission of electrons from the electron gun. The produced electrons are subsequently accelerated to the speed of light in the linear accelerator. Next, the electrons are transferred to the booster ring which allows further acceleration. The electrons are later injected into the storage ring which is a largest part of the synchrotron and has a circular shape. The electrons are stored under vacuum environment and allows the storage for many hours. The storage ring also contains many bending magnets and insertion devices (series of alternating magnets e.g. wigglers and undulators) that can produce X-rays each time an electron passes through them, see Figure 8 [88]. The produced X-rays are directed through optics in the experimental hutch to select the desired X-ray properties that are required for the experiment taking place in the beamline. In this work the Swiss Light Source (Switzerland) and Soleil (France) synchrotron radiation facilities were used to perform the in-situ STXM experiments.

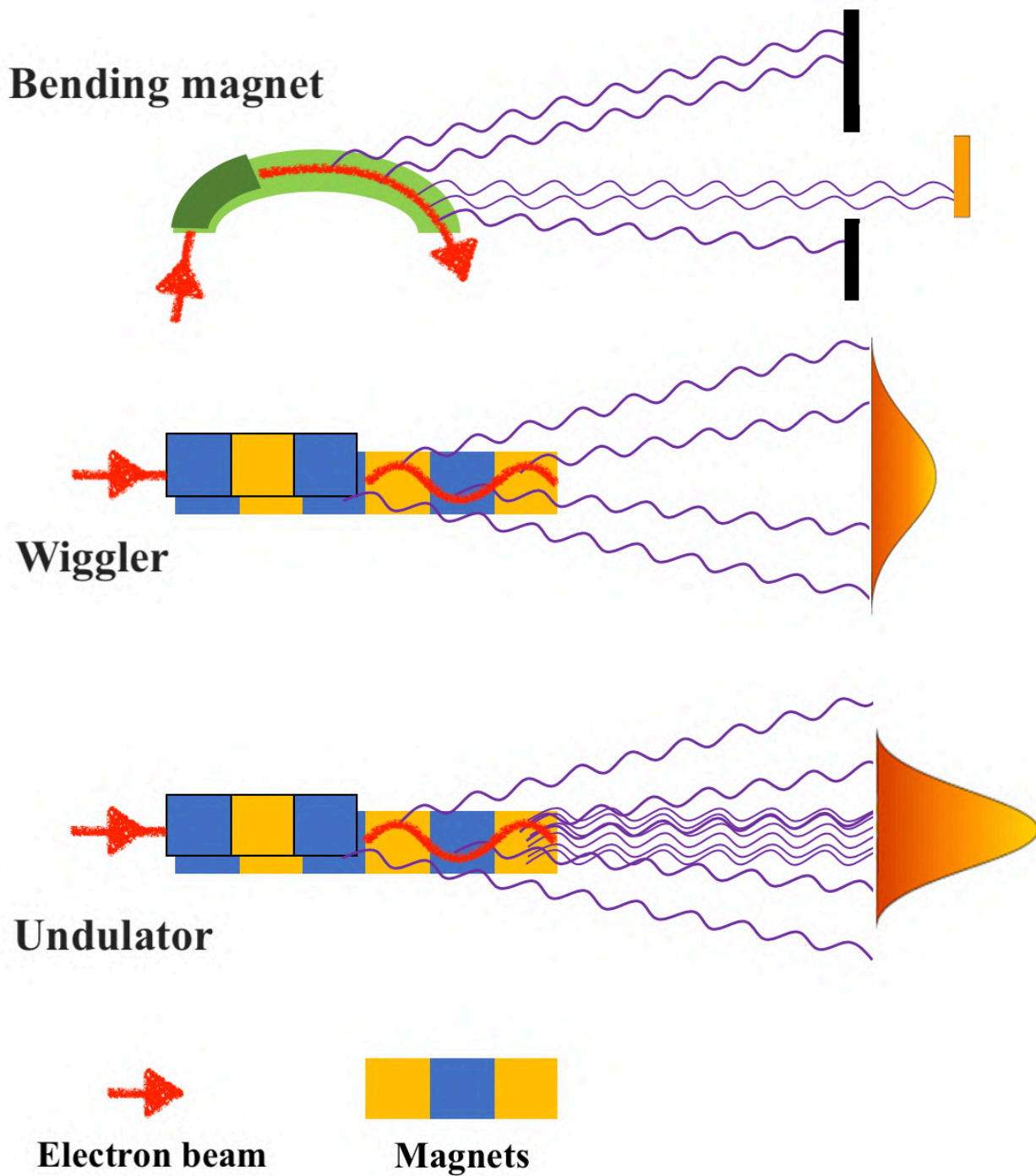


Figure 8: In a synchrotron radiation facility the electrons are guided to travel through bending magnets, wigglers and undulators in the storage ring. When electrons are passed through the magnetic field with opposite magnetic poles (green and orange), X-rays are generated.

1.6 Scanning Transmission X-ray Microscopy

STXM is a soft X-ray based technique that combines spectroscopy with microscopy and covers the absorption edges of elements with an energy ranging from 100-2500 eV [89-91]. In addition, this technique provides information on the morphology and electronic properties of a sample [92]. The intense absorption peak that dominate the soft X-ray region are dipole allowed 2p to 3d transitions [52,93].

In this thesis the L-edges of Ni, Co and Fe in the respective NiO/ γ -Al₂O₃, NiCoO/ γ -Al₂O₃ and NiFeO/ γ -Al₂O₃ are studied by STXM. These experiments are carried out at the state-of-the-art beamlines at high-brilliance third generation synchrotron facilities. Nevertheless, one of the requirements for the STXM experiment is a thin specimen whereby the X-ray is attenuated by less than 80% and therefore the experiments are carried out under high vacuum ($\sim 10^{-5}$ bar).

The optical elements in a STXM microscope which are installed in a specially designed STXM measurement chamber are illustrated in Figure 9. The high spatial resolution (~ 30 nm) is achieved by the resolution of the used Fresnel Zone Plates (FZP). The FZP is made of circular diffractive grating which allows focusing the incident X-rays to a single point on the sample. These delicate plates are made of hundred's small concentric golden rings which are supported on silicon nitride which is X-ray transparent. In recent years there have been many attempts by various research groups to increase the spatial resolution of the zone plate by for instance decreasing the outermost zone thickness by means of controlling the lithographic fabrication process [94-96]. During the interaction between the incident X-rays and the FZP, the light is constructively diffracted by all the concentric rings at the diffraction limited spot.

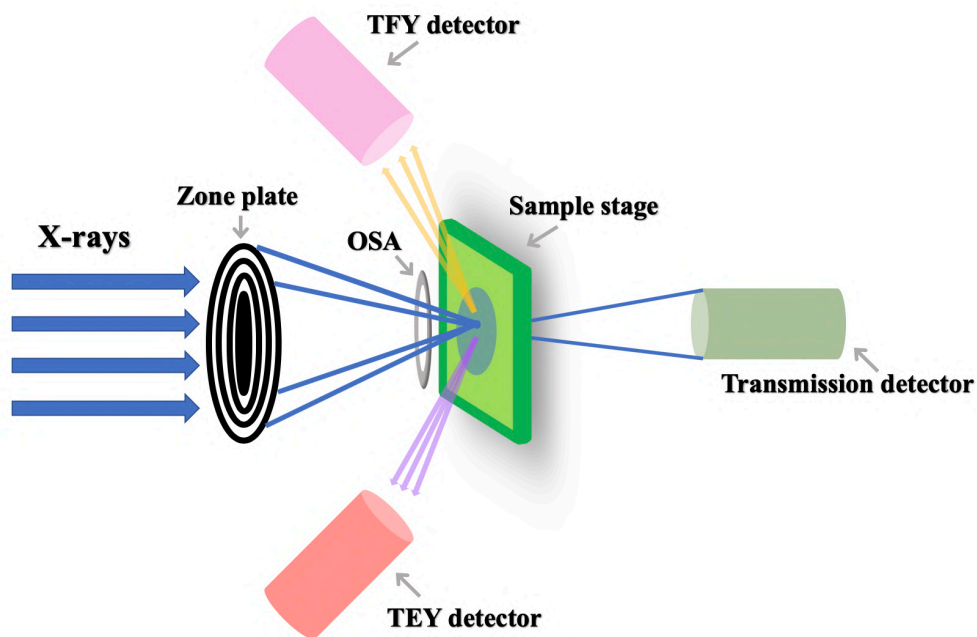


Figure 9: During STXM experiment incident X-rays are focused by the zone plate to the surface of the specimen. All the orders of light except for the first order are blocked by the Order Sorting Aperture (OSA) before reaching the focal point on the sample. In addition to the transmission mode, TFY and TEY detectors are also optional. The state-of-the-art sample stage allows raster scanning the sample in two dimensions.

The next optical element is called the Order Sorting Aperture (OSA) which is positioned just before the sample position (Figure 9). To prevent image artefacts the OSA filters the 1st order light and blocks all the remaining. On the sample plate the stage moves in two dimension (X and Y) and the transmission signal is measured on a selected number of points on the X and Y axis. In addition, the stage is mobile in the Z-axis along the propagation of X-rays and this movement is needed to find the focal point for the selected X-ray energy. In the transmission mode the particle is selected based on I. the dimensions, II. thickness, III. elemental distribution, and IV. Shape. Depending on both the spatial resolution of STXM and the energy of the X-rays, particles are generally selected in the range of 0.2 to 5 μm . The sample is raster scanner through the focal point while a Photo Multiplier Tube (PMT) detector situated to the back of the sample stage detects the transmitted photons. The STXM data is acquired and analyzed by aXiss2000 software (<http://unicorn.mcmaster.ca/aXis2000.html>).

The STXM data are processed by collecting the transmitted X-ray signal from all the selected points and converting the data in the STXM software to a 2D image. Besides, imaging mode also the so-called stacking mode can be used during STXM measurements that provides additional information regarding the presence of different chemical species in a sample. In the stack mode the transmission is acquired from incident energy range covering a few eV's before the rising edge, the main edges and up to $\sim +20$ eV in the post-edge region. The resulting images stack is firstly aligned and then converted into an Optical Density (OD) map. Next, the so called spectral elemental maps are processed by subtracting the pre-edge image from the image obtained at the edge of the element of interest. The resulting elemental maps contain essential information regarding the elemental distributions, morphology of the catalyst particles under ambient, in-situ and operando conditions. Finally, Red, Green, and Blue (RGB) elemental distributions maps are created by aligning the images of two or three different elements or species of interest.

The STXM experiments in this thesis were performed at HERMES beamline at SOLEIL synchrotron radiation facility and the PolLux beamline at the Swiss Light Source at the Paul Scherrer Institute (SLS-PSI) by using nanoreactors supplied by NanoInsight b.v. Table 1 summarizes some of the important parameters for both beamlines.

| | HERMES | PolLux |
|--------------------------------|---------------------|---------------------|
| Energy range (eV) | 70-2500 | 250-1600 |
| Spectral resolution | >5000 | >3000 |
| Polarization | Circular and linear | Circular and linear |
| Spatial resolution (nm) | 25 | 20 |

Table 1: Most important parameters of the HERMES (SOLEIL) and PolLux (SLS) beamlines.

The schematic layout of the HERMES beamline including the energy source, collimating mirror, apertures, monochromator, grating 1, entrance slit, grating 2, exit slit, zone plate and sample is depicted in Figure 10.

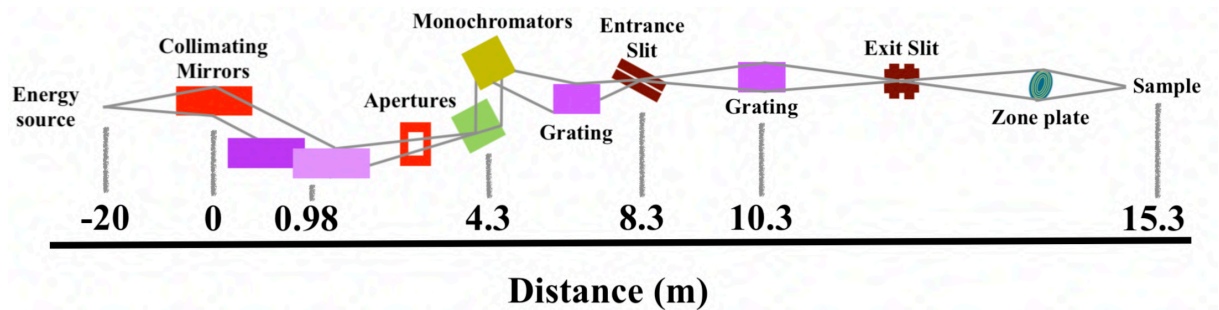


Figure 10: Schematic representation of the spectro-microscopy HERMES beamline at Soleil synchrotron.

In addition, the optical elements in the STXM chamber at HERMES beamline and the recently developed gas-phase setup at the MPI-CEC are shown in Figure 11a and b, respectively. More specifically, the used gas-phase setup has four mass flow controllers that allows the mixing of up to three gasses with the desired concentrations. After producing the mixture, the gasses are first passed through gas inlet pipe before reaching the nanoreactor which contains the sample.

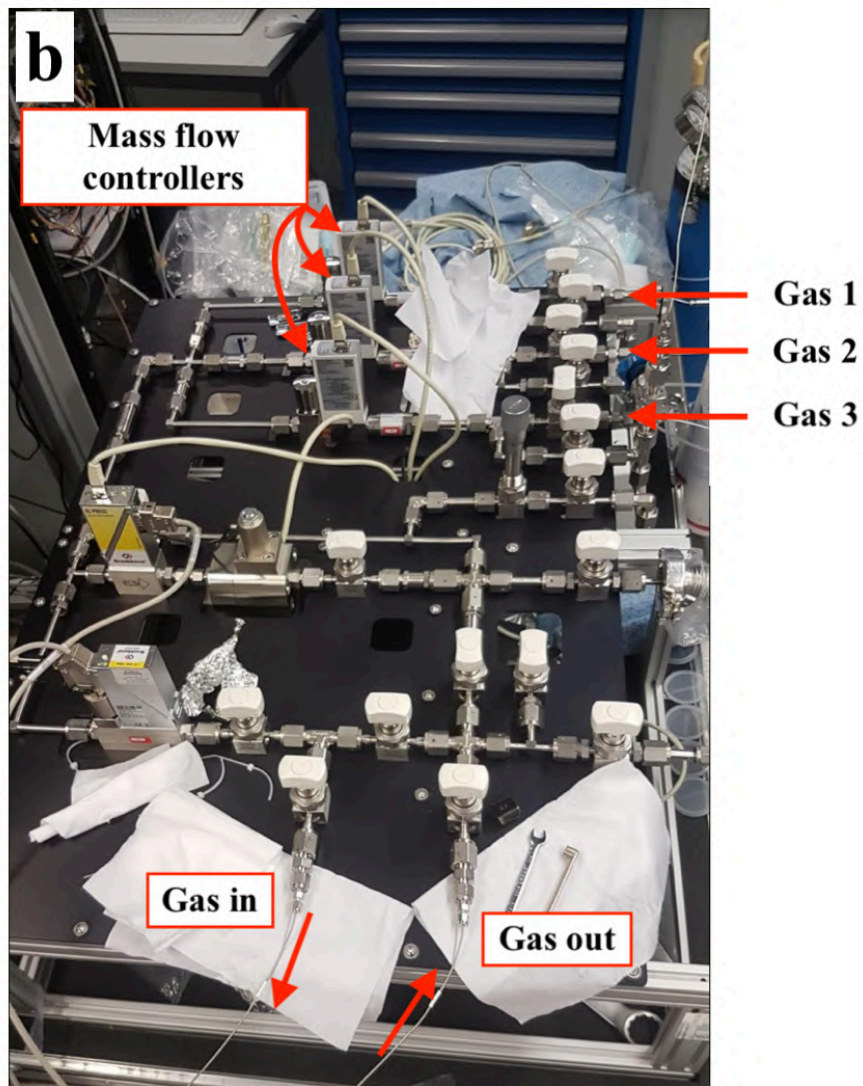
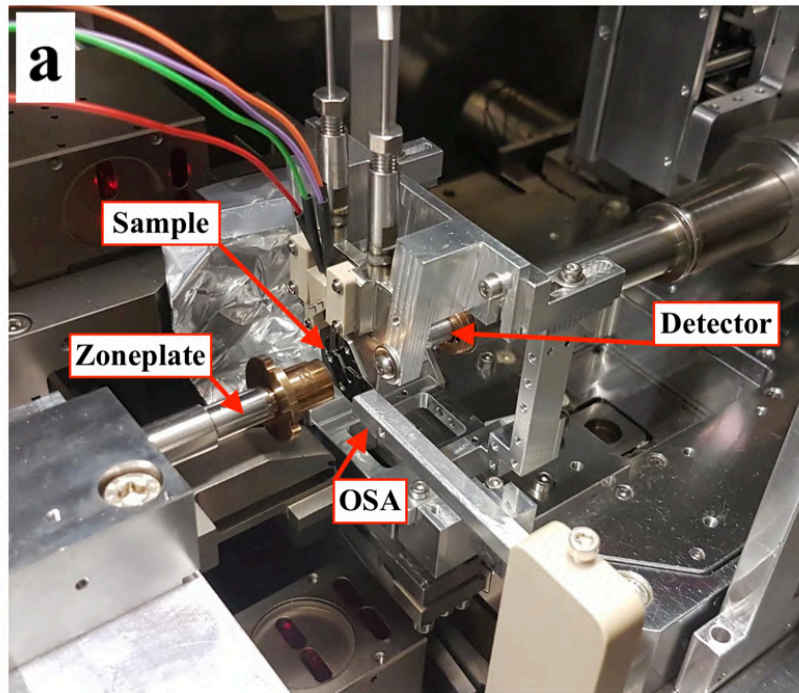


Figure 11: a) Image of the HERMES STXM chamber with all the optical components. b) Gas-phase setup that was used to perform the in-situ STXM experiments.

Figure 12a-c shows the used nanoreactor in this study [97-99]. This nanoreactor is made of silicon nitride (SiN_x) and has an integrated microchannel which is on the surface of a silicon (Si) support. The inert SiN_x enables performing experiments under extreme industrially relevant conditions. The dimensions of the microchannel are in the order of 4.6 mm (length), 0.3 mm (width), and 4.5 μm (height). To prevent bulging and deformations for experiments at high pressures micropillars supports are incorporated inside the channel. In addition, the selected nanoreactor allows heating the sample up to 750 $^\circ\text{C}$ by a microheater spiral made of a thin film of molybdenum incorporated on the top-side of the center of the microchannel. The microheater is equipped with four electrical contacts to regulate and read the actual temperature of the heater area. The nanoreactor also has 41 circular SiN_x windows with a diameter of 6 μm and ~ 18 nm thickness which are etched between the windings of the microheater spiral. The presence of the windows on these locations allows for sufficient transmission of X-ray signal. In principal an equal number of windows is integrated on the bottom part of the microchannel and aligned to the windows on the top. The nanoreactor also contains inlet/outlet which is used to I. load the nanoparticles into the channel and II. for the pressurization of the microchannel by flowing the gasses. Moreover, for the sample loading step, the catalytic nanoparticles are suspended in ethanol and stepwise drop-casted on the reactor inlet.

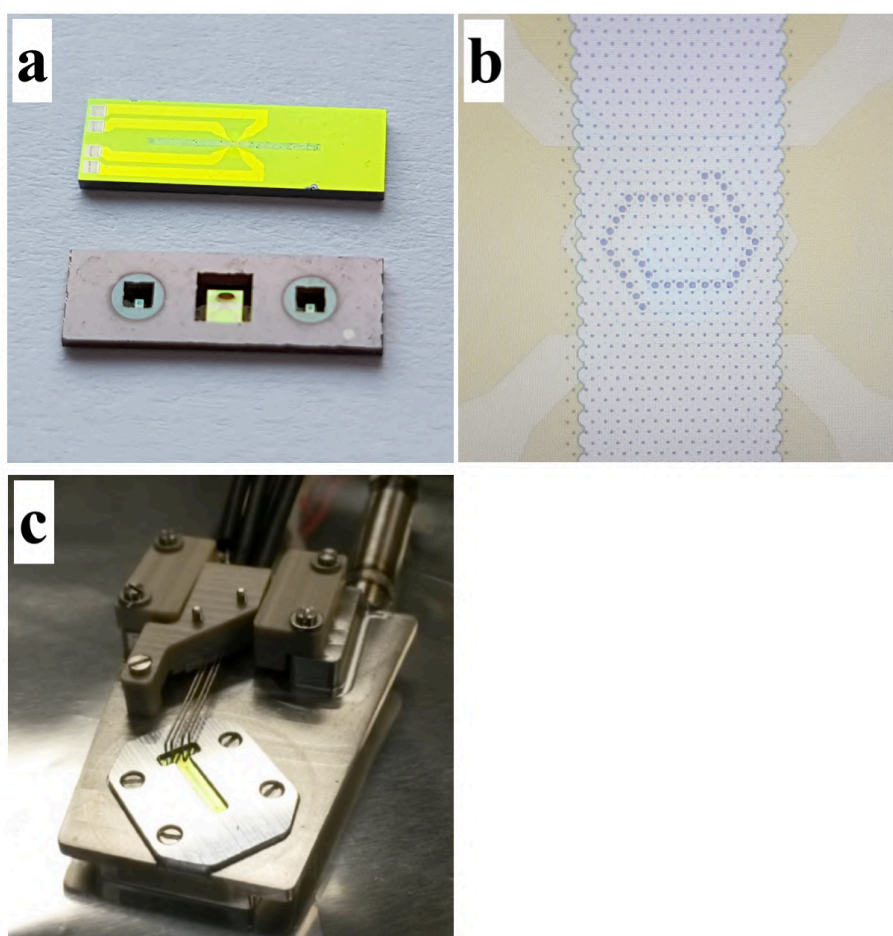


Figure 12: a) Image of the silicon nitride nanoreactor used in this project. b) microscopic image of the microchannel located in the nanoreactor. c) Image of the mounted nanoreactor on the gas-phase holder [97-99].

1.7 X-ray Emission Spectroscopy

In 1882 Henry Rowland developed X-ray Emission Spectroscopy (XES) in the optical wavelength range by using concave grating to focus light [100-101]. Until the late 1940`s this technique was in continuous development to study the valence band properties in the X-ray region by probing the fluorescence channels. For heterogeneous catalysts, XES is primarily used to study the electronic structure of the occupied orbitals to obtain information about the electronic structure of the catalytic active sites [102]. The XES is a second order process that is described by an X-ray absorption event followed by decay of the resulting core-hole [103-104]. Furthermore, in case of 3d transition metals, the X-ray emission decay channels are split into 3 types of non-resonant emissions including the $k\alpha$ (1s2p), $k\beta$ (1s3p), and valence to core (VtC) emission [105-109]. The first step in the XES process includes the absorption of a photon by a core-electron in the ground state $1s^23d^n$ which is directly followed by the formation of a core-hole. The electronic structure of the intermediate state for a K-edge absorption is $1s^13d^{n+1}$. As shown in Figure 3b and Figure 13, following the X-ray absorption event the second and third steps in an XES event involves the decay of the core by an electron from the 2p ($k\alpha$) or 3p ($k\beta$) orbitals and emission of a photon. The energy difference between the core level and final state is directly related to the energy of the emitted photon and acts a fingerprint for the properties of the sample. Further, the $k\alpha$ decay intensity is approximately an order of magnitude higher if compared to $k\beta$. If the energy of the emitted photon is equal to the incident photon energy, the corresponding reaction is called (non) Resonant Elastic X-ray Scattering (REXS). On contrast to REXS, if the incident and emitted photon energy are not equivalent then this process is denoted as Resonant Inelastic X-ray Scattering (RIXS).

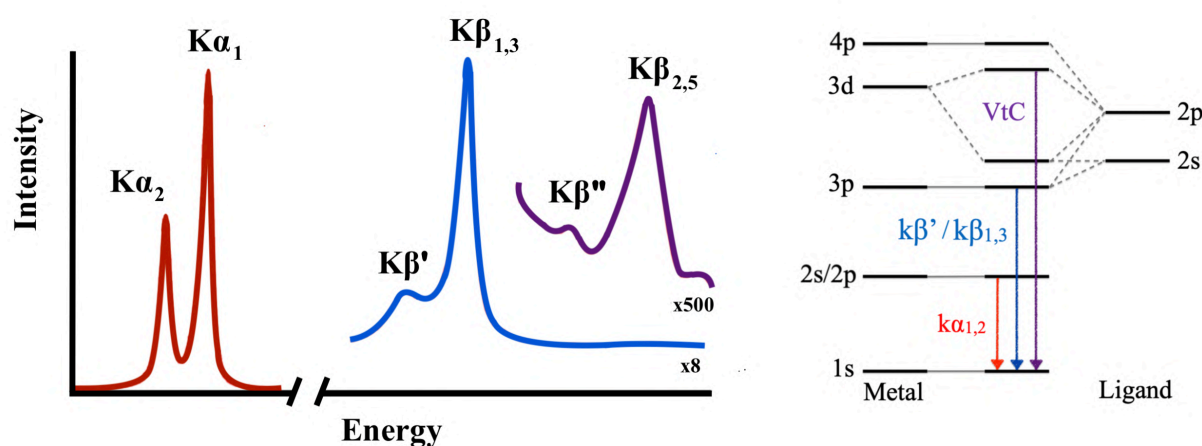


Figure 13: XES spectrum displaying the $K\alpha$ transition together with the enlarged region for the $K\beta$ and VtC transition. On the right side the MO diagram shows the origin of the corresponding transitions [109].

The most important advantage of using a second order process is the ability to probe the unoccupied orbitals in XAS while simultaneously the occupied orbitals are projected in XES. To date, RIXS remains one of the most powerful characterization techniques to obtain information about the electronic structure of solids e.g. heterogeneous catalysts, semiconductors under in-situ and operando reaction conditions [110].

Despite the advantage of RIXS, the emission signal intensity is extremely low and therefore demands the use of high brilliance synchrotron radiation source in combination with highly sensitive detectors. In this study we have used 1s3p RIXS to elucidate different

types of bimetallic methane reforming catalyst under operando conditions. In fact, this is the first RIXS study that endeavored to study methane reforming catalysts under in-situ conditions.

1.8 1s3p Resonant Inelastic X-ray Spectroscopy

The RIXS process can be theoretically described by the Kramers-Heisenberg equation (eq. 12) [83]. In this equation $|n\rangle$ represents the intermediate state which can be reached from the ground state $|g\rangle$ through the transition operator T_1 . The intermediate states $|n\rangle$ in RIXS are the final states in conventional K-edge spectroscopy. In addition, while Ω represents the photon energy, E_g and E_f are the final and ground state energies.

$$(12) \quad F(\Omega, \omega) = \sum_f \left| \sum_i \frac{\langle f|T_2|n\rangle \langle n|T_1|g\rangle}{E_g - E_i + \Omega - i\frac{\Gamma_K}{2}} \right|^2 \frac{\frac{\Gamma_L}{2\pi}}{(E_g - E_f + \Omega - \omega)^2 + \frac{\Gamma_L^2}{4}}$$

During the RIXS process, the energy of the incident and emitted photon are not equivalent and the energy loss is the difference between these two events. Moreover, both Hard X-rays (> 4500 eV) and Soft X-rays (< 1500 eV) are used at various RIXS beamlines in synchrotrons worldwide. In this thesis 1s3p RIXS (hard X-rays RIXS spectroscopy) was used to study bimetallic and monometallic methane reforming catalysts (Chapter 3). In a 1s3p RIXS measurement the excitation energy is tuned to match the binding energy of the 1s core electron and the $3p \rightarrow 1s$ transition is measured by a crystal analyser whereby both the incident energy (Ω) as well as the emitted energy (ω) can be tuned. The measured intensity is proportional to $F(\Omega, \omega)$ (equation 12) and is plotted vs a 2D grid.

The in-situ RIXS experiment in this studied were performed at the Taiwan beamline BL12XU at the SPring-8 synchrotron facility [111]. Figure 14 shows an image from the Taiwan Beamline. This beamline consists of mainly two parts. Part one is located outside the hutch and includes a diamond monochromator (DM) which provides a monochromatic beam in the energy range of 8-32 KeV. Part two is the central part of the beamline, it includes the experimental hutch and is used for RIXS experiments. This part contains the double crystal monochromator (DCM), collimating mirror (CM), high resolution monochromator (HRM), retarding plate (RP) and a focusing mirror (FM).



Figure 14: Image of the Taiwan Beamline BL12XU at Spring-8 synchrotron radiation facility.

In addition, Figure 15 shows a detailed image of the inelastic X-ray spectrometer components.

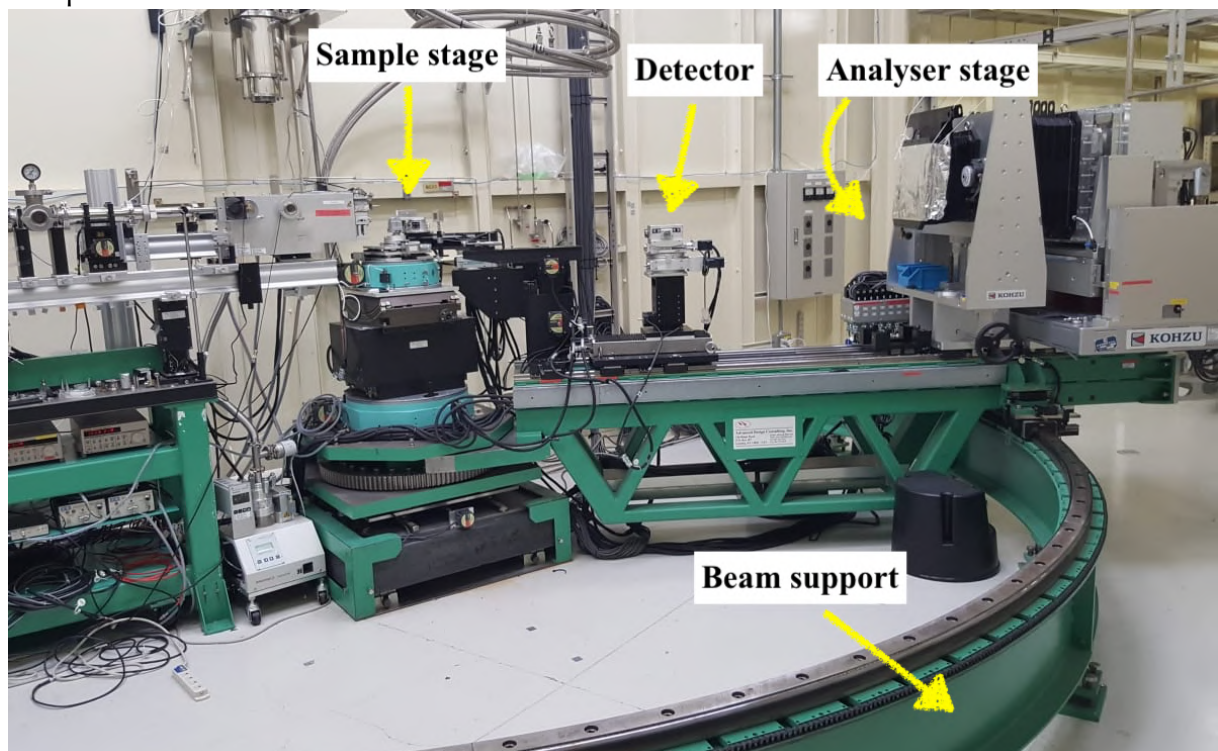


Figure 15: Overview of the inelastic spectrometer setup of BL12XU at SPring-8 synchrotron facility.

1.9 Transmission Electron Microscopy (TEM)

Heterogeneous catalysts are usually made of mono/bimetallic particles in the nano/micro meter range which are evenly dispersed on a support material e.g. Al_2O_3 , SiO_2 , MgO , BaO , TiO_2 [112]. The size of the catalytic particles directly influences crucial parameters such as activity, selectivity and stability. Therefore, the determination of the exact size of the particles is of paramount importance in the field of catalysis. One standard characterization technique with the ability to uncover the morphology and particle size of heterogeneous catalyst is Transmission Electron Microscopy (TEM) [113-114]. TEM has been one of the foremost important characterization techniques in science and industry. A TEM uses a high voltage electron beam to generate a 2D image. The electron beam is generated by using an electron gun (emission source) which is made of tungsten or lanthanum hexabromide. By connecting this emission source to a high voltage (100-400 kV) electrons will be emitted. The whole TEM setup is maintained under high vacuum to make sure the mean free path is optimal. As a result, the electrons can travel through the vacuum and reach the specimen. The electron beam is subsequently passed through condenser lenses and aperture to make sure the electron-beam is properly focused on the specimen. Finally, upon transmission of the electron beam through the specimen the transmission signal is detected. In a TEM image the lighter areas correspond to thinner regions where a relatively higher number of electrons pass through the sample.

The advantage of this TEM if compared to other techniques lies in the ability to [115]:

I: Yield high quality and detailed images

II: Achieve magnifications over one million times

III: Provide detailed information about the morphology of the specimen

IV: Provides information on the elements in the specimen

V: Provide insight into the size and crystallinity

VI: Is easy to operate



Figure 16: The Hitachi HD-2700 spherical aberration corrected scanning transmission electron microscope (STEM) was utilised in this study to get information about the morphology of the catalyst.

On the other hand, there are also some limitations of using TEM e.g.:

I: Expensive

II: Specimens are required to be electron transparent

III: Magnetic specimens are difficult to measure due to charging effects

IV: Sample preparation requires some time

V: Operation of the microscope requires training

VI: particle in the range of a few nm is extremely challenging to visualise

Moreover, for metallic nanoparticles with a size of a few/below a nanometer, on strongly scattering crystalline supports it is extremely challenging to distinguish the properties of the particles. This issue is overcome by using spherical aberration corrected Scanning Transmission Electron Microscope (STEM) to visualize these small nanoparticles [116]. In contrast to TEM, STEM uses a finer focused electron beam to image the sample. Figure 16b shows the STEM microscopy used in this study. Further, information about the elemental composition of heterogeneous catalyst are obtained by Energy Dispersive X-ray (EDX) measurements [117]. The combination of STEM-EDX is the STXM counterpart that is based on a different energy source. EDX allows to perform elemental mapping on

the sample of interest. In an EDX experiment the sample is illuminated with a focused electron beam. In this process the energy of the electron beam has to be larger than the binding energy of the inner-shell electron (Figure 17a,b). Following the excitation process, the core electron is ejected from the atoms and leave behind an instable core hole with an extremely finite lifetime in the order of $\sim 10^{-15}$. Subsequently, the core hole decays by the relaxation of higher shell electrons (Figure 17c). In this process a characteristic X-ray photon is generated, which has an energy equal to the difference of the energy of the shells (Figure 17d). This energy difference is unique to each element/species and reveals the electronic structure, elemental distributions, and concentrations of the presence species. For the experiments described in this thesis the EDX measurements were recorded with an EDAX Octane T Ultra W 200 mm² SDD that was connected to the Hitachi HD-2700 Microscope.

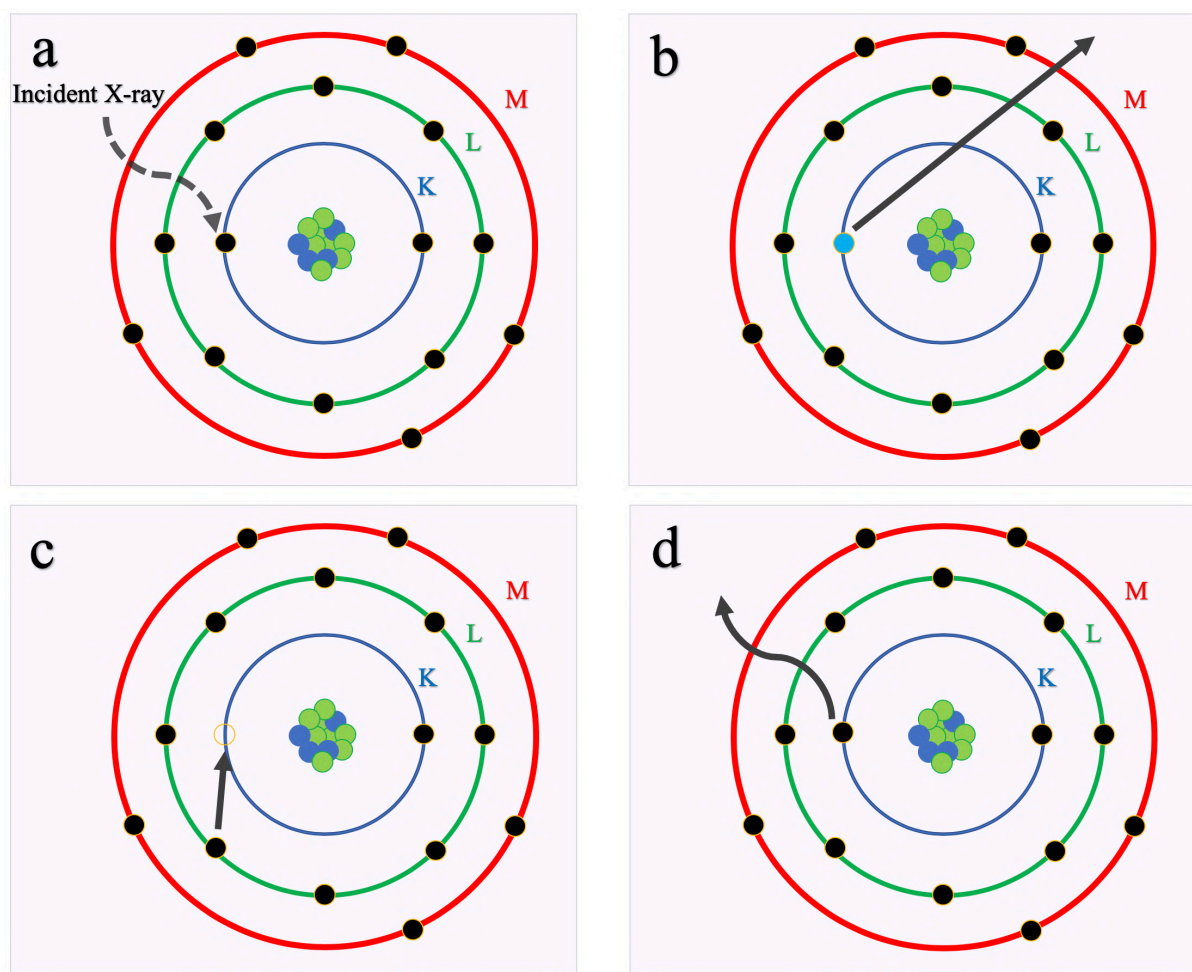


Figure 17: Illustration of a STEM-EDX a) An electron beam with an energy larger than the binding energy of the inner shell electron is absorbed. b) The inner-shell electron is ejected and a core-hole is generated. c) The core-hole is filled by electrons from higher shells. d) X-rays are emitted with an energy equal to the energy difference between the two shells.

1.10 Scope of the PhD thesis

The scope of this PhD thesis is to unravel the promoting role of Co and Fe in the NiCoO/ γ -Al₂O₃ and NiFeO/ γ -Al₂O₃ DMR catalysts. Within this context, the knowledge about the morphology and electronic structure of the samples during the activation/reduction step and under DMR conditions allows the development of DMR catalysts with improved selectivity, activity and stability. Therefore, the main focus of this thesis will be on understanding how the morphology and electronic structure of DMR catalysts are altered under reaction conditions. The synthesis and characterization of heterogeneous catalysts and in particular DMR catalysts is very challenging and requires extensive research and multiple beamtimes to achieve the presented results in this thesis. In **Chapter 2**, in-situ STXM results for the NiCoO/ γ -Al₂O₃ DMR catalyst under relevant reaction conditions are presented. These data illustrate that STXM not only provides insight into the electronic structure, but also reveals the changes in the morphology of the catalytic particles during activation/reduction and under DMR reaction conditions. This approach allows us to obtain crucial information regarding the morphology of NiCoO/ γ -Al₂O₃ particles which has not been previously reported in literature. However, as in **Chapter 2** a direct comparison between various aspects of NiCoO/ γ -Al₂O₃ and the monometallic NiO/ γ -Al₂O₃ was not considered, **Chapter 3** focuses on this missing knowledge by a combination of in-situ K β XES and K β -detected HERFD XAS. These results highlight the promoting effect of Co on the catalytic activity of a NiCoO/ γ -Al₂O₃ catalyst. Further, based on X-ray spectroscopy data additional information regarding the crystal structure of the samples is obtained. In **Chapter 4**, the in-situ STXM results for the bimetallic NiFeO/ γ -Al₂O₃, NiCoO/ γ -Al₂O₃ and monometallic NiO/ γ -Al₂O₃ DMR catalysts are presented and discussed in detail. These data provide valuable information regarding the changes in the electronic structure and morphology of the particles under reaction conditions. Finally, by a combination of TPR and X-ray spectromicroscopy data the role of Co and Fe on the reducibility of Ni oxides is unraveled.

References

- [1] Lund, H. Renewable Energy Strategies For Sustainable Development. *Energy*. **2007**, 32, 912-919.
- [2] Sims, R.; Rogner, H.; Gregory, K. Carbon Emission And Mitigation Cost Comparisons Between Fossil Fuel, Nuclear And Renewable Energy Resources For Electricity Generation. *Energy Policy*. **2003**, 31, 1315-1326.
- [3] Turner, J. A Realizable Renewable Energy Future. *Science*. **1999**, 285, 687-689.
- [4] Shafiee, S.; Topal, E. When Will Fossil Fuel Reserves Be Diminished?. *Energy Policy*. **2009**, 37, 181-189.
- [5] Höök, M.; Tang, X. Depletion Of Fossil Fuels And Anthropogenic Climate Change-A Review. *Energy Policy*. **2013**, 52, 797-809.
- [6] Bertine, K.; Goldberg, E. Fossil Fuel Combustion And The Major Sedimentary Cycle. *Science*. **1971**, 173, 233-235.
- [7] Mariani, A.; Unich, A.; Morrone, B. A Review Of Hydrogen-Natural Gas Blend Fuels In Internal Combustion Engines; INTECH Open Access Publisher, **2012**. ISBN 978-953-51-0277-9.
- [8] Folland, C.K., T.R. Karl, J.R. Christy, R.A. Clarke, G.V. Gruza, J. Jouzel, M.E. Mann, J. Oerlemans, M.J. Salinger and S.-W. Wang, **2001**: Observed Climate Variability and Change. In: *Climate Change 2001: The Scientific Basis*. Cambridge University Press, Cambridge, United Kingdom and New York, NY, USA, 6pp
- [9] Dresselhaus, M.; Thomas, I. Alternative Energy Technologies. *Nature*. **2001**, 414, 332-337.
- [10] Panwar, N.; Kaushik, S.; Kothari, S. Role Of Renewable Energy Sources In Environmental Protection: A Review. *Renewable and Sustainable Energy Reviews*. **2011**, 15, 1513-1524.
- [11] Chu, S.; Cui, Y.; Liu, N. The Path Towards Sustainable Energy. *Nature Materials*. **2017**, 16, 16-22.
- [12] Abdullah, B.; Abd Ghani, N.; Vo, D. Recent Advances In Dry Reforming Of Methane Over Ni-Based Catalysts. *Journal of Cleaner Production*. **2017**, 162, 170-185.
- [13] Aramouni, N.; Touma, J.; Tarboush, B.; Zeaiter, J.; Ahmad, M. Catalyst Design For Dry Reforming Of Methane: Analysis Review. *Renewable and Sustainable Energy Reviews*. **2018**, 82, 2570-2585.

- [14] Barroso-Quiroga, M.; Castro-Luna, A. Catalytic Activity And Effect Of Modifiers On Ni-Based Catalysts For The Dry Reforming Of Methane. *International Journal of Hydrogen Energy*. **2010**, 35, 6052-6056.
- [15] Serrano-Lotina, A.; Daza, L. Influence Of The Operating Parameters Over Dry Reforming Of Methane To Syngas. *International Journal of Hydrogen Energy*. **2014**, 39, 4089-4094.
- [16] Chun, D.; Park, J.; Hong, S.; Lim, J.; Kim, C.; Lee, H.; Yang, J.; Hong, S.; Jung, H. Highly Selective Iron-Based Fischer–Tropsch Catalysts Activated By CO₂ - Containing Syngas. *Journal of Catalysis*. **2014**, 317, 135-143.
- [17] Comazzi, A.; Pirola, C.; Longhi, M.; Bianchi, C.; Suslick, K. Fe-Based Heterogeneous Catalysts For The Fischer-Tropsch Reaction: Sonochemical Synthesis And Bench-Scale Experimental Tests. *Ultrasonics Sonochemistry*. **2017**, 34, 774-780.
- [18] Pakhare, D.; Spivey, J. A Review Of Dry (CO₂) Reforming Of Methane Over Noble Metal Catalysts. *Chem. Soc. Rev.* 2014, 43, 7813-7837.
- [19] Budiman, A.; Song, S.; Chang, T.; Shin, C.; Choi, M. Dry Reforming Of Methane Over Cobalt Catalysts: A Literature Review Of Catalyst Development. *Catalysis Surveys from Asia*. **2012**, 16, 183-197.
- [20] Ginsburg, J.; Piña, J.; El Solh, T.; de Lasa, H. Coke Formation Over A Nickel Catalyst Under Methane Dry Reforming Conditions: Thermodynamic And Kinetic Models. *Industrial & Engineering Chemistry Research*. **2005**, 44, 4846-4854.
- [21] Lavoie, J. Review On Dry Reforming Of Methane, A Potentially More Environmentally-Friendly Approach To The Increasing Natural Gas Exploitation. *Frontiers in Chemistry*. **2014**, 2, 1-17.
- [22] Guo, J.; Lou, H.; Zhao, H.; Chai, D.; Zheng, X. Dry Reforming Of Methane Over Nickel Catalysts Supported On Magnesium Aluminate Spinel. *Applied Catalysis A: General*. **2004**, 273, 75-82.
- [23] Brungs, A.; York, A.; Green, M. Comparison Of The Group V And VI Transition Metal Carbides For Methane Dry Reforming And Thermodynamic Prediction Of Their Relative Stabilities. *Catalysis Letters*. **1999**, 57, 65-69.
- [24] Tsyganok, A.; Inaba, M.; Tsunoda, T.; Uchida, K.; Suzuki, K.; Takehira, K.; Hayakawa, T. Rational Design Of Mg–Al Mixed Oxide-Supported Bimetallic Catalysts For Dry Reforming Of Methane. *Applied Catalysis A: General*. **2005**, 292, 328-343.
- [25] Ay, H.; Üner, D. Dry Reforming Of Methane Over CeO₂ Supported Ni, Co And Ni–Co Catalysts. *Applied Catalysis B: Environmental*. **2015**, 179, 128-138.

- [26] San-José-Alonso, D.; Juan-Juan, J.; Illán-Gómez, M.; Román-Martínez, M. Ni, Co And Bimetallic Ni–Co Catalysts For The Dry Reforming Of Methane. *Applied Catalysis A: General*. **2009**, 371, 54-59.
- [27] Kambolis, A.; Matralis, H.; Trovarelli, A.; Papadopoulou, C. Ni/CeO₂-ZrO₂ Catalysts For The Dry Reforming Of Methane. *Applied Catalysis A: General*. **2010**, 377, 16-26.
- [28] Theofanidis, S.; Galvita, V.; Poelman, H.; Marin, G. Enhanced Carbon-Resistant Dry Reforming Fe-Ni Catalyst: Role Of Fe. *ACS Catalysis*. **2015**, 5, 3028-3039.
- [29] You, X.; Wang, X.; Ma, Y.; Liu, J.; Liu, W.; Xu, X.; Peng, H.; Li, C.; Zhou, W.; Yuan, P. et al. Ni-Co/Al₂O₃ bimetallic Catalysts For CH₄ steam Reforming: Elucidating The Role Of Co For Improving Coke Resistance. *ChemCatChem*. **2014**, 6, 3377-3386.
- [30] Nagaoka, K.; Takanabe, K.; Aika, K. Modification Of Co/TiO₂ For Dry Reforming Of Methane At 2Mpa By Pt, Ru Or Ni. *Applied Catalysis A: General*. **2004**, 268, 151-158.
- [31] Ruckenstein, E.; Hang Hu, Y. Role Of Support In CO₂ Reforming Of CH₄ To Syngas Over Ni Catalysts. *Journal of Catalysis*. **1996**, 162, 230-238.
- [32] Bouarab, R.; Akdim, O.; Auroux, A.; Cherifi, O.; Mirodatos, C. Effect Of MgO Additive On Catalytic Properties Of Co/SiO₂ In The Dry Reforming Of Methane. *Applied Catalysis A: General*. **2004**, 264, 161-168.
- [33] Gallego, G.; Marín, J.; Batiot-Dupeyrat, C.; Barrault, J.; Mondragón, F. Influence Of Pr And Ce In Dry Methane Reforming Catalysts Produced From La_{1-x}A_xNiO_{3-δ} Perovskites. *Applied Catalysis A: General*. **2009**, 369, 97-103.
- [34] Horlyck, J., Lawrey, C., Lovell, E., Amal, R. & Scott, J. Elucidating the impact of Ni and Co loading on the selectivity of bimetallic NiCo catalysts for dry reforming of methane. *Chemical Engineering Journal*. **2018**, 352, 572-580.
- [35] You, X. et al. Ni-Co/Al₂O₃ Bimetallic Catalysts for CH₄ Steam Reforming: Elucidating the Role of Co for Improving Coke Resistance. *ChemCatChem*. **2014**, 6, 3377-3386.
- [36] Tu, W.; Ghoussoub, M.; Singh, C.; Chin, Y. Consequences Of Surface Oxophilicity Of Ni, Ni-Co, And Co Clusters On Methane Activation. *Journal of the American Chemical Society* **2017**, 139 (20), 6928-6945.
- [37] Wei, J.; Iglesia, E. Isotopic And Kinetic Assessment Of The Mechanism Of Reactions Of CH₄ With CO₂ Or H₂O To Form Synthesis Gas And Carbon On Nickel Catalysts. *Journal of Catalysis* **2004**, 224 (2), 370-383.
- [38] AlSabban, B.; Falivene, L.; Kozlov, S.; Aguilar-Tapia, A.; Ould-Chikh, S.; Hazemann, J.; Cavallo, L.; Basset, J.; Takanabe, K. In-Operando Elucidation Of

Bimetallic Coni Nanoparticles During High-Temperature CH₄/CO₂ Reaction. *Applied Catalysis B: Environmental* **2017**, 213, 177-189.

- [39] Wierzbicki, D.; Baran, R.; Dębek, R.; Motak, M.; Gálvez, M.; Grzybek, T.; Da Costa, P.; Glatzel, P. Examination Of The Influence Of La Promotion On Ni State In Hydrotalcite-Derived Catalysts Under CO₂ Methanation Reaction Conditions: Operando X-Ray Absorption And Emission Spectroscopy Investigation. *Applied Catalysis B: Environmental*. **2018**, 232, 409-419.
- [40] Rocha, K.; Santos, J.; Meira, D.; Pizani, P.; Marques, C.; Zanchet, D.; Bueno, J. Catalytic Partial Oxidation And Steam Reforming Of Methane On La₂O₃-Al₂O₃ Supported Pt Catalysts As Observed By X-Ray Absorption Spectroscopy. *Applied Catalysis A: General*. **2012**, 431-432, 79-87.
- [41] Pereñíguez, R.; González-DelaCruz, V.; Holgado, J.; Caballero, A. Synthesis And Characterization Of A Lanthanum Perovskite As Precursor For Methane Reforming Reactions Catalysts. *Applied Catalysis B: Environmental*. **2010**, 93, 346-353.
- [42] Slagtern, A.; Olsbye, U.; Blom, R.; Dahl, I.; Fjellvag, H. In Situ XRD Characterization Of Lanthanum Model Catalysts For CO₂ Reforming Of Methane. *Applied Catalysis A: General*. **1996**, 145, 375-388.
- [43] Theofanidis, S.; Batchu, R.; Galvita, V.; Poelman, H.; Marin, G. Carbon Gasification From Fe-Ni Catalysts After Methane Dry Reforming. *Applied Catalysis B: Environmental*. **2016**, 185, 42-55.
- [44] Maser, J.; Osanna, A.; Wang, Y.; Jacobsen, C.; Kirz, J.; Spector, S.; Winn, B.; Tennant, D. Soft X-Ray Microscopy With A Cryo Scanning Transmission X-Ray Microscope: I. Instrumentation, Imaging And Spectroscopy. *Journal of Microscopy*. **2000**, 197, 68-79.
- [45] Lawrence, J.; Swerhone, G.; Leppard, G.; Araki, T.; Zhang, X.; West, M.; Hitchcock, A. Scanning Transmission X-Ray, Laser Scanning, And Transmission Electron Microscopy Mapping Of The Exopolymeric Matrix Of Microbial Biofilms. *Applied and Environmental Microbiology*. **2003**, 69, 5543-5554.
- [46] Wang, J.; Zhou, J.; Hu, Y.; Regier, T. Chemical Interaction And Imaging Of Single Co₃O₄/Graphene Sheets Studied By Scanning Transmission X-Ray Microscopy And X-Ray Absorption Spectroscopy. *Energy & Environmental Science*. **2013**, 6, 926-934.
- [47] de Groot, F. & Kotani, A. *Core level spectroscopy of solids*. 1 (CRC Press, **2008**).
- [48] Nilsson, A. Applications of core level spectroscopy to adsorbates. *Journal of Electron Spectroscopy and Related Phenomena* **2002**, 126, 3-42.
- [49] Mårtensson, N. et al. On the relation between X-ray Photoelectron Spectroscopy and XAFS. *Journal of Physics: Conference Series* **2013**, 430, 012131.

- [50] Kowalska, J.; DeBeer, S. The Role Of X-Ray Spectroscopy In Understanding The Geometric And Electronic Structure Of Nitrogenase. *Biochimica et Biophysica Acta (BBA) - Molecular Cell Research* **2015**, 1853 (6), 1406-1415.
- [51] Deutschmann, O.; Knözinger, H.; Kochloefl, K.; Turek, T. Heterogeneous Catalysis And Solid Catalysts. *Ullmann's Encyclopedia of Industrial Chemistry* **2009**.
- [52] Nilsson, A. et al. The electronic structure effect in heterogeneous catalysis. *Catalysis Letters* **2005**, 100, 111-114.
- [53] Védrine, J. Heterogeneous Catalysis on Metal Oxides. *Catalysts* **2017**, 7, 341.
- [54] Eley, D. Electron Transfer and Heterogeneous Catalysis. *Zeitschrift für Elektrochemie* **1956**, 8, 798-803.
- [55] DeBeer, S. X-Ray Absorption Spectroscopy. *Nitrogen Fixation* **2011**, 165-176.
- [56] Hall, E.; Pollock, C.; Bendix, J.; Collins, T.; Glatzel, P.; DeBeer, S. Valence-To-Core-Detected X-Ray Absorption Spectroscopy: Targeting Ligand Selectivity. *Journal of the American Chemical Society* **2014**, 136 (28), 10076-10084.
- [57] de Groot, F. High-Resolution X-ray Emission and X-ray Absorption Spectroscopy. *Chemical Reviews* **2001**, 101, 1779-1808.
- [58] de Groot, F. Multiplet effects in X-ray spectroscopy. *Coordination Chemistry Reviews* **2005**, 249, 31-63.
- [59] Safonova, O., Deniau, B. & Millet, J. Mechanism of the Oxidation–Reduction of the MoVSbNbO Catalyst: In Operando X-ray Absorption Spectroscopy and Electrical Conductivity Measurements. *The Journal of Physical Chemistry B* **2006**, 110, 23962-23967.
- [60] Wang, H. et al. In Operando X-ray Absorption Fine Structure Studies of Polyoxometalate Molecular Cluster Batteries: Polyoxometalates as Electron Sponges. *Journal of the American Chemical Society* **2012**, 134, 4918-4924.
- [61] Koziej, D. et al. Operando X-ray absorption spectroscopy studies on Pd-SnO₂ based sensors. *Physical Chemistry Chemical Physics* **2009**, 11, 8620.
- [62] Koga, H. et al. Operando X-ray Absorption Study of the Redox Processes Involved upon Cycling of the Li-Rich Layered Oxide Li_{1.20}Mn_{0.54}Co_{0.13}Ni_{0.13}O₂ in Li Ion Batteries. *The Journal of Physical Chemistry C* **2014**, 118, 5700-5709.
- [63] van Bokhoven, J. & Lamberti, C. *X-Ray Absorption and X-Ray Emission Spectroscopy: Theory and Applications*. (John Wiley & Sons, **2016**).

- [64] Getty, K., Ulises Delgado-Jaime, M. & Kennepohl, P. Assignment of pre-edge features in the Ru K-edge X-ray absorption spectra of organometallic ruthenium complexes. *Inorganica Chimica Acta* **2008**, 361, 1059-1065.
- [65] Hansmann, P. et al. Atomic and itinerant effects at the transition-metal x-ray absorption K pre-edge exemplified in the case of V₂O₃. *Physical Review B* **2012**, 85.
- [66] S.S.R. Kumar, C. *X-ray and neutron techniques for nanomaterials characterization*. 258 (Springer, **2016**).
- [67] Rice, S. & Dinner, A. *Advances in chemical physics, Volume 326*. 4 (John Wiley & Sons, **2013**).
- [68] Feiters, M. & Meyer-Klaucke, W. X-ray Absorption Spectroscopy in Biology (BioXAS). *Practical Approaches to Biological Inorganic Chemistry* **2013**, 131-160.
- [69] Gaur, A., Shrivastava, B. & Nigam, H. X-ray absorption fine structure (XAFS) spectroscopy using synchrotron radiation. *Journal of Physics: Conference Series* **2012**, 365, 921-966.
- [70] Henderson, G., de Groot, F. & Moulton, B. X-ray Absorption Near-Edge Structure (XANES) Spectroscopy. *Reviews in Mineralogy and Geochemistry* **2014**, 78, 75-138.
- [71] Roemelt, M.; Beckwith, M.; Duboc, C.; Collomb, M.; Neese, F.; DeBeer, S. Manganese K-Edge X-Ray Absorption Spectroscopy As A Probe Of The Metal-Ligand Interactions In Coordination Compounds. *Inorganic Chemistry* **2011**, 51 (1), 680-687.
- [72] Schnohr, C. & Ridgway, M. *X-Ray Absorption Spectroscopy of Semiconductors*. 14-15 (Springer, **2014**).
- [73] de Groot, F. & Kotani, A. *Core level spectroscopy of solids*. 229 (CRC Press, **2008**).
- [74] Dronskowski, R., Kikkawa, S. & Stein, A. *Handbook of solid state chemistry, 6 Volume Set*. 366 (John Wiley & Sons, **2017**).
- [75] Achkar, A., Regier, T., Monkman, E., Shen, K. & Hawthorn, D. Determination of total x-ray absorption coefficient using non-resonant x-ray emission. *Scientific Reports* **2011**, 1.
- [76] Schroeder, S. Towards a 'universal curve' for total electron-yield XAS. *Solid State Communications* **1996**, 98, 405-409.
- [77] Asakura, D. et al. Material/element-dependent fluorescence-yield modes on soft X-ray absorption spectroscopy of cathode materials for Li-ion batteries. *AIP Advances* **2016**, 6.

- [78] Dudney, N., West, W. & Nanda, J. *Handbook Of Solid State Batteries*. 83 (World Scientific, **2015**).
- [79] Kotani, A. & Suzuki, N. *Recent advances in magnetism of transition metal compounds*. 12 (World Scientific, **1993**).
- [80] Sá, J. *High-Resolution XAS/XES: Analyzing Electronic Structures of Catalysts*. 64 (CRC Press, **2014**).
- [81] Willmott, P. *An Introduction to Synchrotron Radiation: Techniques and Applications*. 303 (John Wiley & Sons, **2019**).
- [82] Khodaei, M. & Petaccia, L. *X-ray Characterization of Nanostructured Energy Materials by Synchrotron Radiation*. 89 (Intech, **2017**).
- [83] Kotani, A.; Shin, S. Resonant Inelastic X-Ray Scattering Spectra For Electrons In Solids. *Reviews of Modern Physics* **2001**, 73 (1), 203-246.
- [84] Bilderback, D.; Elleaume, P.; Weckert, E. Review Of Third And Next Generation Synchrotron Light Sources. *Journal of Physics B: Atomic, Molecular and Optical Physics* **2005**, 38 (9), S773-S797.
- [85] Bharti, A.; Goyal, N. Fundamental Of Synchrotron Radiations. *Synchrotron Radiation - Useful and Interesting Applications* **2019**.
- [86] Willmott, P. *Introduction to synchrotron radiation - techniques and applications*, 2nd ed. 1-7 (John Wiley, **2019**)
- [87] Inside the Synchrotron. https://www.lightsource.ca/inside_the_synchrotron (accessed Sep 4, **2019**).
- [88] Zhukovsky, K. Undulators For Short Pulse X-Ray Self-Amplified Spontaneous Emission-Free Electron Lasers. *High Energy and Short Pulse Lasers* **2016**, 207.
- [89] Kaznatcheev, K.; Karunakaran, C.; Lanke, U.; Urquhart, S.; Obst, M.; Hitchcock, A. Soft X-Ray Spectromicroscopy Beamline At The CLS: Commissioning Results. *Nuclear Instruments and Methods in Physics Research Section A: Accelerators, Spectrometers, Detectors and Associated Equipment* **2007**, 582 (1), 96-99.
- [90] Al Samarai, M.; Meirer, F.; Karunakaran, C.; Wang, J.; Vogt, E.; Zandbergen, H.; Weber, T.; Weckhuysen, B.; de Groot, F. Unraveling The Redox Behavior Of A Comos Hydrodesulfurization Catalyst: A Scanning Transmission X-Ray Microscopy Study In The Tender X-Ray Range. *The Journal of Physical Chemistry C* **2015**, 2530-2536.

- [91] Karunakaran, C.; Christensen, C.; Gaillard, C.; Lahlali, R.; Blair, L.; Perumal, V.; Miller, S.; Hitchcock, A. Introduction Of Soft X-Ray Spectromicroscopy As An Advanced Technique For Plant Biopolymers Research. *PLOS ONE* **2015**, 10 (3), 1-18.
- [92] V. Rheinheimer, S. Chae, E. Rodríguez, G. Geng, A. Kirchheim, P. Monteiro, *Materials* **2016**, 9, 745.
- [93] de Groot, F.; de Smit, E.; van Schooneveld, M.; Aramburo, L.; Weckhuysen, B. In-Situ Scanning Transmission X-Ray Microscopy Of Catalytic Solids And Related Nanomaterials. *ChemPhysChem* **2010**, 11 (5), 951-962.
- [94] Kurokhtin, A.; Popov, A. Simulation Of High-Resolution X-Ray Zone Plates. *Journal of the Optical Society of America A* **2002**, 19 (2), 315.
- [95] Rehbein, S.; Guttman, P.; Werner, S.; Schneider, G.; McNulty, I.; Eyberger, C.; Lai, B. Soft X-Ray Microscopy At HZB: Zone Plate Development And Imaging Using The Third Order Of Diffraction. *AIP Conference Proceedings* **2011**, 32, 1365.
- [96] Kipp, L., Skibowski, M., Johnson, R. *et al.* Sharper images by focusing soft X-rays with photon sieves. *Nature* **2001**, 414, 184–188.
- [97] Vendelbo, S.; Elkjær, C.; Falsig, H.; Puspitasari, I.; Dona, P.; Mele, L.; Morana, B.; Nelissen, B.; van Rijn, R.; Creemer, J.; Kooyman, P.; Helveg, S. Visualization Of Oscillatory Behaviour Of Pt Nanoparticles Catalysing CO Oxidation. *Nature Materials* **2014**, 13 (9), 884-890.
- [98] Bremmer, G.; Zacharaki, E.; Sjøstad, A.; Navarro, V.; Frenken, J.; Kooyman, P. In Situ TEM Observation Of The Boudouard Reaction: Multi-Layered Graphene Formation From CO On Cobalt Nanoparticles At Atmospheric Pressure. *Faraday Discussions* **2017**, 197, 337-351.
- [99] de Smit, E.; Swart, I.; Creemer, J.; Hoveling, G.; Gilles, M.; Tyliczszak, T.; Kooyman, P.; Zandbergen, H.; Morin, C.; Weckhuysen, B.; de Groot, F. Nanoscale Chemical Imaging Of A Working Catalyst By Scanning Transmission X-Ray Microscopy. *Nature* **2008**, 456 (7219), 222-225.
- [100] Rowland, H. LXI. Preliminary Notice Of The Results Accomplished In The Manufacture And Theory Of Gratings For Optical Purposes. *The London, Edinburgh, and Dublin Philosophical Magazine and Journal of Science* **1882**, 13 (84), 469-474.
- [101] Magnuson, M.; Mattesini, M. Chemical Bonding And Electronic-Structure In MAX Phases As Viewed By X-Ray Spectroscopy And Density Functional Theory. *Thin Solid Films* **2017**, 621, 108-130.

- [102] Rovezzi, M.; Glatzel, P. Hard X-Ray Emission Spectroscopy: A Powerful Tool For The Characterization Of Magnetic Semiconductors. *Semiconductor Science and Technology* **2014**, 29(2), 023002.
- [103] Glatzel, P.; Bergmann, U.; de Groot, F.; Cramer, S. Influence Of The Core Hole On $K\beta$ Emission Following Photoionization Or Orbital Electron Capture: A Comparison Using MnO And $55\text{Fe}_2\text{O}_3$. *Physical Review B* **2001**, 64 (4).
- [104] Glatzel, P.; Bergmann, U. High Resolution 1S Core Hole X-Ray Spectroscopy In 3D Transition Metal Complexes-Electronic And Structural Information. *Coordination Chemistry Reviews* **2005**, 249 (1-2), 65-95.
- [105] DeBeer, S. Advanced X-Ray Spectroscopic Methods For Studying Iron-Sulfur-Containing Proteins And Model Complexes. *Methods in Enzymology* **2018**, 427-450.
- [106] Pollock, C.; Delgado-Jaime, M.; Atanasov, M.; Neese, F.; DeBeer, S. $K\beta$ Mainline X-Ray Emission Spectroscopy As An Experimental Probe Of Metal-Ligand Covalency. *Journal of the American Chemical Society* **2014**, 136 (26), 9453-9463.
- [107] Pollock, C.; Grubel, K.; Holland, P.; DeBeer, S. Experimentally Quantifying Small-Molecule Bond Activation Using Valence-To-Core X-Ray Emission Spectroscopy. *Journal of the American Chemical Society* **2013**, 135 (32), 11803-11808.
- [108] Pollock, C.; DeBeer, S. Valence-To-Core X-Ray Emission Spectroscopy: A Sensitive Probe Of The Nature Of A Bound Ligand. *Journal of the American Chemical Society* **2011**, 133 (14), 5594-5601.
- [109] Kowalska, J.; Lima, F.; Pollock, C.; Rees, J.; DeBeer, S. A Practical Guide To High-Resolution X-Ray Spectroscopic Measurements And Their Applications In Bioinorganic Chemistry. *Israel Journal of Chemistry* **2016**, 56 (9-10), 803-815.
- [110] Al Samarai, M.; Hahn, A.; Beheshti Askari, A.; Cui, Y.; Yamazoe, K.; Miyawaki, J.; Harada, Y.; Rüdiger, O.; DeBeer, S. Elucidation Of Structure-Activity Correlations In A Nickel Manganese Oxide Oxygen Evolution Reaction Catalyst By Operando Ni L-Edge X-Ray Absorption Spectroscopy And 2P3d Resonant Inelastic X-Ray Scattering. *ACS Applied Materials & Interfaces* **2019**, 11 (42), 38595-38605.
- [111] Cai, Y.; Chen, C.; Chow, P.; Tseng, P.; Hwang, C.; Hsiung, G.; Wang, D.; Shew, B.; Tsang, K. A Status Report: Taiwan APCST Contract Beamline BL12XU. *SPRING-8 Information* **2002**, 07 (1), 23-27.
- [112] Deutschmann, O.; Knözinger, H.; Kochloefl, K.; Turek, T. Heterogeneous Catalysis And Solid Catalysts. *Ullmann's Encyclopedia of Industrial Chemistry* **2009**.

- [113] Reimer, L. *Transmission Electron Microscopy*; Springer Berlin / Heidelberg: Berlin, Heidelberg, **2013**; pp 1-16.
- [114] Wang, Z. Transmission Electron Microscopy Of Shape-Controlled Nanocrystals And Their Assemblies. *The Journal of Physical Chemistry B* **2000**, 104 (6), 1153-1175.
- [115] Choudhary, P.; Choudhary, O. Uses Of Transmission Electron Microscope In Microscopy And Its Advantages And Disadvantages. *International Journal of Current Microbiology and Applied Sciences* **2018**, 7 (05), 743-747.
- [116] Zhang, Q.; Xiao, D.; Gu, L. Aberration-Corrected Scanning Transmission Electron Microscopy For Complex Transition Metal Oxides. *Chinese Physics B* **2016**, 25 (6), 066803.
- [117] Shindo, D.; Oikawa, T. *Analytical Electron Microscopy for Materials Science*; Springer Japan: Tokyo, **2002**; pp 81-101.

2

In-situ X-ray Microscopy reveals particle dynamics in a NiCo dry methane reforming catalyst under operating conditions

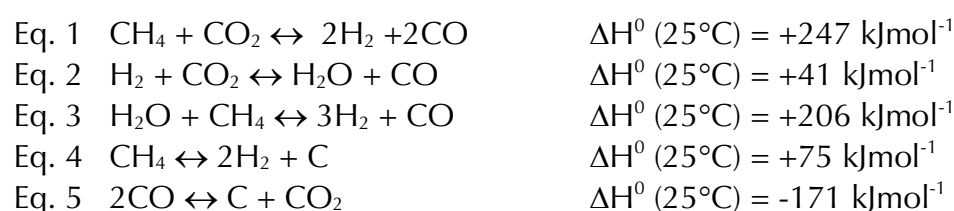
In this Chapter, we report the synthesis of a γ -Al₂O₃-supported NiCo catalyst for dry methane reforming (DMR) reaction and study the catalyst using in-situ Scanning Transmission X-Ray Microscopy (STXM) during the reduction (activation step) and under reaction conditions. During the reduction process, the NiCo alloy particles undergo elemental segregation with Co migrating toward the center of the catalyst particles and nickel forming a shell on the outer surfaces. In addition, L₃-edge XAS spectra showed that through the reduction both Ni and Co are converted into their metallic state. Under DMR conditions, the segregated structure is maintained, thus hinting at the importance of this structure to optimal catalytic function. Finally, the formation of Ni-rich branches on the surface of the particles is observed during DMR, suggesting that the loss of Ni from the shell may play a role in the reduced stability and hence catalyst deactivation. These findings provide insight into the morphological and electronic structural changes that occur in a NiCo based catalyst during DMR. Further, this study emphasizes the need to study catalysts under operating conditions in order to elucidate material dynamics during the reaction.

In-situ X-ray Microscopy reveals particle dynamics in a NiCo dry methane reforming catalyst under operating conditions

Abbas Beheshti Askari, Mustafa al Samarai, Bruno Moran, Lukas Tillmann, Norbert Pfänder, Aleksandra Wandzilak, Benjamin Watts, Rachid Belkhou, Martin Muhler, and Serena DeBeer. **Submitted for publication.**

2. Introduction

The emission of greenhouse gasses associated with the combustion of fossil fuels is believed to be the main cause of global warming [1-2]. Lowering the concentration of these gasses is therefore a matter of utmost importance. An attractive approach would be the development of environmental friendly processes capable of reusing these gasses as feedstock for industrial processes. In this context, a reaction that has received much attention is the Dry Methane Reforming (DMR) [3-5]. In this reaction two major greenhouse gasses, methane (CH₄) and carbon dioxide (CO₂), are converted into hydrogen (H₂) and carbon monoxide (CO), otherwise known as syngas. The DMR reaction (eq. 1) together with the side reactions (eq. 2-5) proceeding under non-ideal conditions are reported below [6-8]:



In the literature, various classes of materials, including noble metals, spinels, hydroxalcalites, and supported base metals are reported as catalysts for the DMR process [9-11]. Among these catalysts noble metals show the highest activity and stability towards this reaction, but are economically not attractive [12]. In recent years, various studies focused on the development of late 3d transition metal-based systems as an alternative to costly noble metals for DMR catalysis [9-11,13]. Within this context, nickel (Ni)-based catalysts are promising candidates due to their relative high activity and earth abundance. Nevertheless, the major drawback of monometallic Ni-based catalysts when compared to noble metal-based catalysts is their lower activity and higher susceptibility to deactivation due to coke formation via either methane cracking or the reverse Boudouard reaction [14-19]. In order to increase catalyst activity and stability researchers have implemented various approaches including: I) depositing the catalytic active phase on different support materials [20-21], II) reducing the catalyst particle size [22-23], and III) developing bimetallic catalysts based on transition metals [24-25]. This last approach has been the most successful in increasing the catalyst activity, stability, and selectivity. Among 3d transition metals, the addition of cobalt (Co) to Ni-based DMR catalysts results in the highest increase in activity. This has been ascribed to the optimal catalytic performance of the Ni/Co alloy [26-27]. Within this context, Zhang et al. investigated NiCo catalyst samples with various Ni and Co loadings and established that a lower Co concentration results in an increased catalytic activity and stability, and prevents the coke formation side reaction to a large extent [28]. An operando X-ray absorption spectroscopy (XAS) study by Takanabe et al. revealed that Co increases the adsorption capacity of CO₂, which eventually leads to carbon elimination from the catalyst surface [29]. Further, in the same study the presence of a homogenous NiCo alloy was directly correlated to the DMR activity. This finding was supported by a combined in-situ Transmission Electron Microscopy (TEM) and X-ray Photoelectron Spectroscopy (XPS) study by Bonifacio and co-workers, which revealed that NiCo core-shell particles tend to form a homogeneous alloy at high temperatures (600 °C) [30]. In addition, an ex-situ TEM and in-situ XPS study by Carencio et al., revealed that the morphology of NiCo

particles under reducing conditions and low temperatures (270 °C) rearrange into a structure consisting of NiCo alloy shell and a nickel-rich core [31]. From these studies and many other reported in literature [31-35], the formation of a NiCo alloy seems to play a crucial role in optimizing the DMR activity. However, none of these studies were performed at optimal operating temperatures for DMR (>750 °C). The differences between the particle morphology at low and high temperatures [30-31], suggest that it is necessary to follow the electronic structure and elemental distributions of Co and Ni during both the reductive activation step and under DMR conditions.

In general, the scarce information regarding the role of transition metals in methane reforming catalysis is mainly due to the lack of experimental techniques capable of simultaneously probing the changes in the electronic structure and visualizing the morphology of the active phase under operating condition. Within this context, STXM is a promising technique whereby soft X-ray spectroscopy is combined with 2D microscopy. Furthermore, recently it has been reported that by employing Micro Electro Mechanical System (MEMS)-based nanoreactors [36-38], in combination with a specifically designed in-situ gas-phase setup, the changes in the particle morphology and electronic structure of catalytic active phase can be probed under operating conditions [39]. Herein, we present a synthetic method for a bimetallic alumina-supported NiCo DMR catalyst, followed by in-situ STXM data collection during the catalyst activation/reduction and under DMR operating conditions. To the best of our knowledge, this is the first in-situ STXM study of a bimetallic DMR catalyst. These data are crucial for the understanding of the catalytic dynamics involved in the reforming of methane and thus fundamental to the development of catalysts with superior properties.

2.1 Experimental

2.1.1 Catalyst synthesis

For the synthesis, cobalt (II) acetate tetrahydrate (>98%, Sigma Aldrich), nickel(II) acetate tetrahydrate (99.998%, Sigma Aldrich), ammonium oxalate monohydrate (98%, Alfa Aesar), Methanol (99%, Alfa Aesar), 1-Hexanol (99%, Alfa Aesar), n-hexane 99% gamma alumina catalyst support (surface area 200 m²/g, Alfa Aesar), were employed.

The NiCoO_x/γAl₂O₃ catalyst was synthesized according to the modified reverse micellar method [40-41]. The advantage of this synthesis method is that it enables the production of bimetallic catalyst with controlled size and elemental ratios from the late transition metals. Other methods are mainly focused to synthesize small particles to increase the activity [22-23,42], and limit coke formation [43-44]. In contrast, for STXM experiments we are limited by the resolution of STXM and therefore large particles are desired. By using this method, we managed to produce highly active and stable particles while having the ideal size for STXM experiments. The first step in the production of the bimetallic catalyst involved preparing four different mixtures. Herein, 2.3 g ammonium oxalate monohydrate, 2.0 g nickel acetate tetrahydrate, 0.71 g cobalt acetate tetrahydrate were separately dissolved in 15 mL water and stirred for 15 minutes to obtain three different solutions. The fourth mixture was prepared by mixing and stirring 0.9 g cetyltrimethylammonium bromide, 9 mL hexanol and 12.6 mL hexane for 20 minutes. This mixture was divided into three equal parts, each of these was then added to the first 3 mixtures and stirred for another 20 minutes. In the last stage, all solutions were added

together and stirred for 48 hours to obtain the bimetallic catalyst. The produced catalyst was purified by centrifuging at 5500 rpm for 5 minutes and washed with a mixture of 30 mL methanol and 30 mL chloroform. This procedure was followed by centrifugation at 5500 rpm for 10 minutes and drying at 50 °C for 12 hours. To deposit the bimetallic catalyst on a support, 2.5 mL water was added to the prepared catalyst and 0.8 g of γ -Al₂O₃ was added to the solution. This was then stirred for 20 minutes and dried at 90 °C for 12 hours. The final phase of this process included calcining the supported catalyst at 400 °C for 10 hours in ambient air. This simple method allows the production of a wide variety of catalyst by selecting the desired metal acetates. In addition, the size of the active phase can be tuned by varying the amount of water and metal acetates used in this process. Figure S1 shows the complete synthesis route used in this study to produce the NiCoO/ γ -Al₂O₃ catalyst.

2.1.2 Scanning Transmission Electron Microscopy (STEM) experiments

For the STEM measurements a polymer coated Cu TEM grid was immersed in the dry catalyst powder. The morphology and elemental distribution of the catalyst was imaged by using the Hitachi HD-2700 spherical aberration corrected STEM. Images were acquired with an acceleration voltage of 200kV. In addition, Energy Dispersive X-ray (EDX) spectra were recorded with an EDAX Octane T Ultra W 200 mm² SDD attached to the STEM Microscope.

2.1.3 Activity measurements

During the activity measurements, the bed temperature was recorded with a K-type thermocouple positioned in the inner tube. The effluent gas was analyzed using an Agilent 3000 Micro-GC equipped with PLOT-Q and Molsieve 5A PLOT columns and a TCD for quantification. The gases employed for the activity measurements were: 10% H₂ diluted in N₂ (purity 99.999 %), CH₄ (purity 99.995 %), CO₂ (purity 99.995 %), N₂ (purity 99.999 %).

2.1.4 Temperature Programmed Reduction (TPR) measurements

The TPR profile was recorded in a quartz cell filled with 81.9 mg of the calcined catalysts. The sample was heated up to 850°C with a rate of 6 °C/min in a continuous flow of 4.6% H₂ in Ar (purity 99.99), adding up to a total volume of 84.1 mL/min. The H₂ consumption was determined by using a thermal conductivity analyzer (Hydros® 100, Rosemount).

2.2 Results

2.2.1 STEM

STEM images of the calcined sample displayed the formation of large agglomerates consisting of coalesced nanoparticles in the range of 5-20 nm (Figure 1a and S2). In addition, Energy Dispersive X-ray spectroscopy (EDX) data showed the distribution of Co (violet)- and Ni (green) oxides (Figure 1b-d) on the alumina support (yellow). Moreover, it is shown that both Ni and Co are not homogeneously distributed through the large agglomerates and specific domains with mainly a NiO character are also encountered as determined from X-ray Diffraction (XRD) (Figure S3). Furthermore, the metal loadings in atomic % for the NiCoO_x/γ-Al₂O₃ catalyst were predetermined from the bulk EDX analysis and corresponded to 56.4 (oxygen), 1.1 (cobalt), 9.2 (nickel), and 33.3 (aluminium). In addition, the Ni:Co ratio in this sample was close to 9:1 (Figure S4).

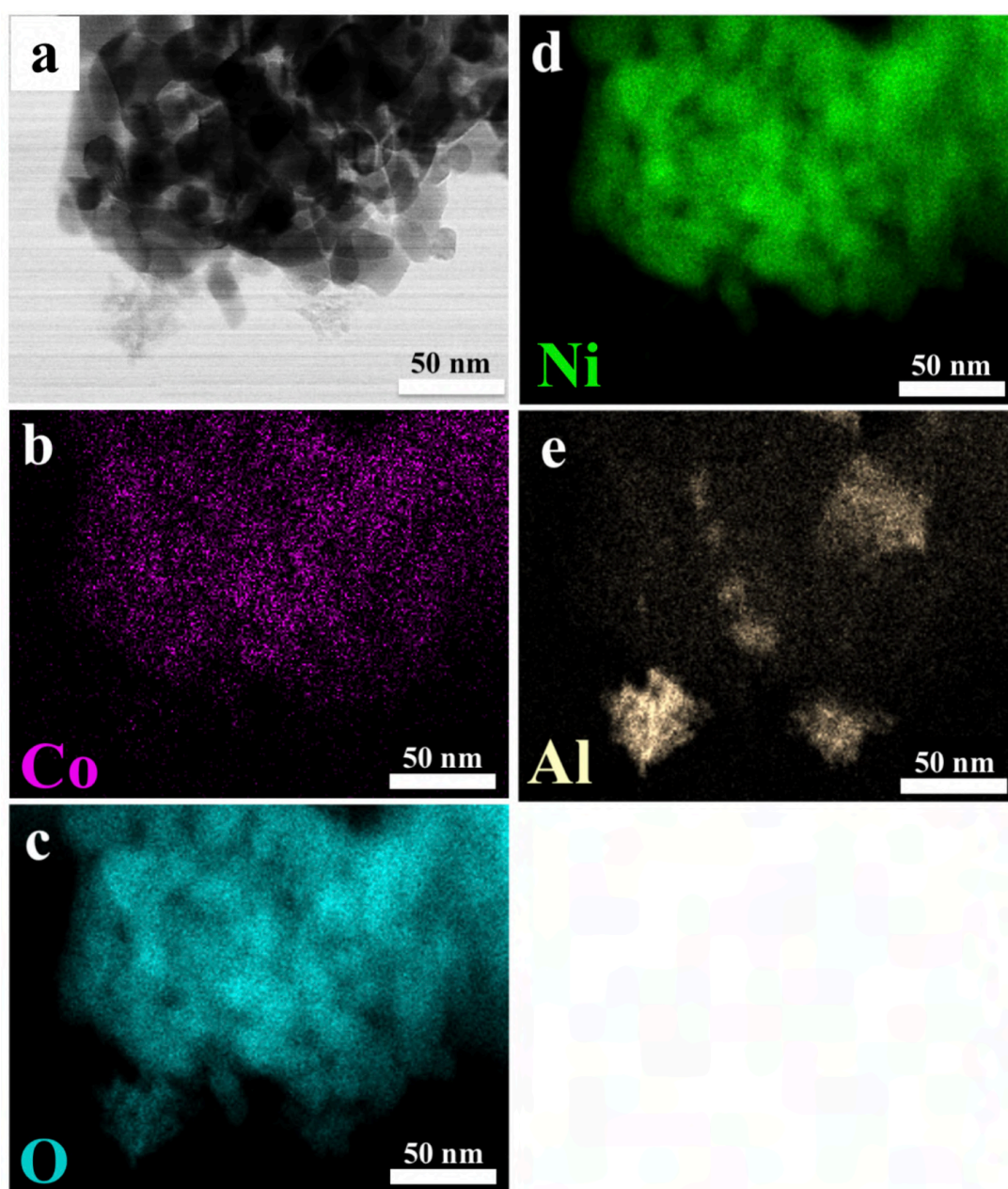


Figure 1: a) Bright field STEM image of the calcined (400 °C) catalyst. b,c,d,e) STEM-EDX elemental mapping images of respectively Co, O, Ni and Al indicated with violet, blue, green and yellow. c) The measured oxygen signal originating from the metal oxides and the alumina.

2.2.2 TPR and Catalytic activity tests

Prior to the in-situ STXM experiment the TPR profile and the catalytic activity for the NiCoO/ γ -Al₂O₃ DMR catalyst were measured (Figure S5). The TPR profile shows the presence of two clear reduction peaks and suggests the reduction of metal-oxides in the temperature range of 250-500 °C. The first peak at 265 °C is assigned to the reduction of Co³⁺ species to Co²⁺ whereas the main peak at 325 °C is assigned to the reduction of Ni²⁺ and Co²⁺ to their metallic states [45-48]. Further, these data indicate that full reduction of the metal oxides into the metallic state already occurs at temperatures lower than 500 °C. Next, the DMR activity of the NiCoO/ γ -Al₂O₃ catalyst was investigated on a lab scale via a fixed-bed reactor by loading 50 mg of the catalyst particles that were sieved down to <200 μ m. In the first stage of the experiment, the catalyst was activated by performing a reduction treatment under 10% H₂ in N₂ at 850 °C. The catalyst was then cooled down to 800 °C and, after switching to the DMR gas mixture (7% CH₄ & 9.5% CO₂ in N₂), the DMR activity was measured on stream for 2 hours (Figure 2). The degrees of conversion after 2 hours stabilized at 86% and 77% for CH₄ and CO₂, respectively. In addition, the corresponding yields for H₂ and CO were ~78% and ~80%, respectively. The activity of the NiCoO/ γ -Al₂O₃ DMR catalyst in terms of CH₄ conversion is of the same order of magnitude as that exhibited by bimetallic NiCo catalysts in literature (75-90%), which was found to exceed that of monometallic Ni or Co DRM catalysts (<70%) [21,30-31]. These findings hint to the synergistic effect between the Ni and Co in the bimetallic NiCo DMR catalyst. Further, Figure S6 shows the activity measurements results after exposing the catalyst to DMR conditions for 15 hours.

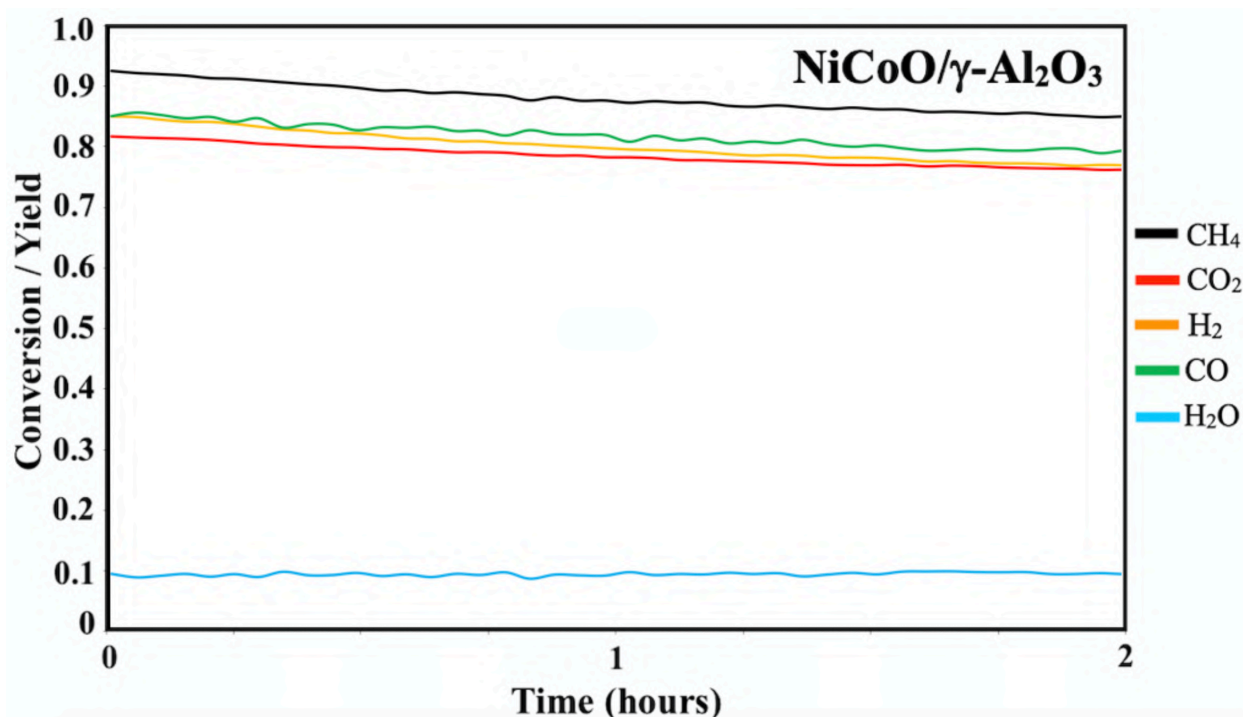


Figure 2: Activity measurements for the NiCoO/ γ -Al₂O₃ DMR catalyst. Conversion/Yield fractions during the DMR experiment at 800 °C under 7% CH₄ and 9.5% CO₂ in N₂ and a flow rate of 490 mL/min. Prior to the DMR activity measurements the catalyst was treated for 30 minutes under 10% H₂ in N₂ with a flowrate of 100 mL/min.

2.2.3 In-situ STXM

For the in-situ STXM experiment, the X-ray transmission signal of a selected particle at both Ni (in green) and Co (in violet) was acquired for: I. the freshly calcined sample, II. during reduction with 5% H₂ in Ar, and III. through the DMR process under 7% CH₄ & 9.5% CO₂ in N₂, Figure S7. Further, Figure SI. 8 illustrates that multiple particles were investigated to confirm the reproducibility of the in-situ STXM results. The average lateral dimensions and thicknesses of the selected calcined catalyst particles were in the order of 0.4-1.2 μm and 200-300 nm, respectively. The spectral elemental images were obtained by subtracting the pre-edge spectral elemental map from the that obtained at the L₃-edge maximum. The elemental composition maps are presented in Figure 3, and the corresponding Co and Ni L₃-edge XAS spectra are shown in Figure 4. For the sake of comparison, L₃-edge XAS spectra of the metallic Ni- and Co oxides are also included in Figure 4.

In general, the elemental composition maps for the freshly calcined sample (Figure 3a) shows a rather inhomogeneous distribution of Ni and Co on the γ-Al₂O₃ support. This observation is further supported by the individual elemental composition maps of Co and Ni acquired for the same calcined particle (Figure SI. 9). There are, however, some Ni-rich regions in the calcined catalyst, consistent with the corresponding STEM-EDX data (Figure 1). Based on a comparison with reference spectra the formation of Co₃O₄ (2xCo³⁺ O_h and 1xCo²⁺ T_d) and NiO (Ni²⁺ O_h) species, as a result of the calcination process, is confirmed as reported in other studies [24,49].

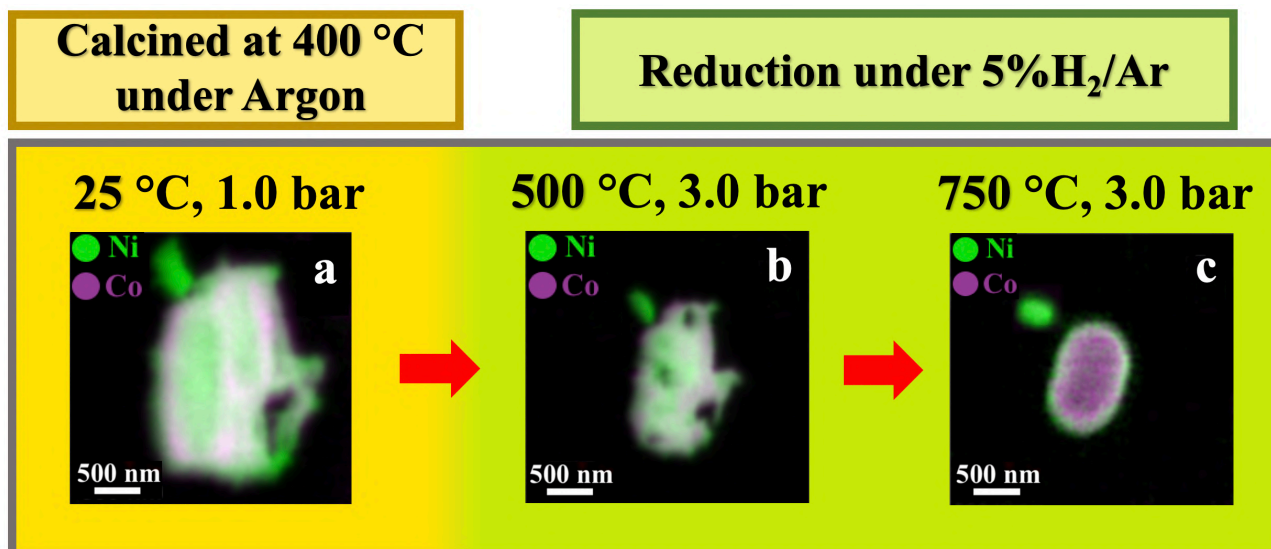


Figure 3: a) Elemental composition maps showing the distribution of Ni (in green) and Co (in violet) for: a) the freshly calcined particles, b) following the reduction step at 500 °C under 5% H₂ in Ar, where the Ni and Co oxides are reduced, and c) at 750 °C and under 5% H₂ in Ar flow where the Ni and Co Al₂O₄ are fully reduced. This last Image confirms the elemental segregation within the large agglomerates during (full) reduction.

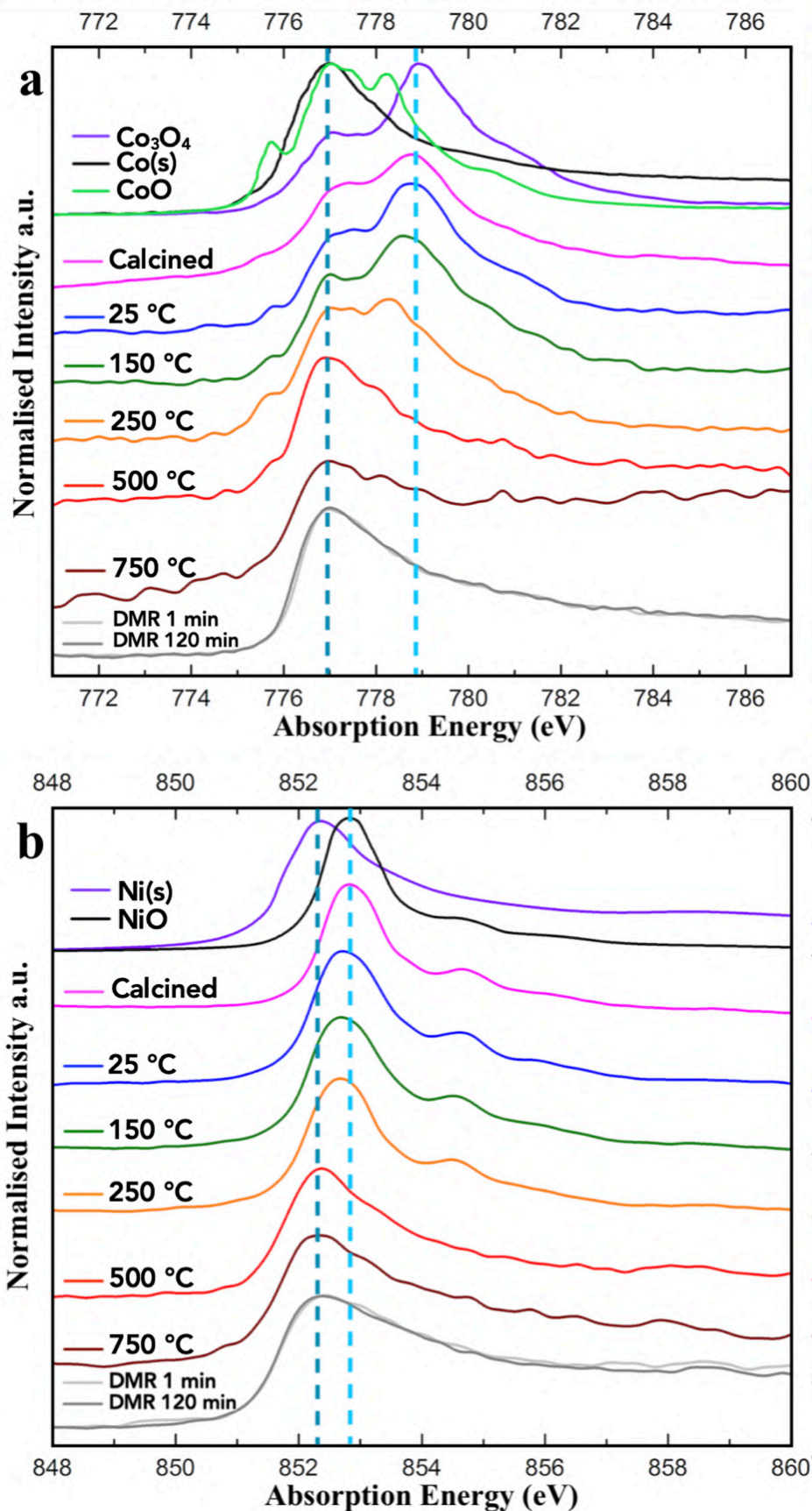


Figure 4: a) Co L₃-edge spectrum of the NiCoO/ γ -Al₂O₃ sample collected under operating conditions. The L₃-edge of calcined catalyst has the same shape and energy position when compared to Co₃O₄. Under reducing conditions at 500 °C Co₃O₄-like compound is converted into metallic Co. b) The collection of Ni L₃-edge spectra of the fresh catalyst has the same shape and energy position if compared to NiO. Under DMR conditions both the Ni and Co stay reduced.

Next, the catalyst was activated by heating the sample stepwise from 25 to 750 °C under continuous 5% H₂ in Ar flow, the corresponding Co and Ni L₃-edges are shown in Figures 4, S10 and 11. At 250 °C the Ni L-edge remains essentially unaffected, indicating Ni²⁺ is still present. However, the Co L-edge have changed quite significantly both in the multiplet structure and in the average energy. The observed changes are consistent with the reduction of the Co³⁺ O_h sites to most probably octahedrally coordinated Co²⁺ oxide. These results are in agreement with the TPR data (Figure S5), and with literature studies, where the partial reduction of Co₃O₄ was found to occur at a relatively lower temperature compared with the Ni site [50-51]. The most prominent changes in the L-edge spectra are observed at 500 °C. At this temperature the shift in both Co and Ni L-edges together with the resulting spectral shape indicate the full reduction of the metal oxides to their metallic state. This data is again consistent with the measured TPR profiles (see Figure S5). Further, as displayed in Figure 3b, the elemental composition maps collected at 500 °C show a change in the morphology and elemental distribution for the NiCo particle. In addition, this figure clearly shows the formation of voids within the particle, which may be a result of restructuring upon loss of oxygen from the lattice [52-53].

In the second phase of the reduction process, the temperature was increased to 750 °C. While effectively no changes in either the Co or Ni L-edges are observed (Figure 4), the elemental composition maps in Figure 3c display a rather dramatic change in the morphology of the active phase with Co migrating inward and a Ni-rich shell forming on the surface of the large agglomerate. The elemental composition maps shown in Figure 3 and SI. 12 demonstrate that in this step the formed structure consists of two parts; I. the surface, made of only nickel II. the core, consisting of both Co and Ni. This behaviour demonstrates the increase in surface mobility of Ni and Co at high temperature and under 5% H₂ in Ar flow. While previous studies have suggested that alloy formation between Ni and Co is key to optimizing DMR activity and stability [29,32,54-55], instead here we show that elemental segregation to form a Ni-rich surface is involved in the activation of the catalyst. We note that previous in situ XPS studies by Wu et al. in a related NiCo catalyst indicated that Co migrates inward during the reduction of NiCo and that at the completion of reduction, the surface of the nanoparticle is a 50:50 mixture of Co and Ni [32]. However, we note that their experiments are performed well below atmospheric pressure (1×10⁻⁷ Bar) and it may be that at such reduced pressures full conversion does not occur. Further, while XPS is a surface sensitive measurement, it can only indirectly infer particle morphology, in contrast to the present STXM study which directly probes the structure. Hence, these results emphasize the importance of spectromicroscopy for identifying morphological changes in nanoparticle composition during the activation of the catalyst. The results also bring into question whether an alloyed surface is required for optimal catalysis. Interestingly, we note that while STXM shows a Ni rich outer shell on the particle, the inner part of the particle may be an alloy.

Finally, under DMR reaction conditions, we focused on another NiCo particle with much smaller dimensions in order to precisely follow the morphological changes. Herein, elemental composition maps and L-edge XAS spectra were obtained during the DMR reaction at 750 °C under 7% CH₄ & 9.5% CO₂ in N₂ at I) 1 minute and II) 120 minutes exposure time. The data collected after 1 minute exposure to the DMR conditions clearly indicate that the segregated structure is preserved (Figure 5 b) and that both Ni and Co remained reduced based on the L-edge spectra (Figure 4). A close inspection of Figure 5b reveals that in certain locations on the surface of the large NiCo particle, which are

shown with red arrows, the Ni concentration has increased. After 120 minutes under DMR conditions, while the Ni and Co are still reduced as seen from the L-edges, however, the formation of Ni-rich branches at the surface of the particle is observed (Figure 5c). In this process, the unexpected formation of Ni-rich branches may be associated with the growth of filamentous carbon on the surface of the catalytically active sites [56-57]. This result is consistent with that of Takahashi et al. where it was demonstrated that carbonaceous species are removed at a slower rate on pure Ni surfaces which ultimately leads to deactivation due to carbon deposition [29].

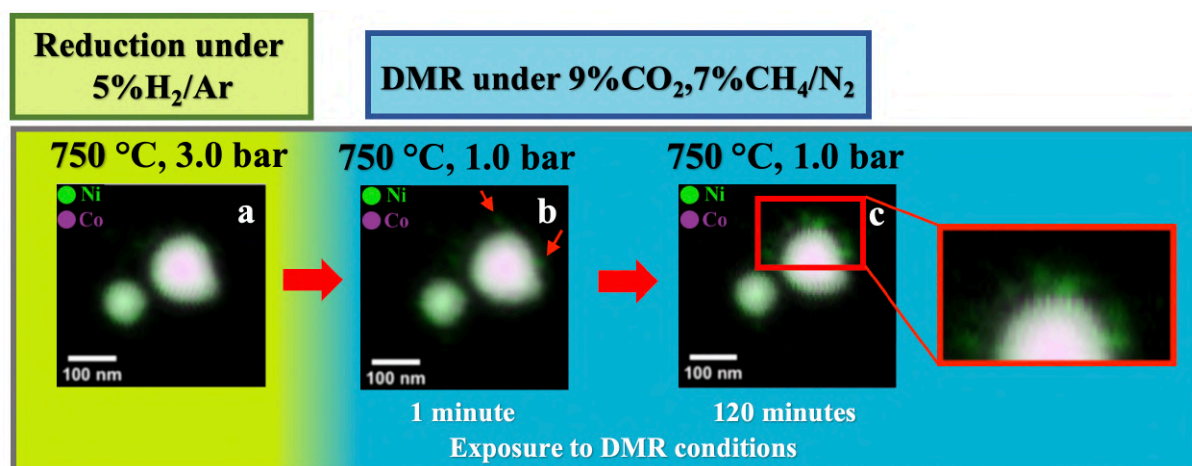


Figure 5: a) The image confirms the elemental segregation within the large agglomerates during reduction. Finally, in b and c the elemental composition maps were obtained following the DMR process after 1 minute and 120 minutes exposure time show the formation of Ni branches at the surface of the particle.

2.3 Conclusion

In summary, we have successfully developed a modified route for the controlled synthesis of a NiCo catalyst with high activity and stability towards the DMR reaction. In-situ STXM measurements show that while in the calcined form the particles exhibit an inhomogeneous distribution of Ni and Co, during the reductive activation step at 750 °C (5% H₂ in Ar) a clear elemental segregation is observed; with Co migrating toward the center of the agglomerated nanoparticles and Ni forming a shell on the outer surface of the particle. The segregated structure is preserved during DMR, suggesting that Ni is the primary active site, while the more readily oxidized Co may serve as an electron donor to Ni during catalysis.

The dynamics of the particle morphology highlights a mechanism by which the synergistic interaction between the metals is optimized in order to maximize catalytic activity and minimize coking [58]. These studies highlight the ability of in-situ STXM to monitor the evolution of particle morphology and electronic structure under operating conditions. The presented methods provide promising means to evaluate not only the catalytic mechanisms, but also deactivation processes. We thus believe that in the future, in-situ STXM will provide important contributions toward knowledge-based catalytic design.

Acknowledgements

The Max Planck Society and the European Research Council under the European Union's Seventh Framework Programme (FP/2007-2013) ERC Grant Agreement No. 615414 (S.D.) and NFFA EU grant (H2020) No. 654360 (R.B.) are acknowledged for funding. The PolLux end station was financed by the German Ministerium für Bildung und Forschung (BMBF) through contracts 05KS4WE1/6 and 05KS7WE1. The authors thank Christian W. Lehmann from the Max-Planck-Institut für Kohlenforschung for supporting the STEM measurements.

References

- [1] Barelli, L.; Ottaviano, A. Solid Oxide Fuel Cell Technology Coupled With Methane Dry Reforming: A Viable Option For High Efficiency Plant With Reduced CO₂ Emissions. *Energy* **2014**, *71*, 118-129.
- [2] Dufour, J.; Serrano, D.; Galvez, J.; Moreno, J.; Galrcia, C. Life Cycle Assessment Of Processes For Hydrogen Production. Environmental Feasibility And Reduction Of Greenhouse Gases Emissions. *Int. J. Hydrogen Energy* **2009**, *34* (3), 1370-1376.
- [3] Das, S.; Shah, M.; Gupta, R.; Bordoloi, A. Enhanced Dry Methane Reforming Over Ru Decorated Mesoporous Silica And Its Kinetic Study. *J. CO₂ Util.* **2019**, *29*, 240-253.
- [4] Świrk, K.; Gálvez, M.; Motak, M.; Grzybek, T.; Rønning, M.; Da Costa, P. Syngas Production From Dry Methane Reforming Over Yttrium-Promoted Nickel-KIT-6 Catalysts. *Int. J. Hydrogen Energy* **2019**, *44* (1), 274-286.
- [5] Li, X.; Li, D.; Tian, H.; Zeng, L.; Zhao, Z.; Gong, J. Dry Reforming Of Methane Over Ni/La₂O₃ Nanorod Catalysts With Stabilized Ni Nanoparticles. *Appl. Catal., B* **2017**, *202*, 683-694.
- [6] Lavoie, J. Review On Dry Reforming Of Methane, A Potentially More Environmentally-Friendly Approach To The Increasing Natural Gas Exploitation. *Front. Chem.* **2014**, *2*.
- [7] Wang, Y.; Yao, L.; Wang, S.; Mao, D.; Hu, C. Low-Temperature Catalytic CO₂ Dry Reforming Of Methane On Ni-Based Catalysts: A Review. *Fuel Process. Technol.* **2018**, *169*, 199-206.
- [8] Serrano-Lotina, A.; Rodríguez, L.; Muñoz, G.; Daza, L. Biogas Reforming On La-Promoted Ni/gal Catalysts Derived From Hydrotalcite-Like Precursors. *J. Power Sources* **2011**, *196* (9), 4404-4410.
- [9] Muraza, O.; Galadima, A. A Review On Coke Management During Dry Reforming Of Methane. *Int. J. Energy Res.* **2015**, *39* (9), 1196-1216.
- [10] Usman, M.; Wan Daud, W.; Abbas, H. Dry Reforming Of Methane: Influence Of Process Parameters—A Review. *Renewable Sustainable Energy Rev.* **2015**, *45*, 710-744.
- [11] Dębek, R.; Zubek, K.; Motak, M.; Da Costa, P.; Grzybek, T. Effect Of Nickel Incorporation Into Hydrotalcite-Based Catalyst Systems For Dry Reforming Of Methane. *Res. Chem. Intermed.* **2015**, *41* (12), 9485-9495.
- [12] Pakhare, D.; Spivey, J. A Review Of Dry (CO₂) Reforming Of Methane Over Noble Metal Catalysts. *Chem. Soc. Rev.* **2014**, *43* (22), 7813-7837.

- [13] Medeiros, R.; Macedo, H.; Melo, V.; Oliveira, Â.; Barros, J.; Melo, M.; Melo, D. Ni Supported On Fe-Doped MgAl₂O₄ For Dry Reforming Of Methane: Use Of Factorial Design To Optimize H₂ Yield. *Int. J. Hydrogen Energy* **2016**, *41* (32), 14047-14057.
- [14] Margossian, T.; Larmier, K.; Kim, S.; Krumeich, F.; Fedorov, A.; Chen, P.; Müller, C.; Copéret, C. Molecularly Tailored Nickel Precursor And Support Yield A Stable Methane Dry Reforming Catalyst With Superior Metal Utilization. *JACS* **2017**, *139* (20), 6919-6927.
- [15] Baudouin, D.; Rodemerck, U.; Krumeich, F.; Mallmann, A.; Szeto, K.; Ménard, H.; Veyre, L.; Candy, J.; Webb, P.; Thieuleux, C.; Copéret, C. Particle Size Effect In The Low Temperature Reforming Of Methane By Carbon Dioxide On Silica-Supported Ni Nanoparticles. *J. Catal.* **2013**, *297*, 27-34.
- [16] Carencó, S. Describing Inorganic Nanoparticles In The Context Of Surface Reactivity And Catalysis. *Chem. Commun.* **2018**, *54* (50), 6719-6727.
- [17] Gonzalez-de-laCruz, V.; Pereñíguez, R.; Ternero, F.; Holgado, J.; Caballero, A. In Situ XAS Study Of Synergic Effects On Ni-Co/ZrO₂ Methane Reforming Catalysts. *J. Phys. Chem. C* **2012**, *116* (4), 2919-2926.
- [18] San-José-Alonso, D.; Juan-Juan, J.; Illán-Gómez, M.; Román-Martínez, M. Ni, Co And Bimetallic Ni-Co Catalysts For The Dry Reforming Of Methane. *Appl. Catal., A* **2009**, *371* (1-2), 54-59.
- [19] Wang, H.; Blaylock, D.; Dam, A.; Liland, S.; Rout, K.; Zhu, Y.; Green, W.; Holmen, A.; Chen, D. Steam Methane Reforming On A Ni-Based Bimetallic Catalyst: Density Functional Theory And Experimental Studies Of The Catalytic Consequence Of Surface Alloying Of Ni With Ag. *Catal. Sci. Technol.* **2017**, *7* (8), 1713-1725.
- [20] Sánchez-Sánchez, M.; Navarro, R.; Fierro, J. Ethanol Steam Reforming Over Ni/M_xO_y-Al₂O₃ (M=Ce, La, Zr And Mg) Catalysts: Influence Of Support On The Hydrogen Production. *Int. J. Hydrogen Energy* **2007**, *32* (10-11), 1462-1471.
- [21] Bouarab, R.; Akdim, O.; Auroux, A.; Cherifi, O.; Mirodatos, C. Effect Of MgO Additive On Catalytic Properties Of Co/SiO₂ In The Dry Reforming Of Methane. *Appl. Catal., A* **2004**, *264* (2), 161-168.
- [22] Wei, J.; Iglesia, E. Isotopic And Kinetic Assessment Of The Mechanism Of Reactions Of CH₄ With CO₂ Or H₂O To Form Synthesis Gas And Carbon On Nickel Catalysts. *J. Catal.* **2004**, *224* (2), 370-383.
- [23] Ligthart, D.; van Santen, R.; Hensen, E. Influence Of Particle Size On The Activity And Stability In Steam Methane Reforming Of Supported Rh Nanoparticles. *J. Catal.* **2011**, *280* (2), 206-220.

- [24] Theofanidis, S.; Galvita, V.; Poelman, H.; Marin, G. Enhanced Carbon-Resistant Dry Reforming Fe-Ni Catalyst: Role Of Fe. *ACS Catal.* **2015**, *5* (5), 3028-3039.
- [25] You, X.; Wang, X.; Ma, Y.; Liu, J.; Liu, W.; Xu, X.; Peng, H.; Li, C.; Zhou, W.; Yuan, P.; Chen, X. Ni-Co/Al₂O₃ bimetallic Catalysts For CH₄ steam Reforming: Elucidating The Role Of Co For Improving Coke Resistance. *ChemCatChem* **2014**, *6* (12), 3377-3386.
- [26] Mohamedali, M.; Henni, A.; Ibrahim, H. Recent Advances In Supported Metal Catalysts For Syngas Production From Methane. *Chem. Eng.* **2018**, *2* (1), 9.
- [27] Bian, Z.; Das, S.; Wai, M.; Hongmanorom, P.; Kawi, S. A Review On Bimetallic Nickel-Based Catalysts For CO₂ Reforming Of Methane. *ChemPhysChem* **2017**, *18* (22), 3117-3134.
- [28] Zhang, J.; Wang, H.; Dalai, A. Effects Of Metal Content On Activity And Stability Of Ni-Co Bimetallic Catalysts For CO₂ Reforming Of CH₄. *Appl. Catal., A* **2008**, *339* (2), 121-129.
- [29] AlSabban, B.; Falivene, L.; Kozlov, S.; Aguilar-Tapia, A.; Ould-Chikh, S.; Hazemann, J.; Cavallo, L.; Basset, J.; Takanahe, K. In-Operando Elucidation Of Bimetallic CoNi Nanoparticles During High-Temperature CH₄/CO₂ Reaction. *Appl. Catal., B* **2017**, *213*, 177-189.
- [30] Bonifacio, C.; Carenco, S.; Wu, C.; House, S.; Bluhm, H.; Yang, J. Thermal Stability Of Core-Shell Nanoparticles: A Combined In Situ Study By XPS And TEM. *Chem. Mater.* **2015**, *27* (20), 6960-6968.
- [31] Carenco, S.; Wu, C.; Shavorskiy, A.; Alayoglu, S.; Somorjai, G.; Bluhm, H.; Salmeron, M. Synthesis And Structural Evolution Of Nickel-Cobalt Nanoparticles Under H₂ and CO₂. *Small* **2015**, *11* (25), 3045-3053.
- [32] Wu, Z.; Yang, B.; Miao, S.; Liu, W.; Xie, J.; Lee, S.; Pellin, M.; Xiao, D.; Su, D.; Ma, D. Lattice Strained Ni-Co Alloy As A High-Performance Catalyst For Catalytic Dry Reforming Of Methane. *ACS Catal.* **2019**, *9* (4), 2693-2700.
- [33] De, S.; Zhang, J.; Luque, R.; Yan, N. Ni-Based Bimetallic Heterogeneous Catalysts For Energy And Environmental Applications. *Energy Environ. Sci.* **2016**, *9* (11), 3314-3347.
- [34] Wang, L.; Li, D.; Koike, M.; Watanabe, H.; Xu, Y.; Nakagawa, Y.; Tomishige, K. Catalytic Performance And Characterization Of Ni-Co Catalysts For The Steam Reforming Of Biomass Tar To Synthesis Gas. *Fuel* **2013**, *112*, 654-661.
- [35] Takanahe, K.; Nagaoka, K.; Nariai, K.; Aika, K. Titania-Supported Cobalt And Nickel Bimetallic Catalysts For Carbon Dioxide Reforming Of Methane. *J. Catal.* **2005**, *232* (2), 268-275.

- [36] Vendelbo, S.; Elkjær, C.; Falsig, H.; Puspitasari, I.; Dona, P.; Mele, L.; Morana, B.; Nelissen, B.; van Rijn, R.; Creemer, J.; Kooyman, P.; Helveg, S. Visualization Of Oscillatory Behaviour Of Pt Nanoparticles Catalysing CO Oxidation. *Nat. Mater.* **2014**, *13* (9), 884-890.
- [37] Bremmer, G.; Zacharaki, E.; Sjøstad, A.; Navarro, V.; Frenken, J.; Kooyman, P. In Situ TEM Observation Of The Boudouard Reaction: Multi-Layered Graphene Formation From CO On Cobalt Nanoparticles At Atmospheric Pressure. *Faraday Discuss.* **2017**, *197*, 337-351.
- [38] Creemer, J.; Santagata, F.; Morana, B.; Mele, L.; Alan, T.; Iervolino, E.; Pandraud, G.; Sarro, P. An All-In-One Nanoreactor For High-Resolution Microscopy On Nanomaterials At High Pressures. *2011 IEEE 24th Int. Conf. on Micro Electro Mech. Syst.* **2011**.
- [39] van Ravenhorst, I.; Vogt, C.; Oosterbeek, H.; Bossers, K.; Moya-Cancino, J.; van Bavel, A.; van der Eerden, A.; Vine, D.; de Groot, F.; Meirer, F.; Weckhuysen, B. Capturing The Genesis Of An Active Fischer-Tropsch Synthesis Catalyst With Operando X-Ray Nanospectroscopy. *Angew. Chem. Int. Ed.* **2018**, *57* (37), 11957-11962.
- [40] Menezes, P.; Indra, A.; Levy, O.; Kailasam, K.; Gutkin, V.; Pfrommer, J.; Driess, M. Using Nickel Manganese Oxide Catalysts For Efficient Water Oxidation. *Chem. Commun.* **2015**, *51* (24), 5005-5008.
- [41] Al Samarai, M.; Hahn, A.; Beheshti Askari, A.; Cui, Y.; Yamazoe, K.; Miyawaki, J.; Harada, Y.; Rüdiger, O.; DeBeer, S. Elucidation Of Structure–Activity Correlations In A Nickel Manganese Oxide Oxygen Evolution Reaction Catalyst By Operando Ni L-Edge X-Ray Absorption Spectroscopy And 2P3d Resonant Inelastic X-Ray Scattering. *ACS Appl. Mater. Interfaces* **2019**, *11* (42), 38595-38605.
- [42] Raberg, L.; Jensen, M.; Olsbye, U.; Daniel, C.; Haag, S.; Mirodatos, C.; Sjøstad, A. Propane Dry Reforming To Synthesis Gas Over Ni-Based Catalysts: Influence Of Support And Operating Parameters On Catalyst Activity And Stability. *J. Catal.* **2007**, *249* (2), 250-260.
- [43] Chen, D.; Christensen, K.; Ochoafernandez, E.; Yu, Z.; Totdal, B.; Latorre, N.; Monzon, A.; Holmen, A. Synthesis Of Carbon Nanofibers: Effects Of Ni Crystal Size During Methane Decomposition. *J. Catal.* **2005**, *229* (1), 82-96.
- [44] Kim, J.; Suh, D.; Park, T.; Kim, K. Effect Of Metal Particle Size On Coking During CO₂ Reforming Of CH₄ Over Ni–Alumina Aerogel Catalysts. *Appl. Catal., A* **2000**, *197* (2), 191-200.
- [45] M. Cesário, C. Gennequin, Catalytic Materials For Hydrogen Production And Electro-Oxidation Reactions. *Frontiers In Ceramic Science Volume 2*, Bentham Science Publishers, **2018**, p140.

- [46] Moongraksathum, B.; Shang, J.; Chen, Y. Photocatalytic Antibacterial Effectiveness Of Cu-Doped TiO₂ Thin Film Prepared Via The Peroxo Sol-Gel Method. *Catal.* **2018**, *8* (9), 352.
- [47] Zhang, X.; Liu, J.; Jing, Y.; Xie, Y. Support Effects On The Catalytic Behavior Of NiO/Al₂O₃ For Oxidative Dehydrogenation Of Ethane To Ethylene. *Appl. Catal., A* **2003**, *240* (1-2), 143-150.
- [48] Nyathi, T.; Fischer, N.; York, A.; Claeys, M. Effect Of Crystallite Size On The Performance And Phase Transformation Of Co₃O₄/Al₂O₃ Catalysts During CO-Prox-An In Situ Study. *Faraday Discuss.* **2017**, *197*, 269-285.
- [49] Wang, H.; Hung, S.; Chen, H.; Chan, T.; Chen, H.; Liu, B. In Operando Identification Of Geometrical-Site-Dependent Water Oxidation Activity Of Spinel Co₃O₄. *JACS* **2015**, *138* (1), 36-39.
- [50] M. Cesário, D. de, C. Gennequin, *Catalytic Materials For Hydrogen Production And Electro-Oxidation Reactions*, Bentham Science Publishers, Sharjah, **2018**.
- [51] Wang, D.; Li, S.; Du, Y.; Wu, X.; Chen, Y. Self-Templating Synthesis Of 3D Hierarchical NiCo₂O₄@NiO Nanocage From Hydrotalcites For Toluene Oxidation. *Catal.* **2019**, *9* (4), 352.
- [52] Jeangros, Q.; Hansen, T.; Wagner, J.; Damsgaard, C.; Dunin-Borkowski, R.; Hébert, C.; Van herle, J.; Hessler-Wyser, A. Reduction Of Nickel Oxide Particles By Hydrogen Studied In An Environmental TEM. *J. Mater. Sci.* **2012**, *48* (7), 2893-2907.
- [53] Faes, A.; Nakajo, A.; Hessler-Wyser, A.; Dubois, D.; Brisse, A.; Modena, S.; Van herle, J. Redox Study Of Anode-Supported Solid Oxide Fuel Cell. *J. Power Sources* **2009**, *193* (1), 55-64.
- [54] Zhang, J.; Wang, H.; Dalai, A. Development Of Stable Bimetallic Catalysts For Carbon Dioxide Reforming Of Methane. *J. Catal.* **2007**, *249* (2), 300-310.
- [55] Fan, X.; Liu, Z.; Zhu, Y.; Tong, G.; Zhang, J.; Engelbrekt, C.; Ulstrup, J.; Zhu, K.; Zhou, X. Tuning The Composition Of Metastable Co_xNi_{1-y}Mg_{100-x-y}(OH)(OCH₃) Nanoplates For Optimizing Robust Methane Dry Reforming Catalyst. *J. Catal.* **2015**, *330*, 106-119.
- [56] Wolfbeisser, A.; Sophiphun, O.; Bernardi, J.; Wittayakun, J.; Föttinger, K.; Rupprechter, G. Methane Dry Reforming Over Ceria-Zirconia Supported Ni Catalysts. *Catalysis Today* **2016**, *277*, 234-245.
- [57] Bang, S.; Hong, E.; Baek, S.; Shin, C. Effect Of Acidity On Ni Catalysts Supported On P-Modified Al₂O₃ For Dry Reforming Of Methane. *Catal. Today* **2018**, *303*, 100-105.

- [58] Nagaoka, K.; Takanabe, K.; Aika, K. Modification Of Co/TiO₂ For Dry Reforming Of Methane At 2Mpa By Pt, Ru Or Ni. *Appl. Catal., A* **2004**, 268 (1-2), 151-158.

2.4 Supporting Information

In-situ X-ray Microscopy reveals particle dynamics in a NiCo dry methane reforming catalyst under operating conditions

Abbas Beheshti Askari^(a), Mustafa al Samarai^(a), Bruno Morana^(b), Lukas Tillmann^(c), Norbert Pfänder^(a), Aleksandra Wandzilak^(a), Benjamin Watts^(d), Rachid Belkhou^(e), Martin Muhler^{*(a, c)}, and Serena DeBeer^{*(a)}

(a) Max Planck Institute for Chemical Energy Conversion, Stiftstraße 34-36, D-45470 Mülheim an der Ruhr, Germany

(b) NanoInsight, Feldmannweg 17, 2628 CT Delft, The Netherlands

(c) Laboratory of Industrial Chemistry, Ruhr-University Bochum, Universitätsstraße 150, D-44801 Bochum, Germany

(d) Paul Scherrer Institute, 5332 Villigen PSI, Switzerland

(e) Synchrotron SOLEIL, L'Orme des Merisiers, Saint-Aubin – BP 48, F-91192 Gif-sur-Yvette cedex, France

2.4.1 Catalyst loading

The NiCoO_x/γ-Al₂O₃ dry methane reforming catalyst was synthesized according to the newly developed reverse micellar method. For loading the nanoparticles into the nanoreactor an ethanol suspension containing the catalyst was prepared and sonicated for 1 minute. Next, with the aid of a dispensing pipette, 1 μL of this suspension was added to the inlet of the nanoreactor. Due to capillary forces the suspension entered and filled the microchannel. Afterwards the nanoreactor was placed on a hotplate and heated up to 40 °C for 1 hour. This allowed to remove/evaporate all the ethanol leaving the nanoparticles into the microchannel. An optical microscope was then employed to verify the presence of the nanoparticle on the SiNx windows of the nanoreactor. The loading procedure was repeated until the desired number of particles was found on the windows.

2.4.2 Sample imaging

Scanning Transmission X-ray Microscopy experiments for particles 1 and 3 were performed at the Hermes beamline at SOLEIL synchrotron radiation facility [1], while particle 2 was investigated at the PolLux beamline of the Paul Scherrer Institute [2]. The spatial resolution of the used zone plates were 35 nm.

During the STXM measurements, the sample is raster-scanned in two dimensions and the transmission from a selected number of points on either dimension is converted to their respective Optical Density (OD) maps. The resulting 2D image contains information regarding the elemental distribution, oxidation state and the local coordination. In the stack mode, a series of the spectral elemental composition maps are collected from a selected energy range, including the pre-edge, edge and post-edge regions.

As an example, to generate the elemental composition maps for each calcined particle the Co and Ni L-edges were measured as shown in Figure SI. 9. The Ni L-edges illustrate that there are some regions containing a higher Ni concentration (shown in red) than others. In addition, by investigating the Co L-edge, we observe that Co is not evenly distributed though the particles and it appears that there are some Co-deficient regions. Next, to determine the relative distributions of the elements, spectral images of different Ni and Co in the same particle or selected regions were aligned and overlaid to obtain the Red, Green, and Blue (RGB) maps. To obtain the RGB maps we have to specify which

element corresponds to red, green and blue. In addition, since only two elements (Ni and Co) were probed during this study blue and red were assigned to Co, while green was used for Ni. The proximity of Co to Ni (in green) yields the white color. Thus, the light (white) areas in Figure SI. 8h correspond to the areas with an equal concentration of both elements.

Furthermore, during the STXM measurements we only probed the Ni and Co L-edges, whereas due to the low absorption cross section of Al K-edge and the thin alumina support, these were not measured. For the in-situ STXM measurements surface micromachined nanoreactors were employed [3-5]. The in-situ sample was loaded into the nanoreactors by drop casting the catalyst suspension on the inlet of the nanoreactors, whereas the *ex situ* reference samples were directly drop-casted from a suspension on thin Si₃N₄ membranes.

2.4.3 Data processing

The acquired data were processed by using the aXis2000 software package (<http://unicorn.mcmaster.ca/aXis2000.html>) and OriginPro 9.0.

2.4.4 Nanoreactor

The nanoreactors employed for the in-situ measurements were similar those employed in [3-5] and were produced by NanoInsight. These are silicon-based miniaturized chemical reactors realized by means of microfabrication techniques as described in [6]. The nanoreactor is shown in Figure SI. 13, it consists of a silicon-rich silicon nitride (SiN_x) microchannel integrated on the surface of a silicon (Si) rectangular support. The microchannel has a length of 4.6 mm, a width of 0.3 mm, and a height of only 4.5 μm. To prevent deformation under pressurization and to increase its strength the top and bottom part of the microchannel are connected together by an array of micropillars. Thanks to this structure pressures up to 9 bar can be reached. A microheater spiral made of a thin film of molybdenum (Mo) is integrated on the top-side of the central part of the microchannel. The microheater is equipped with four contacts to allow its powering while enabling the accurate reading of the temperature of the heated area. A maximum temperature of 750 °C can be reached by flowing a current through the microheater. An array of 41 circular windows each having a diameter of 6 μm, is integrated between the windings of the microheater spiral. The same number of windows is integrated on the bottom part of the microchannel and aligned to the top ones. The windows are made of SiN_x and have a thickness of only 18 nm making them highly transparent to X-rays. The Si support is removed in a square area of 1 mm x 1 mm making the central part of the microchannel and the microheater suspended. This configuration provides the thermal isolation needed for the functioning of the microheater while allowing the transmission of soft X-rays. Finally, the Si support is also removed in two small square-shaped areas located in correspondence of the ends of the microchannel. This way inlet/outlet apertures are achieved and employed for flowing the liquid containing the nanoparticles and for the pressurization of the microchannel by means of gasses.

Experimental details

2.4.5 STXM holder

Custom-made holders were designed and produced by NanoInsight to interface the nanoreactor and to allow its mounting on the piezo-stage of the Pollux-PSI and of the HERMES-Soleil STXM chambers. Each of the holders is provided with a housing slot and a retaining lid for the mounting and fixing of the nanoreactor. To allow transparency both the holder and the lid are provided with holes in correspondence of the central part of the microchannel. The holder integrates two gas channels ending in the housing slot in correspondence of the inlet/outlet apertures of the nanoreactor are present. Here a leak-tight connection is achieved by means of O-rings. The holders are equipped with four spring-loaded probe-needles connecting to the four contact-pads of the microheater. For the experiments, the gas channels of the holder were connected to PEEK tubing. A gas feedthrough flange was employed to connect to the PEEK tubing from the external side of the STXM chamber. In a similar way, electrical wires were soldered to the probe-needles and brought to the external side of the STXM chamber by using a flange provided with electric feedthroughs.

2.4.6 Pressurization of the nanoreactor

A custom-made gas mixing and pressurization system designed and produced by NanoInsight was employed to flow the employed gas mixtures into the nanoreactor. The system makes use of mass flow meters and a backward pressure controller to mix up to four different gasses. A forward pressure controller is employed to withdraw the gas mixture from the mixing section and to inject it into the inlet of the nanoreactor with the desired pressure. During the in situ experiments the gas mixtures were flown into the nanoreactor by pressurizing the inlet at 2 bar for the DMR mixture, and at 3 bar or 6 bar for the 5% H₂ in Ar mixture. At the same time vacuum was applied at the outlet of the nanoreactor by means of a scroll pump. In this configuration the pressure in the central part of the microchannel (reaction zone) is the average of the pressures at the inlet and the outlet of the nanoreactor. This is due to the fact that the design of the microchannel is symmetric and that this has a very low flow conductivity compared to that of the tubing. The outlet pressure was measured with a pressure gauge installed at the exit of the tubing connected at the outlet of the nanoreactor. This pressure changed with the pressure applied at the inlet of the nanoreactor and with the composition of the gas mixture. In any case, during the in situ experiments the outlet pressure was always lower than 10 mbar. Therefore, the pressure in the reaction zone of the nanoreactor can be considered simply as the half of that applied at the inlet, that is 1 bar for the DMR mixture, and at 1,5 bar or 3 bar for the 5% H₂ in Ar mixture.

2.4.7 Powering and temperature measurement

The temperature in the reaction zone of the nanoreactor was increased by flowing a current through the Mo microheater. This was done while monitoring its electrical resistance, which provided a measure of the average temperature. For this purpose, a Keithley 2611 source meter was employed in a four-wire sensing configuration. For each temperature, the current was increased stepwise until the corresponding resistance was reached. The nanoreactors employed during the experiments were calibrated on a hotplate beforehand to generate a resistance-temperature table.

Figure S1

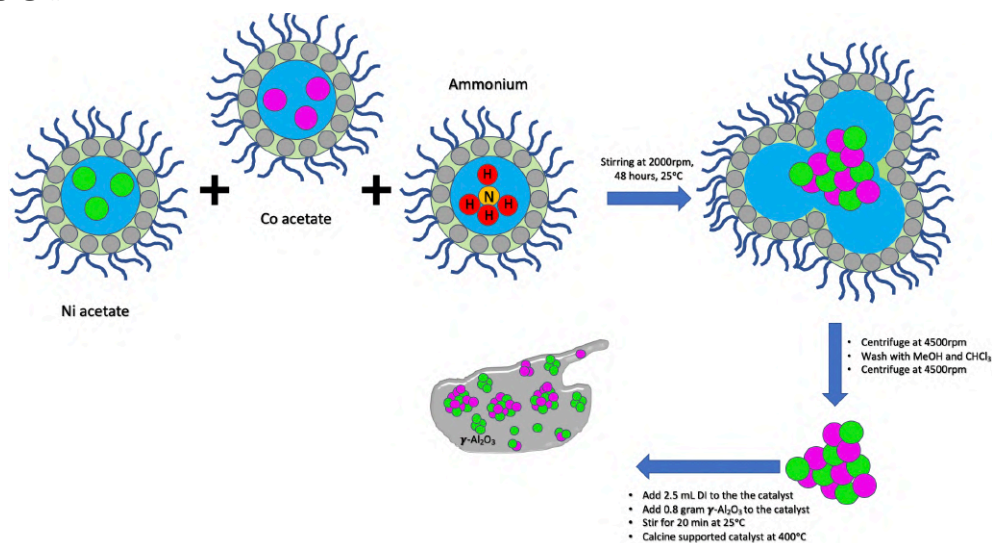


Figure S1): Synthesis pathway to produce NiCoO/ γ -Al₂O₃ catalyst involving the reverse micellar method.

Figure S2

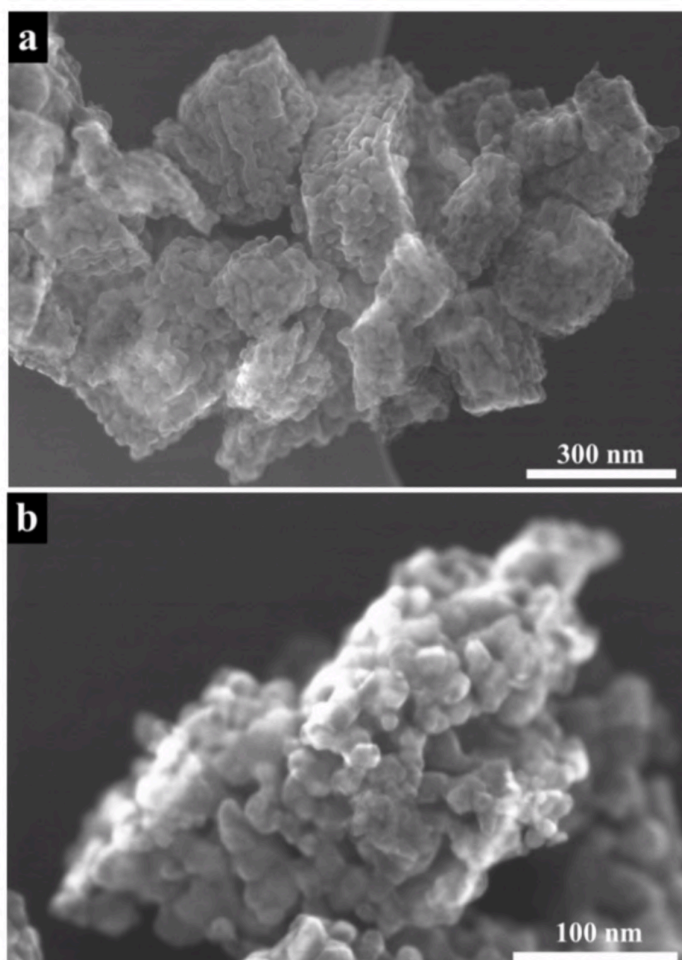


Figure S2: a, b) Overview STEM image of the calcined NiCoO/ γ -Al₂O₃ catalyst prior to the activation step. Both images illustrate that the catalyst is composed of small nanoparticles that have coalesced large agglomerates with a cubic structure.

Figure S3

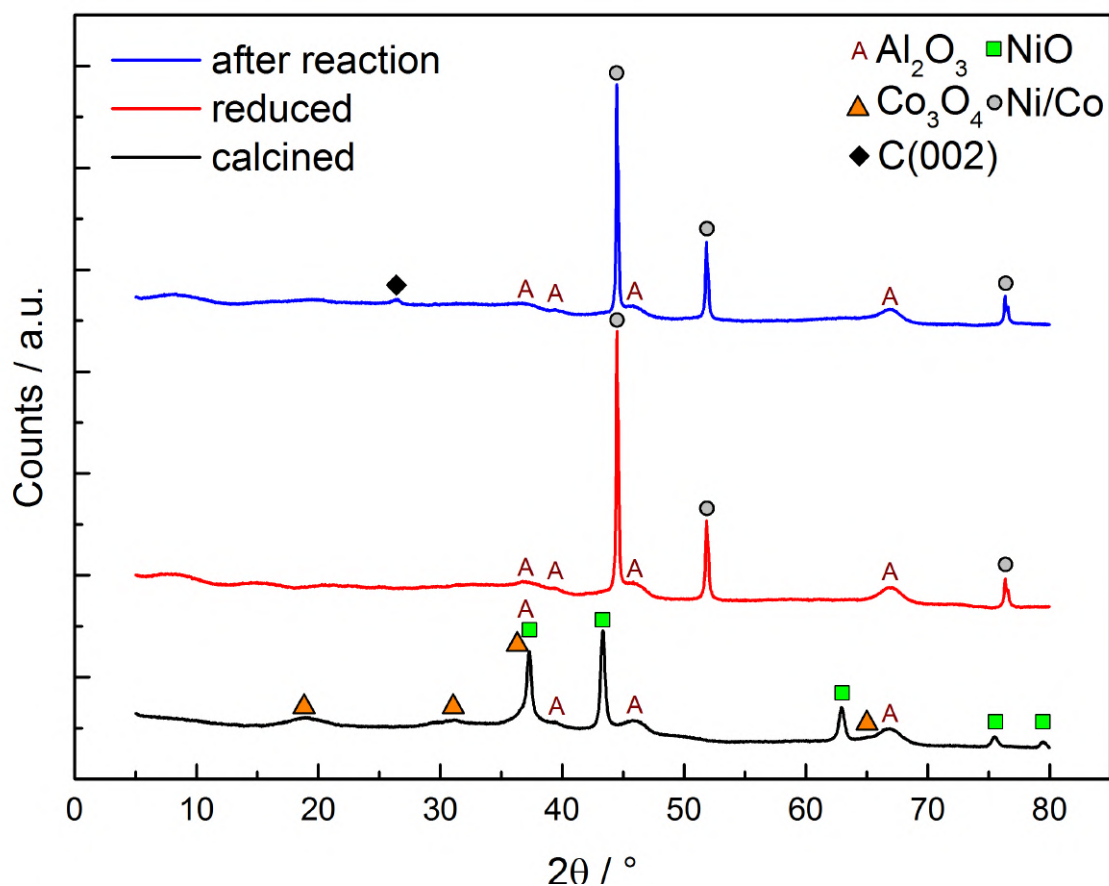


Figure S3): XRD profile for the fresh, reduced and spent NiCoO/ γ -Al₂O₃ DMR catalyst. The green squares and orange triangles indicate that the calcined catalyst contains NiO and Co₃O₄ as active species. After exposure to DMR conditions the formation of coke is confirmed by the peak at approximately 26 ° (black square).

Figure S4

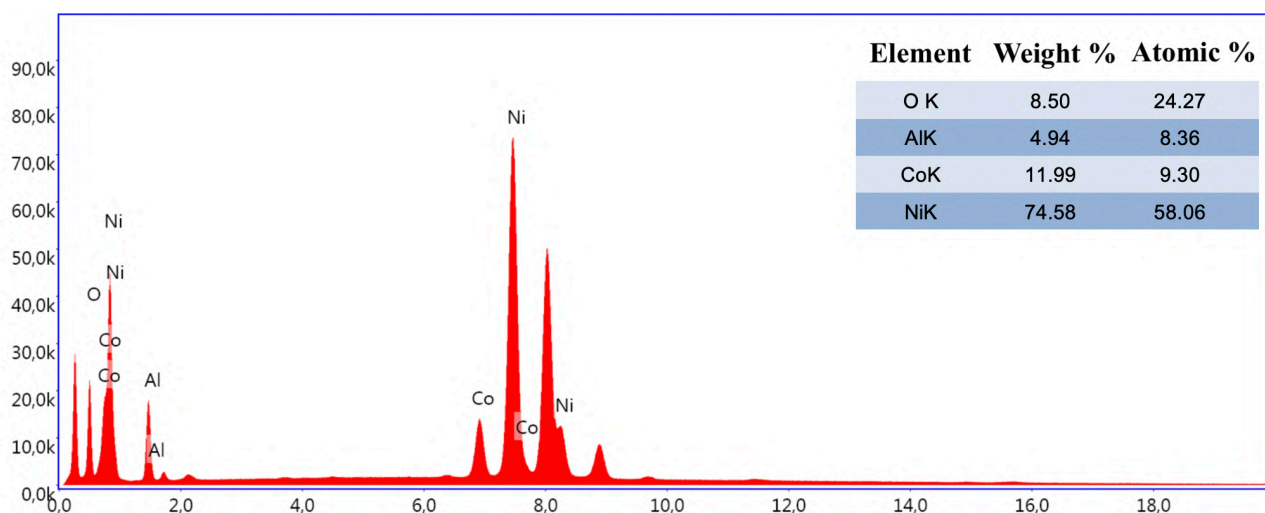


Figure S4): EDX analysis on the NiCoO/ γ -Al₂O₃ catalyst the metal concentration in this sample.

Figure S5

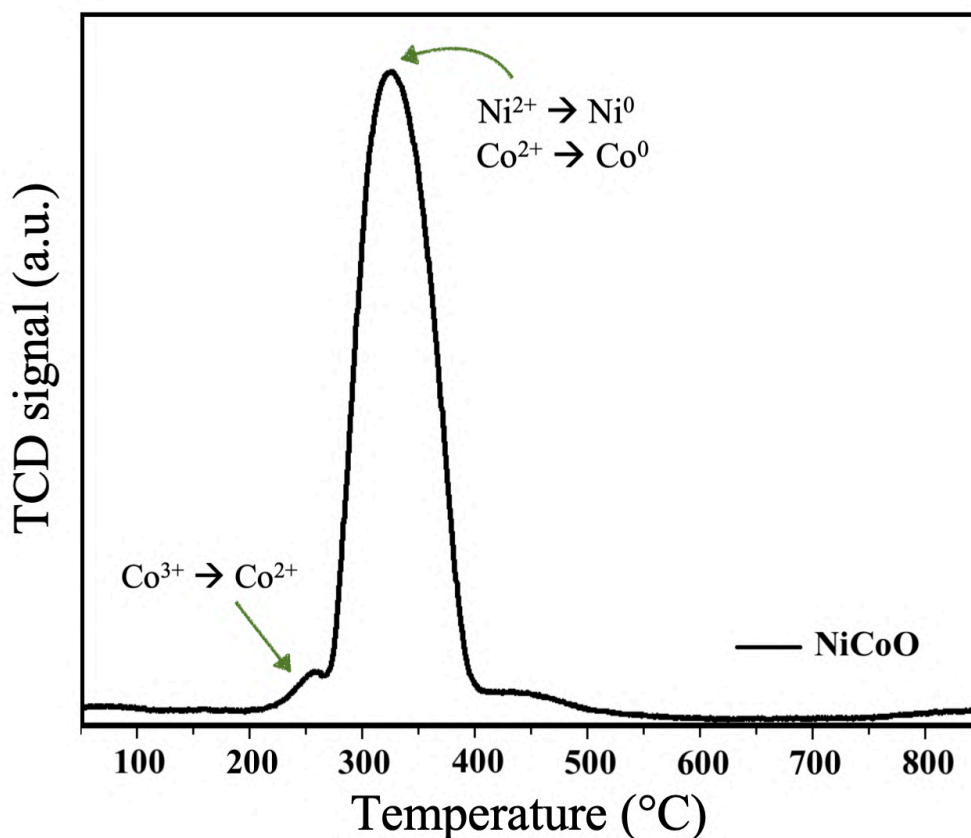


Figure S5): TPR profile of the NiCoO/ γ -Al₂O₃ catalyst measured from 30 °C to 800 °C. This profile indicates that at temperatures higher ~550 °C both Ni and Co are fully reduced the metallic.

Figure S6

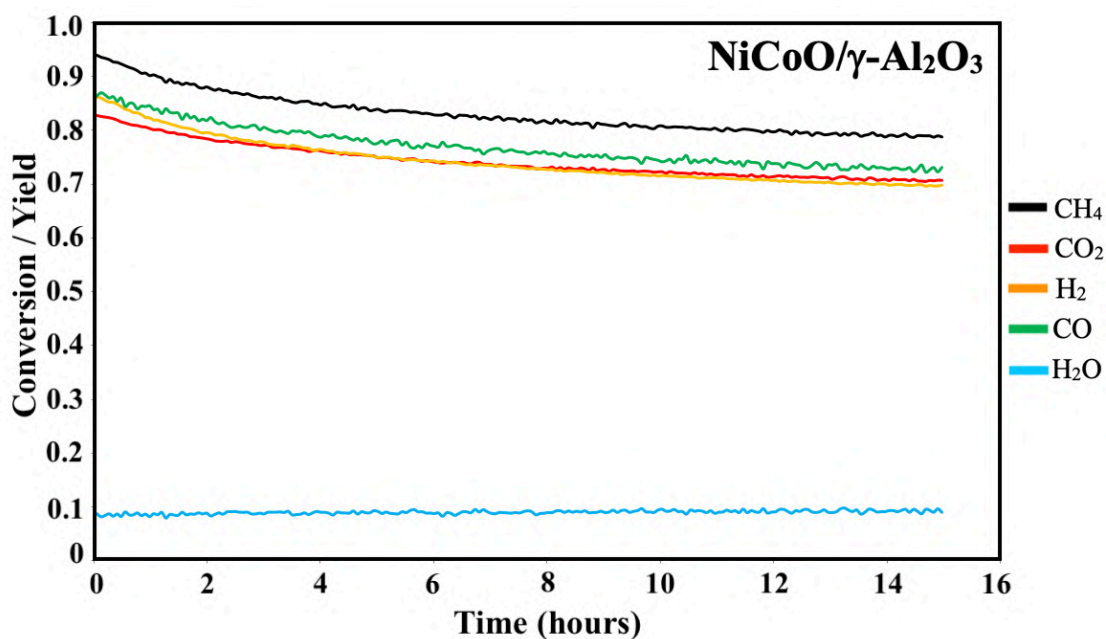


Figure S6): Activity measurements for the NiCoO/ γ -Al₂O₃ DMR catalyst. Conversion/Yield fractions during the DMR experiment at 800 °C under 7% CH₄ and 9.5% CO₂ in N₂ and a flow rate of 490 mL/min. The degrees of conversion after 15 h were stabilized at 80% and 70% for CH₄ and CO₂, respectively. The corresponding yields for H₂ and CO were ~70% and ~73%, respectively.

Figure S7

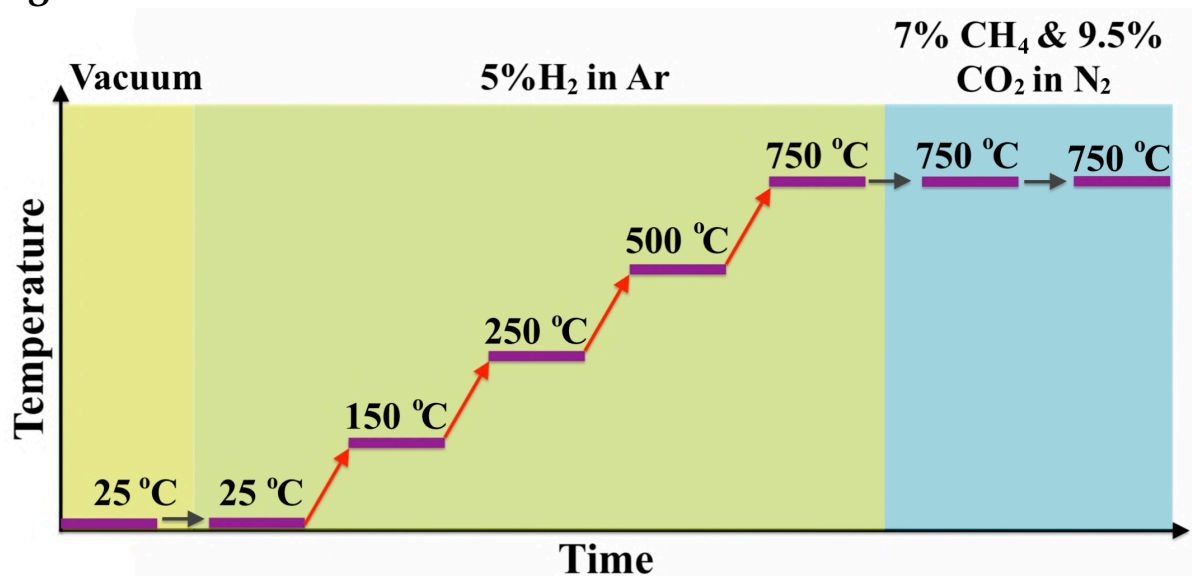


Figure S7: Schematic illustration of the in-situ STXM experiment. In the first stage of the experiment the calcined sample is measured at RT and vacuum. The next step involves heating the sample under reducing conditions. In the last step the sample is exposed to DMR conditions for 1 minute and 2 hours.

Figure S8

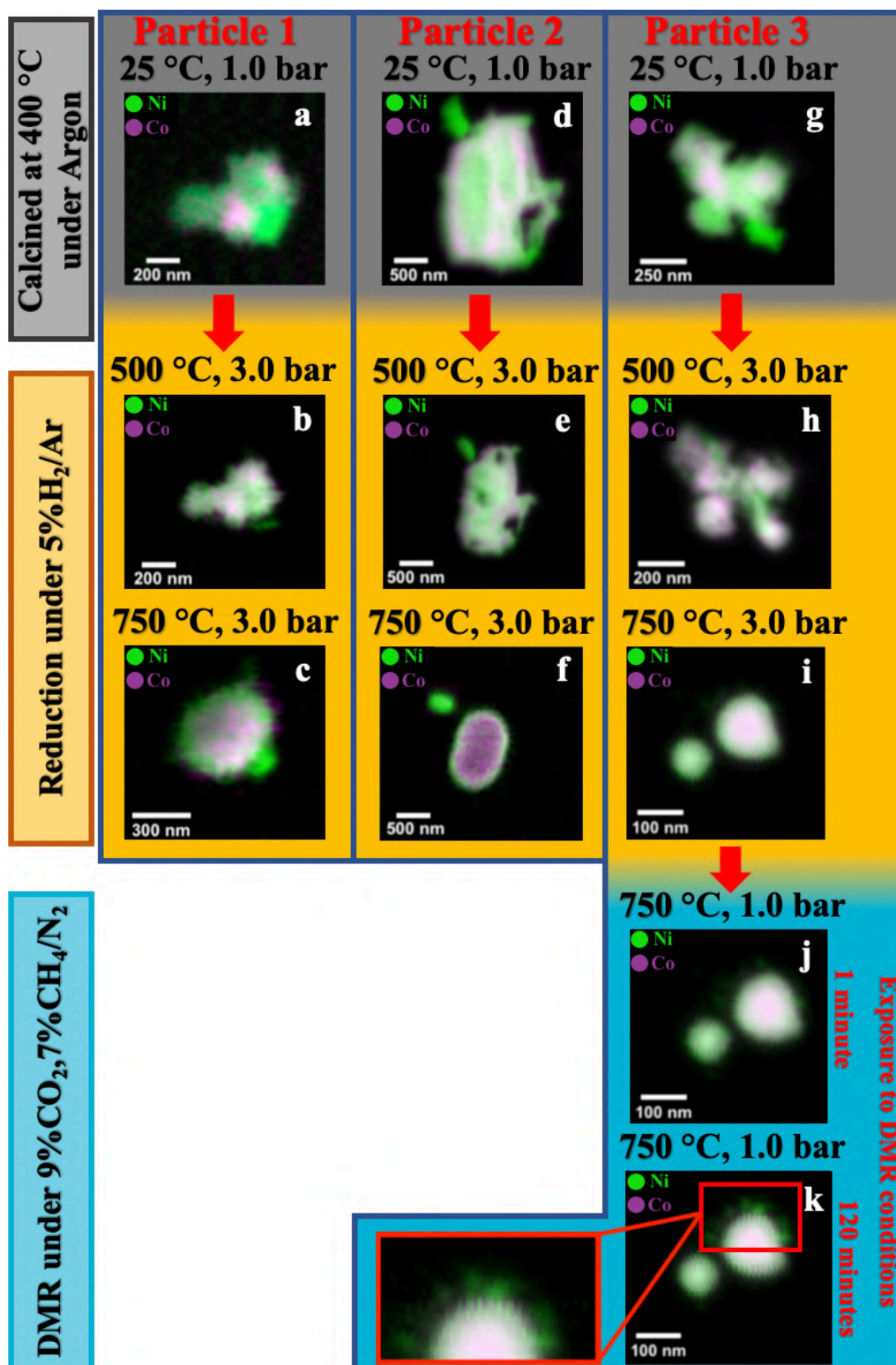


Figure S8: a) Elemental composition maps of three different NiCoO particles which show the distribution of Ni (in green) and Co (in violet) for: a,d,g) the freshly calcined particles, bc,h) following the reduction step at 500 °C under 5% H₂ in Ar, where the Ni and Co oxides are reduced, c,f,i) at 750 °C and under 5% H₂ in Ar flow where the Ni and Co Al₂O₄ are fully reduced, and j,k) after exposure to DMR conditions for 1 minute and 120 minutes respectively.

Figure S9

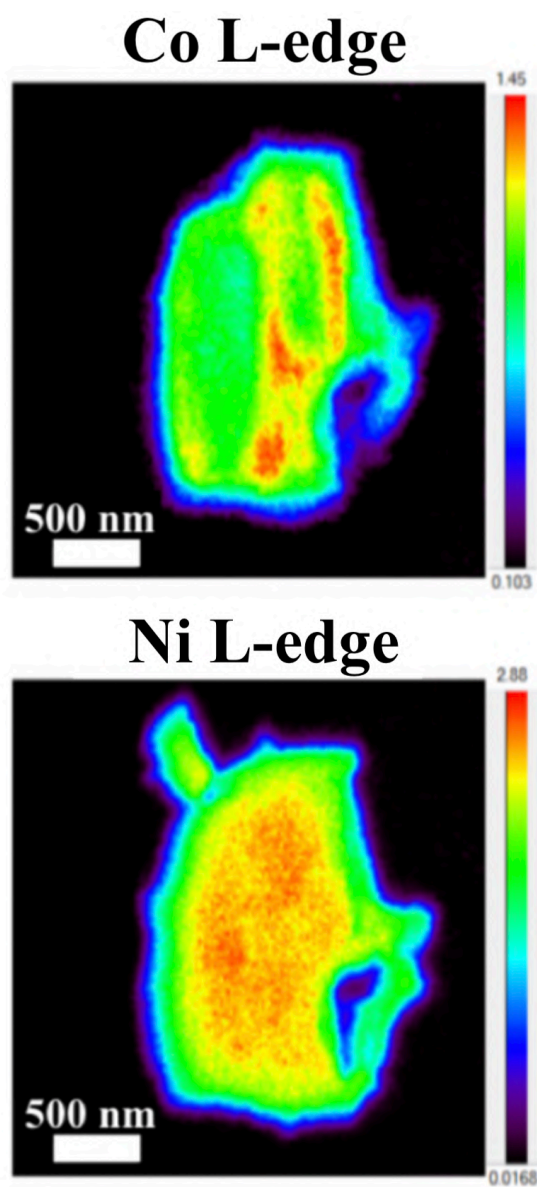


Figure S9: Elemental composition maps of the calcined NiCo particle showing that Co and Ni are mixed through the particles. However, there are some areas with high Ni content while other regions are Co deficient.

Figure S10

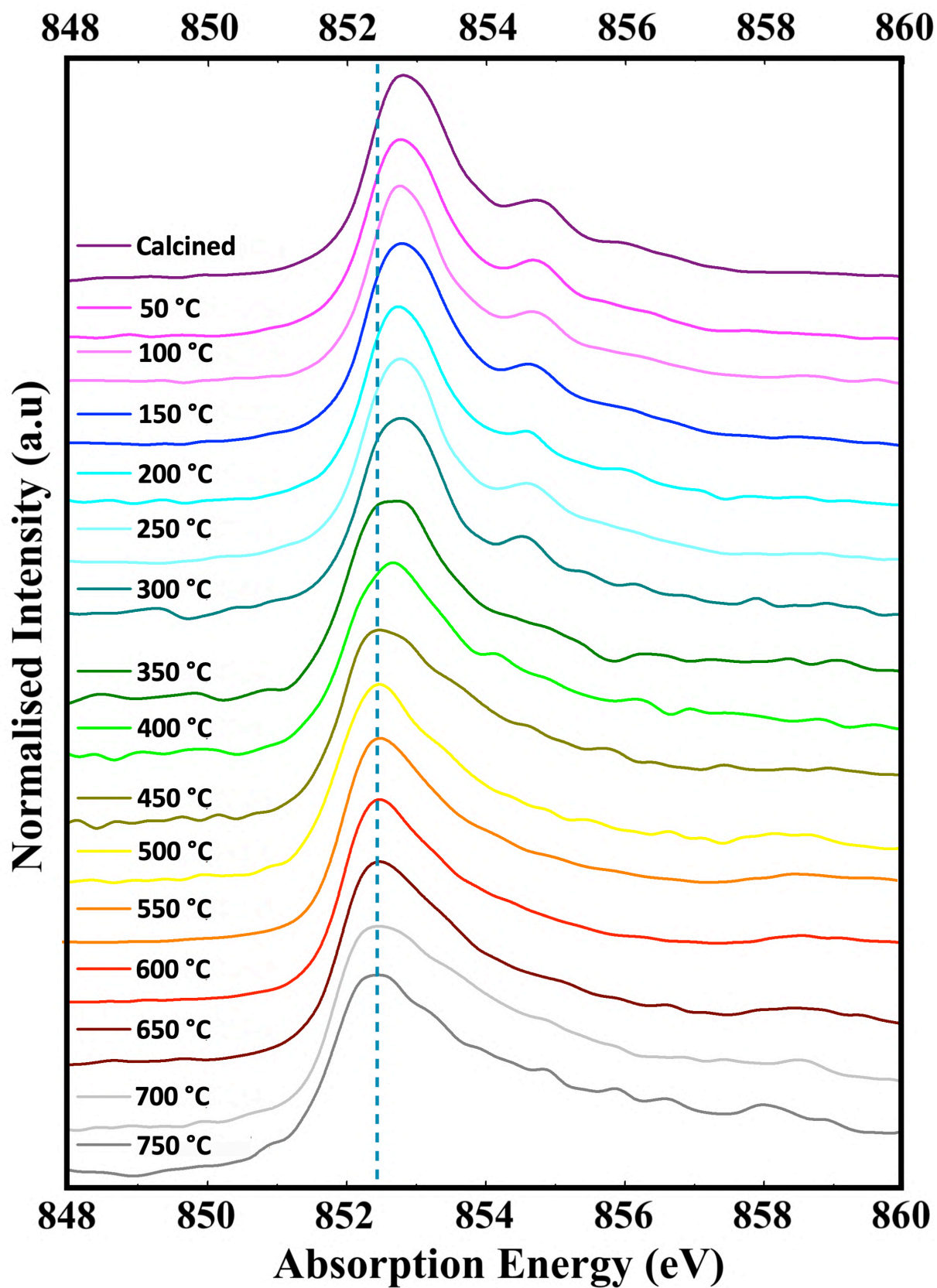


Figure S10: Ni L₃-edge spectra measurements on the calcined NiCoO/ γ -Al₂O₃ sample and during the reduction/activation process. At temperatures higher than 500 °C the Ni gets fully reduced into metallic Ni.

Figure S11

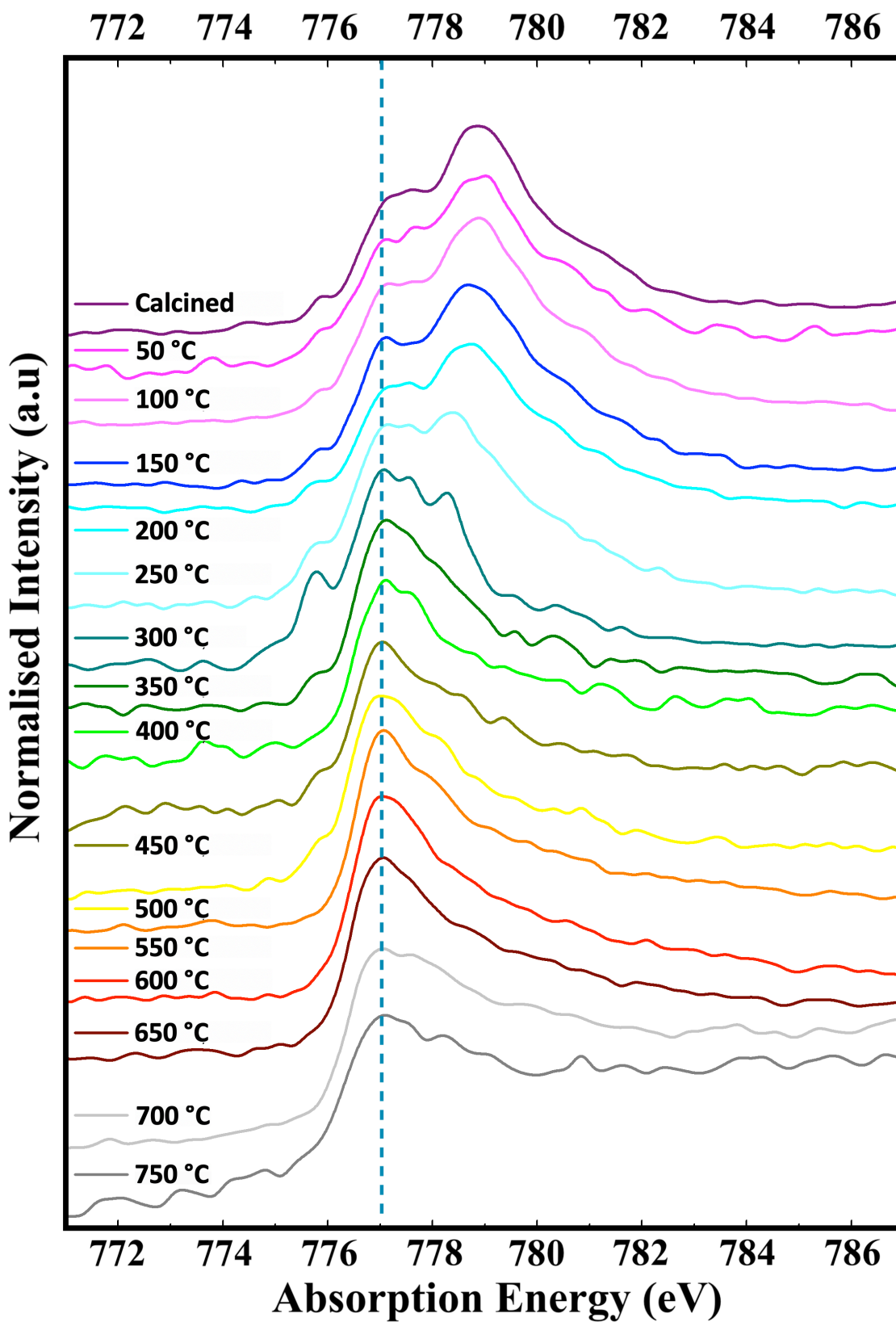


Figure S11: Co L₃-edge spectra measurements on the calcined NiCoO/ γ -Al₂O₃ sample and during the reduction/activation process. At temperatures higher than 350 °C the Co gets fully reduced into metallic Co.

Figure S12

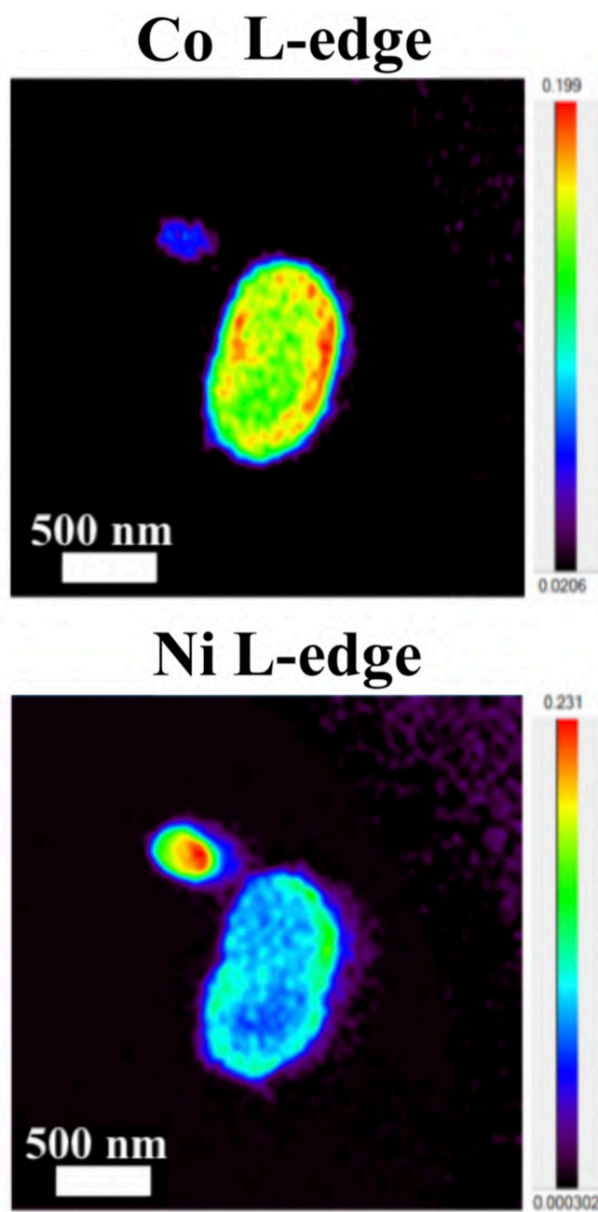


Figure S12: Elemental composition maps of the reduced (750 °C) NiCo particles showing that Co and Ni are mixed through the particles.

Figure S13

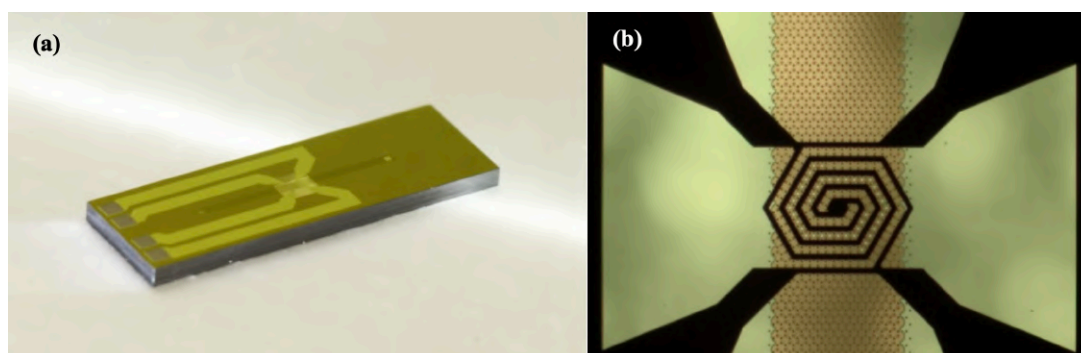


Figure S13: (a) Surface micromachined nanoreactor used in for the in-situ STXM experiments. (b) Optical microscope image of the central part of the nanoreactor showing the microchannel, the microheater, and the X-ray transparent windows.

References

- [1] Belkhou, R.; Stanescu, S.; Swaraj, S.; Besson, A.; Ledoux, M.; Hajlaoui, M.; Dalle, D. HERMES: A Soft X-Ray Beamline Dedicated To X-Ray Microscopy. *J. Synchrotron Radiat.* **2015**, *22* (4), 968-979.
- [2] Raabe, J.; Tzvetkov, G.; Flechsig, U.; Böge, M.; Jaggi, A.; Sarafimov, B.; Vernooij, M.; Huthwelker, T.; Ade, H.; Kilcoyne, D.; Tyliczszak, T.; Fink, R.; Quitmann, C. Pollux: A New Facility For Soft X-Ray Spectromicroscopy At The Swiss Light Source. *Rev. Sci. Instrum.* **2008**, *79* (11), 113704.
- [3] Vendelbo, S.; Elkjær, C.; Falsig, H.; Puspitasari, I.; Dona, P.; Mele, L.; Morana, B.; Nelissen, B.; van Rijn, R.; Creemer, J.; Kooyman, P.; Helveg, S. Visualization Of Oscillatory Behaviour Of Pt Nanoparticles Catalysing CO Oxidation. *Nat. Mater.* **2014**, *13* (9), 884-890.
- [4] Bremmer, G.; Zacharaki, E.; Sjøstad, A.; Navarro, V.; Frenken, J.; Kooyman, P. In Situ TEM Observation Of The Boudouard Reaction: Multi-Layered Graphene Formation From CO On Cobalt Nanoparticles At Atmospheric Pressure. *Faraday Discuss.* **2017**, *197*, 337-351.
- [5] van Ravenhorst, I.; Vogt, C.; Oosterbeek, H.; Bossers, K.; Moya-Cancino, J.; van Bavel, A.; van der Eerden, A.; Vine, D.; de Groot, F.; Meirer, F.; Weckhuysen, B. Capturing The Genesis Of An Active Fischer-Tropsch Synthesis Catalyst With Operando X-Ray Nanospectroscopy. *Angew. Chem.* **2018**, *130* (37), 12133-12138.
- [6] Creemer, J. F. et al. *Proc. 2011 IEEE 24th Int. Conf. MEMS* 1103 1106.

In situ X-ray emission and high-resolution X-ray absorption spectroscopy applied to Ni-based Bimetallic Dry Methane Reforming Catalysts

3

In Chapter 2 the bimetallic NiCoO/ γ -Al₂O₃ Dry Methane Reforming (DMR) catalysts were studied by in-situ STXM to reveal the changes in the electronic structure and morphology during the activation/reduction and DMR reaction conditions. However, a direct comparison with the monometallic NiO/ γ -Al₂O₃ catalyst was not made. This is interesting and important since it allows us to unravel the role of cobalt in the bimetallic NiCoO/ γ -Al₂O₃ catalyst.

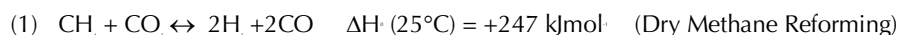
As a result, in this chapter the promoting effect of cobalt on the catalytic activity of a NiCoO Dry Methane Reforming (DMR) catalyst was studied by a combination of in-situ K β X-ray Emission Spectroscopy (XES) and K β -detected High Energy Resolution Fluorescence Detected X-ray absorption spectroscopy (HERFD XAS). Following the calcination process, Ni XES and K β -detected HERFD XAS data revealed that the NiO coordination in the NiCoO catalyst has a higher degree of symmetry and is different than that of pure NiO/ γ -Al₂O₃. Following the reductive activation, it was found that the NiCoO/ γ -Al₂O₃ catalyst required a relatively higher temperature compared to the monometallic NiO/ γ -Al₂O₃ catalyst. This finding suggests that Co is hampering the reduction of Ni in the NiCoO catalyst by modulation of its electronic structure. It has also been previously shown that the addition of Co enhances the DMR activity. Further, the K β XES spectrum of the partly reduced catalysts at 450 °C reveals that the Ni sites in the NiCoO catalyst are electronically different from the NiO catalyst. The in-situ X-ray spectroscopic study demonstrates that reduced metallic Co and Ni are the primary species present after reduction and are preserved under DMR conditions. However, the NiCo catalyst appears to always be somewhat more oxidized than the Ni-only species, suggesting that the presence of cobalt modulates the Ni electronic structure. The electronic structural modulations resulting from the presence of Co may be the key to the increased activity of the NiCo catalyst relative to the Ni-only catalyst. This study emphasizes the potential of in-situ X-ray spectroscopy experiments for probing the electronic structure of catalytic materials during activation and under operating conditions.

In situ X-ray emission and high-resolution X-ray absorption spectroscopy applied to Ni-based Bimetallic Dry Methane Reforming Catalysts

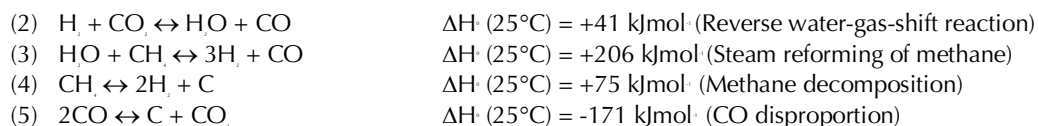
Abbas Beheshti Askari, Mustafa al Samarai, Nozomu Hiraoka, Hirofumi Ishij, Lukas Tillmann, Martin Muhler, and Serena DeBeer. **Submitted RCS Nanoscale, 2020.**

3. Introduction

The development of catalysts that enable environmentally friendly means for the production of fuels is currently a subject of intense research.[1-3] These efforts are motivated not only by the depletion of fossil fuels, but also the emission of greenhouse gases, which are known to have a devastating impact on the environment.[4-6] One reaction that has been receiving increasing attention due to its high potential for converting CH₄ and CO₂ to syngas (H₂ and CO) (reaction 1) is the Dry Methane Reforming (DMR) process.[7-8]



In addition, various undesired side reactions (reactions 2-5) can occur during the DMR reaction that eventually lead to carbon deposition on the active phase.



Due to the carbon deposition side reactions, the active sites are gradually blocked, leading to catalyst deactivation.[9] In the literature, numerous studies aimed at preventing coke formation on the DMR catalysts have been reported in which the catalyst structure, reaction temperature and the DMR gas-mixture ratios during the operating conditions have been varied.[10-13] Presently, the best strategy to reduce carbon deposition on DMR catalysts is based on operating at high temperatures (> 700 °C) and selected CO₂:CH₄ ratios e.g. 1:1. Among the various classes of DMR catalysts, the highest DMR activity, selectivity, and stabilities are achieved by noble-metals based systems.[14] However, due to their scarcity, they are not considered as sustainable candidates for the large scale industrial DMR catalysis.[15] Alternatively, nickel-based catalysts with comparable activities have been pursued. However, a major disadvantage for the Ni-based catalyst is their relatively high carbon deposition rate when compared to noble-metals based catalysts.[16-17] Various approaches have been reported in literature which aim to reduce coke formation on the Ni-based catalysts. Chang and co-workers illustrated that the activation of CO₂ is promoted by supporting the active phase on basic supports/promoters of alkali metals e.g. CaO, K₂O and MgO.[18-19] Separate studies have shown that alloying Ni-based catalysts with other metals, such as Co, Fe, Mo, Mn, Sn, Ce and Cu, increases the catalytic activity, selectivity and coke resistivity as compared to monometallic Ni catalysts.[20-22] Furthermore, Zhang et al. reported that the synthesis of bimetallic catalysts results in a decreased Ni domain size, which results in a lower sensitivity to coking.[22] It was also found that among 3d transition metals, Co most efficiently promotes the DMR activity of Ni-based catalysts.[23-24] However, to date the synergistic interaction between Co and Ni in optimizing DMR activity is not fully understood. In a previous study, we utilized in-situ Scanning Transmission X-ray Microscopy (STXM) to follow the changes in the morphology and electronic structure of multiple NiCoO/γ-Al₂O₃ DMR catalyst particles during activation and under DMR reaction conditions.[24] It was found that through the activation step, Co and Ni oxides were gradually reduced by heating the catalyst under 5% H₂ in Ar. Further, the formation of a segregated structure with a Ni-rich shell was observed. This

structure was also conserved after exposure to DMR conditions, thus hinting at the significance of the segregated structure for the DMR catalysis. Despite these findings, no direct comparison to the monometallic Ni-based methane reforming catalyst and the effect of Co on both the reduction of Ni site and the DMR activity was made.

In the present study, both the Ni and Co species in NiCoO/ γ -Al₂O₃ and NiO/ γ -Al₂O₃ DMR catalysts are investigated under the reduction/activation and DMR operating conditions by using hard X-ray spectroscopies. Specifically, we utilize a combination of Ni K-Beta X-ray emission spectroscopy (XES) and Ni and Co K-Beta detected High Energy Resolution Fluorescence Detected X-ray absorption spectroscopy (HERFD XAS) in order to obtain insight in the local geometric and electronic structural changes that occur at both the Ni and the Co sites.[25-33] In addition, Scanning Transmission Electron Microscopy-Energy Dispersive X-ray spectroscopy (STEM-EDX), Temperature Programmed Reduction (TPR) and activity measurements were performed to elucidate the differences in the morphology, reducibility and activity of both catalysts. Taken together, these data allow us to draw structure-function correlations and to better understand the role of Co in optimizing NiO-based catalysts for DMR.

3.1 Experimental section

3.1.1 NiO/ γ -Al₂O₃ Catalyst synthesis

For the synthesis of the NiCoO/ γ -Al₂O₃ and NiO/ γ -Al₂O₃ catalyst, the following chemicals were used without any purification: cobalt(II) acetate tetrahydrate (>98%, Sigma Aldrich), nickel(II) acetate tetrahydrate (99.998%, Sigma Aldrich), ammonium oxalate monohydrate 98% (Alfa Aesar), methanol 99% (Alfa Aesar), 1-hexanol 99% (Alfa Aesar), n-hexane 99%, and γ -alumina support (Alfa Aesar).

The NiCoO/ γ -Al₂O₃ catalyst was synthesized according to a previously reported protocol.[24,34] The NiO/ γ -Al₂O₃ catalyst was prepared by an adaptation of the reverse micellar method.[35] In this approach, two different aqueous mixtures were prepared by dissolving 2.3 g ammonium oxalate monohydrate and 3 g nickel acetate tetrahydrate in 15 mL demineralized water and stirring for 15 minutes. A third mixture was prepared by mixing 0.9 g cetyltrimethylammonium bromide, 9 mL hexanol and 12.6 mL hexane and stirring for 20 minutes. This mixture was split into two equal portions and consequently added to the aqueous solutions and stirred for additional 20 minutes. Next, the resulting three solutions were mixed and stirred for additional 48 hours. The sample was purified by centrifuging the mixture at 5500 rpm for 5 minutes and washed with a mixture of 30 mL methanol and 30 mL chloroform. This procedure was followed by centrifugation at 5500 rpm for 15 minutes and drying at 50 °C for hours. Finally, to deposit the catalyst on the γ -Al₂O₃ support, a mixture of the prepared sample and 2.5 mL demineralized water was mixed under stirring with 0.8 g of the support and dried at 90 °C for 12 hours. Drying was performed by transferring the sample to a quartz boat positioned in a tubular quartz tube of an electrical furnace. To convert the metal acetates to their respective oxides, the samples were calcined at 400 °C for 10 hours under dynamic air flow. A gas stream of 60 mL min⁻¹ synthetic air (20% O₂ in He) was applied while heating the oven with a rate of 2 K min⁻¹ up to the final temperature of 400 °C. After calcining the sample for 10 hours, the temperature was reduced to room temperature at a rate of 2 K min⁻¹.

3.1.2 STEM-EDX

The STEM measurements for the NiO/ γ -Al₂O₃ and NiCoO/ γ -Al₂O₃ catalyst were performed by depositing small quantity of the respective catalyst powder on a polymer coated Cu TEM grid. The Hitachi HD-2700 spherical aberration corrected Scanning Transmission Electron Microscope (STEM) was used to get information about the morphology of the catalyst. EDX measurements were recorded with an EDAX Octane T Ultra W 200 mm² SDD that was connected to the Hitachi HD-2700 Microscope.

3.1.3 TPR

In an earlier study, the details of the TPR experimental setup and the reduction profile for the NiCoO/ γ -Al₂O₃ catalyst were reported.[24] Additionally, the TPR profile of the NiO/ γ -Al₂O₃ was measured by filling a quartz cell with 64 mg of the calcined catalysts. In this experiment, the temperature was increased to 850 °C, with a temperature ramp of 6 °C min⁻¹ in a flow of 4.6% H₂ in Ar, 84.1 mL min⁻¹ total. The H₂ consumption was measured by a thermal conductivity detector (Hydros, Rosemount).

3.1.4 DMR activity tests

The DMR activity for the NiCoO/ γ -Al₂O₃ sample was reported in an earlier publication.[24] The experimental setup for measuring the activity of the NiO/ γ -Al₂O₃ DMR catalysts has been described in detail elsewhere by Tillmann et al. [24,36], Figure S1. Based on both the obtained data from STXM study [24], on the NiCoO/ γ -Al₂O₃ catalyst and the limitation of the hard X-ray reactor, additional DMR catalytic activity data were collected at 750 °C, 600 °C, 500 °C, and 450 °C.

3.1.5 Synchrotron based experiments

In-situ XES and HERFD data for the NiCoO/ γ -Al₂O₃ and NiO/ γ -Al₂O₃ catalyst were obtained at the Taiwan beamline BL12XU at the SPring-8 synchrotron facility (8 GeV, 99 mA).[37] The beamline has four main optical elements, a high heat-load Si (111) double-crystal pre-monochromator, a four-bounce channel-cut Si (220) monochromator, a cylindrical Si collimating mirror and a toroidal Pt-coated focusing mirror. A Pt-coated mirror was used to focus the beam both vertically and horizontally to ~ 80 (V) \times 120 (H) μm^2 at the sample position. The incident energy was calibrated with references to the first inflection points of Ni and Co foils at 8333 eV and 7709 eV, respectively. A crystal spectrometer aligned in a Rowland geometry was utilized to detect the fluorescence from the sample. The Ni K β (1s3p) emission spectra using a 1 m radius spherically bent Si (551) analyzer. For the Co K β measurements, a Ge (444) analyzer was used. A He-filled path was used between the sample and spectrometer to reduce signal attenuation and emitted X-rays. The signal selected by the spectrometer crystals was collected using an energy-resolving Si detector. A set of four Ni K β XES spectra were collected in the emission energy region of 8220 to 8335 eV using an incident energy of 8450 eV. The Co K β emission was collected from 7615 to 7700 eV energy range using a 7800 eV excitation energy (Figures S2-S3). All XES spectra were normalized to the energy maximum of the K $\beta_{1,3}$ peak. Co and Ni XES data were calibrated by setting the K β maximum of Co₃O₄ and NiO to 7649.1 and 8264.8 eV, [37] respectively.

The HERFD spectra were measured by setting the spectrometer to the maximum of the $K\beta_{1,3}$ XES peak. For Co and Ni HERFD data, four sets of scans in the region from 7700 to 7900 eV and 8320 to 8450 eV were selected, respectively. This protocol was repeated for each step of the in-situ experiment.

To validate the quality of the collected data, radiation damage studies were conducted by measuring multiple XES and HERFD spectra during 3h exposure. To avoid beam damage, filters were inserted before the sample to attenuate the incident beam until no observable damage in the pre-edge or edge region was observed.

3.1.6 Sample preparation

The sample preparation step involved placing a pressed pellet of the catalysts powders in the sample holder shown in Figure S4a. Next, the holder was fixed inside the heating stage and afterwards the reactor was sealed. Figure S4c shows how the incident window is covered with Kapton tape to prevent gas leakage.

3.1.7 Data collection

First, the $K\beta$ XES and HERFD of the freshly calcined samples were measured. Then, the catalyst activation was followed by measuring the XES and HERFD XAS by reducing the samples under 5% H_2 in Ar flow and gradually increasing the temperature from 25 °C to 600 °C, Figure S5. The selected temperature range is based on the limits of the reactor and is within the operating regime of the catalyst. Finally, for the DMR reaction the temperature was kept at 600 °C under the flow of the DMR gas mixture (7% CH_4 & 9.5% CO_2 diluted in N_2).

3.2 Results

3.2.1 STEM

The STEM data in Figure 1a show the formation of small coalesced nanoparticles for the calcined NiCoO/ γ -Al₂O₃ sample, as previously demonstrated.[24] The elemental distributions for the Ni (green) and oxygen (blue) for the NiCoO sample are shown in Figure 1b-c. Based on the Co-EDX image (in Figure 1d) and the Ni-EDX image (1b), rather unequal distributions for Ni and Co on the γ -Al₂O₃ support are seen. These observations are also consistent with STEM-EDX and STXM results from an earlier study which demonstrated the existence of Ni-rich domains and a variable distribution of Co through the NiCoO/ γ -Al₂O₃ particle.[24] These data also suggest a similar morphology for both NiO/ γ -Al₂O₃ and NiCoO/ γ -Al₂O₃ samples (Figure 1a,e).

The STEM-EDX images for the NiO/ γ -Al₂O₃ sample indicates rather homogeneous distributions for nickel (green) and oxygen (blue) on the support (Figure 1f-g).

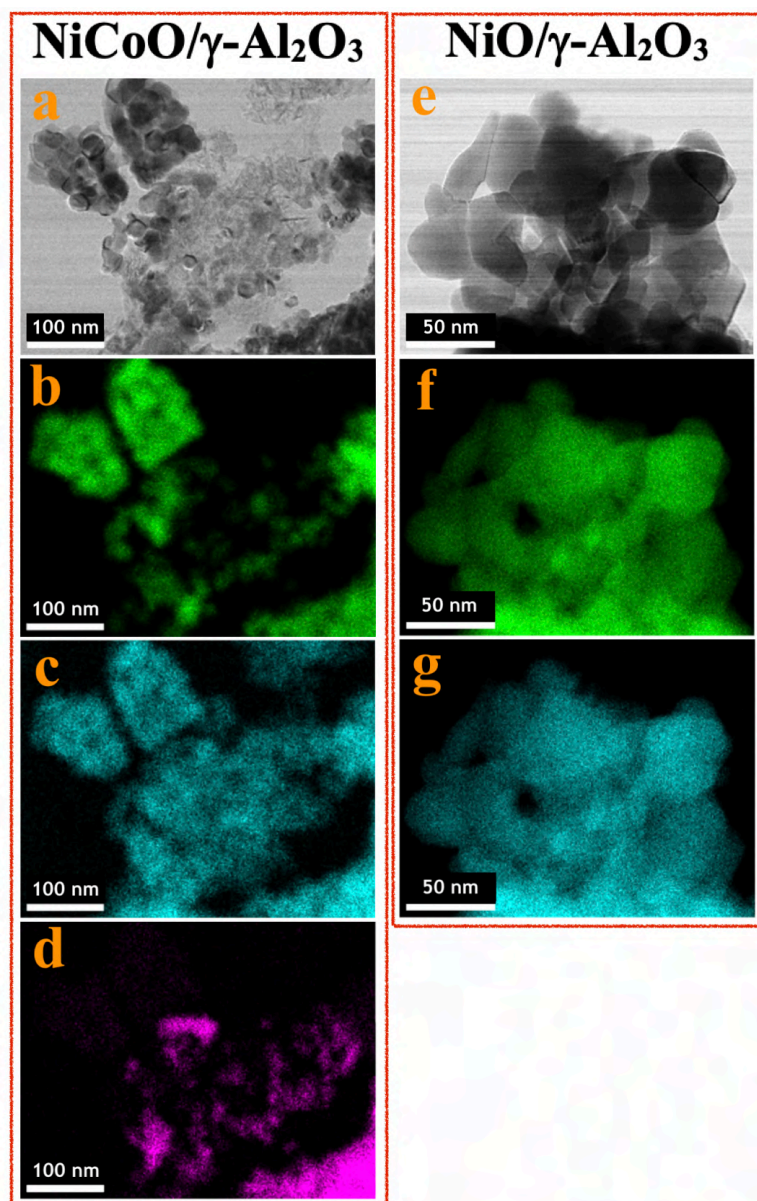


Figure 1: (STEM)-EDX images of the; a-d NiCoO/ γ -Al₂O₃ and e-g NiO/ γ -Al₂O₃ samples after the calcination step at 400 °C. b,f nickel (green); c,g oxygen (blue); d cobalt (purple).

3.2.2 TPR

To follow the reduction and conversion of the oxides to the metallic active phase, TPR profiles were obtained for the NiO/ γ -Al₂O₃ (Figure 2) and NiCoO/ γ -Al₂O₃ [24] DMR catalysts. For the NiCoO sample, there are two prominent reduction peaks. There is a relatively small peak at 265 °C which is assigned to the reduction of Co³⁺ species to Co²⁺ [38-39] followed by the main reduction peak at 325 °C where both Ni²⁺ and Co²⁺ are reduced to their metallic states.[40-41] This result is consistent with in-situ Ni and Co L-edges spectra for this catalyst.[24] However, from the TPR profile of the NiO catalyst in Figure 2, a single peak reduction is observed at 317 °C which corresponds to the reduction of Ni²⁺ to the metallic nickel.[42-43] By comparing the TPR profiles for both samples, it appears that the reduction of Ni²⁺ in the NiO sample initiates at a relatively lower temperature. These data suggest that due to the presence of cobalt in the NiCoO catalyst the reduction temperature is modulated and therefore Ni²⁺ is reduced at relatively higher temperature as compared to the monometallic NiO catalyst.

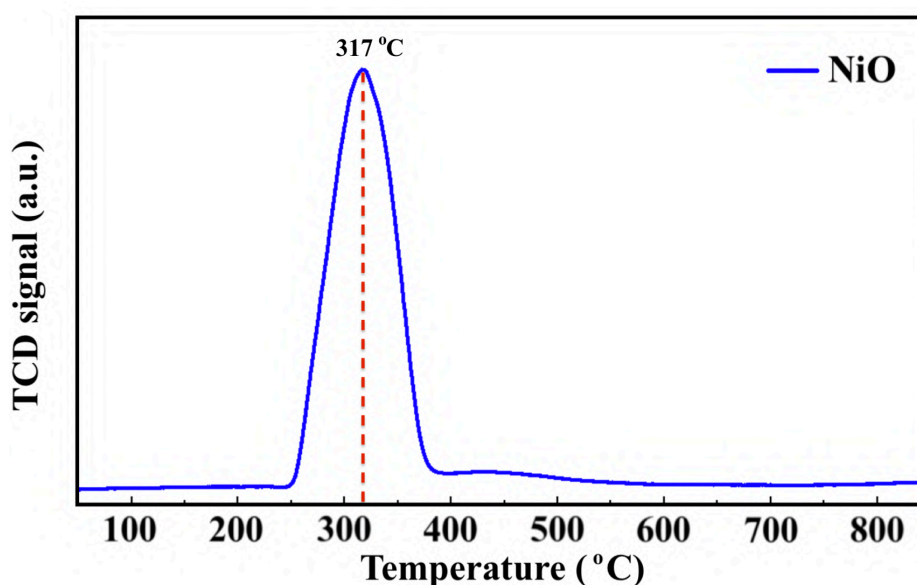


Figure 2: H₂ TPR profile of the NiO/ γ -Al₂O₃ catalyst.

3.2.3 DMR activity experiments

Prior to the DMR activity measurements, the catalysts were activated by reducing the oxides at 850 °C for 20 minutes under 10% H₂ in N₂. The DMR activities of the NiCoO/ γ -Al₂O₃ [24], and NiO/ γ -Al₂O₃ catalysts (Figure 3) were obtained at 800 °C under dynamic flow of the DMR gas mixture (7% CH₄ & 9.5% CO₂ diluted in N₂). The conversion values for NiO and NiCoO systems vary substantially with NiCoO at ~90% [24], and NiO at only ~50%. The initial activity of the NiCoO catalyst is similar to other recently reported highly active DMR catalyst systems.[44-45] Table S1 summarizes the stabilized conversion/yield values for the NiCoO and NiO catalysts under DMR conditions for 15 hours. These data suggest that following the DMR experiment, the activity of both catalysts has stabilized and thus suggests a high resistivity against coke formation.

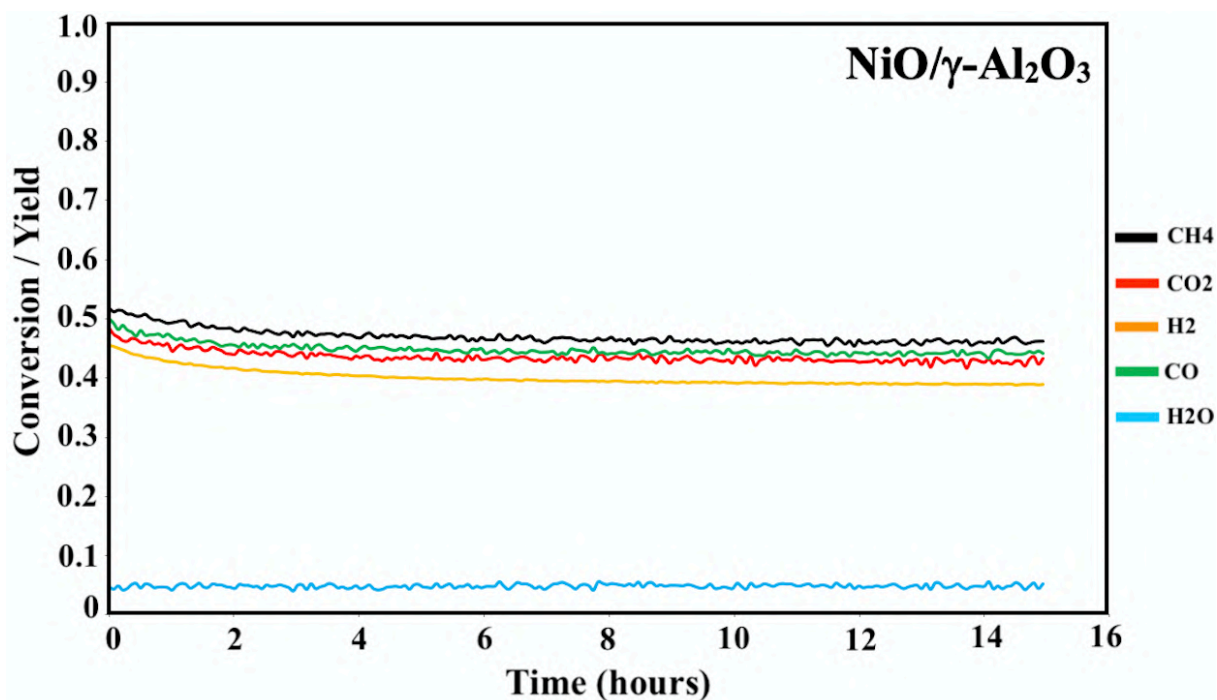


Figure 3: Activity profile of the NiO/γ-Al₂O₃ DMR catalysts for 15 hours under methane reforming conditions. Prior to the DMR activity measurements, the catalyst was activated for 20 minutes under 10% H₂ in N₂ with a flow rate of 100 mL min⁻¹. The DMR experiment was performed at 800 °C under 7% CH₄ and 9.5% CO₂ in N₂ and a flow rate of 490 mL min⁻¹. DMR activity profiles for the NiCoO/γ-Al₂O₃ catalysts has been measured in our previous study.[24]

The DMR activity data shows that the presence of cobalt in the NiCoO DMR catalysts has a promoting effect on the catalytic activity, resulting in an almost two-fold higher conversion when compared to the monometallic NiO catalyst. In addition, to understand the effect of temperature on the catalytic activity of the NiCoO catalyst additional DMR activity tests at 750 °C, 600 °C, 500 °C and 450 °C under a continuous flow of DMR gas mixture (7% CH₄, 9.5 % CO₂ in N₂) for 35 hours were performed (Figure S6). This data shows that decreasing the DMR reaction temperature dramatically reduces the achieved conversion which may be enhanced by the increase in the rate of coke deposition on the active phase.[46] Nonetheless the activity data for the NiCoO catalyst collected at 600 °C shows modest DMR activity, indicating that the X-ray spectroscopic data correspond to an operating catalyst.

3.2.4 Ni Kβ XES of NiCoO/γ-Al₂O₃ vs NiO/γ-Al₂O₃

Figure 4 shows the Ni Kβ mainline XES spectra (Ni 3p to 1s) for both the NiO/γ-Al₂O₃ and NiCoO/γ-Al₂O₃ catalysts in their calcined form, during the reductive activation step, and during the DMR reaction. The black and grey spectra correspond to the Ni XES for the freshly calcined NiO and NiCoO samples, respectively. The spectra exhibit subtle differences with the Kβ_{1,3} maxima occurring at 8264.5 eV and 8264.4 eV, for the NiO and NiCoO, respectively. Both calcined samples also exhibit a Kβ' feature at ~8253.1 eV, which is typical for a triplet (S=1) Ni²⁺ oxide species (Figure S7).[47] The slight differences in the mainline position could reflect modulations in site symmetry and/or covalency of the Ni site [33,48].

The samples were activated by flowing 5% H₂ in Ar gas and by gradually increasing the temperature from 25 °C to 600 °C. The selected temperature range for the reduction is

based on the previously collected TPR data (Figure 2), which revealed a full reduction of the active phase at $T < 500$ °C. To follow the reduction of the Ni sites and make a correlation with the TPR data, XES spectra were measured in a selected temperature range. First, following the reduction of the metal oxides at 150 °C and 300 °C, the Ni XES peak for the NiO sample shifts by -0.05 and -0.78 eV, respectively to lower emission energies and the $K\beta'$ peak at 8253 eV has largely vanished (Figure 4 and table S2). Next, by increasing the temperature to 450 °C and 600 °C, the Ni XES $K\beta_{1,3}$ peak position for NiO shifts to lower emission energies, which indicated the full reduction of NiO- γ - Al_2O_3 at $T > 400$ °C (Figure 2).[49] This is consistent with in situ STXM data for the NiCoO sample which showed that full reduction occurs at 500 °C.[24] Finally, due to the reduction of NiO- γ - Al_2O_3 sites to metallic Ni at 600 °C, the Ni $K\beta_{1,3}$ emission peak shifts by ~ -1 eV relative to the emission spectrum for the calcined sample to 8263.48 eV.

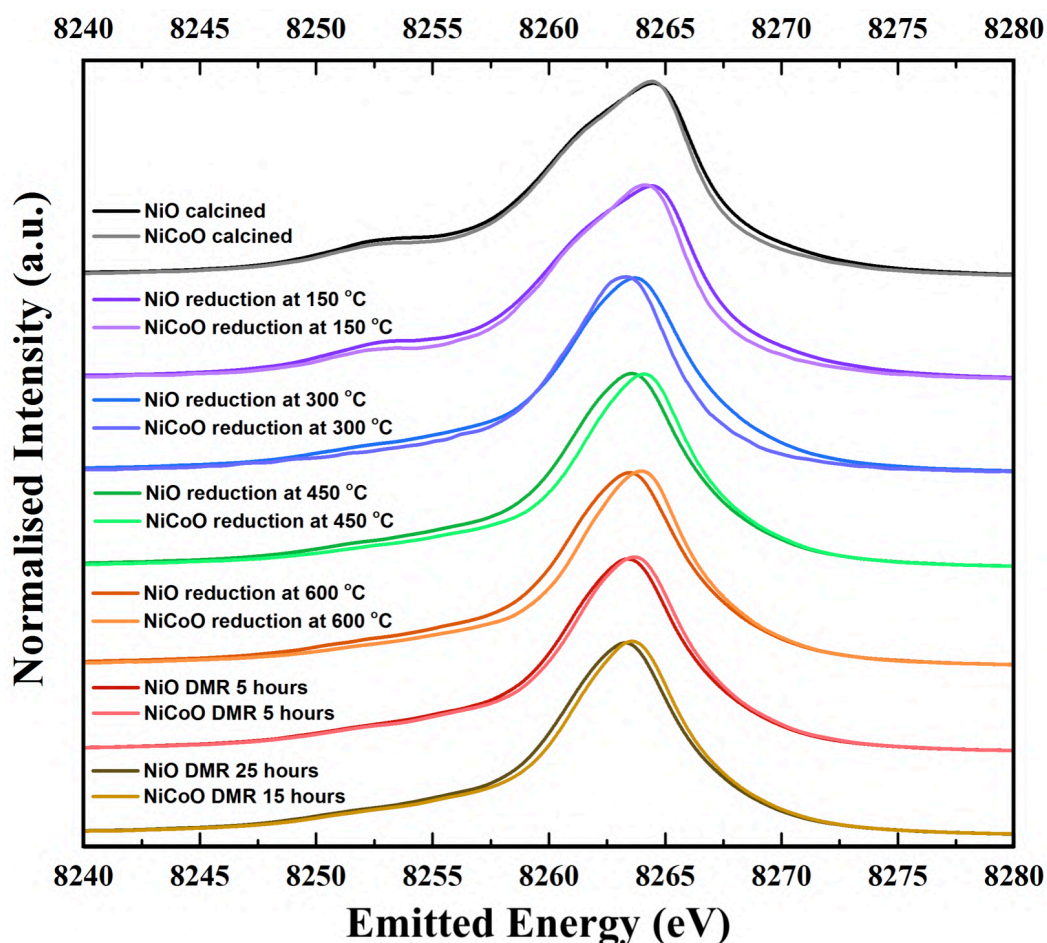


Figure 4: Ni $K\beta$ XES spectra of the NiO/ γ - Al_2O_3 and NiCoO/ γ - Al_2O_3 samples obtained under ambient, reductive activation, and DMR conditions.

Figure 4 shows that the Ni $K\beta_{1,3}$ XES peak for the NiCoO sample at 150 °C and 300 °C shifts by -0.30 eV and -1.12 eV, respectively, relative to the emission spectrum of the calcined sample. Based on a previous study, the full reduction of Co ions in NiCoO is proposed to proceed by a two-step process whereby first $Co^{3+}(O_h)$ is reduced to Co^{2+} and its electronic and spin configurations changes from a $3d^6$, $S=2$ to $3d^7$, $S=3/2$. Subsequently at elevated temperatures the remaining $Co^{2+}(T_d)$ and $Co^{2+}(O_h)$ are fully reduced to metallic Co.[24] Following the reduction at $T \leq 300$ °C the XES spectra of the NiO vs. the NiCoO samples have different spectral shape and peak positions (Figure 4 and S8-9). At 450 °C the shift in the emission spectra of NiCoO is reversed and moves

towards higher emission energies. Further, by increasing the reduction temperature to 450 °C the Ni XES peak position for the NiO is shifted by additional -0.53 eV to lower energies with respect to the NiCoO spectrum and its $K\beta'$ peak intensity is slightly higher, thus suggesting the formation of distinct Ni species (Figure S10). To understand the origin of this behavior and test if the sample at 300 °C is simply a mixture of both the oxide phase and reduced Ni, the emission spectra for the calcined and reduced NiO sample at 450 °C were averaged in different ratios (Figure S11). The $K\beta$ spectrum of the reduced NiCo catalyst at 450 °C is clearly different from any of other spectra presented in Figure S11, indicating that this is not simply a partially converted species, but rather that the NiCoO sample has a Ni site that is electronically distinct from the Ni only catalyst. Further, upon full reduction of the Ni ions in NiCoO at 600 °C the $K\beta_{1,3}$ XES peak position for the sample at 600 °C is shifted by -0.45 eV relative to the calcined sample. This energy shift is smaller when compared to the NiO case and thus suggests a different reduction mechanism for the Ni ions in NiCoO. Further, the $K\beta_{1,3}$ XES peak position for the fully reduced monometallic catalyst is shifted by \sim -0.5 eV relative to the bimetallic catalyst at 600 °C (Figure S12 and Table S2). These results confirm that the fully reduced NiO and NiCoO are not identical at 600 °C.

Finally, the XES spectra collected under dynamic flow of DMR gas mixture at 600 °C for both NiCoO and NiO indicate that a dominantly metallic Ni phase remains during the course of catalysis (Figure 4). This observation is further supported by the XES data analysis in Figures S13 and S14. However, it is important to note that even during the DMR reaction the spectra of both catalysts remain somewhat different from each other, with the NiCoO catalyst appearing slightly more oxidized than the NiO catalyst at all stages. The changes that occur in the Ni local geometric and electronic structure may be key to understanding the increased activity of the NiCo catalyst relative to the Ni-only catalyst.

3.2.5 Ni $K\beta$ HERFD of NiCoO/ γ -Al₂O₃ vs NiO/ γ -Al₂O₃

The Ni $K\beta$ -detected HERFD XAS spectra for the calcined NiCoO/ γ -Al₂O₃ and NiO/ γ -Al₂O₃, during the reductive activation, and under DMR conditions are shown in Figure 5. The Ni K-edge HERFD spectra for the calcined NiO and NiCoO samples are different in terms of their spectral shapes and their K-edge peak positions is at 8350.37 eV and 8350.40 eV, respectively. The pre-edge of the NiO catalyst has a higher intensity than the NiCoO catalyst, which suggests that the former has a more distorted local structure (Figure S15).^[50] In addition, HERFD indicates the nature of Ni in both calcined catalyst as Ni²⁺.^[51] Ni HERFD XAS data acquired during the catalyst activation in the temperature range from 150 °C to 600 °C are shown in Figure S16-19. Due to the induced reduction of the Ni at 150 °C, the K-edge peak positions for both catalysts equally shift by -0.3 eV relative to the spectra for the calcined samples (Figure 5). In contrast to the NiCoO case, following the reductive activation at 300 °C the pre-edge feature of the NiO sample diminishes and its K-edge peak position shifts to lower energies indicating a further reduction of the Ni and consistent with loss of oxygen from the crystal structure. The most striking difference during the catalyst activation step is the full reduction of the Ni ions in the NiO catalyst at just below 300 °C, while for the NiCoO catalyst the full conversion to the metallic state just occurs at just below 450 °C (Figure 5). We note that a one-to-one comparison to the TPR temperatures is limited by the 150 °C temperature steps that were taken for the XAS measurements.

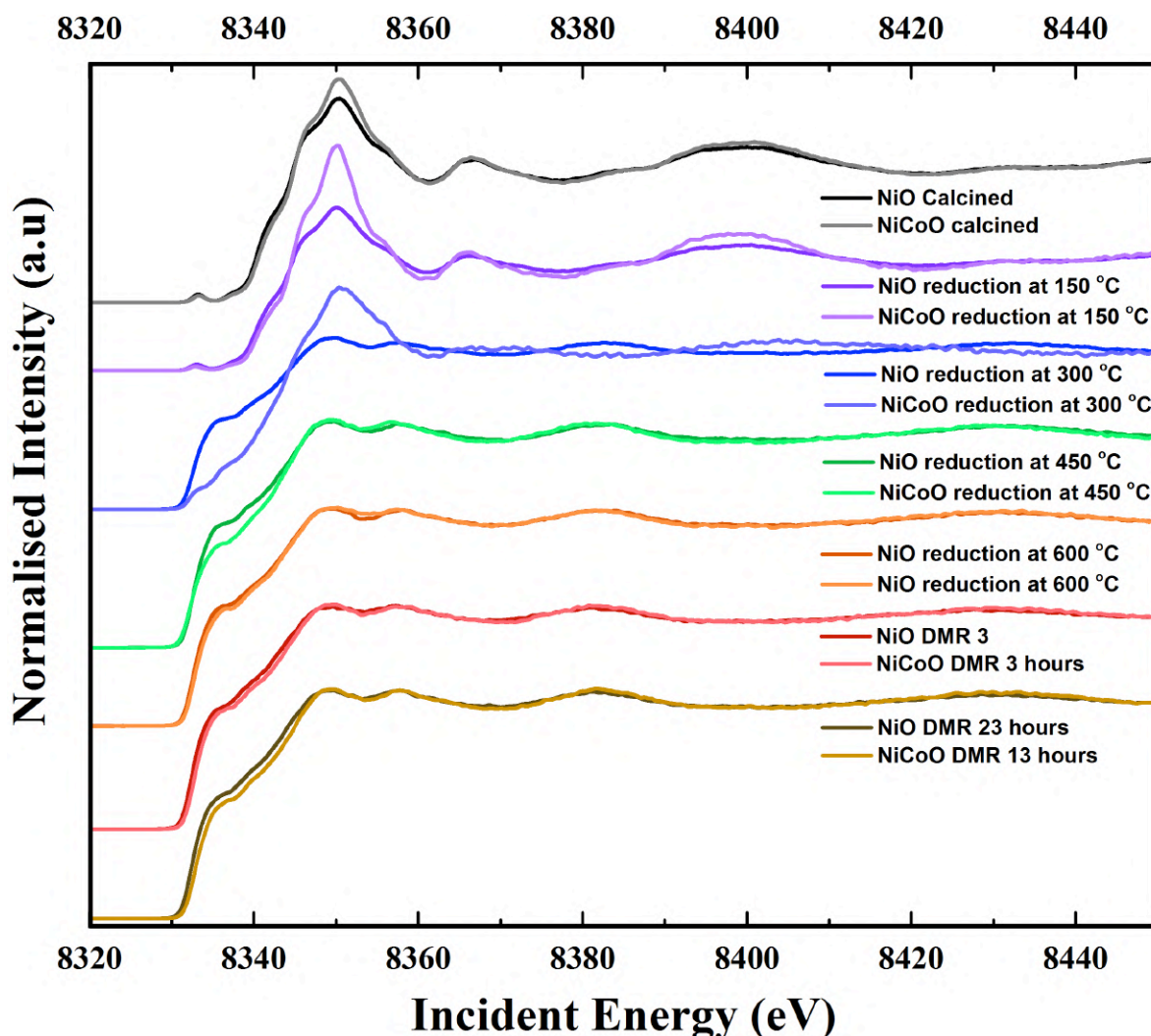


Figure 5: Ni K β -detected HERFD XAS spectra of NiO/ γ -Al₂O₃ and NiCoO/ γ -Al₂O₃ collected for the freshly calcined samples, during the reduction/activation step, and under DMR conditions.

To test if the more oxidized appearance of the Ni K-edge HERFD in the NiCoO catalyst (at 300 °C) is simply a result of incomplete conversion, a similar data analysis as in the case of XES spectra was performed by mixing the HERFD spectra of the calcined NiO and reduced sample at 450 °C (Figure S20). This analysis reveals that the EXAFS region of the spectrum for the reduced NiCoO samples at 450 °C and any of the obtained mixed spectra are not superimposable with the NiCoO catalyst at 300 °C. Therefore, we propose that this species in NiCoO is very likely a distinct Ni species, which results from the presence of Co in the catalyst. In addition, the overlaid HERFD spectra for the NiO and NiCoO samples at 450 °C indicate a different electronic structure (Figure S18). The HERFD spectra for reduced NiO and NiCoO at 600 °C remain distinct from each other. While both catalysts appear to be comprised of dominantly reduced metallic Ni, the NiCo catalysts shows a slightly larger contribution of oxidized Ni (Figure S19). Finally, HERFD data were continuously collected during exposure to DMR conditions and revealed the high stability of Ni in its metallic state under the DMR conditions (Figure 5 and S21-22).

3.2.6 Co K β HERFD of NiCoO/ γ -Al $_2$ O $_3$

Co K β HERFD spectra for the NiCoO/ γ -Al $_2$ O $_3$ catalyst in the calcined form, activated form, and under the DMR conditions are presented in Figure 6. Based on the HERFD spectrum and previous Co L-edge XAS data [24], the Co species in the freshly calcined sample is consistent with Co $_3$ O $_4$. [52] At 150 °C, the reduction of Co $^{3+}$ (O $_h$) sites to most probably Co $^{2+}$ oxide initiates, and the Co K-edge HERFD white line position dramatically shifts from 7729.8 eV to 7726.96 eV ($\Delta E=2.8$ eV). In the following step, Co HERFD data collected at 300 °C shows an additional shift of +1.6 eV to higher energies which is assigned to the reduction of the remaining Co $^{2+}$ species to metallic cobalt. Following the full reduction to metallic Co at 450 °C and 600 °C, the Co HERFD spectrum white line peak position is shifted from 7730 eV to 7726.5 eV (Figure S23). Finally, upon exposing the NiCo catalyst to DMR conditions for 8 h the HERFD spectra remain unchanged and confirms the stability of metallic Co under the DMR conditions.

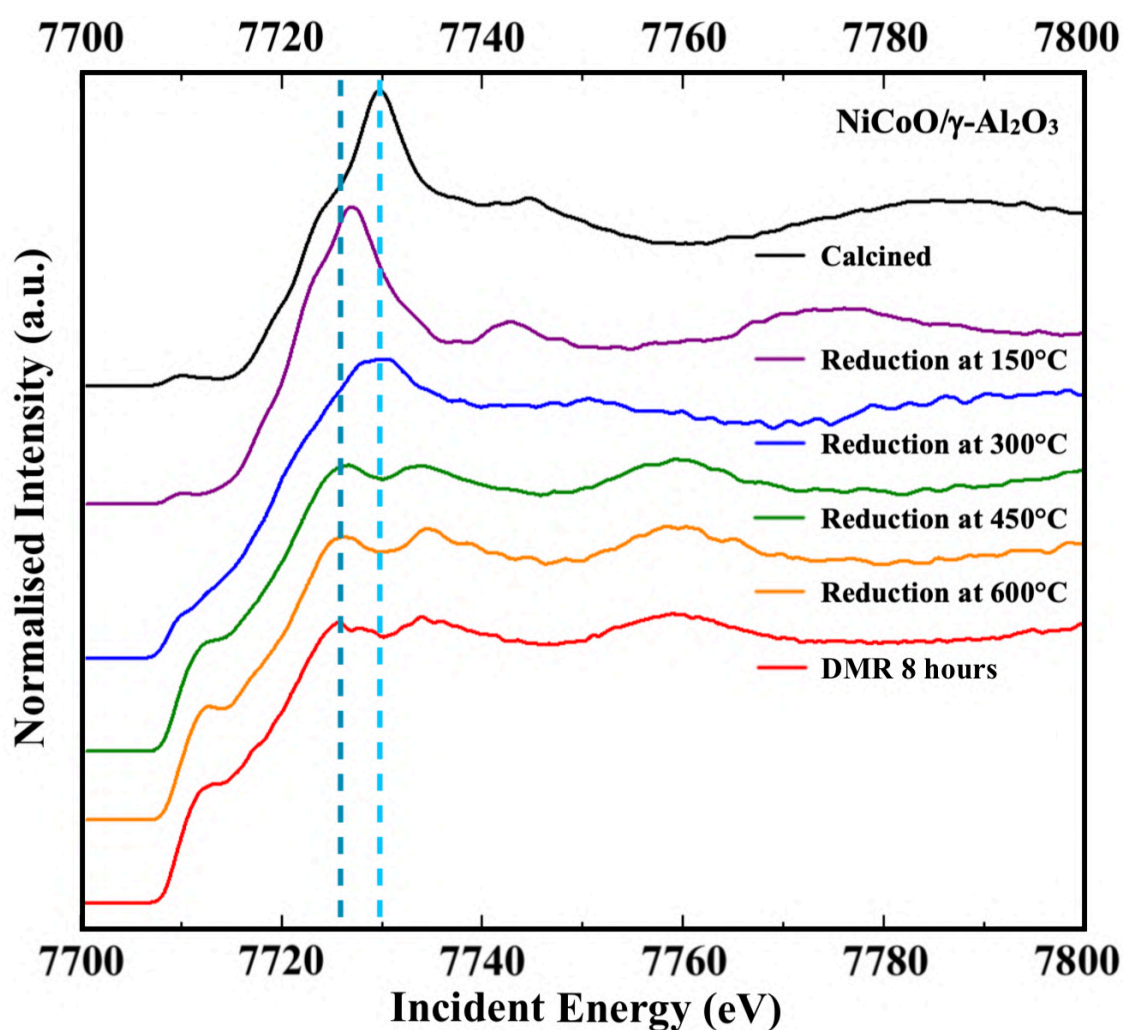


Figure 6): Co K β detected HERFD spectra of the NiCoO/ γ -Al $_2$ O $_3$ sample measured under ambient, reduction activation (5% H $_2$ in Ar), and DMR (7% CH $_4$ and 9.5% CO $_2$ diluted in N $_2$) conditions.

3.3 Conclusion

We studied the structural and electronic properties of NiO/ γ -Al₂O₃ and NiCoO/ γ -Al₂O₃ DMR catalysts in the calcined and reduced states and in-situ under DMR conditions. DMR activity measurements revealed a significantly higher activity for the bimetallic NiCoO catalyst compared to the pure NiO catalyst. In-situ XES spectroscopy for the calcined DMR catalysts showed subtle differences in the Ni K β mainline spectral shape and positions, which are attributed to differences in site symmetry and/or covalency of the Ni sites upon addition of Co. Further, during the course of the reduction/activation of the catalyst, and also during the DMR reaction, the NiCoO catalyst appears to be slightly more oxidized when compared to the NiO catalyst. K β -detected HERFD XAS data revealed that the structure of the NiCoO/ γ -Al₂O₃ catalyst is less distorted (based on the pre-edge intensities) relative to the NiO/ γ -Al₂O₃ catalyst. In addition, Co in NiCoO was identified as being structural analogous to Co₃O₄. Based on both Ni K β XES and HERFD spectra, it was shown that due to the presence of Co in the NiCoO sample, the Ni ions under reductive activation conditions are reduced at relatively higher temperatures as compared to the NiO catalyst. Following the reduction of the NiCoO catalyst at 300 °C, a Ni species with a distinct geometric and electronic structure is formed. At 600 °C, both catalysts are activated and the metal oxides are largely reduced to the metallic phase. Both catalysts remain unchanged during DMR, but distinct differences remain between the Ni-only and the NiCo catalyst, which provide experimental evidence that the presence of Co modulates the Ni geometric and electronic structure.

Acknowledgements

The authors would like to thank the Max Planck Society and the European Research Council under the European Union's Seventh Framework Programme (FP/2007-2013) ERC Grant Agreement No. 615414 (S.D.). We acknowledge F.M.F de Groot and A. van der Eerden from Utrecht University for providing the hard X-ray reactor and Christian W. Lehmann from the Max-Planck-Institut für Kohlenforschung for supporting the STEM measurements.

References

- [1] A. Lee, J. Bennett, J. Manayil, K. Wilson, *Chem. Soc. Rev.* 2014, **43**, 7887-7916.
- [2] C. Descorme, P. Gallezot, C. Geantet, C. George, *ChemCatChem*, 2012, **4**, 1897-1906.
- [3] P. Anastas, J. Warner, *Green Chemistry*; Oxford University Press: New York, **1998**.
- [4] P. Mohanty, K. Pant, S. Naik, J. Parikh, A. Hornung, J. Sahu, *Renewable Sustainable Energy Rev.*, 2014, **38**, 131-153.
- [5] R. de Richter, T. Ming, P. Davies, W. Liu, S. Caillol, *Prog. Energy Combust. Sci.*, 2017, **60**, 68-96.
- [6] W. Chen, T. Suzuki, M. Lackner, *Handbook Of Climate Change Mitigation And Adaptation*; Springer: Cham, **2016**; pp. pp2827-2880.
- [7] J. Lavoie, *Front. Chem.*, 2014, **2**.
- [8] Y. Wang, L. Yao, S. Wang, D. Mao, C. Hu, *Fuel Process. Technol.*, 2018, **169**, 199-206.
- [9] B. Hua, N. Yan, M. Li, Y. Sun, J. Chen, Y. Zhang, J. Li, T. Etsell, P. Sarkar, J. Luo, *J. Mater. Chem. A*, 2016, **4**, 9080-9087.
- [10] J. Han, C. Kim, J. Park, H. Lee, *ChemSusChem*, 2014, **7 (2)**, 451-456.
- [11] P. Djinović, I. Osojnik Črnivec, B. Erjavec, A. Pintar, *Appl. Catal., B*, 2012, **125**, 259-270.
- [12] S. Arora and R. Prasad, *RSC Adv.*, 2016, **6 (110)**, 108668-108688.
- [13] O. Muraza and A. Galadima, *Int. J. Energy Res.*, 2015, **39**, 1196-1216.
- [14] A. Şener, M. Günay, A. Leba, R. Yildirim, *Catal. Today*, 2018, **299**, 289-302.
- [15] M. Usman, W. Wan Daud, H. Abbas, *Renewable Sustainable Energy Rev.*, 2015, **45**, 710-744.
- [16] A. Budiman, S. Song, T. Chang, C. Shin, M. Choi, *Catal. Surv. Asia*, 2012, **16**, 183-197.
- [17] J. Rostrupnielsen and J. Hansen, *J. Catal.*, 1993, **144**, 38-49.
- [18] J. Chang, S. Park, H. Chon, *Appl. Catal., A*, 1996, **145 (1-2)**, 111-124.

- [19] J. Juan-Juan, M. Román-Martínez, M. Illán-Gómez, *Appl. Catal., A*, 2006, **301 (1)**, 9-15.
- [20] M. Fan, A. Abdullah, S. Bhatia, *ChemSusChem*, 2011, **4 (11)**, 1643-1653.
- [21] T. Huang, W. Huang, J. Huang, P. Ji, *Fuel Process. Technol.*, 2011, **92 (10)**, 1868-1875.
- [22] J. Zhang, H. Wang, A. Dalai, *J. Catal.*, 2007, **249**, 300-310.
- [23] J. Zhang, H. Wang, A. Dalai, *Appl. Catal., A*, 2008, **339**, 121-129.
- [24] A. Beheshti Askari, M. al Samarai, B. Morana, L. Tillmann, N. Pfänder, A. Wandzilak, B. Watts, R. Belkhou, M. Muhler, S. DeBeer, *ACS Catal.*, 2020, under revision.
- [25] P. Glatzel and U. Bergmann, *Coord. Chem. Rev.*, 2005, **249**, 65-95.
- [26] P. Glatzel, G. Smolentsev, G. Bunker, *J. Phys. Conf. Ser.*, 2009, **190**, 012046.
- [27] F. de Groot and A. Kotani, *A. Core Level Spectroscopy Of Solids*; CRC Press: Boca Raton, **2008**.
- [28] C. Natoli, M. Benfatto, S. Della Longa, K. Hatada, *J. Synchrotron Radiat.*, 2002, **10**, 26-42.
- [29] R. Castillo, R. Banerjee, C. Allpress, G. Rohde, E. Bill, L. Que, J. Lipscomb, S. DeBeer, *JACS*, 2017, **139 (49)**, 18024-18033.
- [30] M. Baker, M. Mara, J. Yan, K. Hodgson, B. Hedman, E. Solomon, *Coord. Chem. Rev.*, 2017, **345**, 182-208.
- [31] C. Pollock and S. DeBeer, *Acc. Chem. Res.*, 2015, **48 (11)**, 2967-2975.
- [32] J. Kowalska, F. Lima, C. Pollock, J. Rees, S. DeBeer, *Isr. J. Chem.*, 2016, **56 (9-10)**, 803-815.
- [33] C. Pollock, M. Delgado-Jaime, M. Atanasov, F. Neese, S. DeBeer, *JACS*, 2014, **136 (26)**, 9453-9463.
- [34] M. Al Samarai, A. Hahn, A. Beheshti Askari, Y. Cui, K. Yamazoe, J. Miyawaki, Y. Harada, O. Rüdiger, S. DeBeer, *ACS Appl. Mater. Interfaces*, 2019, **11 (42)**, 38595-38605.
- [35] P. Menezes, A. Indra, O. Levy, K. Kailasam, V. Gutkin, J. Pfrommer, M. Driess, *Chem. Commun.*, 2015, **51**, 5005-5008.
- [36] L. Tillmann, J. Schulwitz, A. van Veen, M. Muhler, *Catal. Lett.*, 2018, **148**, 2256-226.

- [37] M. Al Samarai, M. Delgado-Jaime, H. Ishii, N. Hiraoka, K. Tsuei, J. Rueff, B. Lassale-Kaiser, B. Weckhuysen, F de Groot, *J. Phys. Chem. C*, 2016, **120**, 24063-24069.
- [38] M. Cesário, C. Gennequin, E. Abi-Aad, D. de Macedo *Catalytic Materials for Hydrogen Production and Electro-Oxidation Reactions*. 140 (Bentham Science Publishers, **2018**).
- [39] D. Wang, S. Li, Y. Du, X. Wu, Y. Chen, *Catalysts*, 2019, **9**, 352.
- [40] Y. Ji, Z. Zhao, A. Duan, G. Jiang, J. Liu, *J. Phys. Chem. C*, 2009, **113**, 7186-7199.
- [41] T. Nyathi, N. Fischer, A. York, M. Claeys, *Faraday Discuss.*, 2017, **197**, 269-285.
- [42] X. Zhang, J. Liu, Y. Jing, Y. Xie, *Appl. Catal., A*, 2003, **240**, 143-150.
- [43] Y. Kobayashi, J. Horiguchi, S. Kobayashi, Y. Yamazaki, K. Omata, D. Nagao, M. Konno, M. Yamada, *Appl. Catal., A*, 2011, **395**, 129-137.
- [44] J. Horlyck, C. Lawrey, E. Lovell, R. Amal, J. Scott, *Chem. Eng. J.*, 2018, **352**, 572-580.
- [45] K. Mette, S. Kühl, H. Düdder, K. Kähler, A. Tarasov, M. Muhler, M. Behrens, *ChemCatChem*, 2013, **6**, 100-104.
- [46] H. Düdder, K. Kähler, B. Krause, K. Mette, S. Kühl, M. Behrens, V. Scherer, M. Muhler, *Catal. Sci. Technol.*, 2014, **4**, 3317-3328.
- [47] J. Sá, Y. Kayser, C. Milne, D. Abreu Fernandes, J. Szlachetko, *PCCP*, 2014, **16**, 7692.
- [48] S. Hugenbruch, H. Shafaat, T. Krämer, M. Delgado-Jaime, K. Weber, F. Neese, W. Lubitz, S. DeBeer, *PCCP*, 2016, **18 (16)**, 10688-10699.
- [49] X. You, X. Wang, Y. Ma, J. Liu, W. Liu, X. Xu, H. Peng, C. Li, W. Zhou, P. Yuan, X. Chen, *ChemCatChem*, 2014, **6 (12)**, 3377-3386.
- [50] E. Krüger, arXiv:1911.08190v1.
- [51] S. Bare, F. Modica, A. Ringwelski, *J. Synchrotron Radiat.*, 1999, **6**, 436-438.
- [52] A. Khodakov, W. Chu, P. Fongarland, *ChemInform* 2007, **38**.

3.4 Supporting Information

In situ X-ray emission and high-resolution X-ray absorption spectroscopy applied to Ni-based Bimetallic Dry Methane Reforming Catalysts

Abbas Beheshti Askari^(a), Mustafa al Samarai^(a), Nozomu Hiraoka^(b), Hirofumi Ishii^(b), Lukas Tillmann^(c), Martin Muhler^{*(a, c)} and Serena DeBeer^{*(a)}

(a) Max Planck Institute for Chemical Energy Conversion, Stiftstraße 34-36, D-45470 Mülheim an der Ruhr, Germany

(b) National Synchrotron Radiation Research Center, Hsinchu Science Park, Hsinchu 30076, Taiwan

(c) Laboratory of Industrial Chemistry, Ruhr-University Bochum, Universitätsstraße 150, D-44780 Bochum, Germany

Figure S1

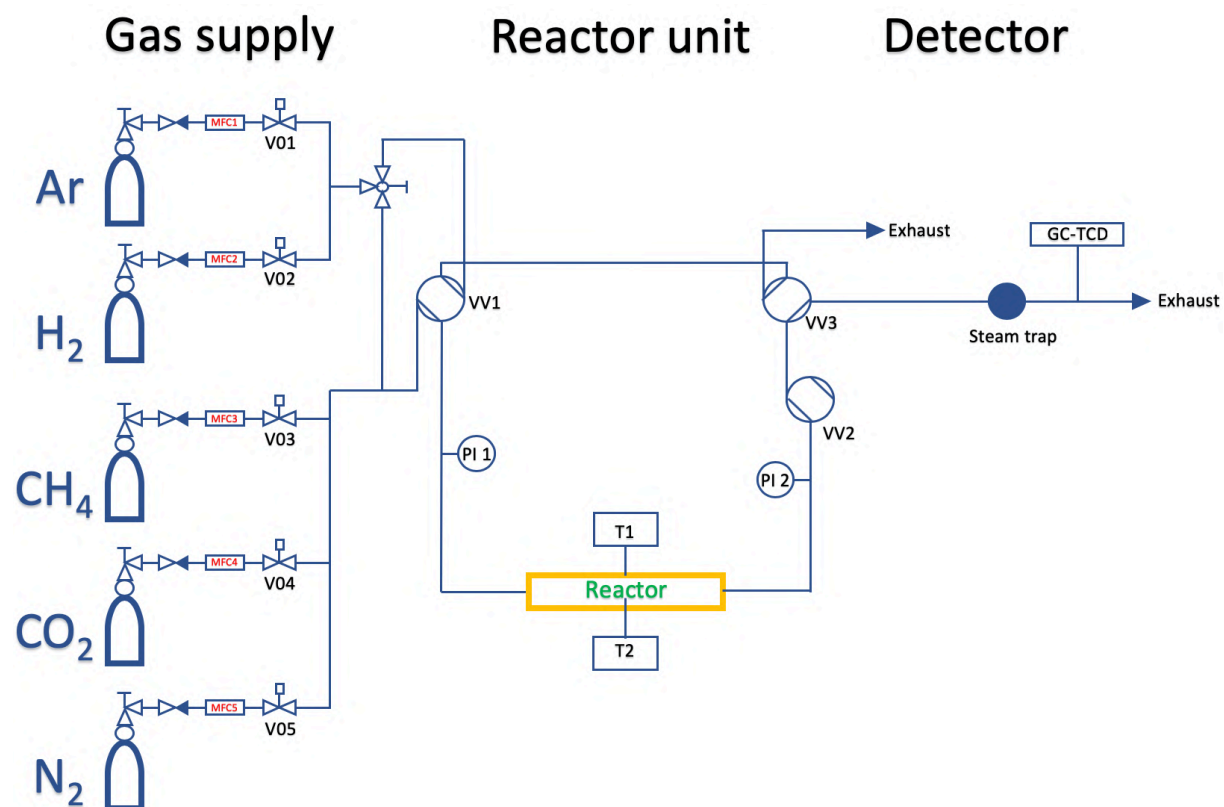


Figure S1: Flow scheme of the reactor used for the DMR activity measurements.

Figure S2

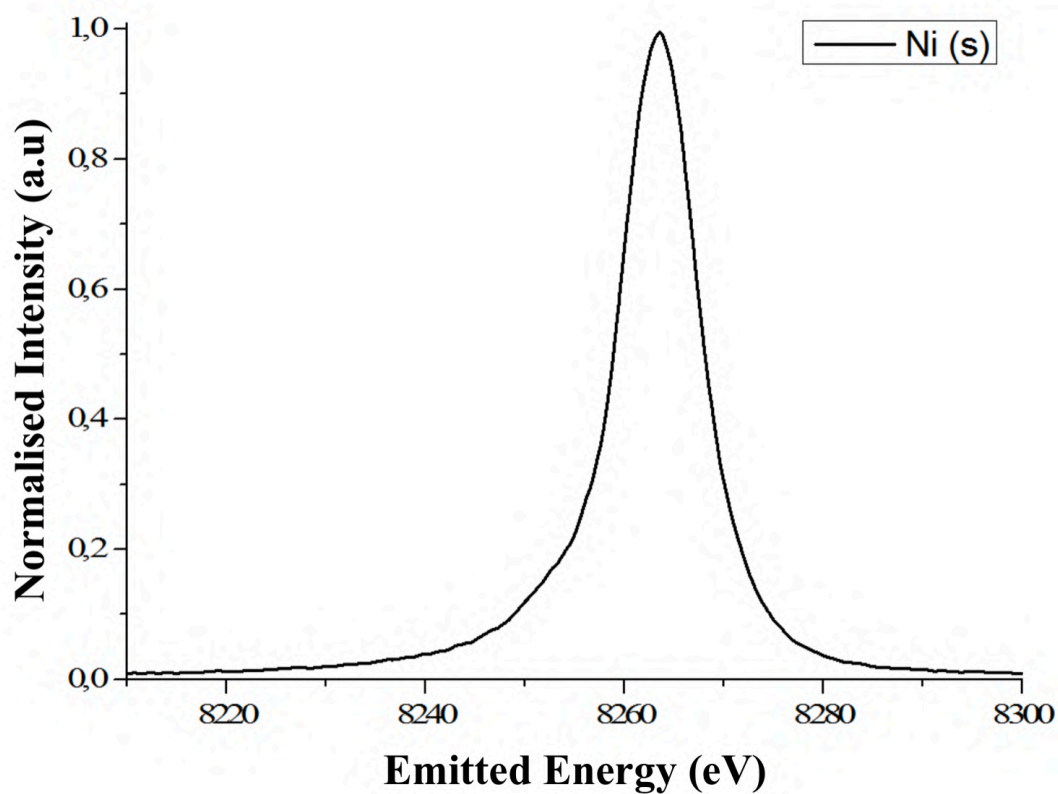


Figure S2: Reference Ni XES spectra of Ni foil.

Figure S3

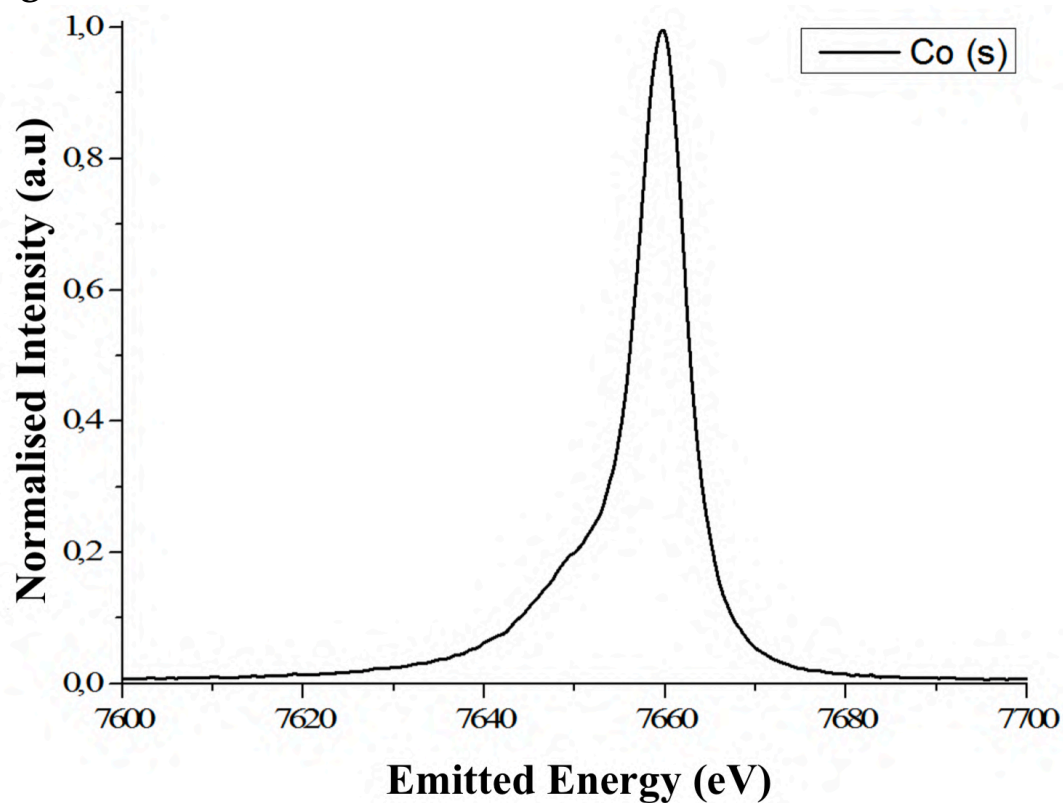


Figure S3: Reference Co XES spectra of Co foil.

Figure S4

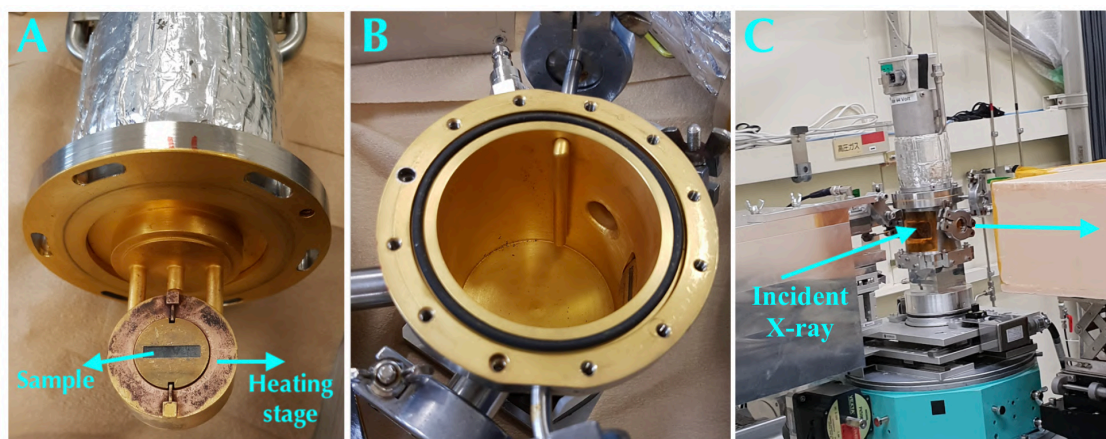


Figure S4: A) The sample powder is pressed into a pellet that is located in the sample holder. The heating stage allows heating up to 600°C. B) image showing that interior of the used reactor. C) Operational reactor setup used in this experiment. During this process the Incident X-ray beam enters the reactor from the window covered with Kapton tape and the scattered emission is measured from the 90° angle.

Figure S5

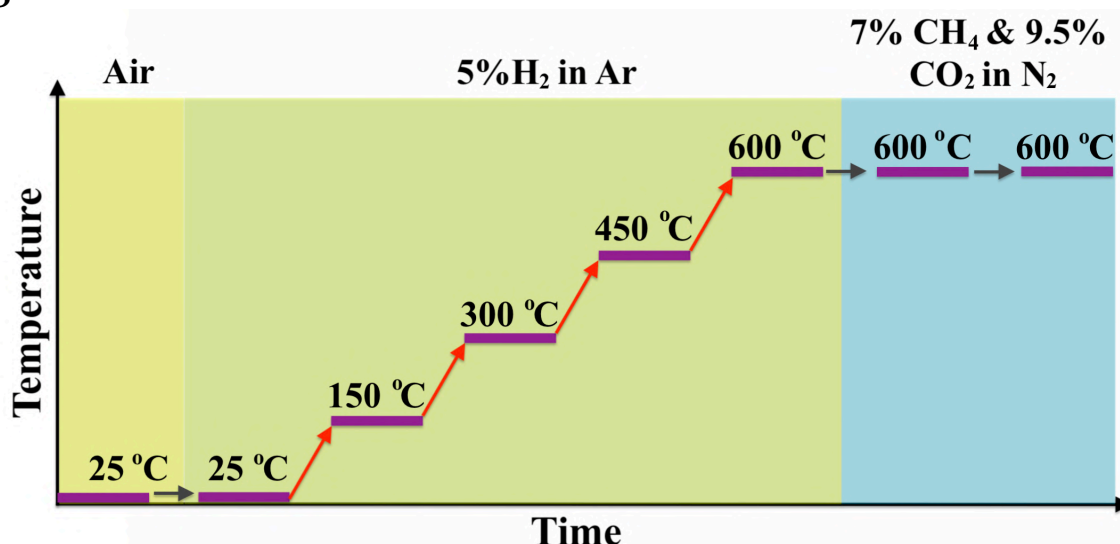


Figure S5: Schematic illustration of the hard X-ray experiments. In the first stage of the experiment the calcined samples were measured at 25 °C under air. The next step involves heating the sample under reducing conditions. In the last step the sample is exposed to DMR conditions.

Table S1

Table S1: Stabilized conversion/yield values for the NiCoO/ γ -Al₂O₃ and NiO/ γ -Al₂O₃ DMR catalysts.

| | NiCoO/ γ -Al ₂ O ₃ | NiO/ γ -Al ₂ O ₃ |
|--------------------------------|---|---|
| CH ₄ Conversion (%) | 79 | 46 |
| CO ₂ Conversion (%) | 71 | 43 |
| H ₂ Yield (%) | 70 | 39 |
| CO Yield (%) | 73 | 44 |
| H ₂ O Yield (%) | 9 | 5 |

Figure S6

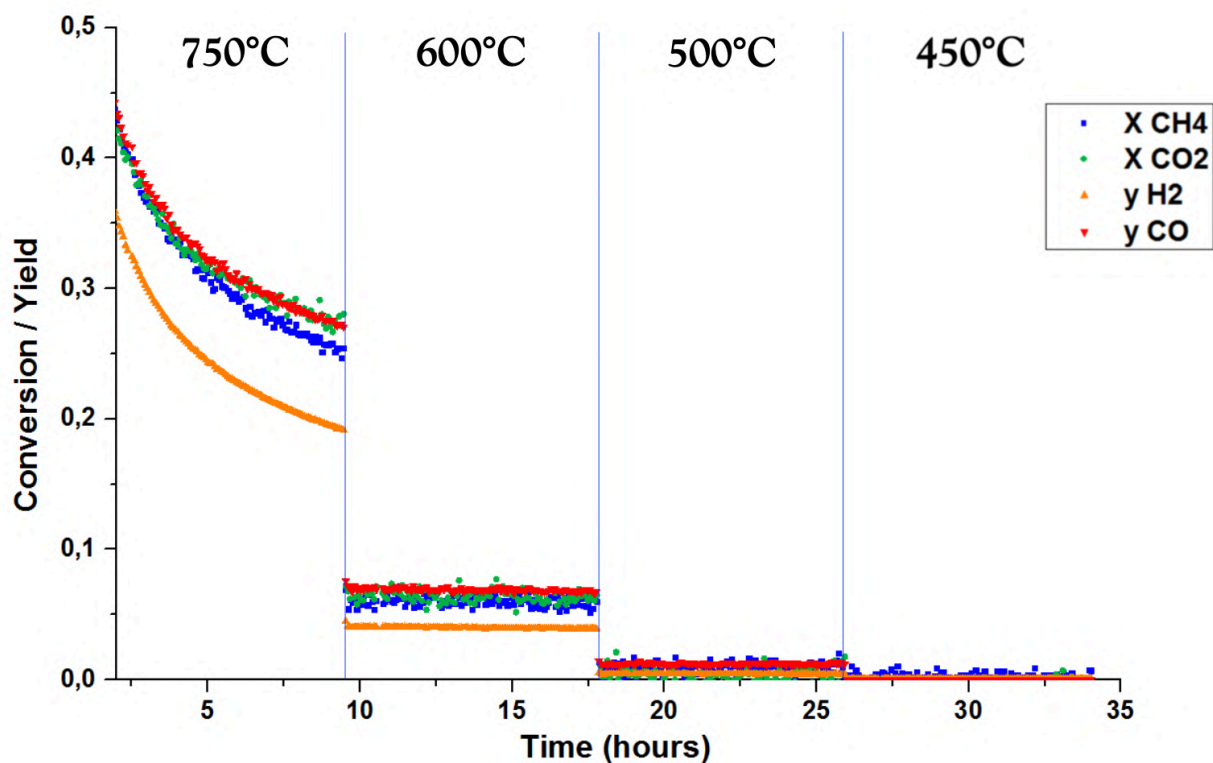


Figure S6: Conversion/Yield values of the NiCoO catalyst during the DMR experiment at 750 °C, 600 °C, 500 °C and 450 °C with 7% CH₄, 9.5 % CO₂ in N₂ and a flow rate of 490 mL/min.

Figure S7

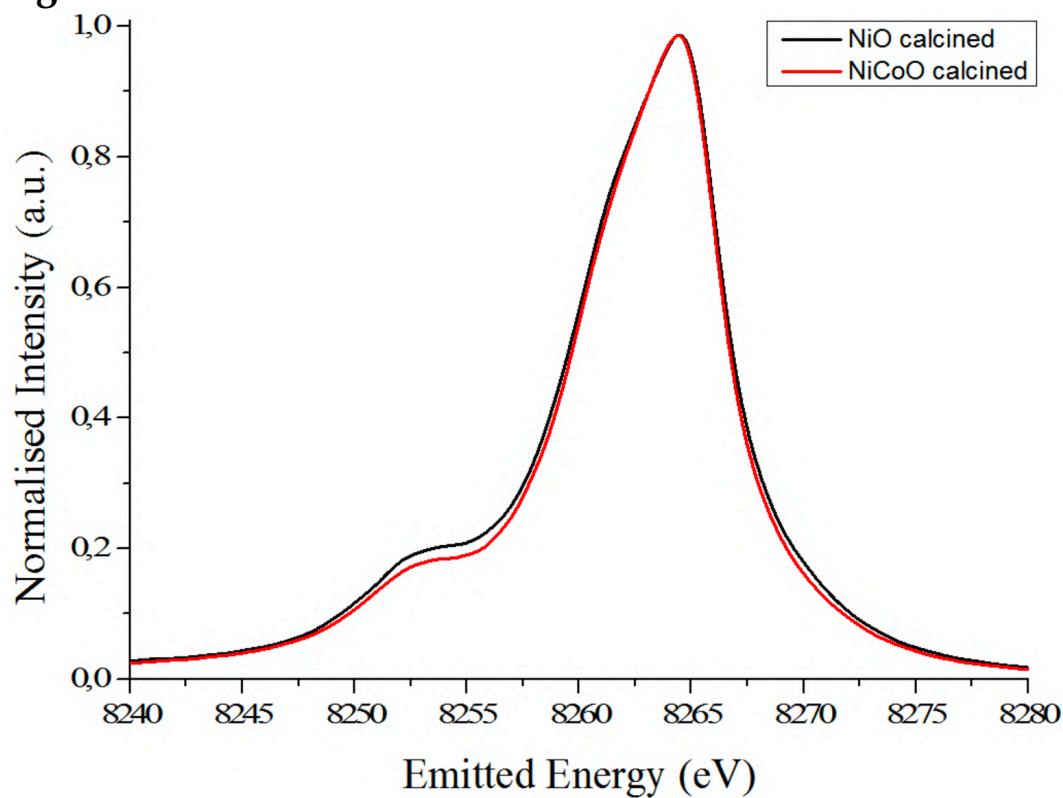


Figure S7: Overlay of the XES spectra for the NiO and NiCoO calcined catalysts.

Table S2

Table S2: $K\beta_{1,3}$ peak position for both $\text{NiO}/\gamma\text{-Al}_2\text{O}_3$ and $\text{NiCoO}/\gamma\text{-Al}_2\text{O}_3$ catalysts measured under activation and DMR conditions.

| | $\text{NiO}/\gamma\text{-Al}_2\text{O}_3$ | $\text{NiCoO}/\gamma\text{-Al}_2\text{O}_3$ |
|--------------------------|---|---|
| <i>Calcined</i> | 8264.50 eV | 8264.44 eV |
| <i>Reduced at 150 °C</i> | 8264.45 eV | 8264.14 eV |
| <i>Reduced at 300 °C</i> | 8263.72 eV | 8263.32 eV |
| <i>Reduced at 450 °C</i> | 8263.57 eV | 8264.10 eV |
| <i>Reduced 600 °C</i> | 8263.48 eV | 8263.99 eV |
| <i>DMR 5 hours</i> | 8263.40 eV | 8263.68 eV |

Figure S8

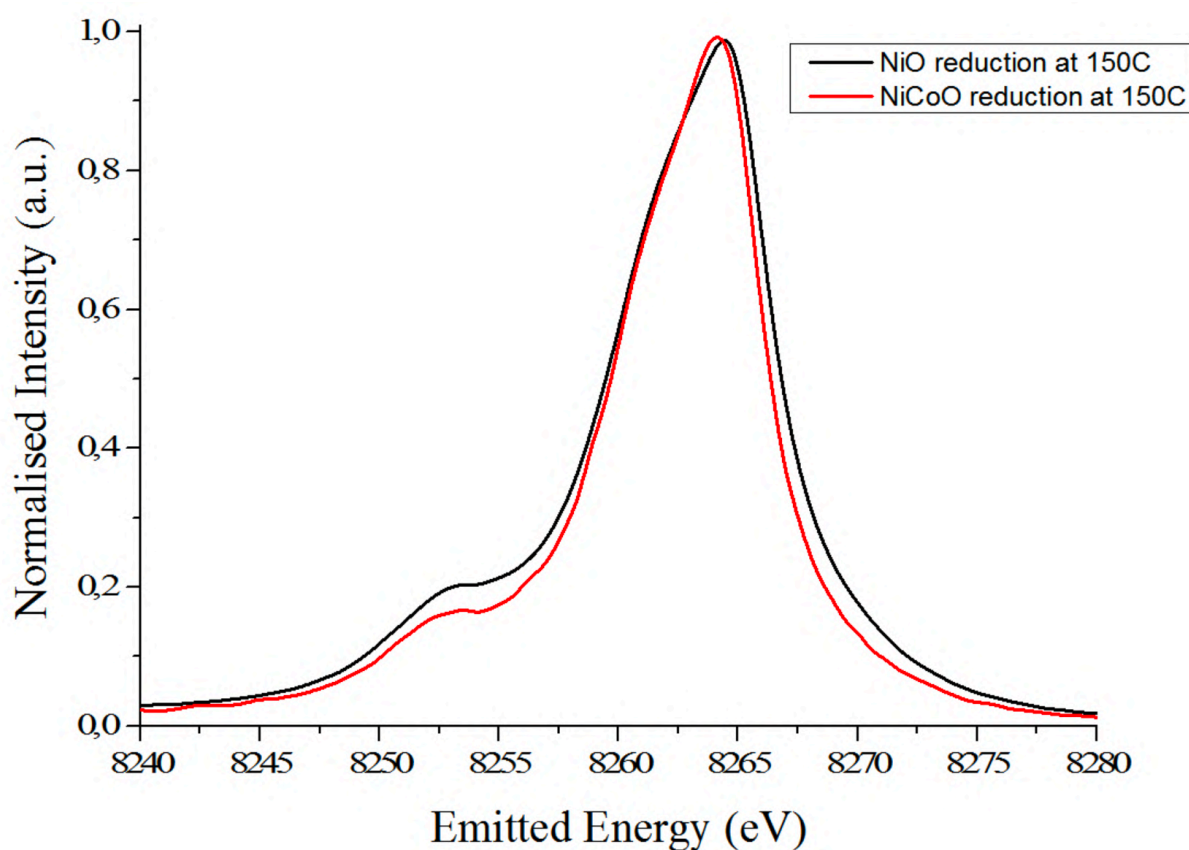


Figure S8: Overlay of the XES spectra for the NiO and NiCoO catalyst after being reduced at 150 °C.

Figure S9

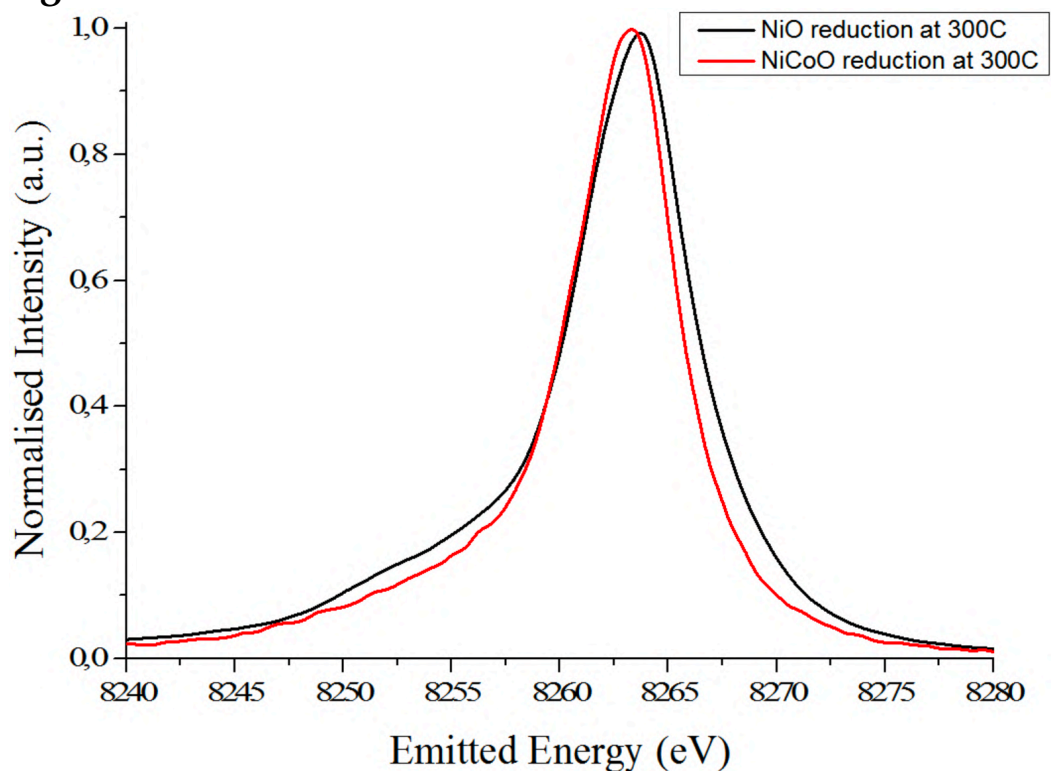


Figure S9: Overlay of the XES spectra for the NiO and NiCoO catalyst after being reduced at 300 °C.

Figure S10

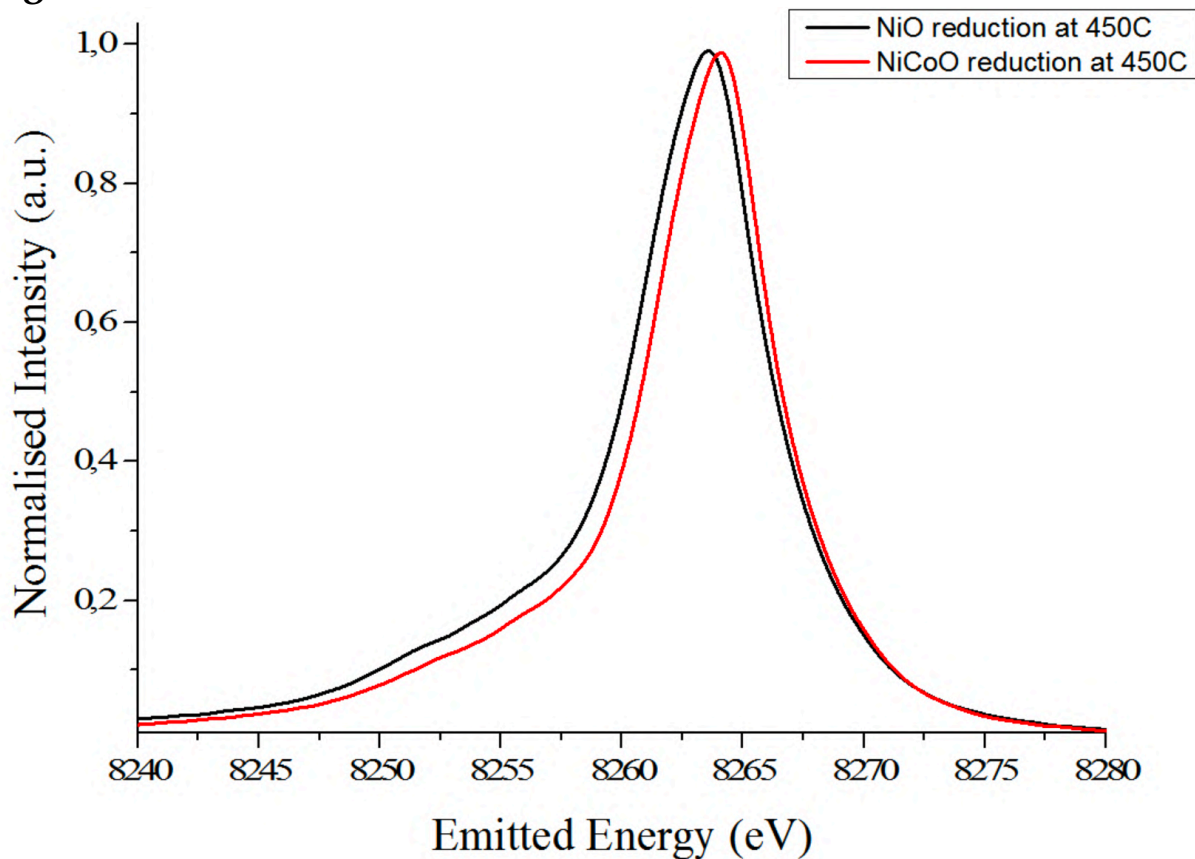


Figure S10: Overlay of the XES spectra for the NiO and NiCoO catalyst after being reduced at 450 °C.

Figure S11

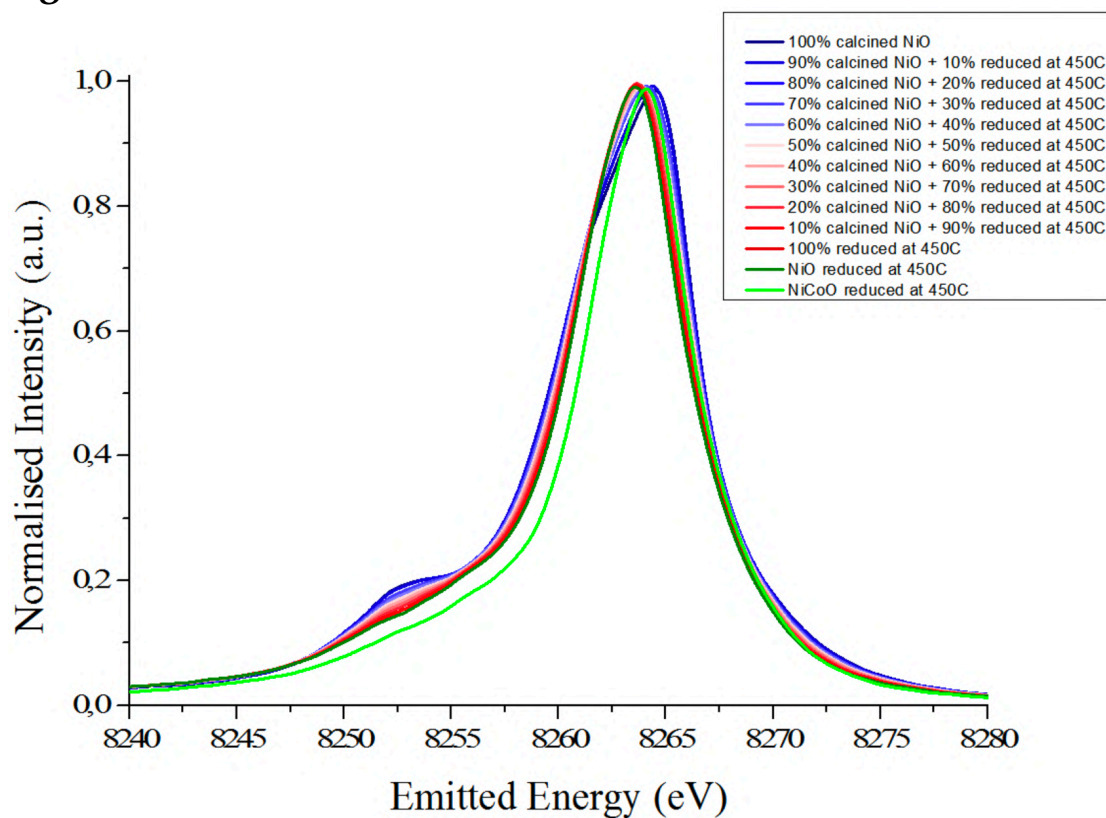


Figure S11: A combination of NiO XES spectra showing the calcined NiO (dark blue), the fully reduced NiO (dark green) and NiCoO (light green) at 450°C. Furthermore, several average spectra were obtained by mixing the spectra of the calcined and reduced NiO sample at 450 °C.

Figure S12

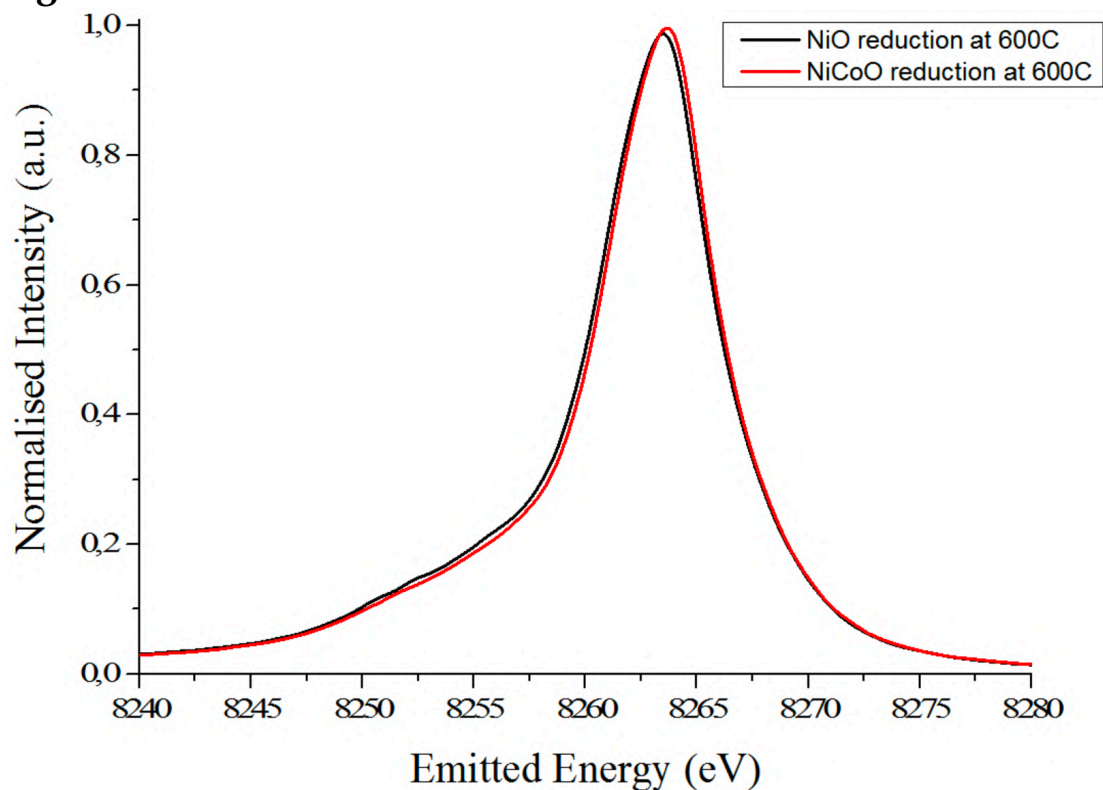


Figure S12: Overlay of the XES spectra for the NiO and NiCoO catalyst after being reduced at 600 °C.

Figure S13

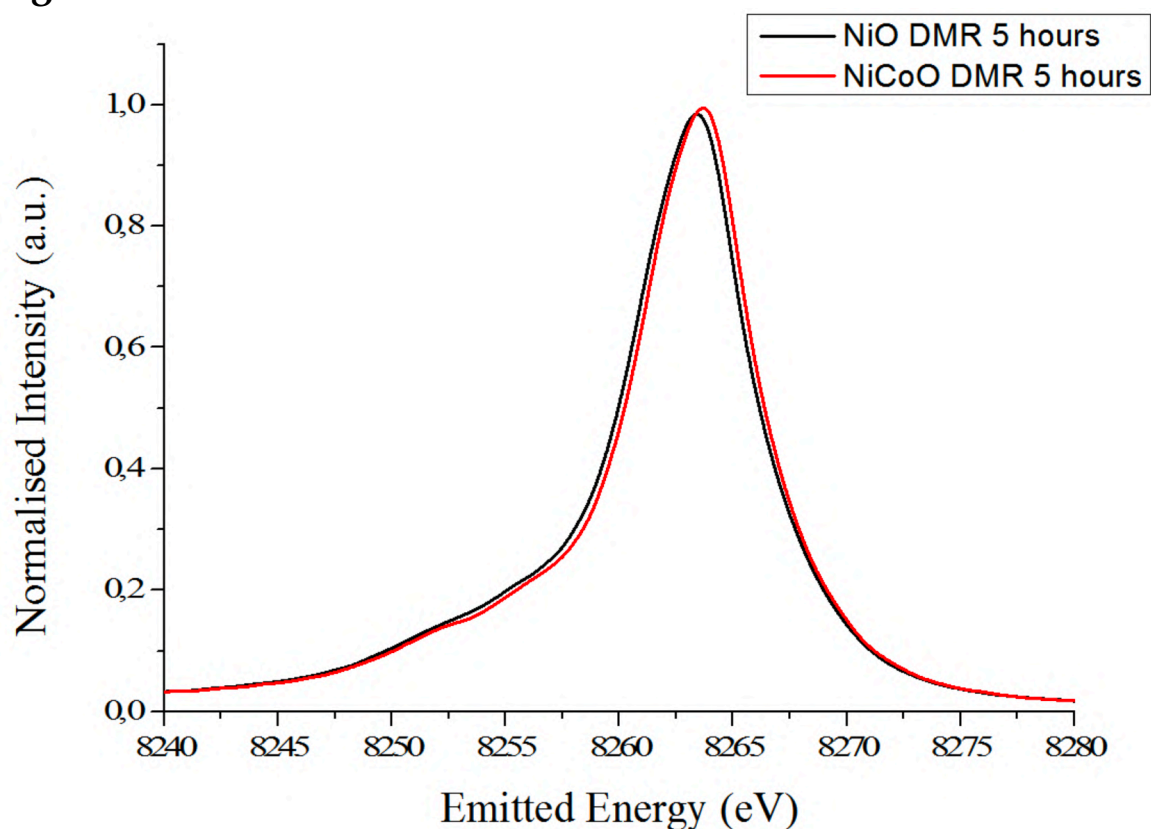


Figure S13: Overlay of the XES spectra for the NiO and NiCoO catalyst after being exposed to DMR conditions for 5 hours.

Figure S14

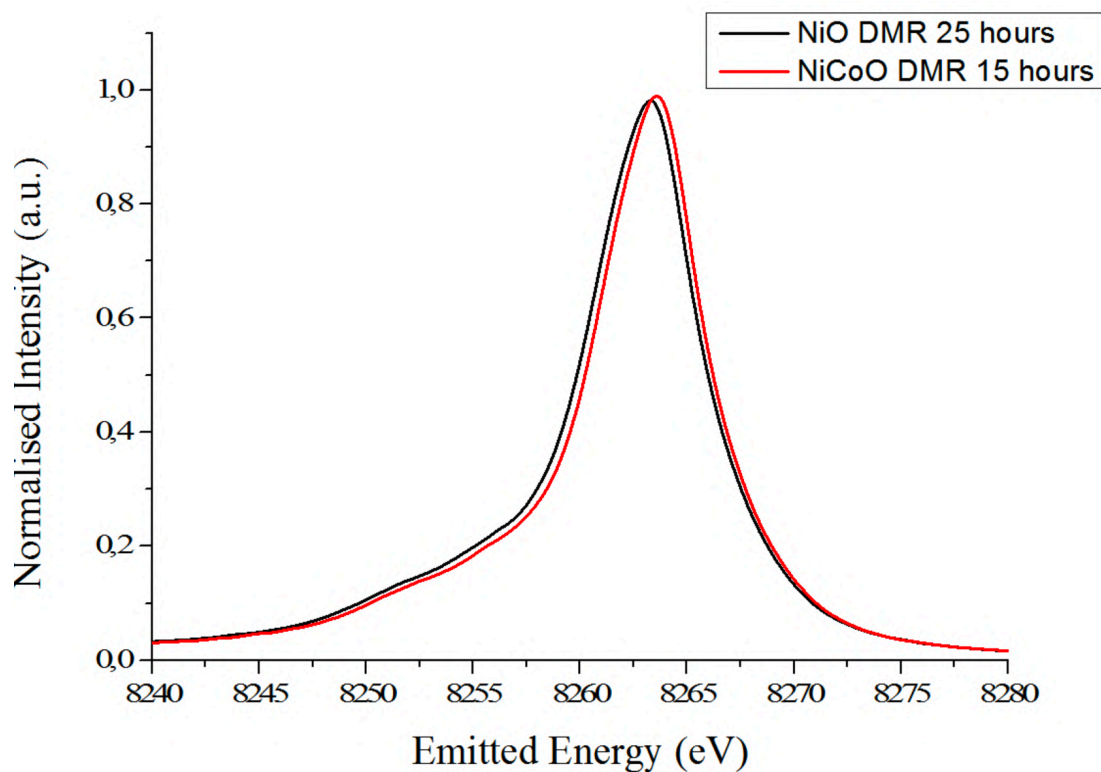


Figure S14: Overlay of the XES spectra for the NiO and NiCoO catalyst after being exposed to DMR conditions for 25 and 15 hours respectively.

Figure S15

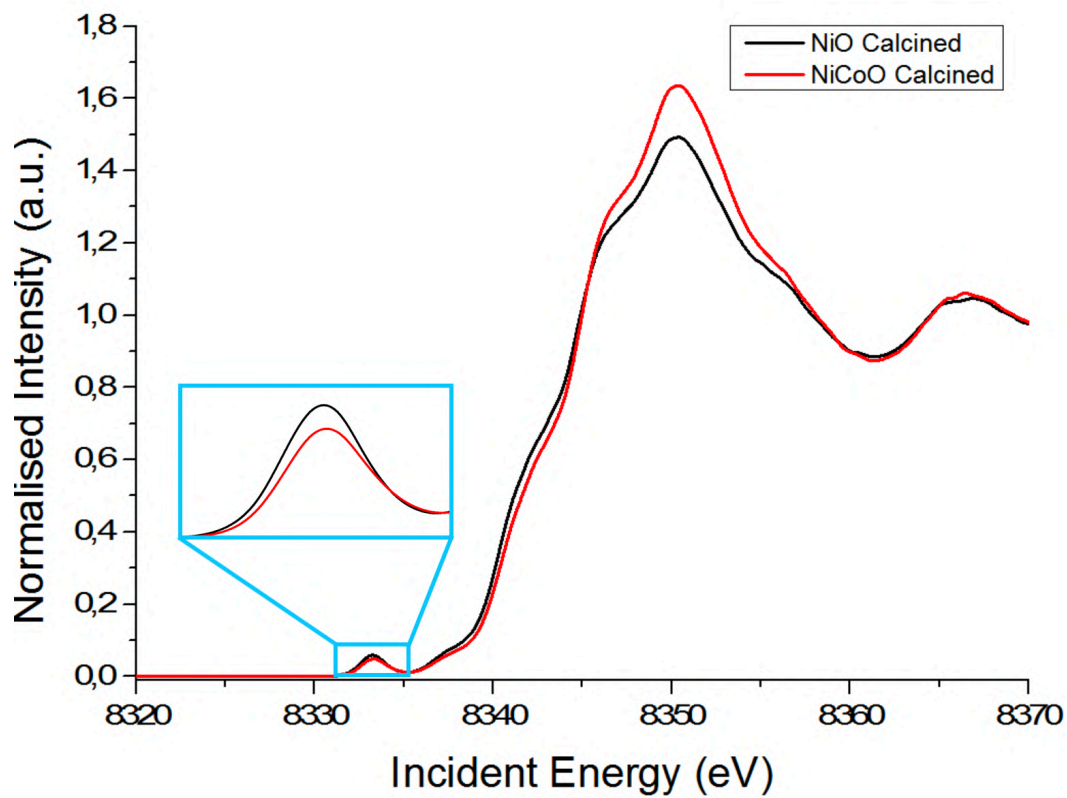


Figure S15: Overlay of the HERFD spectra for the NiO and NiCoO calcined catalysts.

Figure S16

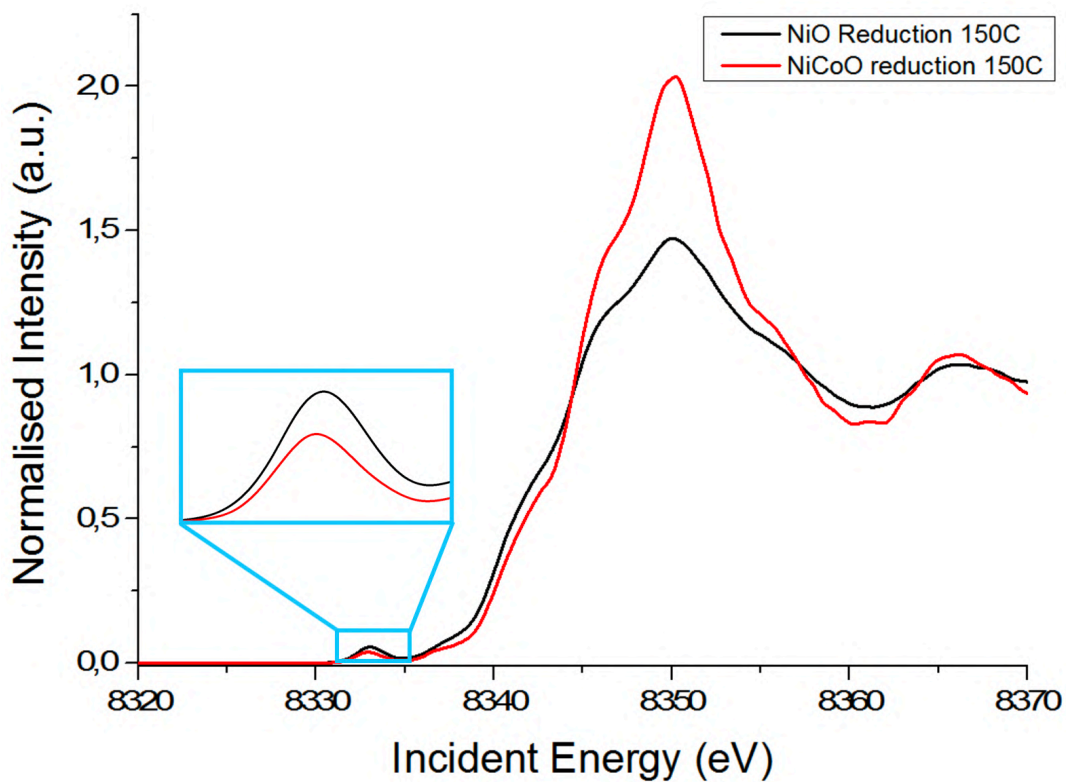


Figure S16: Overlay of the HERFD spectra for the NiO and NiCoO catalyst after being reduced at 150 °C.

Figure S17

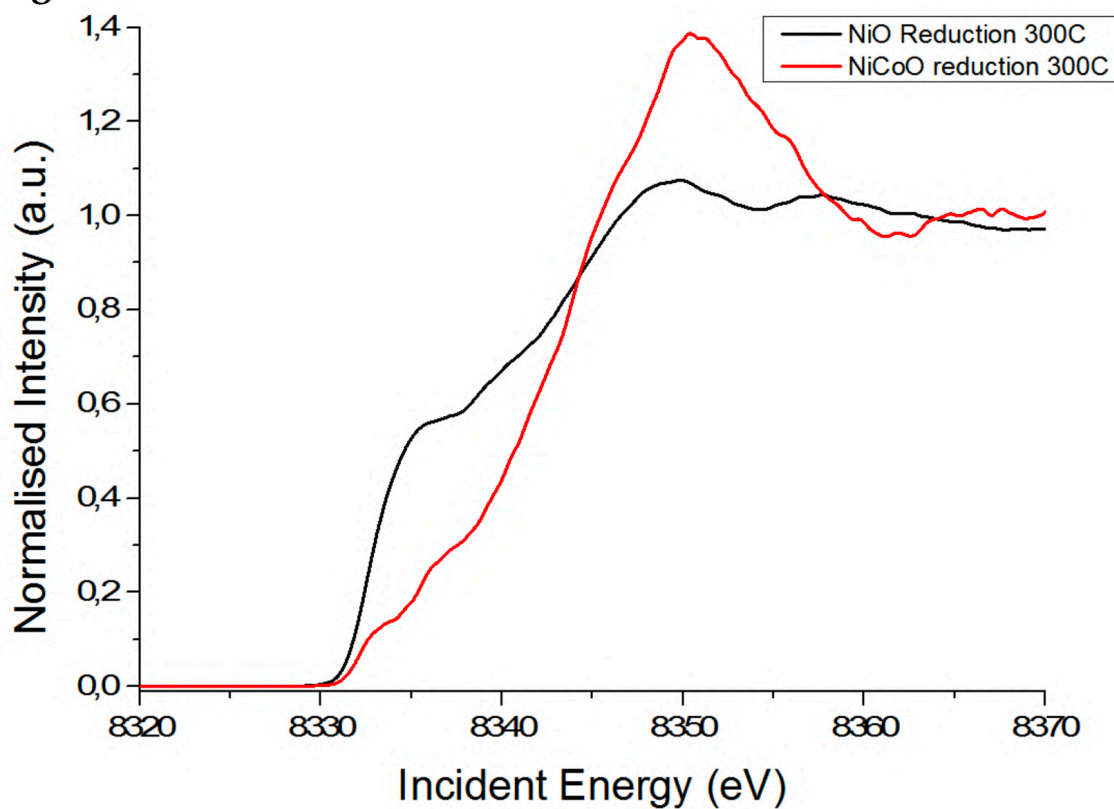


Figure S17: Overlay of the HERFD spectra for the NiO and NiCoO catalyst after being reduced at 300 °C.

Figure S18

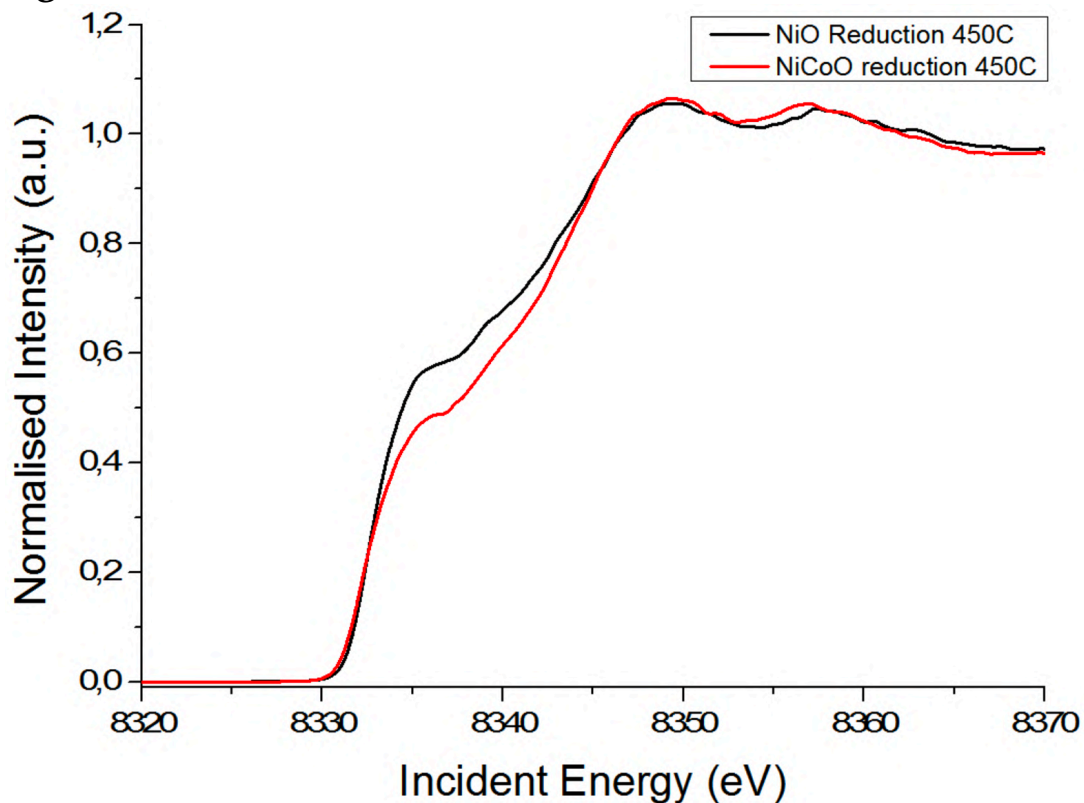


Figure S18: Overlay of the HERFD spectra for the NiO and NiCoO catalyst after being reduced at 450 °C.

Figure S19

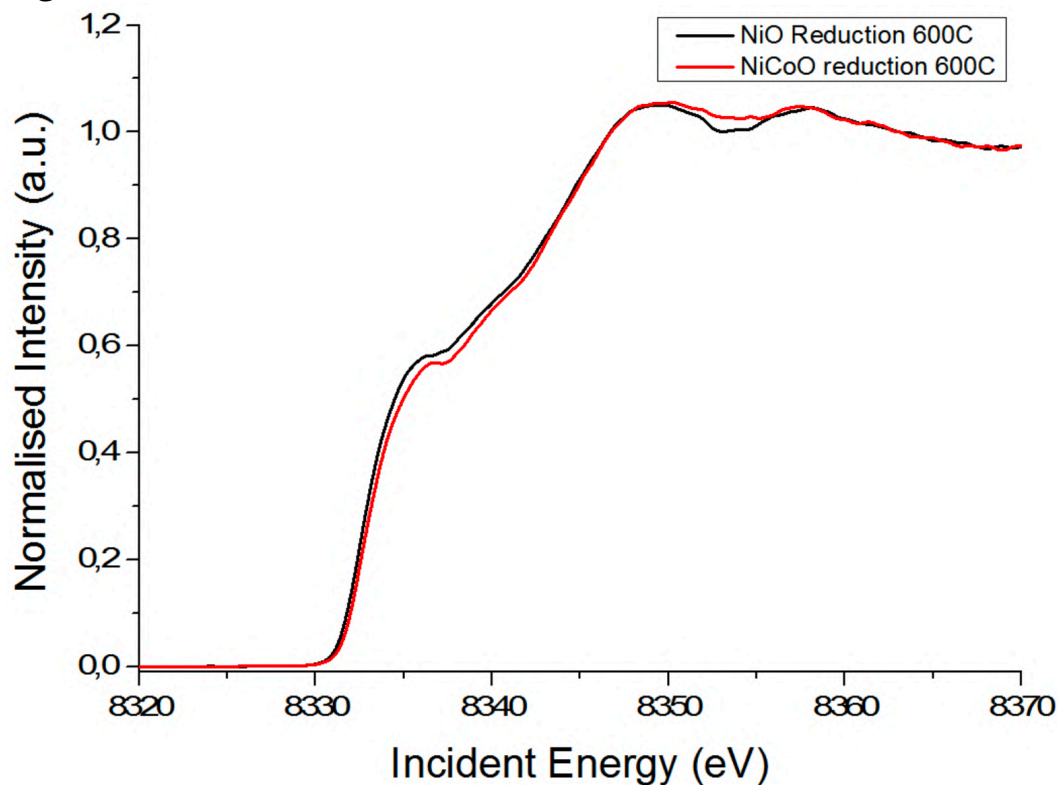


Figure S19: Overlay of the HERFD spectra for the NiO and NiCoO catalyst after being reduced at 600 °C.

Figure S20

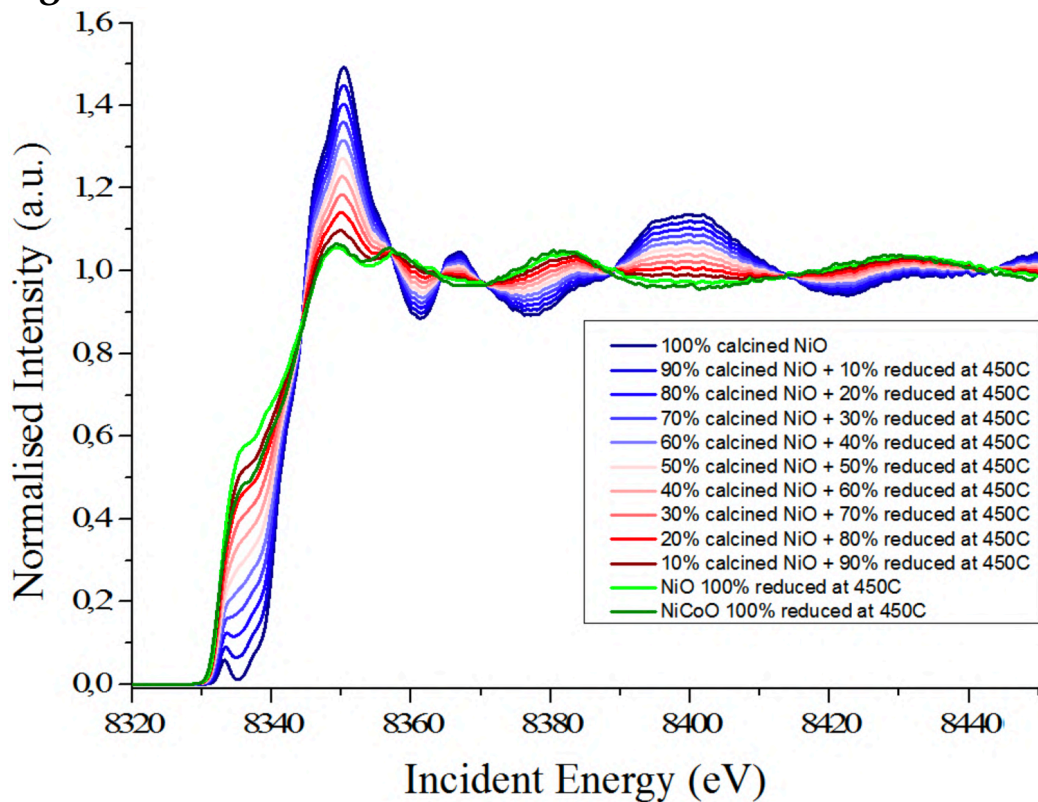


Figure S20: A combination of NiO HERFD spectra showing the calcined NiO (dark blue), the fully reduced NiO and NiCoO at 450 °C.

Figure S21

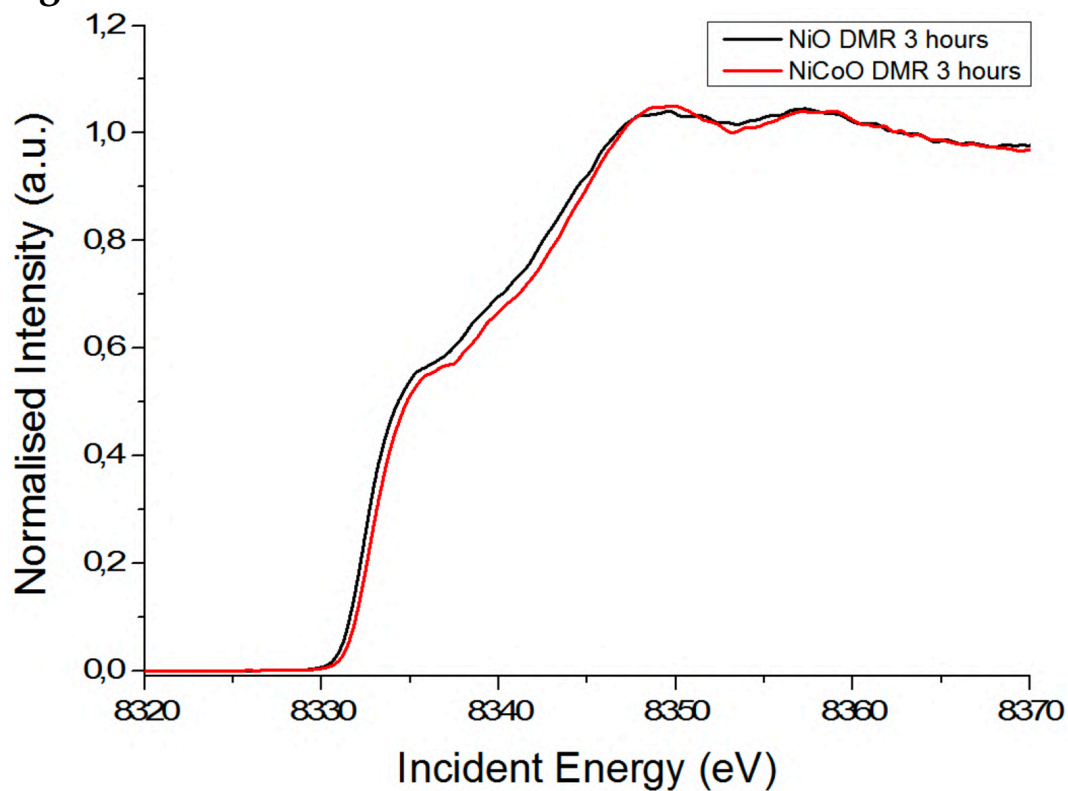


Figure S21: Overlay of the HERFD spectra for the NiO and NiCoO catalyst after being exposed to DMR conditions for 3 hours.

Figure S22

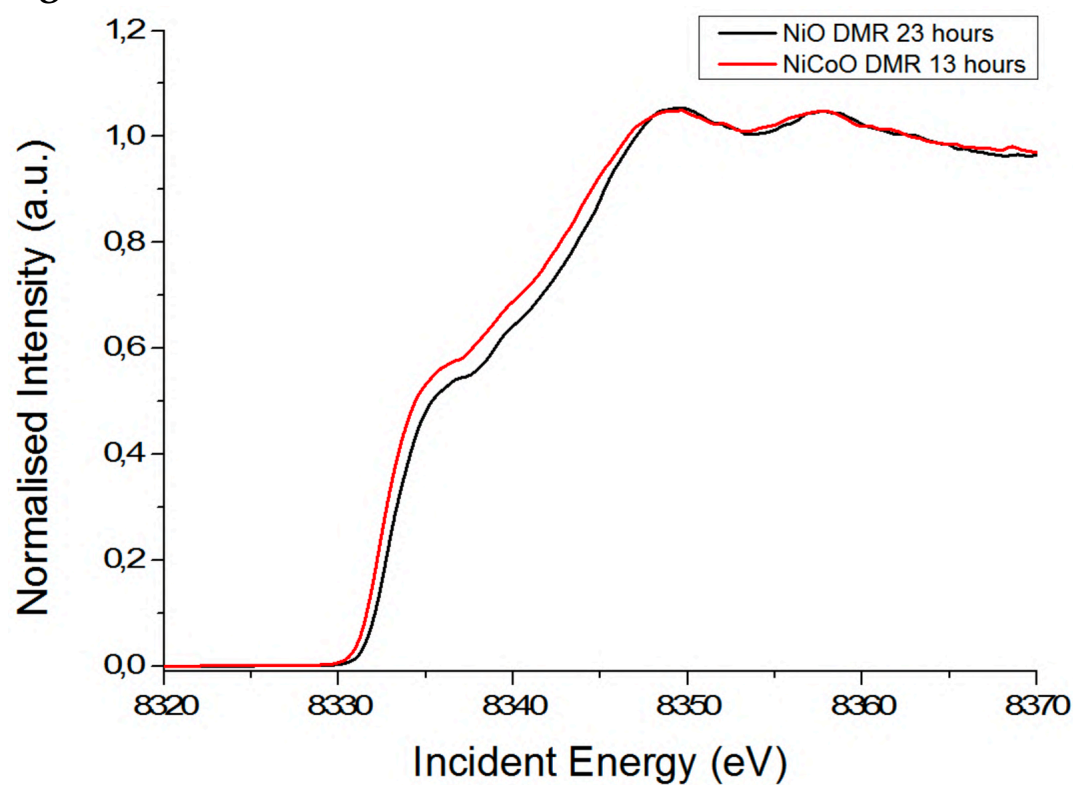


Figure S22: Overlay of the HERFD spectra for the NiO and NiCoO catalyst after being exposed to DMR conditions for 23 and 13 hours respectively.

Figure S23

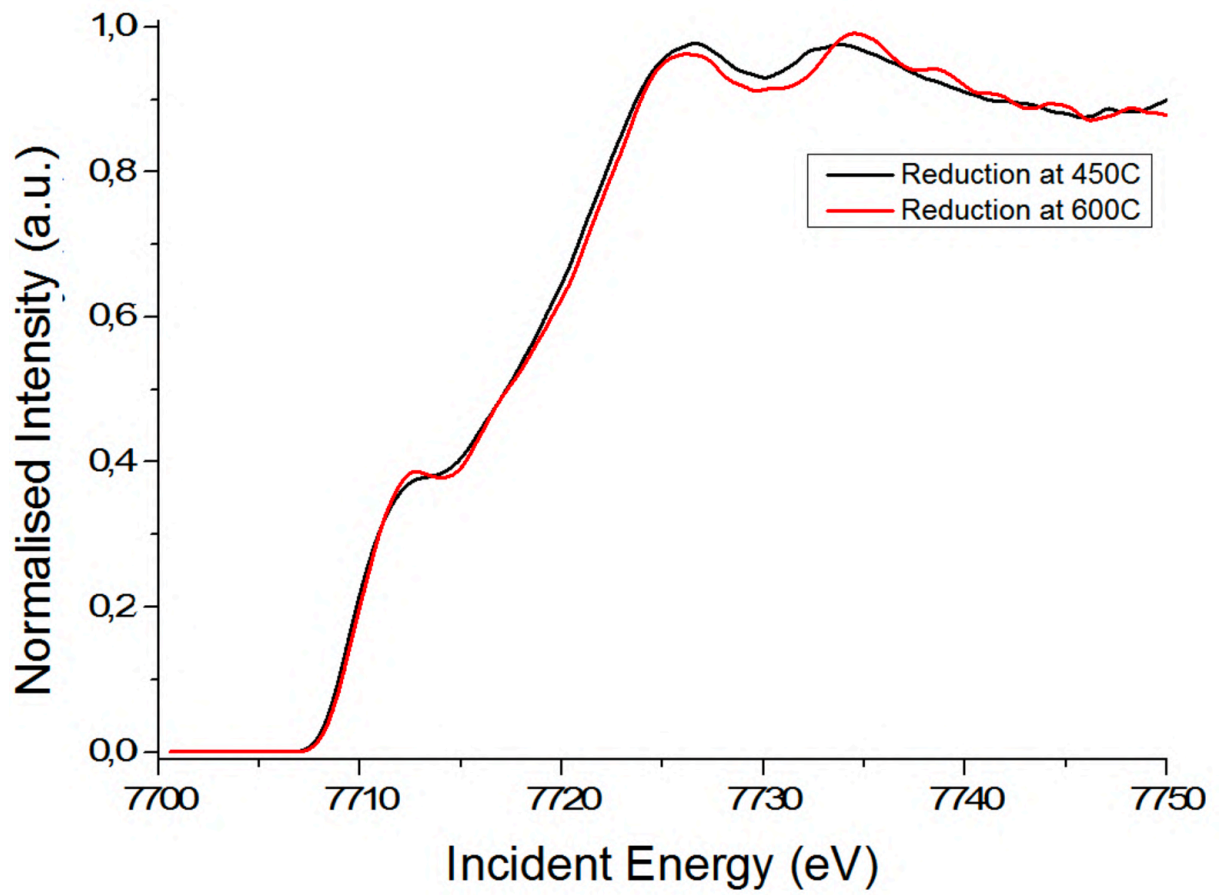


Figure S23: Overlay of the NiCoO HERFD spectra for the catalyst reduced at 450 and 600 °C.

4

The promoting effect of Co vs. Fe on the activation and catalytic activity of supported Ni-based bimetallic dry methane reforming catalysts

In this Chapter a spectromicroscopy study on three Dry Methane Reforming (DMR) catalysts ($\text{NiCoO}/\gamma\text{-Al}_2\text{O}_3$, $\text{NiFeO}/\gamma\text{-Al}_2\text{O}_3$ and $\text{NiO}/\gamma\text{-Al}_2\text{O}_3$) are presented. The changes in the particle morphology and the electronic structure of the metal sites are followed during the reductive activation step and under operating conditions. Catalytic tests indicate that the DMR activity of the $\text{NiCoO}/\gamma\text{-Al}_2\text{O}_3$ is notably higher than the $\text{NiFeO}/\gamma\text{-Al}_2\text{O}_3$ catalysts. Temperature programmed reduction (TPR) data shows that doping with either Fe ($\text{NiFeO}/\gamma\text{-Al}_2\text{O}_3$) or Co ($\text{NiFeO}/\gamma\text{-Al}_2\text{O}_3$) has an opposite effect on the reducibility of the Ni-site during the catalyst activation. Interestingly, Fe promotes the reduction of Ni oxides at low temperatures when compared to the pure $\text{NiO}/\gamma\text{-Al}_2\text{O}_3$ catalyst, while Co inhibits reduction. Earlier in-situ Scanning Transmission X-ray Microscopy (STXM) studies displayed the formation of a segregated structure with a Ni-rich surface for the $\text{NiCoO}/\gamma\text{-Al}_2\text{O}_3$ particles under activation conditions. It was also shown that during the DMR reaction, the segregated structure for the $\text{NiCoO}/\gamma\text{-Al}_2\text{O}_3$ is maintained. In this study we used in-situ STXM to study the $\text{NiFeO}/\gamma\text{-Al}_2\text{O}_3$ and follow the changes in the morphology and the structure under activation and DMR reaction conditions. The obtained results are used to understand the lower DMR activity for $\text{NiFeO}/\gamma\text{-Al}_2\text{O}_3$ catalyst relative to the $\text{NiCoO}/\gamma\text{-Al}_2\text{O}_3$. Based on the obtained data the formation of a rather distinct spherical structures is confirmed for the $\text{NiFeO}/\gamma\text{-Al}_2\text{O}_3$ under both activation and during DMR reaction conditions.

The promoting effect of Co vs. Fe on the activation and catalytic activity of supported Ni-based bimetallic dry methane reforming catalysts

Abbas Beheshti Askari, Mustafa al Samarai, Bruno Morana, Lukas Tillmann, Norbert Pfänder, Benjamin Watts, Martin Muhler, and Serena DeBeer. **In preparation**

4. Introduction

The DMR process is one of the promising reactions for the production of environmentally friendly fuels. During this reaction two major greenhouse gasses i.e. carbon dioxide (CO₂) and methane (CH₄) are simultaneously converted into hydrogen (H₂) and carbon monoxide (CO), eq.1 [1-4]. The resulting gas mixture is known as syngas, has a H₂:CO ratio of close to unity and serves as feedstock for many industrial applications [5-7].



In literature, different types of heterogeneous catalyst are reported for the DMR process, including noble metals, spinels, hydrotalcites, and supported base-metals [5, 8-9]. The high abundance and activity of Ni-based DMR catalysts makes these the prime candidates for the synthesis of syngas. However, the primary drawback when compared to noble metal-based catalysts is their higher susceptibility for deactivation by coke-formation on the catalytic active phase [10-11]. Furthermore, the addition of transition metals promoters e.g. Co, Fe, Mo, Mn and Cu to Ni-based DMR catalysts has been shown to improve the catalysts activity and stability [12-14]. Within this context, the NiCo bimetallic catalyst has been extensively studied due to its high DMR activity and low carbon deposition rate. In an earlier in-situ STXM study, the changes in the electronic structure, active phase distribution, coordination and oxidation state during the catalyst activation and the DMR reaction in a NiCoO/ γ -Al₂O₃ catalyst was studied [15]. It was revealed that during the catalyst activation, the NiCo catalyst transformed into a segregated structure which maintained under DMR conditions. Further, the formation and growth of Ni-rich branches on the surface of the catalyst particles under the DMR reaction was shown. In addition to the NiCo system, the bimetallic NiFe catalyst also shows a high activity and stability towards the DMR reaction. For example, Kim et al. reported a lower activity for the monometallic Ni and Fe catalyst when compared to the bimetallic Ni₄Fe₁ alloy [16]. In the same study, the combination of operando X-ray Absorption Spectroscopy (XAS), X-Ray Diffraction (XRD), and Density Functional Theory (DFT) data revealed the partial oxidation of the Fe to FeO under reforming conditions which results in a Ni-rich NiFe alloy. Nevertheless, there are contradicting reports regarding the promoting effect of Fe in literature [16-18]. For instance, in a study by Zhang et al. it was shown that among the various Ni-M alloys (M= Co, Fe, Cu and Mn), only Co had a promoting effect on the catalytic activity [13]. On the contrary, NiFe alloy showed a high carbon deposition rate and a relatively lower activity. By understanding how the electronic structure and morphology of the NiFe catalyst is modified during the activation/reduction stage and under the DMR conditions, catalysts with improved activity, selectivity, and stability can be realized. Additionally, this will allow us to reveal to role of Fe in the bimetallic NiFe catalyst.

In the current study, we compare the properties of three DMR catalyst (NiO/ γ -Al₂O₃ [19], NiCoO/ γ -Al₂O₃ and NiFeO/ γ -Al₂O₃) through the activation and subsequent DMR process. In order to allow for a facile comparison between the NiCoO/ γ -Al₂O₃ [15], and NiFeO/ γ -Al₂O₃ DMR catalysts, the experiments on the NiCoO catalyst were repeated in parallel with the NiFeO. Further, the NiFeO/ γ -Al₂O₃ was synthesized according the reverse micellar method [15,19-21]. We aim to assess the changes in particle

morphology and electronic structure to understand the effect of the second metal on the Ni-site.

To gain insight into the morphology, particle size and elemental distribution, Scanning Transmission Electron Microscopy (STEM)-Energy Dispersive X-ray Spectroscopy (EDX) experiments were performed. Also, DMR activity experiments were conducted prior to the spectroscopy measurements to compare the activities of the monometallic NiO/ γ -Al₂O₃ catalysts with the bimetallic NiFeO/ γ -Al₂O₃ and NiCoO/ γ -Al₂O₃. In addition, TPR measurements were performed to study the reduction profiles of Ni, Fe and Co oxides and their full conversion into their metallic species. Finally, in-situ STXM was used to study the electronic structure and morphology of the NiFeO/ γ -Al₂O₃, NiCoO/ γ -Al₂O₃ and NiO/ γ -Al₂O₃ catalyst under activation/reduction and DMR conditions.

4.1 Experimental section

4.1.1 Catalyst Synthesis

The synthesis of NiO/ γ -Al₂O₃ and NiCoO/ γ -Al₂O₃ DMR catalysts have been described elsewhere [15,19].

For the synthesis of the NiFeO/ γ -Al₂O₃ catalyst the following chemicals were used without any purifications: iron(II) acetate (>99.99%, Sigma Aldrich), nickel(II) acetate tetrahydrate (99.998%, Sigma Aldrich), ammonium oxalate monohydrate (98%, Alfa Aesar), Methanol (99%, Alfa Aesar), 1-Hexanol (99%, Alfa Aesar), n-hexane (99% gamma alumina catalyst support, Alfa Aesar).

The NiFeO/ γ -Al₂O₃ catalyst was synthesized according to the modified reverse micellar method [15,19-21]. In the first step of the synthesis of NiFeO/ γ -Al₂O₃ catalyst three different mixtures are prepared by individually dissolving: I) 2.3 g ammonium oxalate monohydrate, II) 2.0 g nickel acetate tetrahydrate, and III) 0.71 g iron acetate in 15 mL water and stirred for 15 minutes. Next, a fourth mixture was obtained by mixing and stirring of 0.9 g cetyltrimethylammonium bromide, 9 mL hexanol, and 12.6 mL hexane for 20 minutes. Further, the fourth mixture was divided into three equal parts which were added to mixtures 1-3 and stirred for additional 20 minutes. Finally, to obtain the bimetallic sample/particles all three mixtures were added together and stirred for 48 hours. The bimetallic catalyst was purified by centrifuging the mixture at 5500 rpm for 5 minutes and washed with a mixture of 30 mL methanol and 30 mL chloroform. This procedure was followed by centrifugation at 5500 rpm and drying at 50 °C for 12 hours.

The bimetallic particles were supported on the γ -Al₂O₃ by mixing the dried nanoparticles with 0.8 g of γ -Al₂O₃ support and 2.5 mL demineralized water. The resulting mixture was stirred for 20 minutes and dried at 90 °C for 12 in a tubular quartz tube in an electrical furnace. To convert the metal acetates to their respective oxides, the sample was calcined by heating the catalyst for 10 hours at 400 °C under dynamic synthetic air flow.

4.1.2 STEM-EDX

The experimental setup for the STEM-EDX measurements performed on the NiCoO/ γ -Al₂O₃ are reported in an earlier study [15]. Nevertheless, for the sake of reproducibility,

the experiments on the NiCoO/ γ -Al₂O₃ sample were repeated in this study. In this study the Hitachi HD-2700 spherical aberration corrected Scanning Transmission Electron Microscope (STEM) was used to gain insight into the morphology of the NiCoO/ γ -Al₂O₃ and NiFeO/ γ -Al₂O₃ samples. In addition, Energy Dispersive X-ray (EDX) data were recorded with an EDAX Octane T Ultra W 200 mm² SDD. The STEM-EDX measurements for the freshly calcined samples were performed by dispersing the respective catalyst powder on a polymer-coated Cu TEM grid.

4.1.3 TPR

Detailed TPR experimental setup and the TPR profiles for the NiCoO/ γ -Al₂O₃ and NiO/ γ -Al₂O₃ catalysts were also reported in a previous study [15,19].

The TPR measurements for the NiFeO/ γ -Al₂O₃ were obtained by filling a quartz cell with 61 mg of the calcined catalysts. For the TPR measurements the samples were heated with a rate of 6 °C/min to 850 °C while constantly flowing 84.1 mL/min of 4.6% H₂ in Ar. The hydrogen consumption was determined by a thermal conductivity detector (Hydros, Rosemount).

4.1.4 DMR activity tests

The experimental setup for the DMR activity tests has been reported in our previous study [15,22].

4.1.5 N₂-Physisorption

The specific surface area, pore volume, and pore diameter of NiFeO/ γ -Al₂O₃, NiCoO/ γ -Al₂O₃ and NiO/ γ -Al₂O₃ was obtained by N₂-physisorption using the NOVA 2000 (quantachrome Instruments) setup.

4.1.6 In-situ STXM

In-situ STXM experiments for the NiFeO/ γ -Al₂O₃, NiCoO/ γ -Al₂O₃ and NiO/ γ -Al₂O₃ DMR catalysts were performed at the PolLux beamline at the Swiss Light Source (SLS) [23]. The spatial resolution of the used zone plates during the STXM measurements were 35 nm. During the in-situ STXM measurements the Ni, Co and Fe L-edges were selected, whereas due to the low absorption cross section of the Al K-edge and the thin alumina support it was not measured. For the in-situ STXM measurements MEMS-based nanoreactors were employed [15,24-26]. To load the nanoreactors a catalyst suspension in ethanol was drop-casted on the inlet of the nanoreactors. During the STXM measurement, the sample was raster-scanned in two dimensions and the transmission signal from a selected number of points on two dimensions was converted to their respective Optical Density (OD) maps. The resulting 2D image contains information regarding the elemental distribution, oxidation state and the local coordination. In the stack mode, a series of the spectral elemental composition maps are collected from a selected energy range, including the elements pre-edge, edge and post-edge regions. The acquired data were all processed by the aXis2000 software package (<http://unicorn.mcmaster.ca/aXis2000.html>).

4.2 Results

4.2.1 STEM

The STEM images for the calcined NiCoO/ γ -Al₂O₃, and NiFeO/ γ -Al₂O₃ samples are shown in Figures 1a and b, respectively. Darkfield TEM images revealed the formation of relatively large agglomerates of coalesced nanoparticles with an average size of ~20 nm (Figures SI. 1-2). As displayed in Figures 1a and b, the oxygen (blue) signal which originates from the oxide particles and alumina support is rather evenly distributed for both samples. For the NiCoO catalyst, both the nickel (green) and cobalt (violet) show a rather inhomogeneous dispersion throughout the sample and thus hint for variations in the Ni:Co ratios on the alumina support. In contrast to the NiCoO sample, the Ni in the NiFeO is homogeneously distributed while iron (red) is mainly confined to specific regions of the particle.

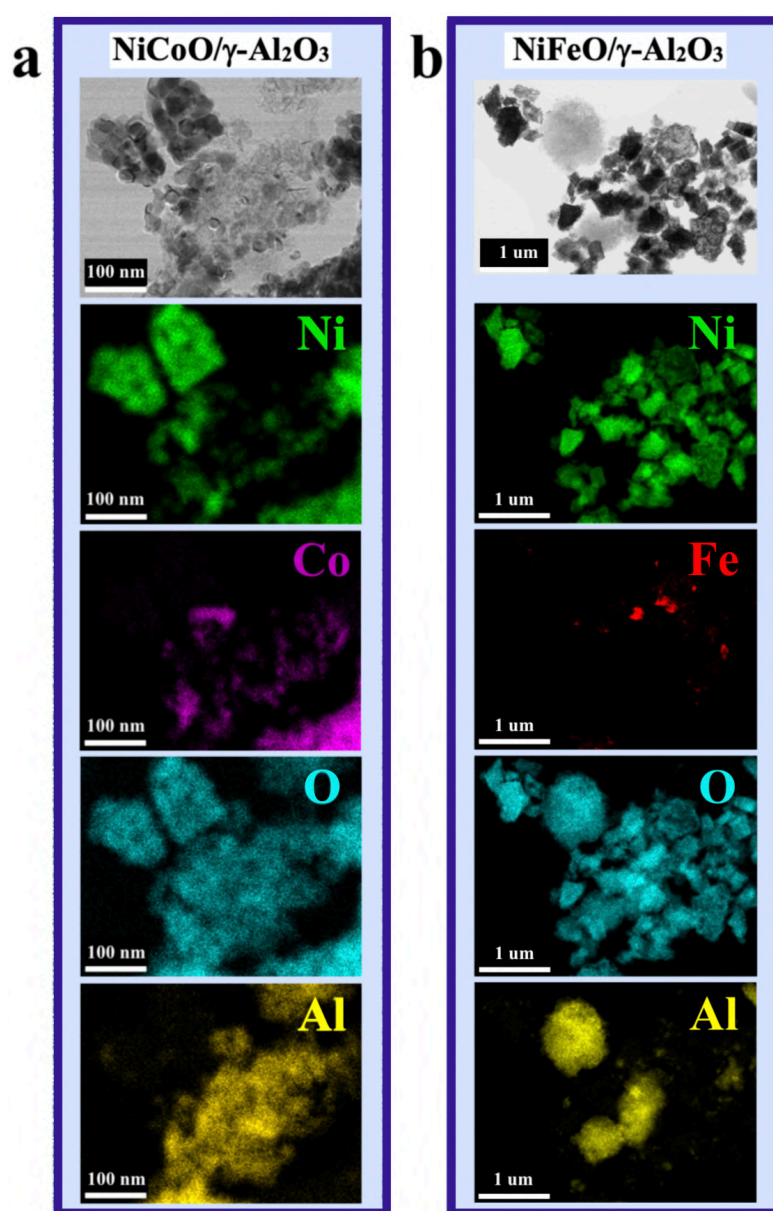


Figure 1: a) STEM-EDX images of the calcined NiCoO/ γ -Al₂O₃ DMR catalyst showing the morphology and elemental distributions in the sample. The Ni:Co ratio in this sample corresponds to 9:1, b) STEM-EDX images of the freshly calcined NiFeO/ γ -Al₂O₃ DMR catalyst. The Ni:Fe ratio correspond to 8.7:0.16. In the STEM-EDX images Ni is shown in green, cobalt in violet, iron in red, oxygen in blue and aluminium in yellow.

In addition, the TEM image in Figure SI. 2a also depicts the existence of irregular shaped structures on certain regions (highlighted in red) of the NiFeO agglomerates. These structures hint for relatively high concentrations of iron which were found to be confined to specific regions (Figure 1b). Finally, bulk EDX spectroscopy results revealed the cobalt and iron concentrations (Atomic %) in the NiCoO/ γ -Al₂O₃, and NiFeO/ γ -Al₂O₃ catalysts corresponds to 12% and 2%, respectively (Figure SI. 3).

4.2.2 TPR

The TPR profiles and DMR activities for the NiCoO/ γ -Al₂O₃ and NiO/ γ -Al₂O₃ catalysts are reported in an earlier study [15,19]. TPR data are used to study the reduction behavior of the metal oxides and conversion to their active/metallic states. The TPR profile of the NiCoO/ γ -Al₂O₃ catalyst (red profile) in Figure 2 shows two distinct reduction peaks at 260 and 325 °C where the first peak at 260 °C is assigned to the reduction of Co³⁺ → Co²⁺ (in Co₃O₄) while the peak at 325 °C is ascribed to the reduction of Co²⁺ and Ni²⁺ oxides to their respective metallic species (Figure 2) [15,27-30]. For the NiFeO/ γ -Al₂O₃ catalyst (blue profile), the TPR profile shows a rather different reduction behavior when compared to the NiCoO sample. The profile shows two reduction peaks at 314 and 344 °C that are assigned to the reduction of Ni- and Fe oxides, respectively [31-33]. The TPR profiles also revealed that full reduction of the metal oxides in NiFeO and NiCoO occurs at 385 and 400 °C, respectively.

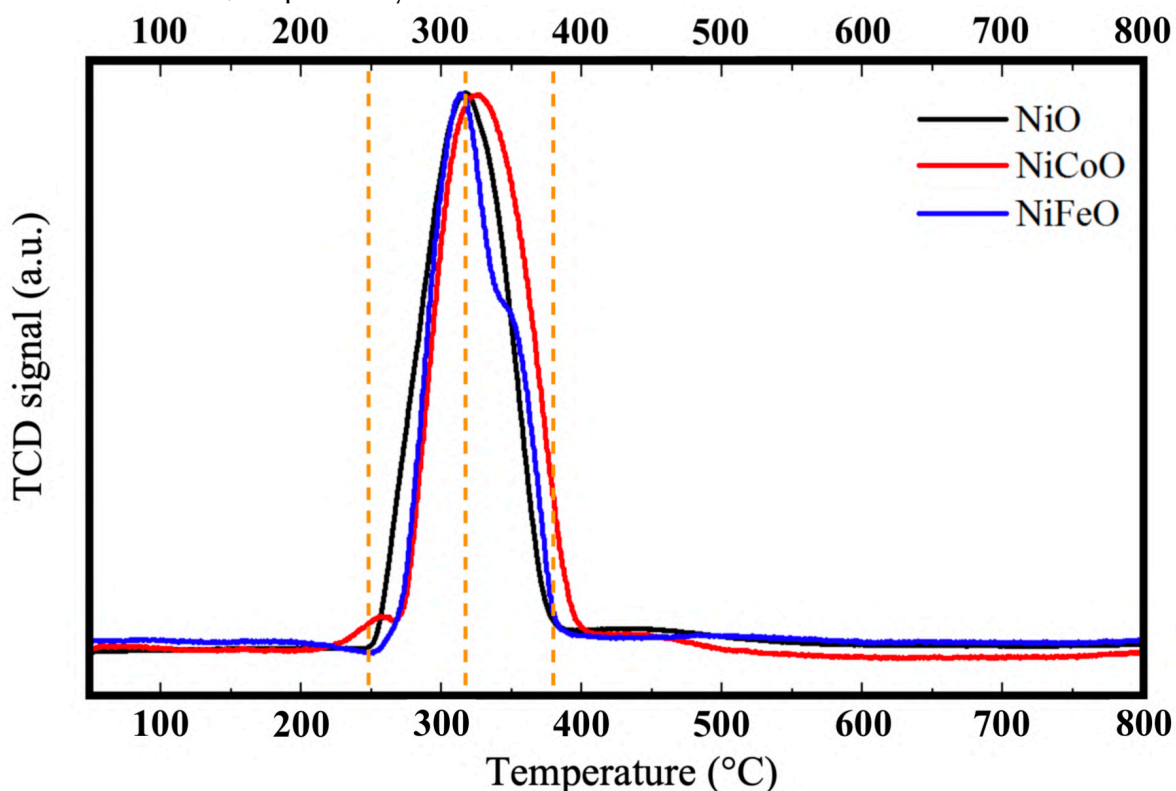


Figure 2: TPR profiles for the NiO/ γ -Al₂O₃, NiCoO/ γ -Al₂O₃ and NiFeO/ γ -Al₂O₃ DMR catalysts indicated in black, red, and blue, respectively. The reduction profile for the NiFeO/ γ -Al₂O₃ sample shows the reduction at relatively lower temperatures when compared to NiCoO/ γ -Al₂O₃ sample.

Based on the different reduction temperatures for the NiFeO, NiCoO, and NiO we note that in contrast to the Co case, Fe is promoting the reduction of Ni oxides at relatively lower temperatures. These results are also in agreement with an earlier DMR study [34].

4.2.3 Activity tests

For the activity experiments, the samples were firstly activated by reduction in a dynamic flow of 10% H₂ in N₂ at 850 °C. Next, the DMR activity of the activated catalysts was determined under flow of the DMR gas-mixture (7% CH₄ & 9.5% CO₂ in N₂) at 800°C for 15 hours. Figure 3 shows a lower initial conversion/yield values for the NiFeO/ γ -Al₂O₃ if compared to the NiCoO/ γ -Al₂O₃ sample (Chapter 2 Figure SI.6). In addition, the lower initial deactivation rate for the NiFeO suggests that it is less susceptible to coking and is more stable if compared to the NiCoO. The activity data reveal that the activities of both bimetallic NiCoO and NiFeO are superior to their monometallic counterparts (Chapter 3 Figure 3, [19,35]). Further, the conversion/yield values for all three catalysts stabilize following the exposure to DMR conditions for 15 hours (Table SI. 1). These results suggest that the introduction of a late transition metal promotor to the Ni-based DMR catalyst improves the activity dramatically and indirectly suppresses the reaction pathways that lead to coke formation and catalyst deactivation.

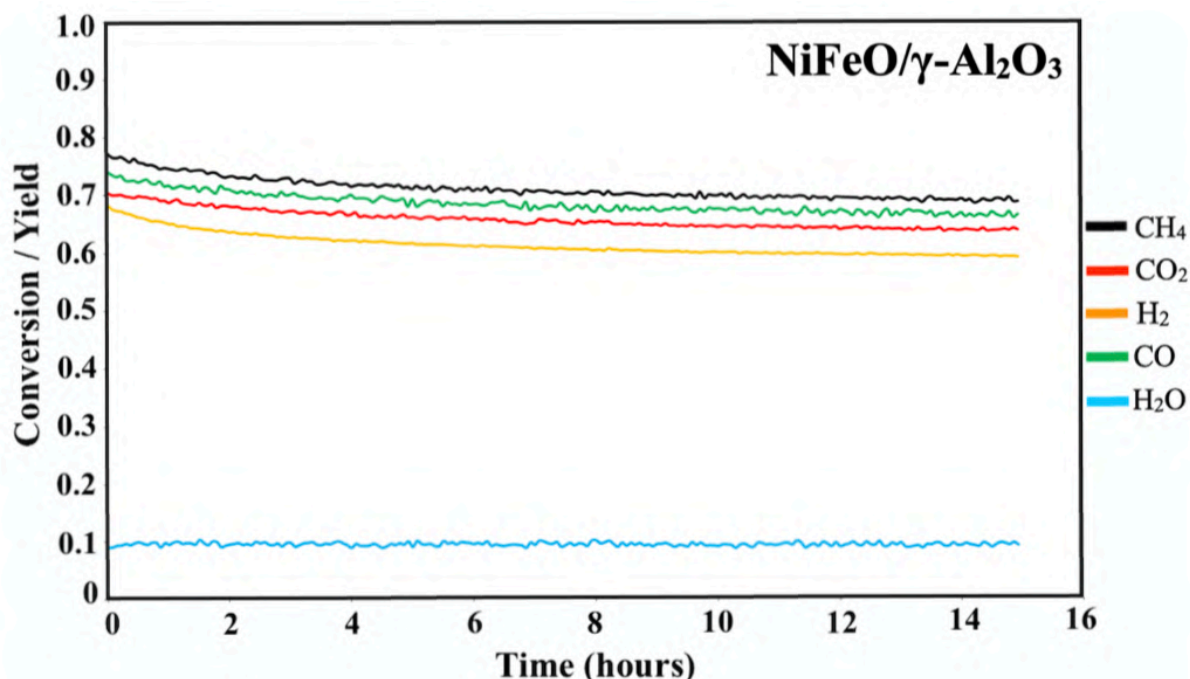


Figure 3: DMR activity data for the NiFeO/ γ -Al₂O₃ DMR catalysts. Preceding the activity tests the catalysts were activated by treating them for 30 minutes under 10% H₂ in N₂ with a flowrate of 100 mL/min. The DMR experiments were performed for 15 hours at 800 °C under 7% CH₄ and 9.5% CO₂ in N₂ and a flow rate of 490 mL/min.

Next, nitrogen physisorption measurements for the NiCoO/ γ -Al₂O₃, NiFeO/ γ -Al₂O₃ and NiO/ γ -Al₂O₃ catalysts revealed a similar surface area, pore volume and pore diameter for the catalysts (Figure SI. 4 and Table SI. 2).

4.2.4 In situ STXM

For the in-situ STXM experiments, STXM spectral elemental maps from relatively thin NiCoO/ γ -Al₂O₃ and NiFeO/ γ -Al₂O₃ DMR particles were collected for the I: freshly calcined, II: during reductive activation with 5% H₂ in Ar, and III: under DMR reaction conditions 7% CH₄, 9.5% CO₂ in N₂ gas-mixture (Figure 4). In addition, Figures SI. 5-20 show the L₃-edge spectral elemental maps for the: I) Ni and Co in the NiCoO/ γ -Al₂O₃, II) Ni, Fe for the NiFeO/ γ -Al₂O₃ and III) Ni in the NiO / γ -Al₂O₃ particles during the various stages of the in-situ STXM experiment.

The RGB composition maps for the freshly calcined NiCoO/ γ -Al₂O₃ and NiFeO/ γ -Al₂O₃ particles display a rather different elemental distribution as shown in Figures 4a,d respectively. In the case of the NiCoO particle, we note that the elemental distributions for nickel (in green) and cobalt (in violet) are not equal over the selected particles (Figure SI. 5). Based on these data there are Ni-rich domains and the Ni:Co ratios varies through the majority of the particle. In contrast, for the NiFeO sample the Fe (in red) concentration is the highest in the center whereas the higher Ni (in blue) ratio is encountered in the outer layer, Figure SI. 10. The STXM data for both calcined samples are also in agreement with the corresponding STEM-EDX results (Figure 1).

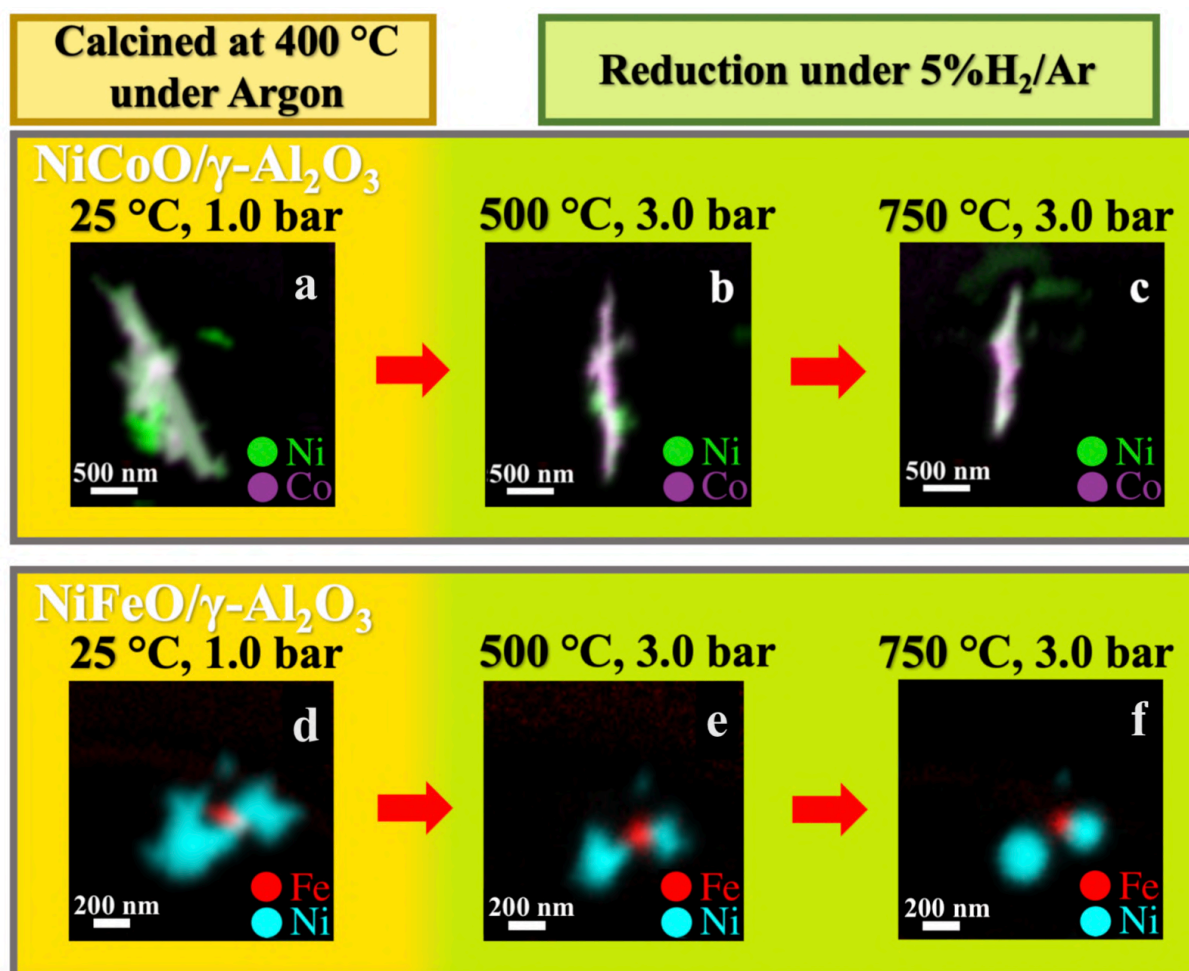


Figure 4: RGB elemental composition maps of the NiCoO/ γ -Al₂O₃ and NiFeO/ γ -Al₂O₃ DMR catalyst showing the distribution of Ni, Co, or Fe: a, d) in the calcined particles; b, e) following the reduction step at 500 °C and under 5% H₂ in Ar flow; c, f) after exposure to reducing conditions at 750 °C under 5% H₂ in Ar flow.

Based on the comparison of the collected Co, Ni and Fe L₃-edge XAS (black spectra in Figures 5 and 6) for the calcined samples with relevant oxides reference spectra, the formation of NiO (Ni²⁺ O_h), Co₃O₄ (1xCo²⁺ T_d and 2xCo³⁺ O_h) for the NiCoO/γ-Al₂O₃ sample and NiO (Ni²⁺ O_h), α-Fe₂O₃ (hematite) species for the NiFeO/γ-Al₂O₃ is confirmed [15, 36-38]. Next, to follow the changes in both the morphology and electronic structure under activation conditions the samples were reduced by gradually heating from 25 to 750 °C under 5% H₂ in Ar flow. Following the reduction at 500 °C a significant decrease in particle size for both NiCo and NiFe is evident which is associated with the removal of oxygen from the oxides and alumina support (Figure 4b,e). In addition, Figure SI. 17 confirms a decrease in particle at 450 °C for the monometallic Ni-based catalysts. In agreement with the TPR data (Figure 2), the Ni and Co L-edge absorption spectra in Figure 5 (shown in blue) confirm the full reduction of Ni and Co oxides in the NiCoO to their metallic species at 500 °C. On the contrary, following the reduction of NiFeO sample at 500 °C the Ni is fully reduced whereas the Fe is only partially reduced (Figure 6). Further, by increasing the temperature to 750 °C, the Fe L-edge spectrum for the NiFe sample confirms the full reduction of the Fe into the metallic state (Figure 6). The L-edge spectra (green) in Figure 5 shows that by increasing the temperature to 750 °C the Ni and Co L₃-edges in the NiCo sample do not shift with respect to the blue spectra collected at 500 °C. The RGB spectral elemental maps collected for the NiCo sample at 750 °C displays the formation of a segregated structure with a Ni-rich surface and NiCo alloy center (Figure 4c). This observation is consistent with our previous study (Chapter 2, [15]). In contrast to the NiCo, for NiFe catalyst, the nickel appears to prefer the formation of a spherical geometry while the iron has a not well-defined shape and is attached to the nickel particle and shows no sign of a segregated structure (Figure 4f).

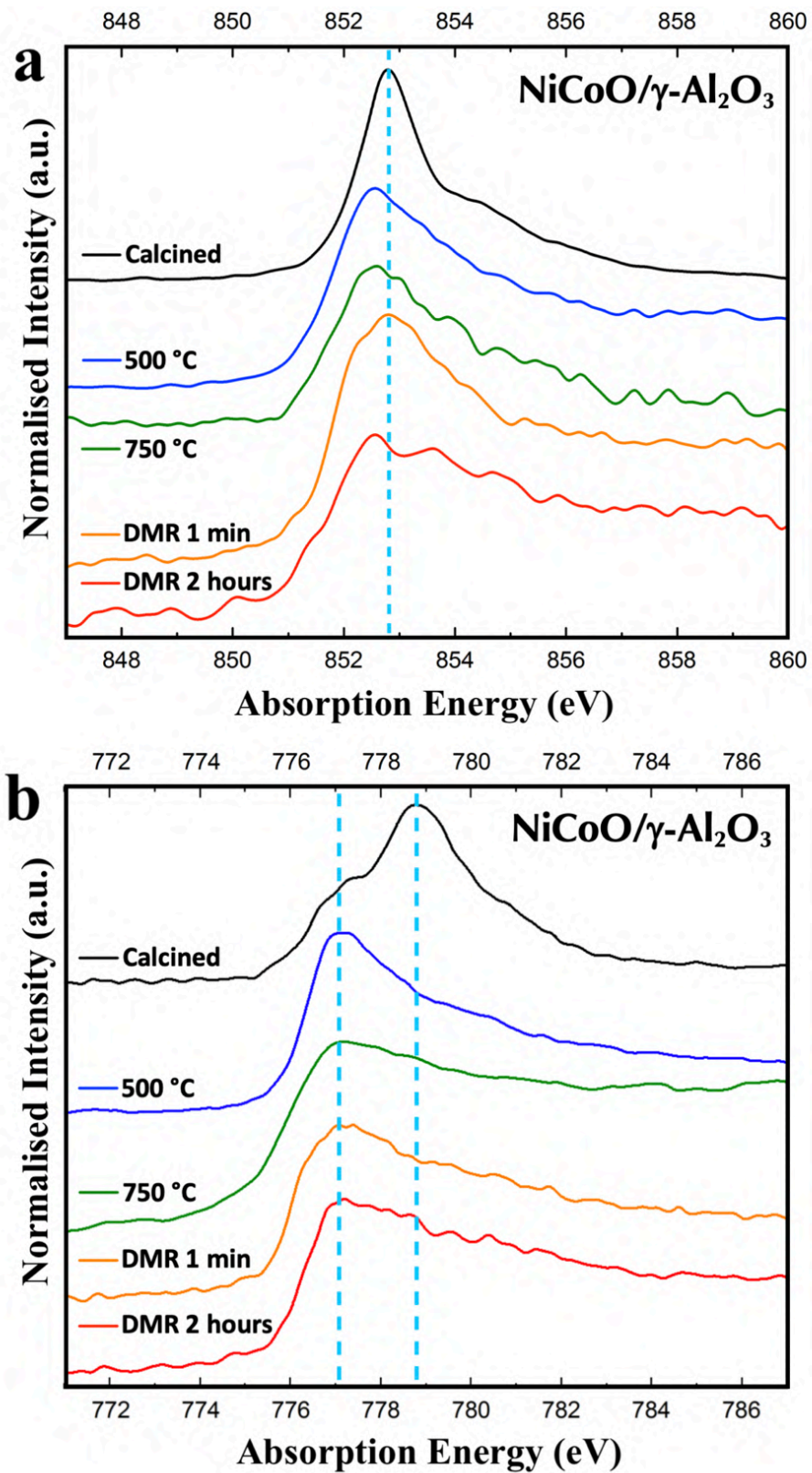


Figure 5: a) Ni L₃-edge XAS spectra of the NiCoO/ γ -Al₂O₃ particle collected under ambient, reducing, and DMR conditions. b) Co L₃-edge XAS spectra of the NiCoO/ γ -Al₂O₃ particle collected under ambient, reducing and DMR conditions.

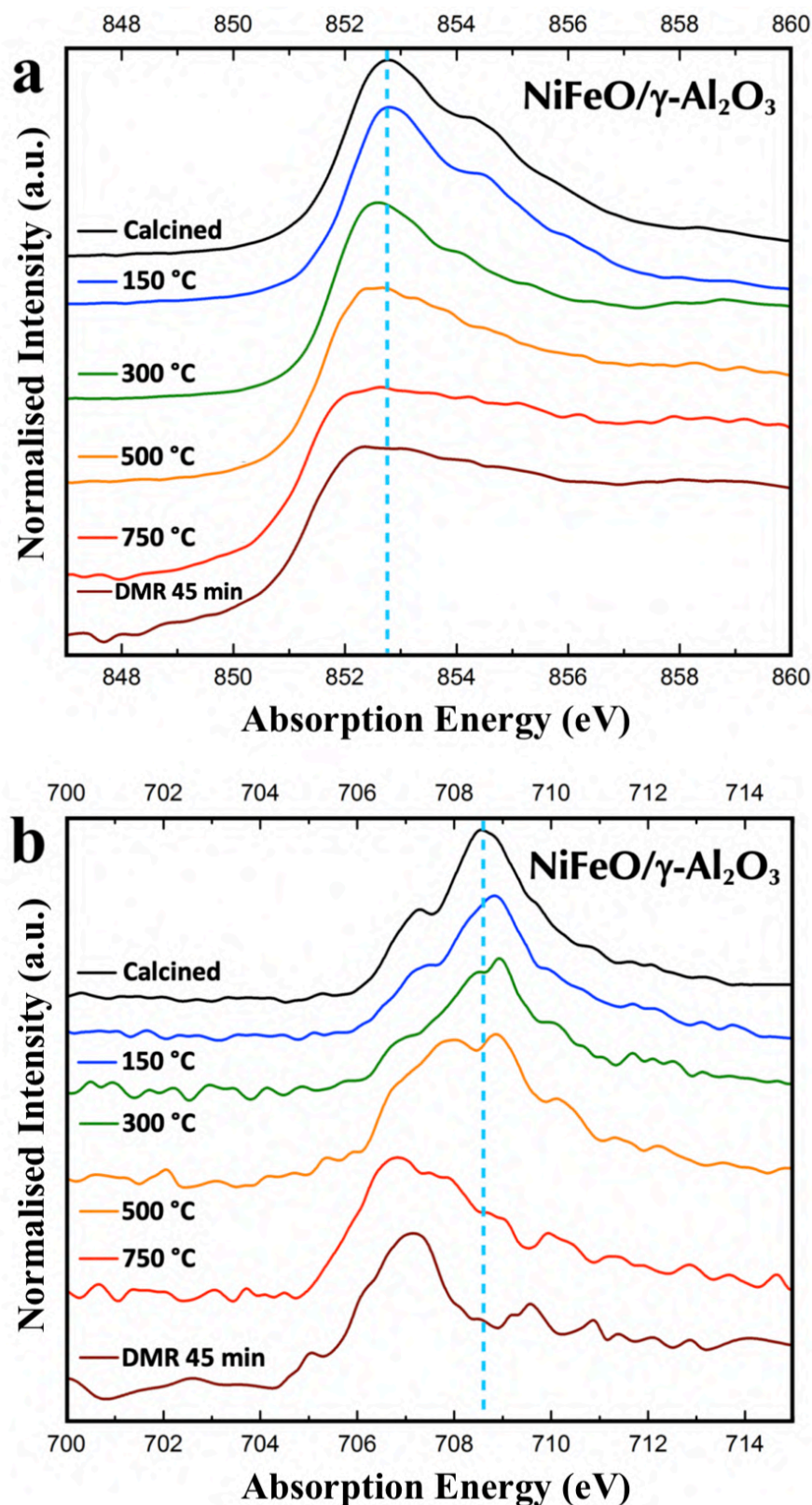


Figure 6: a) Ni L₃-edge XAS spectra of the NiFeO/ γ -Al₂O₃ particle collected under ambient, reduction, and DMR conditions. b) Fe L₃-edge XAS spectra of the NiFeO/ γ -Al₂O₃ particle collected under ambient, reducing, and DMR conditions.

Finally, upon exposing the reduced NiCo DMR catalysts to DMR conditions (7% CH₄, 9.5% CO₂ diluted in N₂) the Ni and Co L₃-edges remain analogous to the spectra of the fully reduced samples and confirms the presence and the significance of the metallic Co

and Ni for the DMR process (Figure 5-red). The RGB elemental composition maps for the NiCo particle under DMR conditions (Figure 7b) displays a rather less homogeneous Ni distribution for certain regions on the surface. This is in agreement with the results from our previous study which illustrated that following the DMR reaction, the Ni-rich outer shell has been fractured by forming Ni-rich branches. On the other hand, for the NiFeO the morphology of the particles and elemental distributions are altered after exposure to DMR conditions (Figure 7d and SI. 13). Moreover, based on the Ni and Fe L₃-edges of the NiFeO sample it is evident that after exposure to the DMR conditions for 45 minutes, the Ni remains fully reduced whereas the Fe is slightly oxidized (Figure 6). This observation is consistent with the study of Kim et al. where it was shown that under reforming conditions the Fe partially oxidizes to FeO [16]. Finally, Figure SI. 20 reveals that the morphology of the NiO / γ -Al₂O₃ particles also changes after exposure to DMR conditions. These data illustrate that the size of the Ni particles has increased which might be attributed to coke formation of the particle surface.

We believe that the formation of Ni-rich branches for the NiCoO catalyst under DMR conditions is directly related to catalyst deactivation. This is consistent with the study of Takanahe et al. where it was shown that pure Ni surfaces suffer from coking due to the low oxophilicity of Ni [39].

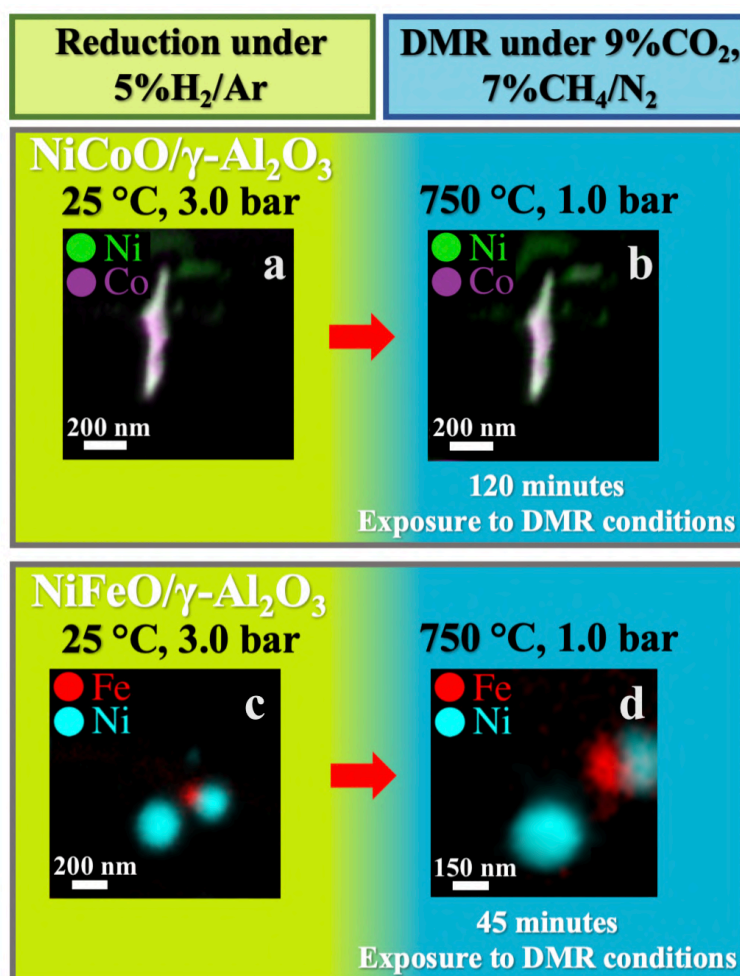


Figure 7: RGB elemental composition maps of the NiCoO/γ-Al₂O₃ and NiFeO/γ-Al₂O₃ DMR catalyst a,c) after being exposed to reduction conditions at 750 °C under 5% H₂ in Ar flow. b,d) after exposing the NiCoO/γ-Al₂O₃ and NiFeO/γ-Al₂O₃ DMR catalyst to DMR conditions for 120 minutes and 45 minutes respectively.

4.3 Conclusions

DMR activity data displayed a superior activity for the NiCoO/ γ -Al₂O₃ catalysts when compared to either the NiO/ γ -Al₂O₃ and NiFeO/ γ -Al₂O₃ catalysts. Both STEM-EDX and STXM elemental maps for the freshly calcined catalysts verified an inhomogeneous distribution of Ni, Co in NiCoO and Fe in NiFeO on the γ -Al₂O₃ support. In contrast, Ni in the NiFeO catalyst shows a rather homogeneous dispersion on the particles. TPR data illustrated that in contrast to the Co in the NiCoO, Fe in the NiFeO is promoting the reduction of Ni oxides at relatively lower temperatures. Further, for the NiCo catalyst, the formation of a segregated structure with Co migrating to the center of the particle and the formation of a nickel rich surface was evident under activation/reduction conditions. Based on the in-situ STXM spectral elemental maps, this structure was also largely conserved during DMR reaction. Interestingly, for the NiFe system the formation of the segregated structure during activation was not encountered. In-situ STXM data for the NiFe displayed the formation of spherical Ni and Fe particles during the activation/reduction process and was maintained under DMR conditions.

Acknowledgements

The Max Planck Society and the European Research Council under the European Union's Seventh Framework Programme (FP/2007-2013) ERC Grant Agreement No. 615414 (S.D.) and NFFA EU grant (H2020). The PolLux end station was financed by the German Ministerium für Bildung und Forschung (BMBF) through contracts 05KS4WE1/6 and 05KS7WE1. The authors thank Christian W. Lehmann from the Max-Planck-Institut für Kohlenforschung for supporting the STEM measurements.

References

- [1] Liu, Z.; Grinter, D.; Lustemberg, P.; Nguyen-Phan, T.; Zhou, Y.; Luo, S.; Waluyo, I.; Crumlin, E.; Stacchiola, D.; Zhou, J.; Carrasco, J.; Busnengo, H.; Ganduglia-Pirovano, M.; Senanayake, S.; Rodriguez, J. Dry Reforming Of Methane On A Highly-Active Ni-CeO₂ Catalyst: Effects Of Metal-Support Interactions On C-H Bond Breaking. *Angewandte Chemie International Edition* **2016**, *55* (26), 7455-7459.
- [2] Aramouni, N.; Touma, J.; Tarboush, B.; Zeaiter, J.; Ahmad, M. Catalyst Design For Dry Reforming Of Methane: Analysis Review. *Renewable and Sustainable Energy Reviews* **2018**, *82*, 2570-2585.
- [3] Alipour, Z.; Rezaei, M.; Meshkani, F. Effect Of Alkaline Earth Promoters (MgO, CaO, And BaO) On The Activity And Coke Formation Of Ni Catalysts Supported On Nanocrystalline Al₂O₃ In Dry Reforming Of Methane. *Journal of Industrial and Engineering Chemistry* **2014**, *20* (5), 2858-2863.
- [4] Li, X.; Li, D.; Tian, H.; Zeng, L.; Zhao, Z.; Gong, J. Dry Reforming Of Methane Over Ni/La₂O₃ Nanorod Catalysts With Stabilized Ni Nanoparticles. *Applied Catalysis B: Environmental* **2017**, *202*, 683-694.
- [5] Usman, M.; Wan Daud, W.; Abbas, H. Dry Reforming Of Methane: Influence Of Process Parameters-A Review. *Renewable and Sustainable Energy Reviews* **2015**, *45*, 710-744.
- [6] Özkara-Aydinoğlu, Ş.; Aksoylu, A. CO₂ Reforming Of Methane Over Pt-Ni/Al₂O₃ Catalysts: Effects Of Catalyst Composition, And Water And Oxygen Addition To The Feed. *International Journal of Hydrogen Energy* **2011**, *36* (4), 2950-2959.
- [7] Bradford, M.; Vannice, M. CO₂ reforming Of CH₄ over Supported Pt Catalysts. *Journal of Catalysis* **1998**, *173* (1), 157-171.
- [8] Dębek, R.; Zubek, K.; Motak, M.; Da Costa, P.; Grzybek, T. Effect Of Nickel Incorporation Into Hydrotalcite-Based Catalyst Systems For Dry Reforming Of Methane. *Research on Chemical Intermediates* **2015**, *41* (12), 9485-9495.
- [9] Muraza, O.; Galadima, A. A Review On Coke Management During Dry Reforming Of Methane. *International Journal of Energy Research* **2015**, *39* (9), 1196-1216.
- [10] Carencio, S. Describing Inorganic Nanoparticles In The Context Of Surface Reactivity And Catalysis. *Chemical Communications* **2018**, *54* (50), 6719-6727.
- [11] Pakhare, D.; Spivey, J. A Review Of Dry (CO₂) Reforming Of Methane Over Noble Metal Catalysts. *Chem. Soc. Rev.* **2014**, *43* (22), 7813-7837.

- [12] Djinović, P.; Osojnik Črnivec, I.; Erjavec, B.; Pintar, A. Influence Of Active Metal Loading And Oxygen Mobility On Coke-Free Dry Reforming Of Ni-Co Bimetallic Catalysts. *Applied Catalysis B: Environmental* **2012**, *125*, 259-270.
- [13] Zhang, J.; Wang, H.; Dalai, A. Development Of Stable Bimetallic Catalysts For Carbon Dioxide Reforming Of Methane. *Journal of Catalysis* **2007**, *249* (2), 300-310.
- [14] Rahemi, N.; Haghighi, M.; Babaluo, A.; Jafari, M.; Khorram, S. Non-Thermal Plasma Assisted Synthesis And Physicochemical Characterizations Of Co And Cu Doped Ni/Al₂O₃ Nanocatalysts Used For Dry Reforming Of Methane. *International Journal of Hydrogen Energy* **2013**, *38* (36), 16048-16061.
- [15] Beheshti Askari, A.; al Samarai, M.; Morana, B.; Tillmann, L.; Pfänder, N.; Wandzilak, A.; Watts, B.; Belkhou, R.; Muhler, M.; DeBeer, S. In-situ X-ray Microscopy reveals particle dynamics in a NiCo dry methane reforming catalyst under operating conditions. *ACS Catalysis* **2020**, **submitted**.
- [16] Kim, S.; Abdala, P.; Margossian, T.; Hosseini, D.; Foppa, L.; Armutlulu, A.; van Beek, W.; Comas-Vives, A.; Copéret, C.; Müller, C. Cooperativity And Dynamics Increase The Performance Of NiFe Dry Reforming Catalysts. *Journal of the American Chemical Society* **2017**, *139* (5), 1937-1949.
- [17] Wang, L.; Li, D.; Koike, M.; Koso, S.; Nakagawa, Y.; Xu, Y.; Tomishige, K. Catalytic Performance And Characterization Of Ni-Fe Catalysts For The Steam Reforming Of Tar From Biomass Pyrolysis To Synthesis Gas. *Applied Catalysis A: General* **2011**, *392* (1-2), 248-255.
- [18] Wang, L.; Chen, J.; Watanabe, H.; Xu, Y.; Tamura, M.; Nakagawa, Y.; Tomishige, K. Catalytic Performance And Characterization Of Co-Fe Bcc Alloy Nanoparticles Prepared From Hydrotalcite-Like Precursors In The Steam Gasification Of Biomass-Derived Tar. *Applied Catalysis B: Environmental* **2014**, *160-161*, 701-715.
- [19] Beheshti Askari, A.; al Samarai, M.; Hiraoka, N.; Ishii, H.; Tillmann, L.; Muhler, M.; DeBeer, S. In situ X-ray emission and high-resolution X-ray absorption studies of Ni-based Bimetallic Dry Methane Reforming Catalyst., **2020**, **In preparation**.
- [20] Al Samarai, M.; Hahn, A.; Beheshti Askari, A.; Cui, Y.; Yamazoe, K.; Miyawaki, J.; Harada, Y.; Rüdiger, O.; DeBeer, S. Elucidation Of Structure–Activity Correlations In A Nickel Manganese Oxide Oxygen Evolution Reaction Catalyst By Operando Ni L-Edge X-Ray Absorption Spectroscopy And 2P3d Resonant Inelastic X-Ray Scattering. *ACS Applied Materials & Interfaces* **2019**, *11* (42), 38595-38605.
- [21] Menezes, P.; Indra, A.; Levy, O.; Kailasam, K.; Gutkin, V.; Pfrommer, J.; Driess, M. Using Nickel Manganese Oxide Catalysts For Efficient Water Oxidation. *Chemical Communications* **2015**, *51* (24), 5005-5008.

- [22] Tillmann, L.; Schulwitz, J.; van Veen, A.; Muhler, M. Dry Reforming Of Methane At High Pressure In A Fixed-Bed Reactor With Axial Temperature Profile Determination. *Catalysis Letters* **2018**, *148* (8), 2256-2262.
- [23] Raabe, J.; Tzvetkov, G.; Flechsig, U.; Böge, M.; Jaggi, A.; Sarafimov, B.; Vernooij, M.; Huthwelker, T.; Ade, H.; Kilcoyne, D.; Tyliszczak, T.; Fink, R.; Quitmann, C. Pollux: A New Facility For Soft X-Ray Spectromicroscopy At The Swiss Light Source. *Review of Scientific Instruments* **2008**, *79* (11), 113704.
- [24] Vendelbo, S.; Elkjær, C.; Falsig, H.; Puspitasari, I.; Dona, P.; Mele, L.; Morana, B.; Nelissen, B.; van Rijn, R.; Creemer, J.; Kooyman, P.; Helveg, S. Visualization Of Oscillatory Behaviour Of Pt Nanoparticles Catalysing CO Oxidation. *Nature Materials* **2014**, *13* (9), 884-890.
- [25] Bremmer, G.; Zacharaki, E.; Sjøstad, A.; Navarro, V.; Frenken, J.; Kooyman, P. In Situ TEM Observation Of The Boudouard Reaction: Multi-Layered Graphene Formation From CO On Cobalt Nanoparticles At Atmospheric Pressure. *Faraday Discussions* **2017**, *197*, 337-351.
- [26] Creemer, J.; Santagata, F.; Morana, B.; Mele, L.; Alan, T.; Iervolino, E.; Pandraud, G.; Sarro, P. An All-In-One Nanoreactor For High-Resolution Microscopy On Nanomaterials At High Pressures. *IEEE 24th International Conference on Micro Electro Mechanical Systems* **2011**.
- [27] M. Cesário, C. Gennequin, *Catalytic Materials For Hydrogen Production And Electro-Oxidation Reactions. Frontiers In Ceramic Science Volume 2*, Bentham Science Publishers, **2018**, p140.
- [28] Wang, D.; Li, S.; Du, Y.; Wu, X.; Chen, Y. Self-Templating Synthesis Of 3D Hierarchical NiCo₂O₄@NiO Nanocage From Hydrotalcites For Toluene Oxidation. *Catalysts* **2019**, *9* (4), 352.
- [29] Zhang, X.; Liu, J.; Jing, Y.; Xie, Y. Support Effects On The Catalytic Behavior Of NiO/Al₂O₃ For Oxidative Dehydrogenation Of Ethane To Ethylene. *Applied Catalysis A: General* **2003**, *240* (1-2), 143-150.
- [30] Nyathi, T.; Fischer, N.; York, A.; Claeys, M. Effect Of Crystallite Size On The Performance And Phase Transformation Of Co₃O₄/Al₂O₃ Catalysts During CO-Prox – An In Situ Study. *Faraday Discussions* **2017**, *197*, 269-285.
- [31] Li, X.; Li, K.; Peng, Y.; Li, X.; Zhang, Y.; Wang, D.; Chen, J.; Li, J. Interaction Of Phosphorus With A FeTiOx Catalyst For Selective Catalytic Reduction Of NO_x With NH₃: Influence On Surface Acidity And SCR Mechanism. *Chemical Engineering Journal* **2018**, *347*, 173-183.
- [32] Jiang, J.; Pan, H.; Sun, G.; Ye, Q.; Shao, Z.; Shi, Y. Promotion Of Ni/H-BEA By Fe For NO_x reduction With Propane In A Lean-Burn Condition. *Energy & Fuels* **2011**, *25* (10), 4377-4383.

- [33] Wang, R.; Wu, X.; Zou, C.; Li, X.; Du, Y. NO_x Removal By Selective Catalytic Reduction With Ammonia Over A Hydrotalcite-Derived NiFe Mixed Oxide. *Catalysts* **2018**, *8* (9), 384.
- [34] Meng, F.; Zhong, P.; Li, Z.; Cui, X.; Zheng, H. Surface Structure And Catalytic Performance Of Ni-Fe Catalyst For Low-Temperature CO Hydrogenation. *Journal of Chemistry* **2014**, *2014*, 1-7.
- [35] Horlyck, J.; Lawrey, C.; Lovell, E.; Amal, R.; Scott, J. Elucidating The Impact Of Ni And Co Loading On The Selectivity Of Bimetallic NiCo Catalysts For Dry Reforming Of Methane. *Chemical Engineering Journal* **2018**, *352*, 572-580.
- [36] You, X.; Wang, X.; Ma, Y.; Liu, J.; Liu, W.; Xu, X.; Peng, H.; Li, C.; Zhou, W.; Yuan, P.; Chen, X. Ni-Co/Al₂O₃ bimetallic Catalysts For CH₄ steam Reforming: Elucidating The Role Of Co For Improving Coke Resistance. *ChemCatChem* **2014**, *6* (12), 3377-3386.
- [37] Wang, H.; Hung, S.; Chen, H.; Chan, T.; Chen, H.; Liu, B. In Operando Identification Of Geometrical-Site-Dependent Water Oxidation Activity Of Spinel Co₃O₄. *Journal of the American Chemical Society* **2015**, *138* (1), 36-39.
- [38] Shen, S.; Zhou, J.; Dong, C.; Hu, Y.; Tseng, E.; Guo, P.; Guo, L.; Mao, S. Surface Engineered Doping Of Hematite Nanorod Arrays For Improved Photoelectrochemical Water Splitting. *Scientific Reports* **2014**, *4* (1).
- [39] AlSabban, B.; Falivene, L.; Kozlov, S.; Aguilar-Tapia, A.; Ould-Chikh, S.; Hazemann, J.; Cavallo, L.; Basset, J.; Takanebe, K. In-Operando Elucidation Of Bimetallic Coni Nanoparticles During High-Temperature CH₄/CO₂ Reaction. *Applied Catalysis B: Environmental* **2017**, *213*, 177-189.

4.4 Supporting Information

The promoting effect of Co vs. Fe on the activation and catalytic activity of supported Ni-based bimetallic dry methane reforming catalysts

Abbas Beheshti Askari^(a), Mustafa al Samarai^(a), Bruno Morana^(b), Lukas Tillmann^(c), Norbert Pfänder^(a), Benjamin Watts^(d), Martin Muhler^{*(a, c)}, and Serena DeBeer^{*(a)}

(a) Max Planck Institute for Chemical Energy Conversion, Stiftstraße 34-36, D-45470 Mülheim an der Ruhr, Germany

(b) NanoInsight, Feldmannweg 17, 2628 CT Delft, The Netherlands

(c) Laboratory of Industrial Chemistry, Ruhr-University Bochum, Universitätsstraße 150, D-44801 Bochum, Germany

(d) Paul Scherrer Institute, 5332 Villigen PSI, Switzerland

Figure SI. 1

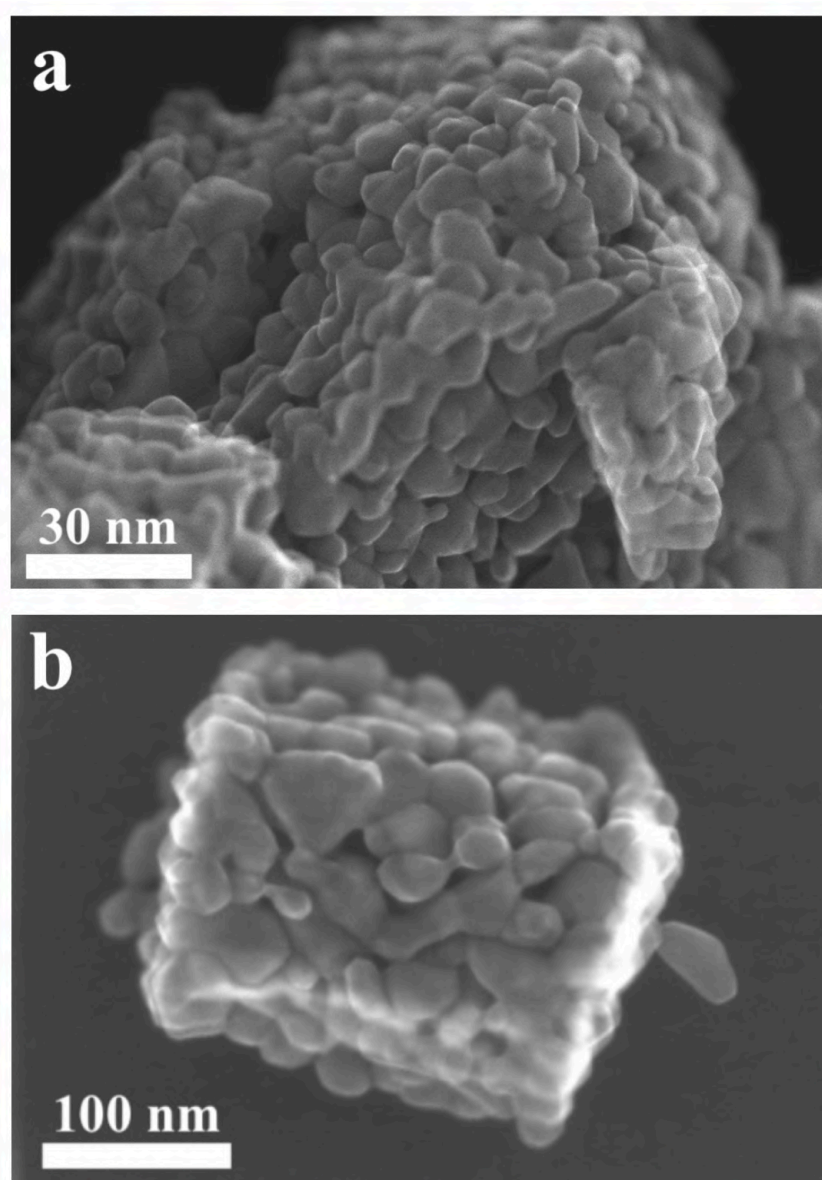


Figure SI. 1: a, b) Overview STEM image of the calcined NiCoO/γ-Al₂O₃ DMR catalyst. Both images illustrate that the catalyst is made of small particles that have coalesced and formed large agglomerates.

Figure SI. 2

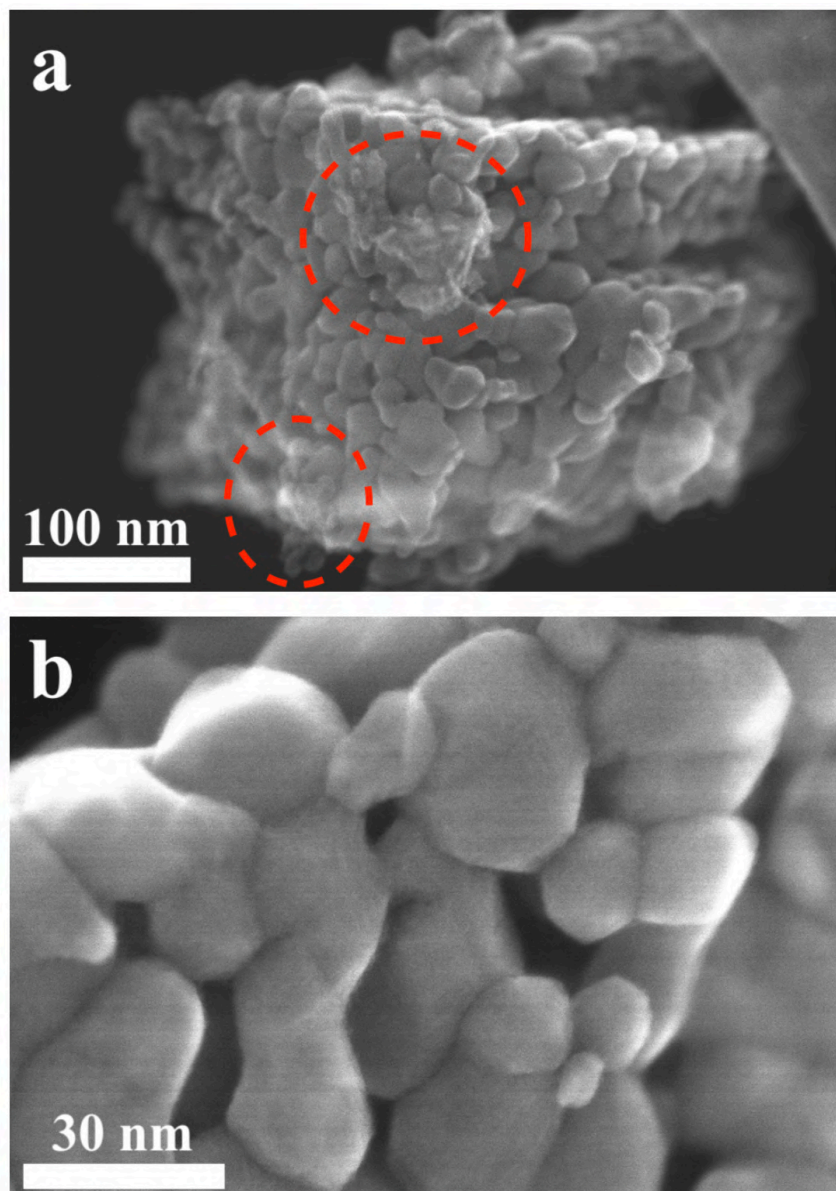


Figure SI. 2: a) Overview STEM image of the calcined NiFeO/ γ -Al₂O₃ DMR catalyst. This highlighted areas on the surface of this sample illustrate that most likely iron is located on the outer surface of the particles. b) The synthesised particles tend to form large agglomerates after the synthesis step.

Figure SI. 3

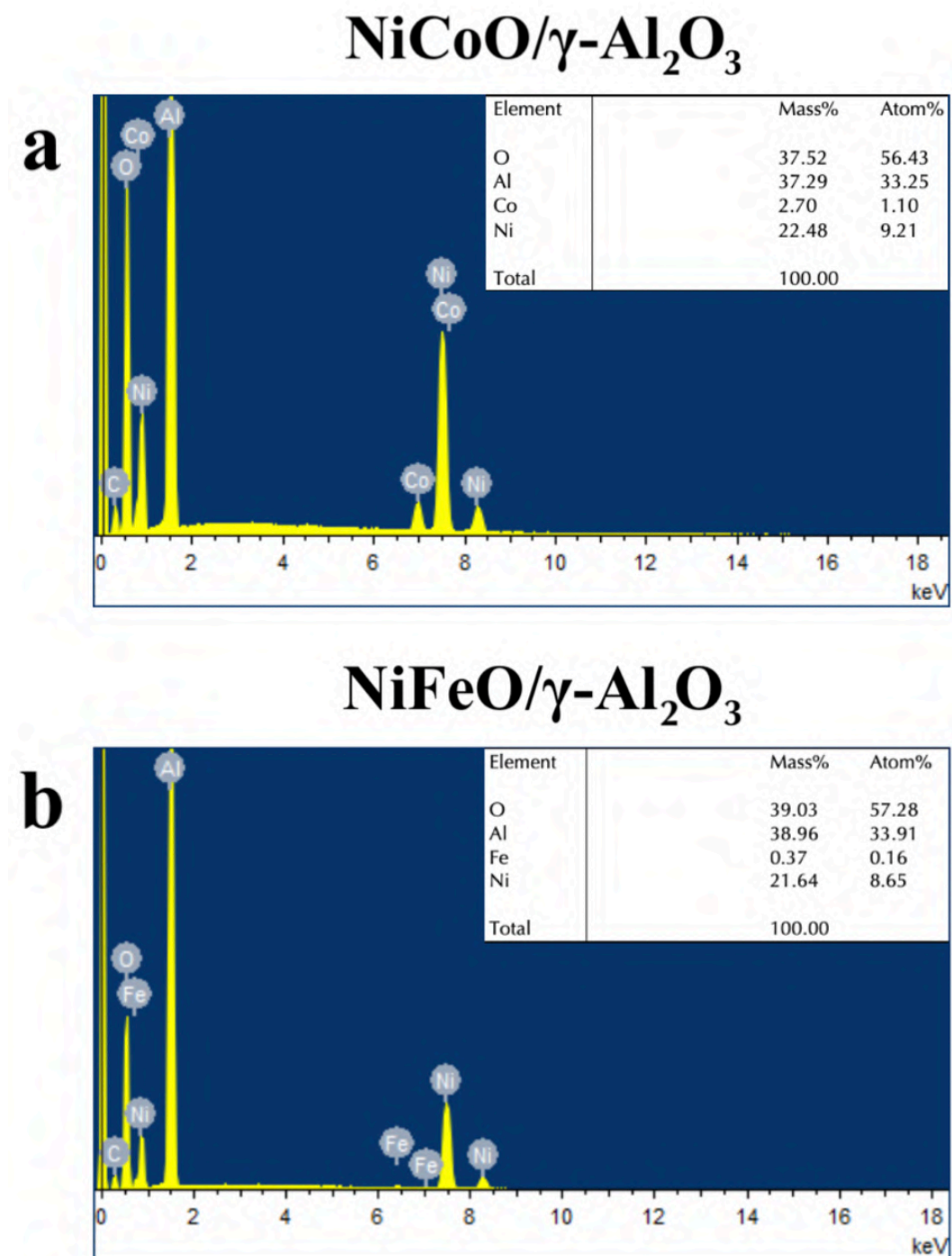


Figure SI. 3: a,b) Bulk EDX measurement for the NiCoO/ γ -Al₂O₃ and NiFeO/ γ -Al₂O₃ samples. These result show that the Ni:Co and Ni:Fe in the related samples corresponds to approx. 9.2:1.1 and 8.7:0.16.

Table SI. 1

| | NiO | NiCoO | NiFeO |
|-----------------------|-----|-------|-------|
| CH_4 Conversion (%) | 46 | 79 | 69 |
| CO_2 Conversion (%) | 44 | 71 | 64 |
| H_2 Yield (%) | 39 | 70 | 59 |
| CO Yield (%) | 44 | 73 | 66 |
| H_2O Yield (%) | 5 | 9 | 9 |

Table SI. 1: Conversion/Yield values for the NiO/ γ -Al₂O₃, NiCoO/ γ -Al₂O₃ and NiFeO/ γ -Al₂O₃ catalysts collected after exposure to DMR conditions for 15 hours.

Figure SI. 4

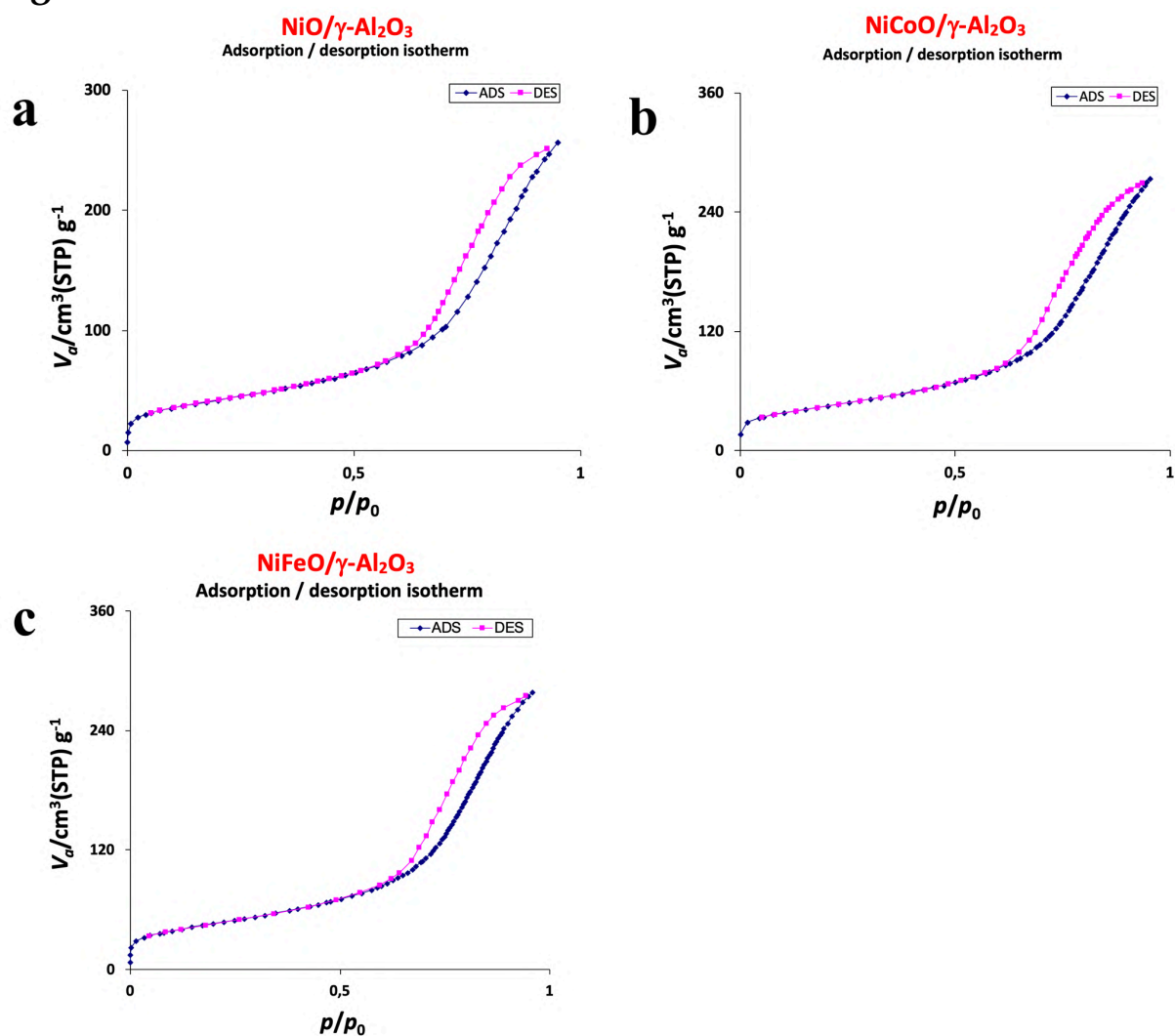


Figure SI. 4: Adsorption and Desorption isotherms for the a) NiO/ γ -Al₂O₃ b) NiCoO/ γ -Al₂O₃ and c) NiFeO/ γ -Al₂O₃ DMR catalysts.

Table SI. 2

| | NiO/ γ -Al ₂ O ₃ | NiCoO/ γ -Al ₂ O ₃ | NiFeO/ γ -Al ₂ O ₃ |
|--|---|---|---|
| V_m (cm ³ (STP) g ⁻¹) | 34.74 | 37.06 | 38.01 |
| $A_{s,BET}$ (m ² g ⁻¹) | 185.36 | 161.30 | 165.71 |
| C | 109.6 | 121.29 | 117.33 |
| Total Pore Volume (cm ³ g ⁻¹) | 0.40 | 0.42 | 0.43 |
| Average pore diameter (nm) | 10.51 | 10.50 | 10.40 |

Table SI. 2: BET surface area and porosity data collected for the NiO/ γ -Al₂O₃, NiCoO/ γ -Al₂O₃ and NiFeO/ γ -Al₂O₃ DMR catalysts.

Figure SI. 5

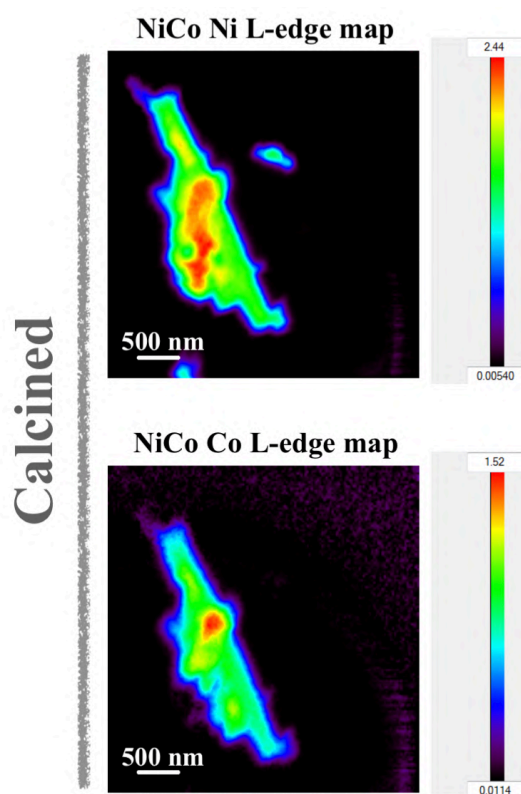


Figure SI. 5: Spectral elemental maps of Ni and Co for the calcined NiCoO/ γ -Al₂O₃ particle.

Figure SI. 6

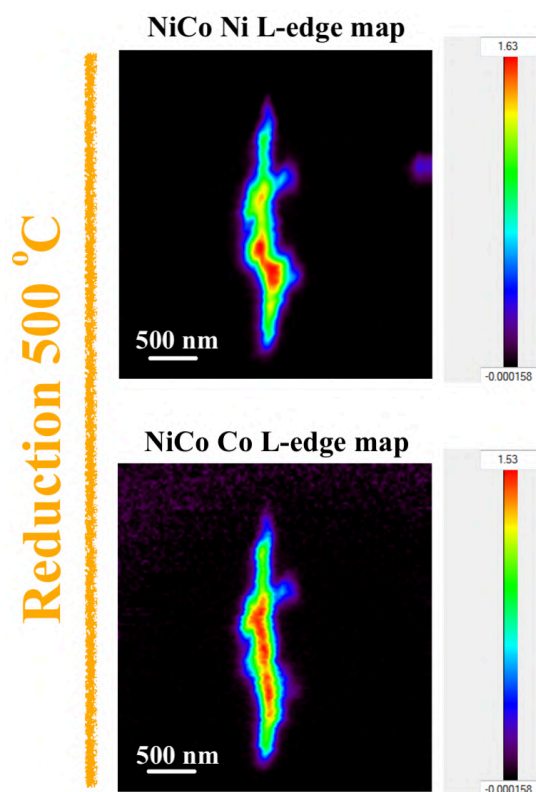


Figure SI. 6: Spectral elemental maps of Ni and Co for the NiCoO/ γ -Al₂O₃ particle reduced at 500 °C.

Figure SI. 7

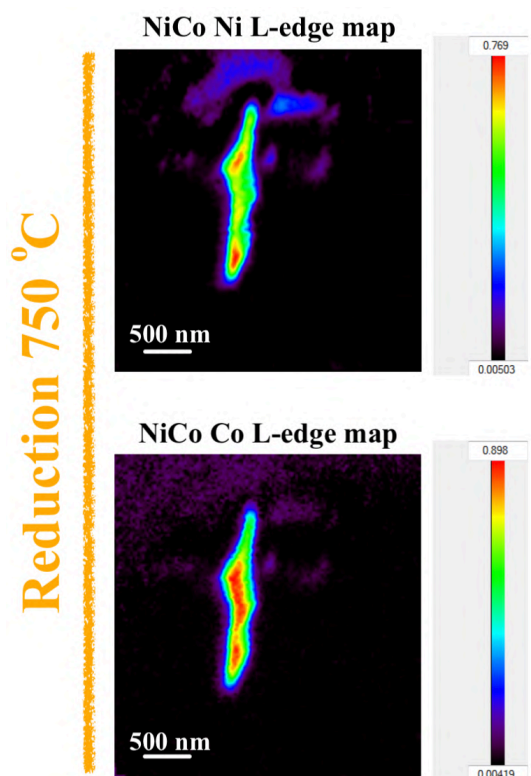


Figure SI. 7: Spectral elemental maps of Ni and Co for the NiCoO/ γ -Al₂O₃ particle reduced at 750 °C.

Figure SI. 8

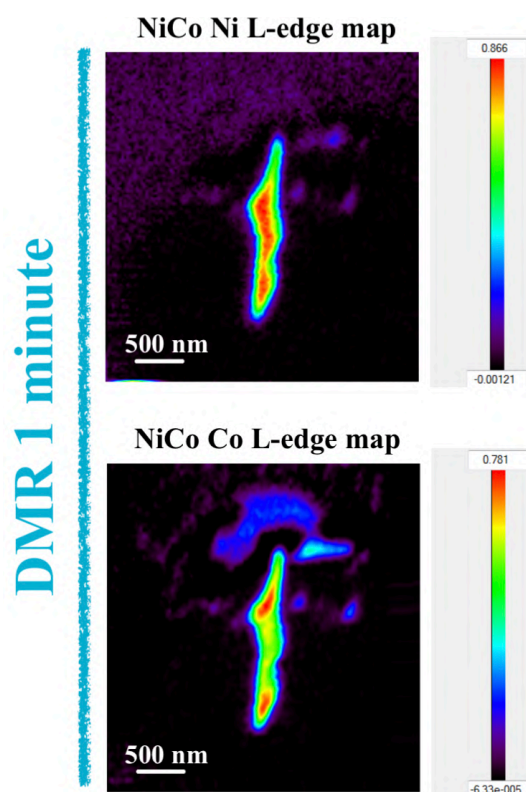


Figure SI. 8: Spectral elemental maps of Ni and Co for the NiCoO/ γ -Al₂O₃ particle after exposure to DMR condition for 1 minute.

Figure SI. 9

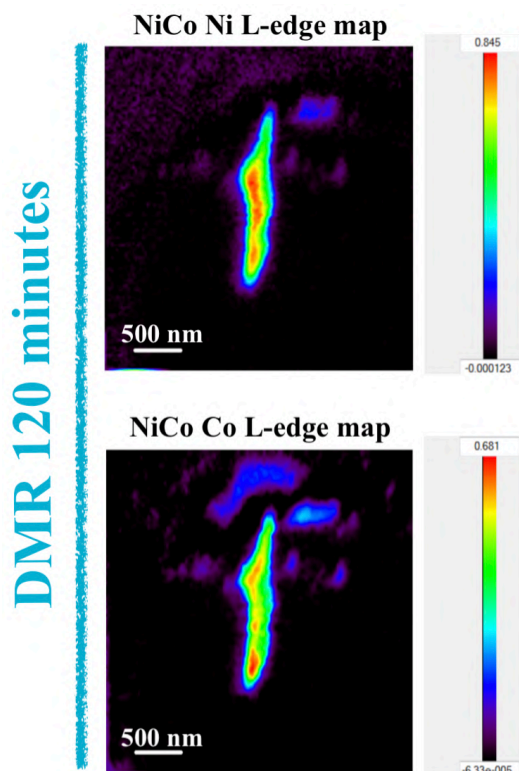


Figure SI. 9: Spectral elemental maps of Ni and Co for the NiCoO/ γ -Al₂O₃ particle after exposure to DMR condition for 120 minutes.

Figure SI. 10

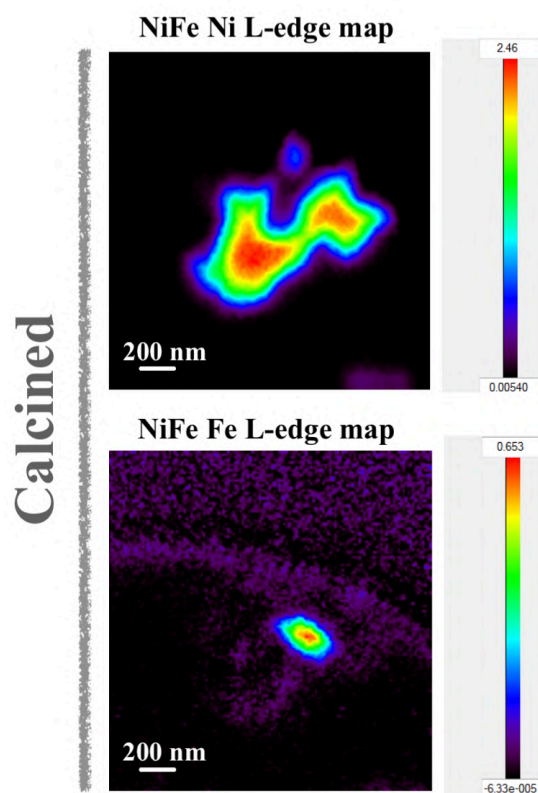


Figure SI. 10: Spectral elemental maps of Ni and Fe for the calcined NiFeO/ γ -Al₂O₃ particle.

Figure SI. 11

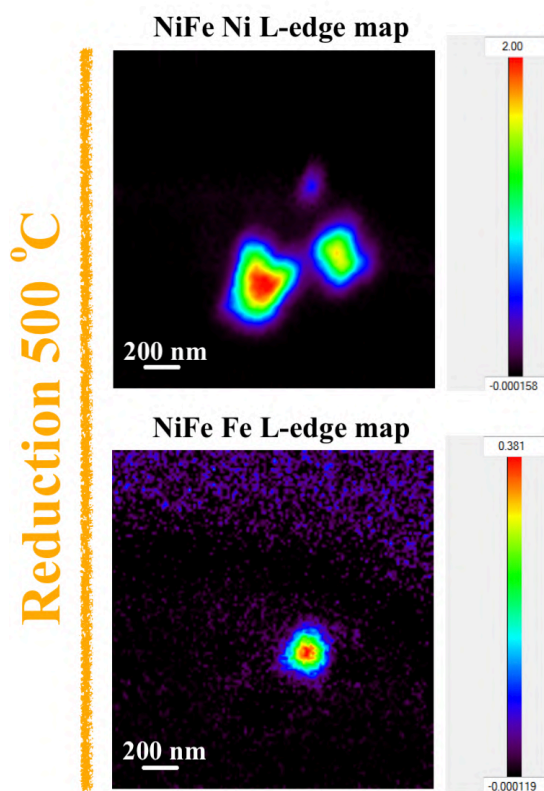


Figure SI. 11: Spectral elemental maps of Ni and Fe for the NiFeO/ γ -Al₂O₃ particle reduced at 500 °C.

Figure SI. 12

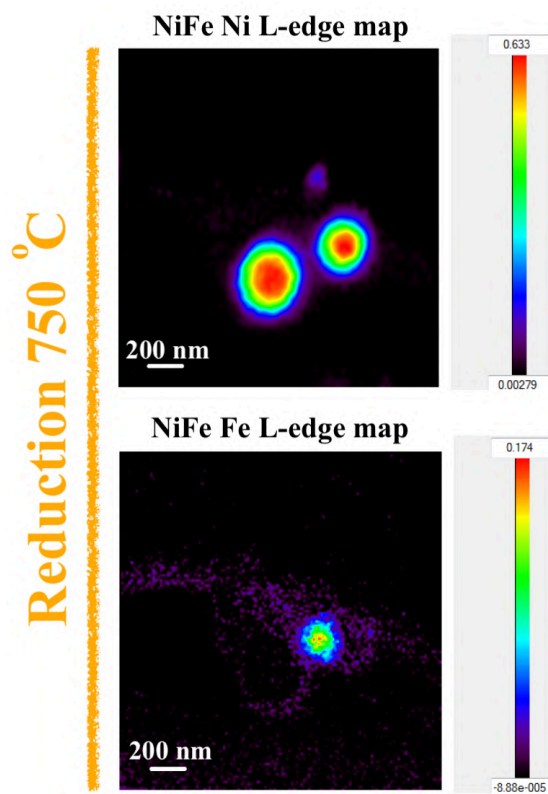


Figure SI. 12: Spectral elemental maps of Ni and Fe for the NiFeO/ γ -Al₂O₃ particle reduced at 750 °C.

Figure SI. 13

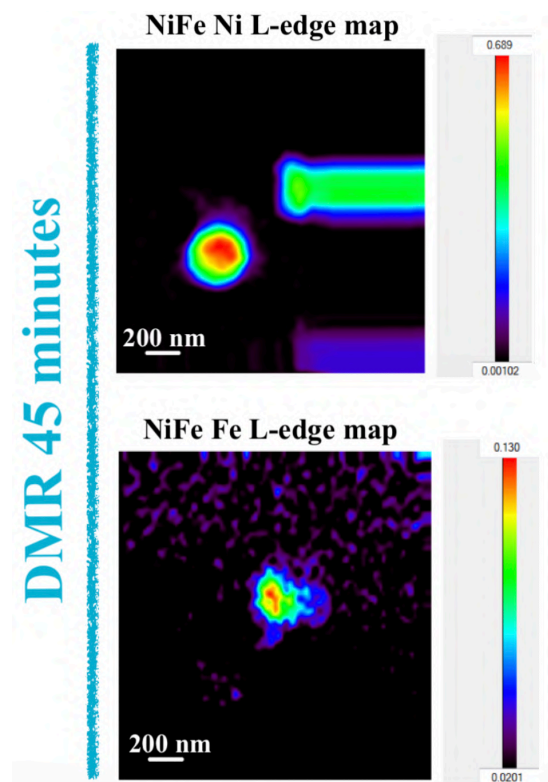


Figure SI. 13: Spectral elemental maps of Ni and Fe for the NiFeO/ γ -Al₂O₃ particle after exposure to DMR condition for 45 minutes.

Figure SI. 14

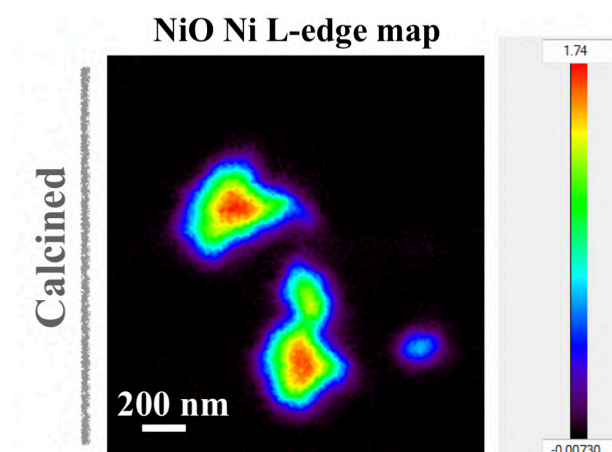


Figure SI. 14: Spectral elemental map of Ni for the calcined NiO/γ-Al₂O₃ particle.

Figure SI. 15

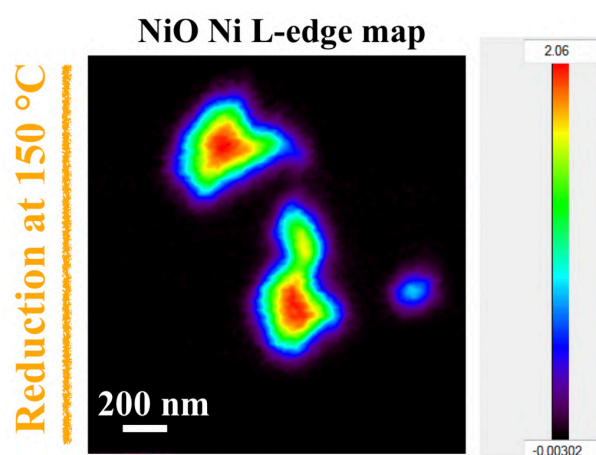


Figure SI. 15: Spectral elemental map of Ni for the NiO/γ-Al₂O₃ particle reduced at 150 °C.

Figure SI. 16

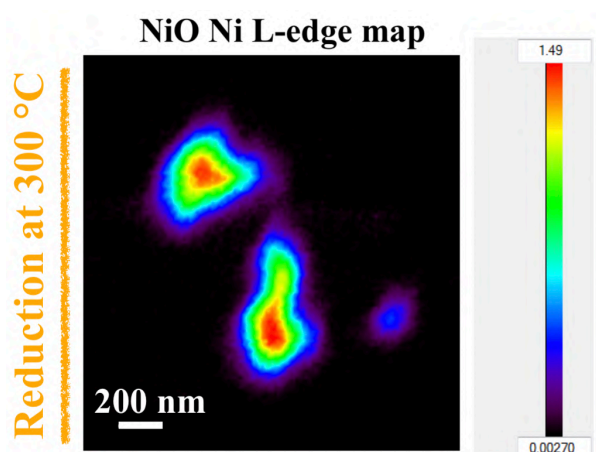


Figure SI. 16: Spectral elemental map of Ni for the NiO/γ-Al₂O₃ particle reduced at 300 °C.

Figure SI. 17

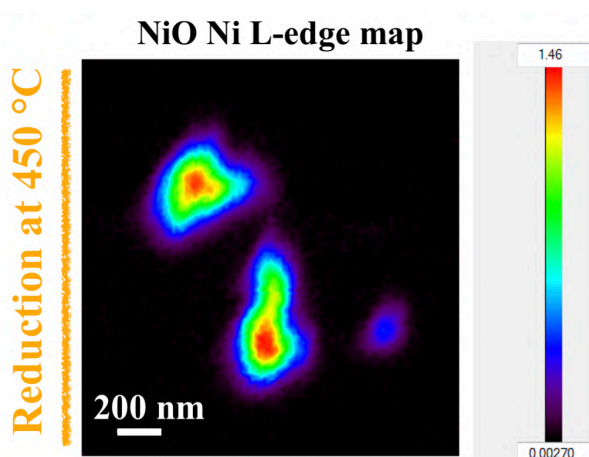


Figure SI. 17: Spectral elemental map of Ni for the NiO/γ-Al₂O₃ particle reduced at 450 °C.

Figure SI. 18

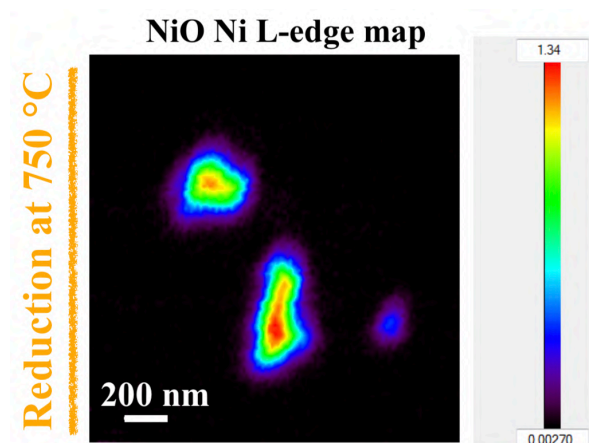


Figure SI. 18: Spectral elemental map of Ni for the NiO/γ-Al₂O₃ particle reduced at 750 °C.

Figure SI 19

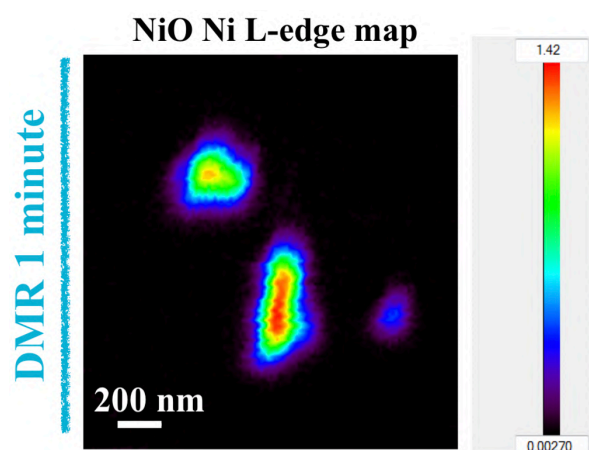


Figure SI. 19: Spectral elemental map of Ni for the NiO/γ-Al₂O₃ particle after exposure to DMR condition for 1 minute.

Figure SI 20

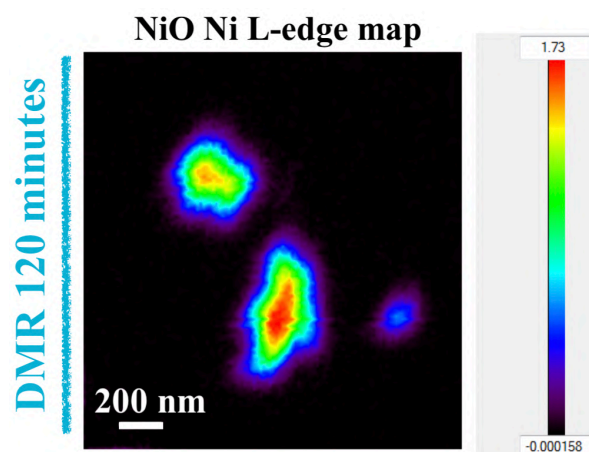


Figure SI. 20: Spectral elemental map of Ni for the NiO/ γ -Al₂O₃ particle after exposure to DMR condition for 120 minutes.

Conclusions

In literature various studies have already demonstrated the huge potential of Ni-based catalysts as promising candidates for the DMR process. Although there have been multiple attempts to unravel the role of transition metals on the DMR catalysts and identify the catalytic active sites, there are still inconsistencies regarding the electronic structure and particle morphology under reductive activation and DMR conditions. Further, a direct correlation between the elemental distribution, electronic structure and particle morphology is missing which is crucial in understanding the role of transition metals. Only a limited number of studies have endeavored to study the properties of DMR catalysts under reaction conditions. Therefore, in this PhD thesis the monometallic NiO/ γ -Al₂O₃ and bimetallic NiCoO/ γ -Al₂O₃, NiFeO/ γ -Al₂O₃ were studied by a combination of STEM-EDX, TPR, DMR activity tests, XRD, in-situ STXM, in-situ XES and HERFD XAS.

With NiCoO being the most frequently studied bimetallic DMR catalyst we mainly used in-situ STXM in **Chapter 2** to expose the electronic structure (of Ni and Co) and morphology of this catalysts. By means of the modified reverse micellar method, we were able to successfully synthesize the NiCoO/ γ -Al₂O₃ DMR catalysts. This method allowed the synthesis of catalysts with the desired elemental ratios and tailored particle size. In this chapter, STEM-EDX data illustrated that both nickel and cobalt are not homogeneously distributed through the sample. Next, TPR profiles highlighted the full reduction of Ni and Co oxides at 500 °C. Activity tests indicated a very high activity for the NiCoO catalysts which was found to be similar to previously reported systems. In-situ STXM measurements showed that the calcined particles exhibit an inhomogeneous distribution of Ni and Co which is consistent with STEM-EDX data. Furthermore, under reductive activation at 500 °C, the formation of voids in the particles was evident. This was assigned to oxygen elimination from the crystal structure. During the reductive activation step at 750 °C a clear elemental segregation was observed; with Co migrating toward the center of the agglomerated nanoparticles and Ni forming a Ni-rich shell on the surface of the particle. The more significant finding was the conservation of the segregated structure under DMR conditions, thus suggesting that Ni is the primary active site, while the more readily oxidized Co may serve as an electron donor to Ni during catalysis. Finally, following the exposure to DMR conditions for 120 minutes Ni-rich branches at the surface of the particles were formed, hence leading to gradual catalyst deactivation.

The experiments presented in **Chapter 2** focused on understanding the changes in both the particle morphology, elemental distributions as well as electronic structure, of Ni and Co in NiCoO particles under reductive activation and DMR reaction conditions. However, a direct comparison with the monometallic NiO/ γ -Al₂O₃ catalyst was not made. Therefore, in **Chapter 3** the structural and electronic properties of NiO/ γ -Al₂O₃ and NiCoO/ γ -Al₂O₃ DMR catalysts were studied by using STEM-EDX, TPR, DMR activity tests, in-situ K $\beta_{1,3}$ XES and HERFD XAS. Firstly, DMR activity tests revealed a significantly higher activity for the bimetallic NiCoO if compared to the monometallic NiO catalyst. Next, in-situ k β -detected XES spectra for the calcined DMR catalysts showed subtle differences in the Ni K β mainline spectral shape and positions which were assigned to subtle variations in the Ni-site symmetry and/or covalency. More specifically, Ni in the

calcined samples was identified as a NiO-like compound with a distorted cubic structure, whereas Co in NiCoO was determined as a Co_3O_4 . Based on both Ni K β XES and HERFD spectra it was shown that the presence of Co in the NiCoO sample increased the reduction temperature of the Ni-site under reductive activation conditions when compared to the monometallic NiO catalysts. Moreover, following the reduction of the NiCoO catalyst at 300 °C, intermediate Ni species with a distinct structure and electronic state were formed. At 600 °C the metal oxides in both catalysts were fully reduced to the metallic phase. An important finding is the stability of both the metallic Co/Ni in the NiCoO and Ni in the NiO of the following the exposure to DMR conditions. These results are in agreement with data from **Chapter 2** which revealed the significance of the metallic Ni and Co for the DMR reaction.

In **Chapter 4** the effect of Fe and Co on the activation of the Ni-site, catalyst activity, stability and catalyst morphology was presented. Hereby the changes in the electronic structure and morphology of monometallic (NiO) and bimetallic (NiCoO and NiFeO) DMR catalysts under reaction conditions was determined. Activity tests revealed that both NiCoO and NiFeO have superior activity when compared to the NiO. Furthermore, STEM-EDX and in-situ STXM experiments confirmed an inhomogeneous Ni and Co distribution in the NiCoO and Fe in the NiFeO catalyst particles. On the contrary, the Ni in the NiFeO was homogeneously distributed on the $\gamma\text{-Al}_2\text{O}_3$ support.

In-situ STXM results reconfirmed the formation of a segregated structure in NiCoO with Co migrating to the center of the particle and consequently the formation of a Ni-rich surface under reduction conditions. STXM spectral elemental maps showed that the segregated structure was conserved during DMR reaction. However, after exposure to DMR conditions for 2 hours a higher Ni to Co ratios were observed on certain regions which finally lead to the formation of Ni-rich branches. On the contrary, for NiFeO sample the formation of a segregated structure was not observed under reduction conditions. In-situ STXM results for the NiFe showed the existence of spherical Ni and Fe particles during the reduction process. Further, this structure was maintained after exposure to DMR conditions for 45 minutes.

Outlook

The results from this dissertation clearly illustrate that using a combination of X-ray spectroscopy and microscopy allows unraveling the properties of complex materials under different reaction conditions. In **Chapter 2** the NiCoO/ γ -Al₂O₃ catalyst was studied with a Ni:Co ratio of 9:1. The synthesis of Ni- and Co oxide samples with different Ni:Co ratios is interesting to confirm the formation of a segregated structure. This will help to understand the effect of Co concentration on both the particle morphology as well as on the activation of the Ni-site during the catalyst activation step. In addition, DMR activity tests using the aforementioned samples can reveal the optimum Ni:Co ratio with the highest DMR activity. Also, studying the effect of various oxides as support material on the dispersion of the active phase and particle morphology during I. catalyst activation and II. under DMR conditions is very interesting. In addition, unravelling the effect of various support materials on the DMR catalytic activity and stability is crucial to develop more effective catalysts.

Additional carbon K-edge STXM measurements on the NiCoO sample under DMR conditions with longer exposure periods is required to understand the carbon deposition on the active phase with greater details. The expected results will provide insight on the deactivation pathway and also show the areas where carbon is deposited.

Due to the relatively limited available beamtime in **Chapter 4** only one NiFeO particle was investigated by in-situ STXM. However, for reproducibility reasons it is crucial to probe multiple NiFeO particles. This allows us to confirm the formation of spherical particles under reduction/activation conditions.

Besides in-situ STXM experiments, additional operando STEM experiments on a new developed setup are being conducted. These data guide us in understanding how the morphology of the particles are influenced by different reaction conditions.

List of Publications

In-situ X-ray Microscopy reveals particle dynamics in a NiCo dry methane reforming catalyst under operating conditions. Beheshti Askari, A.; al Samarai, M.; Morana, B.; Tillmann, L.; Pfänder, N.; Wandzilak, A.; Watts, B.; Belkhou, R.; Muhler, M.; DeBeer, S. *ACS Catalysis*, **2020**. Submitted

In situ X-ray emission and high-resolution X-ray absorption studies of Ni-based Bimetallic Dry Methane Reforming Catalyst. Beheshti Askari, A.; al Samarai, M.; Hiraoka, N.; Ishii, H.; Tillmann, L.; Muhler, M.; DeBeer, S. **In preparation**

The promoting effect of Co vs. Fe on the activation and catalytic activity of supported Ni-based bimetallic dry methane reforming catalysts. Beheshti Askari, A.; al Samarai, M.; Morana, B.; Tillmann, L.; Pfänder, N.; Watts, B.; Muhler, M.; DeBeer, S. **In preparation**

Elucidation Of Structure–Activity Correlations In A Nickel Manganese Oxide Oxygen Evolution Reaction Catalyst By Operando Ni L-Edge X-Ray Absorption Spectroscopy And 2P3d Resonant Inelastic X-Ray Scattering. Al Samarai, M.; Hahn, A.; Beheshti Askari, A.; Cui, Y.; Yamazoe, K.; Miyawaki, J.; Harada, Y.; Rüdiger, O.; DeBeer, S. *ACS Applied Materials & Interfaces* **2019**, *11* (42), 38595-38605.

On the Synergistic Effect of Mn and Ni in the graphene-supported Ni₃MnO₄ system during Operando water oxidation reaction. Al Samarai, M.; Kowalska, J.; Beheshti Askari, A.; Cui, Y.; Hiraoka, N.; Ishii, H.; Lassale-Kaiser, B.; Rüdiger, O.; deBeer, S. **In preparation**